Dissertation
submitted to the
Combined Faculty of Natural Sciences and Mathematics
of Heidelberg University, Germany
for the degree of
Doctor of Natural Sciences

Put forward by
Lennart Volz
born in: Ravensburg, Germany
Oral examination: November 18th , 2020

Particle imaging for daily in-room image guidance in particle therapy

Referees:

Prof. Dr. Joao Seco
Prof. Dr. Oliver Jäkel

Declaration

I, Lennart Volz, declare here that this Ph.D. thesis is the result of my own research, and that all sources used in this work have been duly referenced. This thesis has not been submitted to any other university or institute for a degree award.

Heidelberg, Germany September 7th, 2020

Signed:

Abstract

Particle therapy exploits the highly localized depth dose profile of protons and light ions to deliver a high dose to the target while largely sparing surrounding healthy tissue. The steep dose gradient at the end of the ions range, known as the Bragg peak, however, also makes particle therapy sensitive to range uncertainties. In current clinical practice, a major cause of range uncertainties resides in the conversion of the treatment planning x-ray CT to the patient specific relative stopping power (RSP) map that is crucial for accurate treatment planning. By measuring the energy loss of particles after traversing the patient, particle imaging enables a more direct reconstruction of the RSP. In this thesis, different aspects towards the clinical implementation of particle imaging are investigated. First, a theoretical description of the point-spread function for different particle radiography algorithms is developed in order to explain observed limitations. A novel filtering technique to remove nuclear interaction events in particle imaging is proposed and high quality experimental helium ion CTs are demonstrated. First results from an experimental comparison between particle and x-ray CT modalities for RSP prediction in animal tissue samples are presented. Furthermore, a novel technique for intra-treatment helium ion imaging based on a mixed helium/carbon beam is explored with that relative range changes in the millimeter regime were observable. Finally, novel particle imaging detector designs are investigated. The thesis highlights the potential of helium ion imaging for pre- and intra-treatment image guidance in particle therapy.

Zusammenfassung

Die Teilchentherapie nutzt das hoch-lokalisierte Tiefendosisprofil von Protonen und leichten Ionen, um eine hohe Dosis im Tumorvolumen zu platzieren, während umliegendes, gesundes Gewebe weitreichend geschont wird. Der steile Dosisgradient am Ende der Reichweite der Teilchen in Materie, der Bragg Peak, macht die Teilchentherapie allerdings anfällig gegenüber Reichweitenunsicherheiten. In der aktuellen klinischen Praxis entsteht ein entscheidender Anteil an Reichweitenunsicherheiten durch die Konversion eines konventionellen Röntgen-CTs in das Relative Ionisations-Bremsvermögen (RSP). Die Teilchenbildgebung ermöglicht eine direktere Rekonstruktion der RSP durch das Messen des Energieverlustes von Teilchen nach Durchquerung des Patienten. In dieser Dissertation werden verschiedene Aspekte im Hinblick auf eine klinische Implementierung dieser vielversprechenden Methode untersucht. Zunächst wird eine theoretische Beschreibung der Punktspreizfunktion in der Teilchenradiographie mit verschiedenen Bildgebungsalgorithmen präsentiert. Im Weiteren wird eine neuartige Filtermethode für die Bildgebung mit Helium-Ionen vorgestellt, mit welcher sekundäre Teilchen und solche, die eine nukleare Interaktion erlitten, von den relevanten Primärteilchen unterschieden werden können. Mittels dieser Methode werden experimentelle Helium-Ionen CTs mit einer RSP Genauigkeit von besser als 0.5% erzielt. Erste experimentelle Ergebnisse eines Vergleichs zwischen Teilchen- und Röntgen-CTs für die RSP Rekonstruktion werden präsentiert. Außerdem wird eine neuartige Methode für die Teilchenbildgebung während der Bestrahlung mittels eines gemischten Helium/Kohlenstoff Ionenstrahls untersucht und es wird gezeigt, dass es eine solche Methode ermöglicht, relative Reichweitenunterschiede im Millimeter-Bereich zu detektieren. Abschließend werden neuartige Detektorkonzepte für die Teilchenbildgebung untersucht. Die Ergebnisse der Dissertation verdeutlichen das Potential Teilchenbildgebung und insbesondere der Helium-Ionen Bildgebung für die bildgeführte Teilchentherapie.

Contents

List of Figures

List of Tables

List of Acronyms

ASIC Custom Integrated Circuit

CSDA Continuously Slowing Down Approximation

CSP Cubic Spline Path

CT Computed Tomography

DECT Dual-Energy x-ray CT

DKFZ German Cancer Research Center

ECR Electron Cyclotron Resonance

FBP Filtered Back Projection

FPGA Field-Programmable Gate Array

FWHM Full Width Half Maximum

Geant4 Geometry and Tracking V4

HeCT Helium Computed Tomography

HEBT High Energy Beam Transport

HeRad Helium ion radiography

HIT Heidelberg Ion-Beam Therapy Center

HU Hounsfield Unit

IC Ionization Chamber

LET Linear Energy Transfer

LINAC Linear accelerator

MCS Multiple Coulomb Scattering

MLP Most Likely Path

MTF Modulation Transfer Function

MRI Magnetic Resonance Imaging

MWPC Multi-Wire Proportional Chamber

OAR Organ at Risk

PCT Particle Computed Tomography

pCT Proton Computed Tomography

PET Positron Emission Tomography

PMMA Polymethylmethacrylat

PMT Photo-Multiplier Tube

PRad Particle Radiography

pRad Proton Radiography

RMS Root Mean Square

RSP Relative Stopping Power

RW Range in Water

SECT Single-Energy x-ray CT

SiPM Silicon Photo-Multiplier

SSD Silicon Strip Detector

SLP Straight Line Path

SOBP Spread-Out Bragg Peak

TOPAS TOol for PArticle Simulation

WEPL Water Equivalent Path Length

WET Water Equivalent Thickness

CHAPTER 1

Introduction

> Patients are not water, and accurate range prediction needs an accurate model of the patient, or more precisely, an accurate model of the relative stopping power of different tissues in the patient.
>
> A. J. Lomax - PSI

Particle therapy is a form of cancer radiotherapy that exploits the finite range of protons and light ions to achieve a high dose in the tumor volume while largely sparing the surrounding healthy tissue. Indeed, the energy loss through ionization of the target which is the dominating process for slowing down the particles in the patient increases with decreasing particle velocity. This results in a steep dose peak at the end of the particles' range — the *Bragg peak*. Only little dose is deposited after the Bragg peak, in principle enabling to aim the treatment beam directly at an Organ at Risk (OAR) without inflicting damage to it. This feature of particle therapy presents a sizable advantage compared to the energy loss of photons used in conventional radiotherapy for which the depth dose deposit in the patient decreases exponentially after an initial dose buildup (see Figure 1.1).

The position of the Bragg peak inside the patient can be controlled by changing the particles' initial kinetic energy. To cover a large volume with a prescribed dose, multiple Bragg peaks are superimposed to form a so-called Spread-Out Bragg Peak (SOBP). Due to the kinetic energy necessary for particle ranges to fit typical tumor depths, after the original proposal by Wilson (1946) particle therapy was first limited to pioneer studies at few particle physics institutes. Only with the improvement of accelerator technology in recent decades, especially in terms of size and cost, particle therapy has become a more widespread option for cancer radiotherapy. By the end of 2018, more than 220,000 patients have been treated with particle therapy, of which 190,036 received proton therapy and 27,905 carbon ion therapy (Jermann 2019).

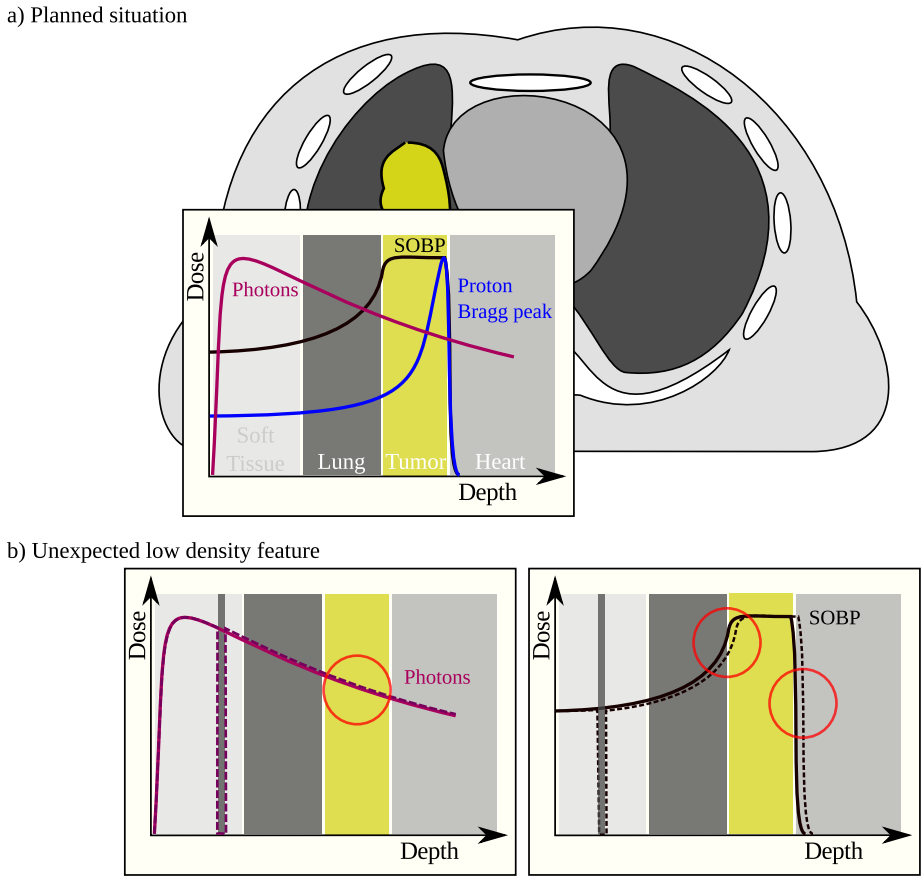

Figure 1.1: Schematic depiction of the concept of particle therapy in comparison to photon therapy. (a) shows the nominal situation, for which the treatment plan was generated. (b) shows the effect of an unexpected low density feature in beam direction on photon and proton treatments. For photons, the dose to target is little affected by the change. For proton therapy the range overshoot resulting from the gap results in an over-dosage of the OAR and under-dosage of the tumor. Figure adapted from Knopf & Lomax (2013).

As with any highly localized dose deposit, the steep dose gradient of the Bragg peak makes particle therapy sensitive to uncertainties in the treatment delivery (Paganetti 2012): differences in the Bragg peak position can lead to severe over-dosage of healthy tissue and/or under-dosage of the tumor volume (shown schematically in Figure 1.1). Such *range uncertainties* can have various stochastic and systematic sources, as detailed in Chapter 3, and limit the exploitation of particle therapy to the full potential. For instance, to avoid under-dosage of the tumor volume, safety margins accounting for known uncertainty sources (Paganetti 2012) are usually added around the clinical target volume. For typical tumor depths the size of these margins can exceed several millimeters, resulting in a significant volume of healthy tissue being administered the target dose. In addition, potentially advantageous treatment directions aiming directly at OARs are usually avoided.

Major efforts in particle therapy research are therefore directed towards reduction of range uncertainty (Parodi & Polf 2018a). Key objectives can be summarized in the development of improved dose delivery techniques (e.g. gating or tumor tracking), treatment planning (e.g. based on Monte Carlo simulations), improved image guidance (e.g. DECT) and in-vivo range verification (e.g. prompt γ). A detailed overview over the state of the art in imaging and treatment monitoring is given in Chapter 3. In this thesis, particle imaging, both in the form of proton and helium ion imaging, is explored as a tool for optimized daily in-room image guidance and online treatment verification.

By measuring the energy loss of particles after they traversed the object particle imaging offers a more direct and in principle more accurate way of reconstructing the tissue-specific Relative Stopping Power (RSP) which is crucial for accurate analytical treatment planning. The RSP information can be retrieved either in the form of a Particle Computed Tomography (PCT) (Hansen et al. 2015, Dedes et al. 2019) or by combining a small number of particle imaging projections with the treatment planning x-ray CT (Schneider et al. 2005, Collins-Fekete et al. 2017a, Gianoli et al. 2020). In addition, Particle Radiographies (PRads) could be used for pre-treatment verification, alignment of the patient setup (Palaniappan et al. 2019), and potentially even for fluoroscopy (Han et al. 2011). At the same time, particle imaging offers a distinct dose advantage over photon based imaging (Schulte et al. 2005, Depauw & Seco 2011, Collins-Fekete et al. 2020), as only the entrance channel of the particles' depth dose profile lies in the patient. A Proton Computed Tomography (pCT) providing highly accurate RSP values for objects of clinically relevant size, for example, might deliver less than 2 mGy (Dedes et al. 2019). In comparison, the dose delivered by a treatment planning head Single-Energy x-ray CT (SECT) can be as much as 20 times larger (Poludniowski et al. 2014). The above therefore makes particle imaging a highly suitable candidate when considering daily in-room image guidance in ion-beam therapy, where an imaging dose as low as possible for a CT scan would be desirable.

In general, image quality in particle imaging suffers from the Multiple Coulomb Scattering (MCS) of the particles inside the patient. In order to improve the image spatial resolution, the concept of *single-event* particle imaging

is to estimate each particle's trajectory through the object based on measurements of its position and direction before and after the patient. To estimate the particle path, various algorithms have been proposed of which the most commonly used is the probabilistic Most Likely Path (MLP) (Schulte et al. 2008). The precision of the MLP is subject to the precision of the tracking information, as well as the probabilistic nature of the scattering (Krah et al. 2018). The latter has been the main argument for investigating heavier ions for single-event imaging (Hansen et al. 2014a, Collins-Fekete et al. 2017d, Gehrke et al. 2018, Piersimoni et al. 2018).

Indeed so far, most research in the field of particle imaging has focused on proton imaging mostly due to the more widespread availability of proton therapy centers. Recently, increased interest has been placed also in imaging with helium ions. The factor 2 reduced MCS of helium ions compared to that of protons enables a more precise path estimation, and with that lower noise in the image and higher spatial resolution. In addition, the lower range straggling of helium ions further benefits the image quality (Gehrke et al. 2018). However, a first experimental study attempting single-event helium ion imaging with a prototype pCT detector, while reporting the expected increase in spatial resolution for Helium ion radiography (HeRad), showed strong image artifacts and comparatively low RSP accuracy for Helium Computed Tomography (HeCT) (Volz et al. 2017).

The overall aim of this thesis was therefore to investigate the optimal detector technology for particle imaging, and in particular, helium ion imaging. As developmental steps towards this goal, first, physical limitations of the image quality achievable with particle imaging are investigated. A key challenge in helium ion imaging is the removal of secondary fragments created from the projectile particles. In this thesis, a novel filtering method based on the well-known ΔE-E particle identification technique is proposed and tested successfully on experimental HeCT data. In addition, it is demonstrated how this method can be useful also for proton imaging by removing uncertainties arising within the energy detection system. Particle imaging is compared to photon imaging modalities as tool for RSP estimation and investigated as potential method for online imaging. These studies aid in identifying the desired features of an ideal imaging system for clinical application. Finally, ways to improve upon current detector systems are investigated. This thesis is presented in the cumulative form, featuring seven manuscripts, five of which are published, one is currently under revision and one is in preparation. Throughout this thesis, the manuscripts are referred to by a capital P followed by a roman numeral indicating their appearance in reverse chronological order.

In Chapter 2, the physical basics underlying particle imaging and therapy will be provided where relevant to this work. In Chapter 3, the current state of the art in image guidance and treatment monitoring for particle therapy is given, in order to embed the thesis results in the greater context of these research areas. Chapter 4 provides a short overview over the individual published manuscripts, presented in Chapter 5. In Chapter 6 and Chapter 7 the thesis will be concluded with a summary discussion.

CHAPTER 2

The physics of particle therapy and imaging

In this chapter, the physical principles underlying particle therapy and particle imaging will be outlined. First, the basic physical interactions necessary for ion beam transport through matter are provided. Then, the production of ion beams with kinetic energies suitable for therapy and imaging at modern medical accelerators is introduced. Finally, scintillation light detectors will be briefly described as such a detector is central to a large part of this thesis. For the sake of conciseness the concepts are only touched upon briefly, and the interested reader is referred to more in-depth literature where applicable.

2.1 Interaction of particles with matter

In order to treat even the most deep seated tumors, ion beams with ranges of up to 30 cm are available at modern treatment facilities (Haberer et al. 2004). The particles' range inside the patient is set via their initial kinetic energy. For protons and helium ions, a range of $\sim$30 cm corresponds to a kinetic energy of $\sim$220 MeV/u, i.e. a velocity of 59 % of the speed of light. For carbon ions, on the other hand, a kinetic energy of $\sim$430 MeV/u is necessary to reach such penetration depth, or 74 % of the speed of light. For particle imaging higher energies than used therapeutically are required such that the ions fully cross the patient. The highest energies currently clinically available are, however, sufficient for full ion CT imaging of head sized objects and to acquire radiographic projections of at least some views of other patient regions (Sarosiek et al. 2019). After traversing the patient, the particles' residual energy/range is then usually measured by stopping them inside a suitable detector.

Ion-beam transport for both therapy and imaging therefore deals with the slowing down of light ions from mid-relativistic energies to rest. In this energy range, the energy loss of the particles in matter is dominated by electromagnetic interactions with the target electrons or (albeit less likely) the target nuclei, leading to ionization of the target atoms and deflection of the projectile.

In addition, elastic or inelastic/non-elastic nuclear interactions with the target nuclei may occur leading to the production of secondary particles and the loss of the primary projectile.

2.1.1 Electronic energy loss

When ions traverse matter they interact in countless Rutherford scatterings with the Coulomb field of the atomic electrons and nuclei. Both the number of interactions per unit length and the energy loss in each single collision are stochastic in nature. As such, the energy loss of particles is subject to a large variation. For a particle with mass M the maximum energy transfer W_{max} in a single collision is described by

$$W_{max} = \frac{2m_e c^2 \beta^2 \gamma^2}{1 + 2\gamma m_e/M + (m_e/M)^2}. \tag{2.1}$$

Here, m_e is the mass of the electron, $\beta = v/c$ is the velocity of the particle relative to the speed of light c, and $\gamma = 1/\sqrt{(1-\beta^2)}$ is the Lorentz factor. For protons at $\beta = 0.59$ the maximum transferable energy is $W_{max} \approx 0.55\,\text{MeV}$. However, such large energy losses are rare, and the most likely energy transfer in each collision is much smaller. For mid-relativistic light ions, the mean energy loss per unit path length, referred to as the *stopping power*, is well described by the renowned Bethe formula (Bethe 1930) with additional correction factors as listed in the particle data group annual report (Tanabashi et al. 2018)

$$-\langle\frac{\mathrm{d}E}{\mathrm{d}x}\rangle = \rho K z_p^2 \frac{Z_t}{A_t}\frac{1}{\beta^2}\left[\frac{1}{2}\ln\left(\frac{2m_e c^2\beta^2\gamma^2 W_{max}}{I^2}\right) - \beta^2 - \frac{\delta}{2} - \frac{C}{Z_t}\right] + L(\beta). \tag{2.2}$$

The constant $K = 4\pi N_A r_e^2 m_e c^2$ comprises Avogadro's constant N_A, the classical electron radius r_e, the electron mass and the speed of light. The primary projectile charge is given as z_p. The target material properties are reflected in the density ρ, the ratio of the atomic charge Z_t and mass A_t, as well as the mean ionization potential I (here denoted I-value). The term $\delta/2$ represents the so-called density correction which accounts for the polarization of the medium by the electric field of the projectile and is relevant for high energies. The term C/Z_t is the shell correction, which corrects for the fact that the target electrons are not stationary. Lastly, the term $L(\beta)$ comprises higher-order (in z_p) corrections relevant at low energies (below 10 MeV for protons): the Barkas correction ($L_1(\beta)$; proportional to z_p^3) and the Bloch correction ($L_2(\beta)$; proportional to z_p^4). Figure 2.1(a) depicts the total stopping power as function of the kinetic energy, as well as the separate contributions from electronic and nuclear interactions, for protons impinging on a homogeneous water absorber.

Equation 2.2 describes the effect an absorber material has on the incident ions (the slowing down). The reciprocal effect on the absorber is called the Linear Energy Transfer (LET) which is defined as the energy absorbed by the medium up to a certain distance (restriction) to the primary track. The stopping power is equivalent to the unrestricted LET, i.e. the energy transfer to a

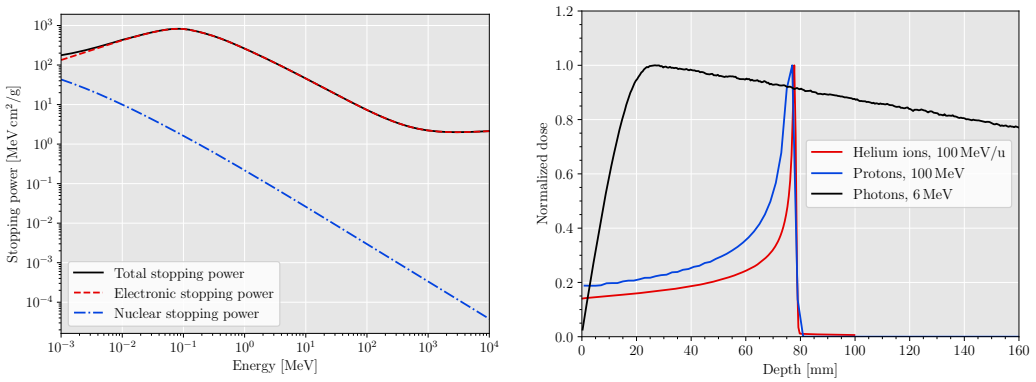

Figure 2.1: Total (solid, black), electronic (dashed, red) and nuclear (dash-dotted, blue) stopping power for protons with kinetic energy relevant for particle therapy and particle imaging impinging on a homogeneous water target. Plot reproduced from the PSTAR program available from the NIST database (Berger et al. 2005). (b) Depth-dose profiles for mono-energetic protons at 100 MeV (blue), helium ions at 100 MeV/u (red) and photons at 6 MeV (black) initial energy impinging on a homogeneous water absorber. The data was simulated using the Geant4 Monte Carlo particle transport code (Agostinelli et al. 2003).

cylinder of infinite radius around the primary track. Equation 2.2 therefore shows the largest dosimetric advantage of ions: at therapeutic energies the stopping power is dominated by the β^{-2} dependence, resulting in the characteristic Bragg peak at the end of the ions' range. Example Bragg peaks are provided in Figure 2.1(b) for 100 MeV protons and 100 MeV/u helium ions impinging on a water target. For comparison, the figure shows the dose distribution for a mono-energetic 6 MeV photon beam.

In the Continuously Slowing Down Approximation (CSDA) the range of the ions can be computed by integrating the inverse stopping power over the energy from their initial kinetic energy (E_{init}) to 0.

$$R_{mat} = \int_{E_{init}}^{0} -\frac{1}{\langle \mathrm{d}E/\mathrm{d}x \rangle_{mat}} \mathrm{d}E, \tag{2.3}$$

where the subscript *mat* is used to specify the stopping power in the absorber material. The range can also be well approximated using an empirical power law known as the Bragg-Kleemann rule (Bortfeld 1997)

$$R = aE_{init}^{p}, \tag{2.4}$$

where a = 0.0024 and p = 1.74 for protons in water. The range of different ions in water as function of the kinetic energy per nucleon is shown in Figure 2.2.

Experimentally, the range of ions can be measured from R_{80}, the position of the 80 % distal dose fall-off of the Bragg peak which for mono-energetic protons corresponds to the depth at which 50 % of the initial particles stop (Paganetti 2012). Since it is not possible to measure the range in all patient tissues, the Range in Water (RW) is used as the reference data underlying the

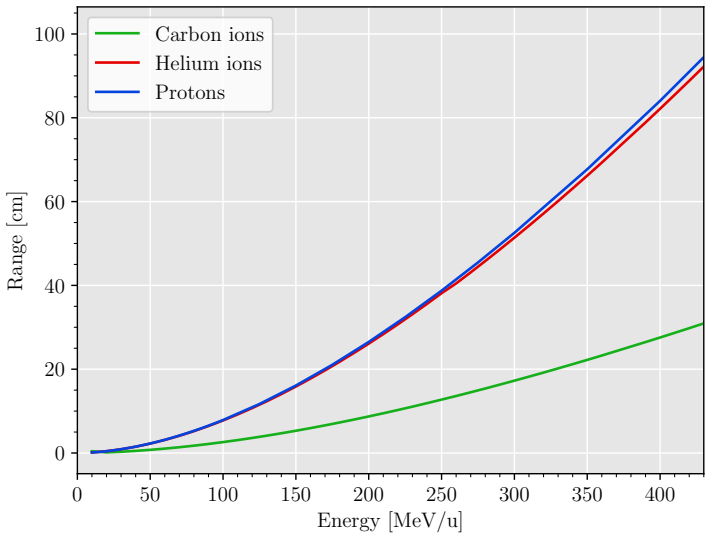

Figure 2.2: Range in water as function of the initial energy per nucleon for protons, helium and carbon ions. The data for protons and helium ions was reproduced from the NIST PSTAR and ASTAR programs (Berger et al. 2005), the data for carbon ions was computed from the ICRU Report 73 (ICRU 2009).

treatment planning at particle therapy facilities. The RW can be translated to the range in the material by using the material RSP which is defined as the material stopping power relative to that of water

$$\mathrm{RSP}_{mat} = \frac{\langle \mathrm{d}E/\mathrm{d}x \rangle_{mat}}{\langle \mathrm{d}E/\mathrm{d}x \rangle_{water}}. \tag{2.5}$$

Since the slope of the stopping power is very similar for different materials, the RSP is nearly constant in energy. This is shown in Figure 2.3 for protons and helium ions in different tissues as simulated with Geant4 (Agostinelli et al. 2003). Arbor et al. (2015) found that in materials relevant for therapy and imaging the RSP varies below 0.7 % in the energy range from 80 MeV to 330 MeV for protons. Hence, the range in a material can be computed from the range in water as

$$R_{mat} \approx R_w / \mathrm{RSP}_{mat}. \tag{2.6}$$

Another useful quantity is the Water Equivalent Thickness (WET). It is defined as the thickness of water that would result in the same energy loss as experienced by the particles when traversing a material of thickness Δx. Denoting the particles' initial kinetic energy E_{init} and their residual energy after passing the absorber E_{res} we can write

$$\mathrm{WET} = \int_{E_{init}}^{E_{res}} -\frac{1}{\langle \mathrm{d}E/\mathrm{d}x \rangle_{water}} \mathrm{d}E \tag{2.7}$$

$$= \int_{\Delta x} \mathrm{RSP}_{mat} \mathrm{d}x \tag{2.8}$$

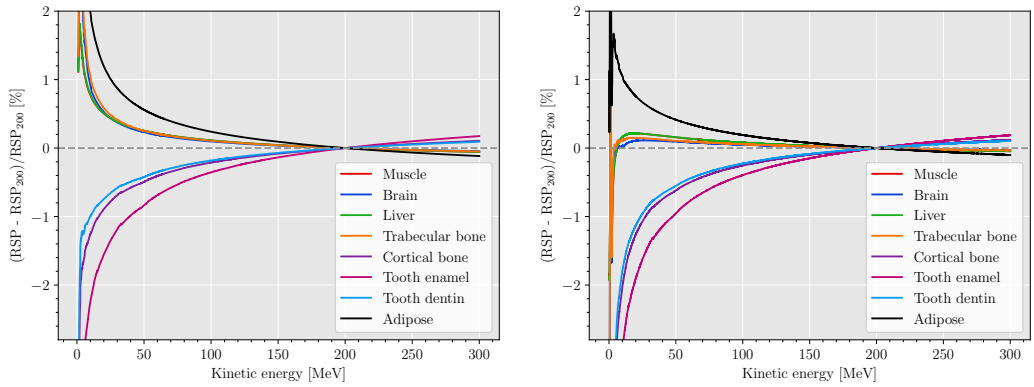

(a) Protons **(b)** Helium ions

Figure 2.3: Relative difference between the RSP calculated as a function of energy and the RSP at nominal energy of 200 MeV/u (RSP_{200}) for (a) protons and (b) helium ions. Different human tissue compositions are shown. For Liver, Muscle and Adipose the tissue composition was taken from Hünemohr et al. (2014b), the other tissues had chemical compositions as given in the ICRP Publication 89 (ICRP 2002). The necessary stopping power tables were calculated with the Geometry and Tracking V4 (Geant4) simulation toolkit.

The position of the ions' Bragg peak can be computed from the length traveled in the patient which corresponds to a WET equal to the particles' RW.

From the above, it becomes immediately clear that accurate (analytical) treatment planning in particle therapy requires an accurate representation of the patient RSP map. Equation 2.8, however, also presents a possible way to extract this information: the WET is the line integral over the RSP. Hence, the methods for back projection of line integral quantities presented already in the seminal work by Cormack (1963) can be applied and the RSP map can be retrieved from Computed Tomography (CT) reconstruction of WET projections acquired of the patient. Hence, Equation 2.8 suggests the use of an Particle Computed Tomography (PCT) for treatment planning in particle therapy. In fact, PCT is one of three potential applications Cormack states in his original work — right along x-ray CT.

2.1.2 Energy and range straggling

For a single ion, the Bragg peak would be much sharper than what is shown in Figure 2.1(b) for proton and helium ion beams. The energy loss experienced by particles traversing a certain thickness of absorber material is subject to fluctuations due to the statistical nature of a large, but finite number of independent interactions. This is referred to as *energy straggling*, the corresponding effect on the range *range straggling*, and results in a broadening of the Bragg peak for a beam of particles.

Energy straggling was first described theoretically by Landau (1965) and later extended by Vavilov (1957). The energy loss distribution, referred to as Landau-Vavilov distribution, is highly skewed with a long tail towards large

energy losses. It describes the energy loss distribution well for thin absorbers (Tanabashi et al. 2018). For absorbers of intermediate thickness, i.e. as long as the relative energy loss of the particles does not exceed ∼35 % (for protons and helium ions) of their initial kinetic energy (Payne 1969), the distribution approximates a Gaussian. For even thicker absorbers, the distribution becomes skewed again as initially described by Tschalär (1968): Consider an ion beam traversing a series of material slabs. With each subsequent slab traversed by the particles the energy loss distribution widens, and therefore also the distribution of the beam particles' kinetic energy. When the kinetic energy of individual particles in the beam can no longer be assumed approximately equal, the difference in energy loss experienced by the beam particles in subsequent slabs becomes significant. Due to the β^{-2} dependence of the stopping power, the particles that have a lower kinetic energy after traversing the first couple of slabs will continue to loose increasingly more energy in subsequent slabs compared to the particles with kinetic energy greater than the mean. The distribution again approaches a form that resembles the shape of the Landau-Vavilov distribution.

The variance of this distribution for particles with initial energy E_{init} and residual energy E_{res} is given in Tschalär & Maccabee (1970) as

$$\sigma^2_{stragg}(E_{res}) = \langle \mathrm{d}E/\mathrm{d}x \rangle \int_{E_{init}}^{E_{res}} \frac{\xi}{\langle \mathrm{d}E/\mathrm{d}x \rangle^3} \mathrm{d}E, \tag{2.9}$$

where ξ is defined as

$$\xi = \rho_e K \frac{1 - 0.5\beta^2}{1 - \beta^2}. \tag{2.10}$$

Here, ρ_e is the relative electron density, and K is a constant as defined for the stopping power formula (Equation 2.2). Tschalär & Maccabee (1970) note that nuclear interactions and particles scattering outside of the detector can have a great impact on the measured energy loss variance. This effects negatively the accuracy of data filters usually applied in proton imaging (Schulte et al. 2005), which is investigated in publication P.XI.

Assuming the particles to traverse a homogeneous absorber and a perfect energy detector, the energy straggling can be related to the variance in WET as in Collins-Fekete et al. (2020), where higher order terms are neglected

$$\sigma^2_{WET} = \sigma^2_{stragg} \left(\frac{\partial WET}{\partial E} \right)^2 = \frac{\sigma^2_{stragg}}{\langle \mathrm{d}E/\mathrm{d}x \rangle_{water}(E_{res})^2} \tag{2.11}$$

In particle imaging, energy straggling is a major source of noise (Schulte et al. 2005, Dickmann et al. 2019, Collins-Fekete et al. 2020). Even with perfect detectors, Equation 2.11 imposes a minimum level of noise in the image.
For particle therapy, the straggling of the ions affects the longitudinal dose gradient achievable in a single-field irradiation. Assuming the energy straggling to be nearly Gaussian, the range straggling can be obtained as (Bethe &

Ashkin 1953)

$$\sigma^2_{range} = \int_0^R \frac{\mathrm{d}\sigma^2_{stragg}}{\mathrm{d}x} \left(\frac{\mathrm{d}E}{\mathrm{d}x}\right)^{-2} \mathrm{d}x. \tag{2.12}$$

A detailed tabulated list of range straggling values can be found in Janni (1982). The range straggling of the ions relative to their initial range is approximately constant. For 200 MeV protons stopping in water the relative range straggling (σ_{range}/RW) is about 1.1 % (Bashkirov et al. 2016a). For light ions at the same initial range, the range straggling scales with inverse ratio of their mass (M_I) compared to the proton mass (M_p) (Durante & Paganetti 2016).

$$\sigma^2_{range,ion} = \frac{M_p}{M_I} \sigma^2_{range,proton} \tag{2.13}$$

Hence, for helium particles, the range straggling is only half that of protons resulting in a sharper Bragg peak, as seen in Figure 2.1(b). The decrease of the straggling with increase of the projectile mass is therefore part of the rationale for the use of light ions for therapy (Durante & Paganetti 2016) and imaging (Gehrke et al. 2018).

2.1.3 Multiple Coulomb scattering

The major obstacle for particle imaging compared to x-ray imaging is the scattering deflection suffered by the particles while traversing the medium, known as Multiple Coulomb Scattering (MCS). Accurate image reconstruction of particle imaging data requires to accurately model the scattering of the particles inside the patient. MCS is also of central importance in particle therapy, as it dominates the lateral dose penumbra and is a potential factor for range uncertainty (Paganetti 2012).

The deflection of particles in matter presents the sum over *countless* individual single Rutherford scattering interactions. The resulting distribution of the angular deflection θ of the beam particles is adequately described by the theory of Molière (1948) who solved the transport theory for a beam of charged particles traversing a thin slab of arbitrary material. Molière describes the scattering distribution through of a series of correction functions, the first of which is a Gaussian.

Indeed, at small angles, i.e. for the core of the pencil beam, the Gaussian function dominates the distribution. At large angles, i.e. the halo of the pencil beam, the angular distribution is dominated by single or plural large angle scattering relative to which the many small angle deflections have less of an effect. Consequently, the distribution approximates the large angle behavior of single Rutherford scattering which is proportional to θ^{-4}.

Molière's theory is known to be accurate to few percent as demonstrated for example with experimental data from a 160 MeV proton beam (Gottschalk et al. 1993). However, its computation is not practical for the purpose of particle therapy or imaging due to its complexity. On the other hand, since most of the particles are anyways contained in the small angle region of the distribution, the full theory can be reasonably well approximated with a Gaussian

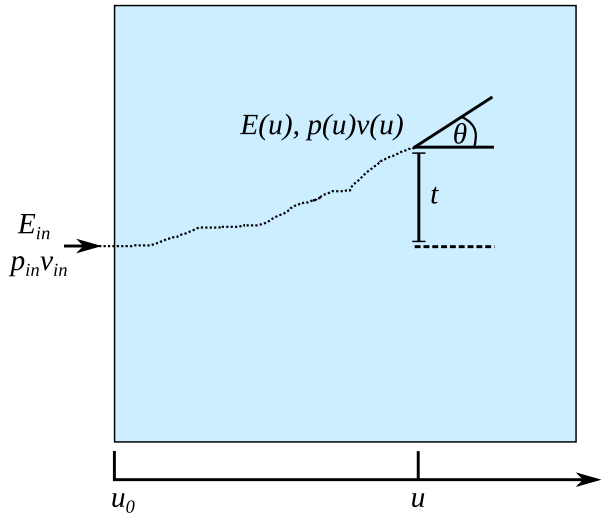

Figure 2.4: Schematic depiction of the scattering of a particle with initial energy E_{in} (corresponding to a momentum velocity of $p_{in}v_{in}$) in a homogeneous water absorber. The beam's direction is marked by the x-axis the lateral direction by the y-axis, the particles angle to the beam axis is denoted θ. Fermi-Eyges theory provides the probability the particle to have a certain lateral and angular displacement at depth u.

function of adequate width. This so-called Fermi-Eyges approximation (Rossi & Greisen 1941, Eyges 1948) of MCS suffers only little in accuracy (Gottschalk 2010), but is much simpler to handle than Molière's theory and hence widely adopted. Consider a particle traversing through homogeneous water absorber as depicted in Figure 2.4. In the Fermi-Eyges approximation, the probability of finding a particle at depth u with a lateral displacement between t and $t + \mathrm{d}t$ and angular displacement between θ and $\theta + \mathrm{d}\theta$ is given as

$$P(t,\theta)\mathrm{d}t\mathrm{d}\theta = \frac{1}{\sqrt{2\pi}B}\exp\left[-\frac{1}{2}\frac{A_0t^2 - 2A_1t\theta + A_2\theta^2}{B}\right]. \tag{2.14}$$

The moments A_n, and B are defined as

$$A_n(u,u_0) = \int_{u_0}^{u}(u-u')^nT(u')\mathrm{d}u \tag{2.15}$$

$$B(u,u_0) = A_0A_2 - A_1^2, \tag{2.16}$$

where $T(u)$ is the so-called *scattering power* which describes the rate of change of the mean squared displacement angle with depth in the absorber

$$T(u) = \frac{\mathrm{d}\langle\theta^2\rangle}{\mathrm{d}u}. \tag{2.17}$$

With the definition of $T(u)$ it is clear that A_0 represents the variance in θ (scattering is a zero-mean process). Similar, A_2 presents the lateral variance of the

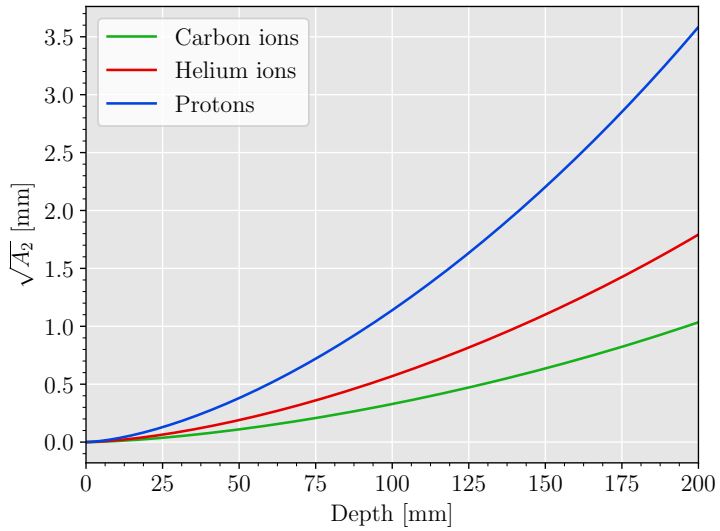

Figure 2.5: Standard deviation of the lateral displacement ($\sqrt{A_2}$) for different ions at initial energy of 200 MeV as a function of depth in a homogeneous water absorber. The plots were generated by evaluating the generalized Highland scattering power with the parametrization of the $1/(p(u)^2v(u)^2)$ function given for 200 MeV protons in (Schulte et al. 2008). The comparison of different ions was achieved by scaling the scattering standard deviation by the square root of the ratio of the protons to the ions mass (Gottschalk 2012)

beam and A_1 presents the angular/lateral co-variance.

The representation of the scattering power is thereby central for the accuracy of the Gaussian approximation to MCS. Several different formulas for the scattering power have been proposed over the decades. A detailed overview over these approximations and evaluation of their validity can be found in Gottschalk (2010). In particle imaging, the generalized Highland scattering power (Gottschalk et al. 1993) is the most widely used. It is based on the scattering variance proposed by Highland (1975) with the corrections brought forward by Lynch & Dahl (1991). Using the generalized Highland scattering power the scattering moments (Equation 2.15) can be computed as

$$A_n(u,u_0) = E_0^2\left[1+0.038\ln\left(\int_{u_0}^{u}\frac{\mathrm{d}u}{X_0(u)}\right)\right]^2\int_{u_0}^{u}\frac{(u-u')^n}{p(u)^2v(u)^2}\frac{z_p^2}{X_0(u)}\mathrm{d}u, \quad (2.18)$$

where $E_0 = 13.6\,\mathrm{MeV}$ is a constant, $p(u)$ is the particles momentum and $v(u)$ its velocity as function of the depth in the absorber (Schulte et al. 2008). X_0 is the radiation length of the material which is defined as the mean distance after that a high-energy electron has lost all but $1/e$ of its initial value.

The ion specific quantities in Equation 2.18 are the projectile charge z_p and the momentum-velocity function. The momentum-velocity function can be described in terms of the kinetic energy (E_{kin}) and mass of the projectile (M_I)

as

$$p(u)v(u) = \frac{E_{kin}(u) + 2M_I c^2}{E_{kin}(u) + M_I c^2} E_{kin}(u) \tag{2.19}$$

The comparison of the scattering for different ions at the same initial range can be achieved by computing Equation 2.15 with Equation 2.19 both for protons and scaling the result by the ratio of the protons to the ions mass (Gottschalk 2012). The increase in scattering for heavier ions due to the z_p dependence is offset by the necessity of higher initial velocities to get to the same range. A comparison of the lateral displacement in water for protons, helium ions and carbon ions at the same range is provided in Figure 2.5.

The factor 2 reduced scattering of helium ions is the main argument of using these ions for imaging (Hansen et al. 2014a, Collins-Fekete et al. 2017d, Volz et al. 2017, Piersimoni et al. 2018, Gehrke et al. 2018). Since the lower scattering also provides better achievable lateral dose penumbra for therapy, a renewed interest has been placed in helium ion therapy at the Heidelberg Ion-Beam Therapy Center (HIT) (Mairani et al. 2016, Krämer et al. 2016).

2.1.4 Nuclear interactions and fragmentation

Aside from the electromagnetic interaction, the particles can undergo nuclear interactions with the target nuclei. Nuclear interactions are of great importance for accurate dose calculation in the treatment planning system (Durante & Paganetti 2016), noise in particle imaging (Schulte et al. 2005, Collins-Fekete et al. 2020) and online treatment monitoring through the production of secondary radiation (Verburg et al. 2015, Bisogni et al. 2017, Félix-Bautista et al. 2019). The following provides a short overview over the important aspects.

Nuclear interactions can be differentiated in coherent (interaction with the target nucleus as a whole) and incoherent (interaction with individual nuclei) (Gottschalk et al. 2014). Coherent interactions can be further subdivided in elastic and inelastic interactions. Elastic interactions leave the projectile energy almost unchanged and the target nucleus only receives a small recoil kinetic energy. For inelastic collisions, the recoil nucleus remains in an excited state after collision and undergoes nuclear de-excitation under emission of secondary radiation (e.g. by emitting a prompt γ). In such interactions, the projectile usually experiences a hard scatter. Hence, coherent interactions will contribute predominantly to the halo of the beam. For particle imaging, these interactions contribute to the image noise, they are usually removed via filters acting on the particle angular displacement (Schulte et al. 2008).

Incoherent interactions, also referred to as non-elastic interactions, generally lead to the fragmentation of the target and/or, in the case of projectiles heavier than protons, the primary. In general, non-elastic nuclear interactions lead to a loss of primary projectiles, and charged secondary radiation produced in these interactions has a significant effect on both therapy and imaging. The loss of primary particles for protons, helium ions and carbon ions at a RW of $\sim$26 cm, i.e. relevant for particle imaging, is shown in Figure 2.7.

Charged target fragments are generally produced isotropically and are usually heavy particles with only short ranges (Loveland et al. 1986). Hence, target

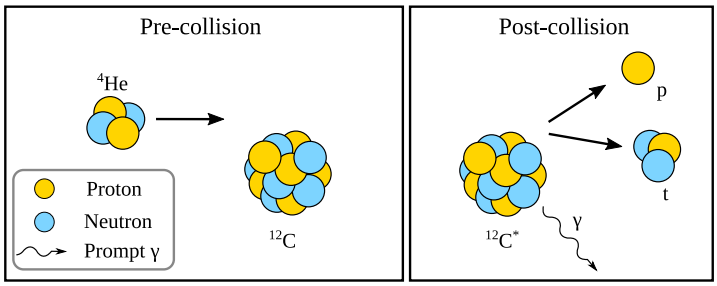

Figure 2.6: Schematic depiction of an example collision between a ^{4}He projectile and a ^{12}C target to explain the effect of nuclear interactions. Specifically the reaction ^{12}C(^{4}He, p t)^{12}C* is depicted. The excited remnant of the target nucleus undergoes nuclear de-excitation, e.g. by emitting a prompt γ photon.

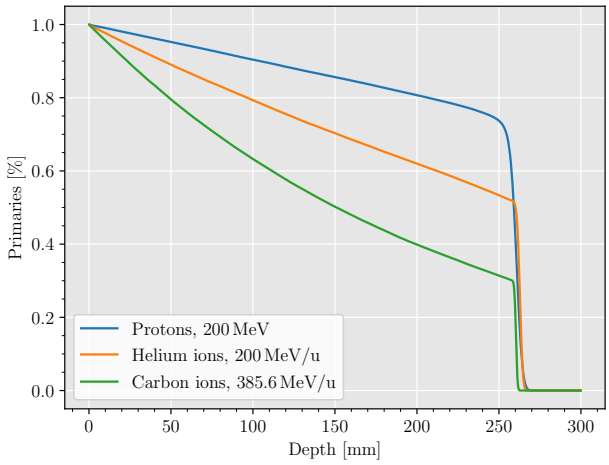

Figure 2.7: Relative loss of projectile particles as function of the depth in water for protons, helium ions and carbon ions. The initial range was ∼26 cm, the respective energies are indicated in the plot. For each curve 10^5 primary particles were propagated through water using the Geant4 simulation toolkit (see Chapter 4).

fragments contribute to a locally advanced dose, which due to the fragments' high LET also corresponds to a high biological effectiveness. For protons, "quasi-free" interaction with the target nuclei can occur, knocking out single protons, neutrons or alpha-particles. Especially the secondary protons are of importance, as these usually have a long range. Hence, in proton therapy, they correspond to the farthest reach of the beam halo (Gottschalk et al. 2014), while in particle imaging they contribute significantly to the image noise (Schulte et al. 2005).

For ions, projectile fragmentation (shown schematically in figure 2.6) complicates the picture. Projectile fragments are produced with only a small shift in direction and velocity (Zeitlin & La Tessa 2016). Consequently, projectile fragments are predominantly found in the core of the beam, albeit with a broader lateral distribution (Rovituso et al. 2017). In addition, they are lighter than the primary particle and may receive additional momentum due to their Fermi motion. As such, they may have longer range than the primary nucleus and deposit dose beyond the Bragg-peak. This characteristic *dose-tail* in the depth-dose profiles of ions is a limiting factor when considering treatment directions aiming at OARs. Moreover, the potential of further fragmentation of the secondaries also needs to be considered in accurate dose planning.

To describe fragmentation processes, usually the abrasion-ablation (also denoted cascade-evaporation) model is considered. It consists of two steps: the abrasion step in which pre-fragments are generated from the ion-ion interaction, and the ablation step where excited pre-fragments de-excite under emission of light particles and prompt γ.

The cross section σ_R of the fragmentation process can in a first approximation be described by empirical Bradt-Peters formula (Bradt & Peters 1950). Assuming the radius of the nucleus to be described by $r_N = r_0 A_I^{1/3}$ (Durante & Paganetti 2016), where r_0 is a constant and A the atomic mass, the cross section can be written as:

$$\sigma_R = \pi r_0^2 (A_1^{1/3} + A_2^{1/3} - b)^2, \tag{2.20}$$

where b is the overlap factor, and the subscripts 1 and 2 denote the partaking nuclei. For the energy range of concern in particle therapy and imaging, the formula has to be extended to also include the general energy dependence of the total cross section. Sihver et al. (1993) and Tripathi et al. (1996) provide empirical parametrization, both of which are used in Monte Carlo transport codes. Especially, the model by Tripathi has recently been experimentally bench-marked for helium ions on various targets of clinical relevance in the extensive studies by Horst et al. (2017) and Horst et al. (2019). In their study, the Tripathi light ion model was found to accurately describe the helium total reaction cross section after a small parameter change.

Let us digress briefly here to discuss in more detail the special case of the helium nucleus, as the effect of fragmentation in helium particle imaging is investigated in publication P.XII. The helium nucleus is especially tightly bond with the first excited state lying about 20 MeV above the ground state (Cucinotta et al. 1993). Consequently, helium ions are especially stable and fragment significantly less compared to other light ions (Zeitlin & La Tessa 2016). In addition, the number of projectile fragments is small, amounting to

only five particles – neutrons (n), protons (p), deuterons (d), tritons (t), ^{3}He – that for the collision with hydrogen are produced in only 6 possible reaction channels (Krämer et al. 2016). The possible combination of fragments (excluding pick-up channels) is (Cucinotta et al. 1993)

$$^4\mathrm{He} + T = \begin{cases} ^3\mathrm{He} + n + X, \\ t + p + X \\ d + d + X \\ d + p + n + X \\ p + p + n + n + X \end{cases}, \tag{2.21}$$

where T denotes the target, and X the target remnants after collision. The most dominantly produced fragments are protons, which given the same velocity (energy per nucleon) have approximately the same range as the primary helium ion (see Figure 2.2). This is of special advantage for the distal dose gradient in helium ion therapy (Krämer et al. 2016). However, for particle imaging, the charged helium fragments are readily detected by the imaging detectors and the similarity in range between primary helium ions and secondary fragments makes discerning them difficult. Due to the detrimental effect these fragments have on the image quality, accurate methods for removing the fragment contamination from the primary signal are needed for high quality helium ion imaging.

2.2 Particle acceleration

In this section the acceleration of light ions to kinetic energies suitable for imaging and therapy, as well as the important aspects of beam delivery will be briefly introduced as relevant for ion imaging and the helium/carbon ion mixed beam evaluated in publication P.VII. A schematic illustration of the HIT complex, where all experimental campaigns of this thesis have been conducted, is provided in Figure 2.8. The facility comprises three Electron Cyclotron Resonance (ECR) ion sources, a Linear accelerator (LINAC) injector and a synchrotron main accelerator. The High Energy Beam Transport (HEBT) leads to two horizontal treatment rooms, one experimental cave and one ion gantry.

2.2.1 Ion sources

Ion sources in particle therapy applications need to fulfill high standards regarding safety, flexibility, cost-effectiveness and ease of maintenance. Several different source types are used in proton therapy facilities and a detailed overview can be found in Muramatsu & Kitagawa (2012). For therapy centers utilizing carbon ion beams, the only source type in use is the ECR ion source. The principle of an ECR ion source is to feed a neutral source gas into a plasma chamber, in which a constant magnetic field is present. Inside the chamber, the free electrons in the plasma circulate in the magnetic field

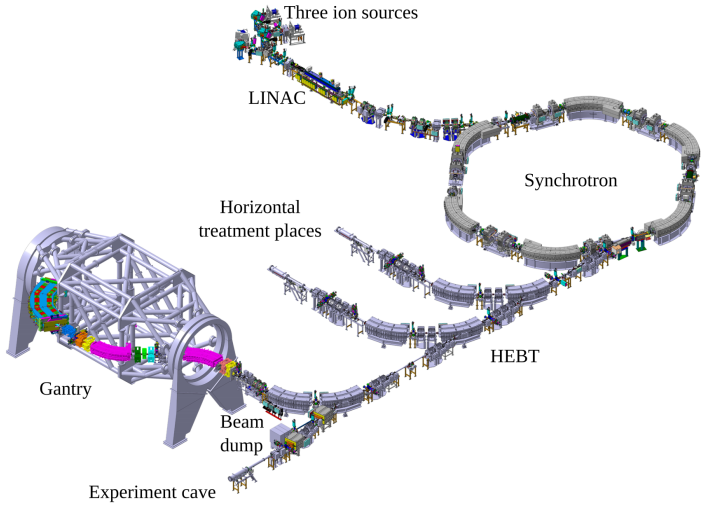

Figure 2.8: Accelerator complex of the HIT facility. The facility comprises three ECR ion sources, an RFQ-Linac pre-accelerator, a synchrotron accelerator, and a high energy beam transport system leading to three horizontal irradiation rooms, as well as a heavy ion gantry. Figure adapted from Winkelmann et al. (2014) with kind permission by the authors.

with the cyclotron frequency. By feeding in a high-frequency electromagnetic wave into the plasma, the plasma electrons can be accelerated resonantly if the wave-frequency is equal to the cyclotron frequency. With this, enough energy can be imparted on the electrons that they can ionize the gas nuclei creating positively charged ions. The charge state of the ions thereby depends on the kinetic energy of the plasma electrons and the confinement time of the ions in the plasma. Contemporary ECR sources used at medical accelerators can produce sufficient currents of multiply charged carbon ions where usually $^{+4}$C is extracted (Drentje et al. 2008, Winkelmann et al. 2014). At the HIT facility, the partially stripped ions are fully stripped of their electrons by a stripping foil placed after the LINAC pre-accelerator.

2.2.2 Accelerator

Although recently, new concepts for light ion medical LINACs (Mustapha et al. 2019) and superconducting isochronous cyclotrons (Cyclone®400; IBA, Louvain-La-Neuve, Belgium) are under development, contemporary carbon therapy facilities rely exclusively on synchrotron accelerators, while proton therapy centers are predominantly using cyclotrons. A detailed overview over medical accelerator technology can be found in Owen et al. (2016).

The principal concept of circular accelerators is to use a magnetic field to keep the particles on a circular trajectory such that they traverse the same accelerating HF field multiple times. The radius (also denoted gyroradius) the

particles trace in the applied magnetic field is

$$r = \frac{\gamma M_I v}{q|B|}, \tag{2.22}$$

where q is the charge of the ion, v its velocity and M_I its mass. $|B|$ is the magnetic field. To quantify the stiffness of a particle against deflection by a magnetic field, usually the magnetic rigidity $\rho = r|B|$ is used. The magnetic rigidity depends only on the velocity and charge/mass ratio of the particles. This opens up an interesting application, explored in publication P.VII: The similarity in the charge/mass ratio of fully stripped helium and carbon ions might enable their simultaneous acceleration to the same velocity. While the carbon ions are used to treat the tumor, the helium ions, due to their larger range at the same velocity (Figure 2.2) can fully penetrate the patient, enabling online dose monitoring. This is the key concept exploited in publication P.VII.

When the energy of the particles is increased, for a constant magnetic field, the particles will trace a spiral. This is the concept of cyclotrons, where the particles are accelerated between two half circles (the"dee's") until they reach the maximum energy determined by the cyclotron's radius and magnetic field strength. The extracted beam is degraded to the desired energy by inserting aborbers and collimators in the HEBT. The cyclotron delivers quasi-continuous beam, with very short particle bunch widths and distances (order of 2 ns and 10 ns, respectively) (Krimmer et al. 2018). For most contemporary proton medical cyclotrons, the maximum energy is 230 MeV (Owen et al. 2016), limiting the capability for particle imaging of thick patient regions.

In synchrotrons, on the other hand, the particles are kept on a constant radius through several bending magnets, and the magnetic field is changed with the particle acceleration. As a consequence of the design of the synchrotron, the particles in the synchrotron are tightly distributed around a single energy and are grouped in bunches created by the interplay of the particle arrival time at the RF cavity and the phase of the accelerating RF wave. The acceleration of the particles to the desired energy takes several seconds, due to the time needed to increase the field of the bending magnets. Once at the desired energy, the slow extraction of the particles over several seconds - the *spill* - is performed (Schoemers et al. Sep 2015). Deceleration or re-acceleration of the particles within a spill might also be feasible (Schömers et al. 2017). After the spill, the accelerator ramp-down also takes around a second. Ramp-up and -down together create the spill pause, which at the HIT facility is $\sim$4 s in duration.

For particle imaging at synchrotron facilities, the above has important consequences: firstly, the bunch spacing at synchrotron facilities is in the order of 100-200 ns, depending on the circulation frequency (i.e. the energy) of the bunches (Krimmer et al. 2018). Each bunch then has a time width in the order of 20-50 ns. If single-event particle imaging is performed, the effective particle rate the scanner needs to resolve can therefore be several times greater than the average intensity specified in the system if more than one particle is delivered per bunch. This puts a tight constraints on either the maximum beam intensity or the particle imaging scanner used. Second, the spill pause and maximum

spill duration set the minimum time necessary to complete a full particle CT scan. These limitations will be discussed in Chapter 6.

2.2.3 Nozzle and gantry

After passing the HEBT, the beam is either actively or passively adapted to the lateral dimensions of the tumor site. Although passive beam shaping is now mostly replaced by the more flexible active pencil beam scanning, it is still in use in some facilities, like for example the Loma Linda Medical Center (Loma Linda, CA, USA) (Jermann 2019).

Active beam shaping utilizes two dipole bending magnets several meters upstream the isocenter to scan the thin pencil beam offered by the accelerator laterally across the irradiation field. For this so-called pencil beam or raster scanning technique, the treatment volume is divided in iso-energy slices which are then irradiated spot-by-spot before the energy of the beam is changed for the next iso-energy slice (Haberer et al. 2004). The focus of the pencil beam is controlled by a focusing multipole magnet upstream the scanning magnets. However, also the scattering inside the beam monitoring system and air between nozzle and patient contributes to the spot width. Therefore, in general, thinner spots are available for higher energies and heavier particles. At HIT, the finest spot sizes available are $\sim$4 mm for carbon ions and helium ions, and $\sim$7 mm for protons (Kleffner et al. 2009). Small spot sizes are beneficial for path estimation in single-event particle imaging, when considering substituting the position sensitive detector before the patient with the pencil beam scanning information, as explored in publications P.VI and P.III.

To enable different treatment (and in the future maybe also imaging) directions, a gantry can be used which is HEBT line mounted on a rotating structure. Inside the gantry the beam is bent by a 270° angle such that the irradiation direction can be rotated around the patient. As one of only two facilities worldwide, the HIT facility offers a gantry capable of delivering carbon ions. Aside from a gantry, another solution to enable different treatment and imaging directions would be the use of a rotating patient chair (Farr et al. 2018), although this is usually avoided due to increased setup uncertainty.

2.3 Scintillation detectors

Accurate and precise determination of the particles' residual range sets the RSP accuracy and noise of the acquired PCT images (Bashkirov et al. 2016a). Hence, tight constraints are placed on the energy/range detector of the particle imaging system. The experimental work conducted as part of this thesis is focused on the use of scintillator detectors to achieve this task. The principle of organic scintillator is the prompt fluorescent de-excitation of molecules excited by the incident radiation, resulting in the production of scintillation photons (Knoll 2010). While it is difficult to manufacture large pure organic scintillators, a small percentage of organic scintillator can be dissolved in a monomer solvent that can subsequently be polymerized. As such a so-called

plastic scintillator polystyrene is often used. Plastic scintillator have the advantage that they can easily be produced in different shapes and sizes, and retain a relatively high light yield, as well as a fast decay time (Seco et al. 2014). For example, the polystyrene based scintillator used in Kelleter et al. (2020) has a scintillation light yield exceeding 9000 photons/MeV at a decay constant of only 2.5 ns (www.nuviatech-instruments.com). Moreover, the near water-equivalence of plastic scintillator with densities between 1.03 and 1.06 $\mathrm{g/cm^3}$ makes plastic scintillator detector especially suitable for radiation dosimetry (Beddar & Beaulieu 2016).

While the energy transferred to the plastic scintillator is proportional to the light output, this proportionality is in general not direct. Rather, non-radiative de-excitation of excited molecules is possible through different processes grouped together under the term *quenching*. Scintillation light quenching is generally dependent on the LET of the incident ionization, where higher LET causes greater quenching of the scintillation light production. This was first described by Birks (1952), who modeled the quenching of short range particles with an empirical formula, referred to as Birk's law. In the formula, the differential scintillation light yield per unit length ($\mathrm{d}S/\mathrm{d}x$) is found from the stopping power as

$$\mathrm{d}S/\mathrm{d}x = S_0 \frac{\langle \mathrm{d}E/\mathrm{d}x \rangle}{1 + k_B \langle \mathrm{d}E/\mathrm{d}x \rangle} \tag{2.23}$$

where S_0 is the scintillation light constant of the material, and k_B is the so-called Birk's constant. Usually S_0 is in the order of 10^3 to 10^4 photons per MeV for plastic scintillator, and k_B is in the order of 0.01 mm/MeV.

Although Birk's law postulates the quenching to be solely dependent on the LET of the incident ionization, it is known that the quenching factor is not the same for different ion species at the same LET (Kelleter & Jolly 2020). However, only at LET above $\sim$100 $\mathrm{MeV/(g/cm^2)}$ (Badhwar et al. 1967) the quenching was found to be better approximated by more advanced formulas as e.g. proposed by Chou (1952). For protons, the average energy loss along the Bragg curve does not exceed 25 $\mathrm{MeV/(g/cm^2)}$ (Kelleter & Jolly 2020) such that the application of Birk's law is justified to describe the scintillator response. Since the helium ions' energy loss is approximately a factor of 4 greater than that of protons, Birk's law may still be a good approximation.

The produced scintillation light is then usually read out by photo-diodes, Photo-Multiplier Tubes (PMTs), Silicon Photo-Multipliers (SiPMs) or even CCD cameras (Seco et al. 2014, Beddar & Beaulieu 2016). As a consequence of their low noise, high gain and fast response time, PMTs are the most commonly used device for scintillation light detection (Seco et al. 2014), and especially suited for single-particle detection. The PMT signal output generally depends on the temperature of the PMT, fluctuations in the high-voltage supply and the event rate, i.e. the particle rate of the incident ion beam (Bashkirov et al. 2016a). Especially, higher particle rate will lead to the reduction of the signal output. In addition, due to the optical transport of the produced scintillation light, the detector response varies with the distance of the incident radiation to the PMT. To ensure highest accuracy in particle imaging, the light output of the detector therefore has to be calibrated (Bashkirov et al. 2016a).

CHAPTER 3

State of the art in imaging and treatment monitoring

In this chapter, first the state of the art in clinical stopping power determination, as well as associated range uncertainties in the treatment delivery will be introduced. Then, dual-energy x-ray CT is presented which has been proposed and developed in recent years as improvement over the currently used single-energy x-ray CT for treatment planning. Methods for on-line treatment monitoring, i.e. verification of the treatment during irradiation, will be briefly presented and their individual benefits and setbacks discussed. Finally, the methods of particle imaging will be introduced in detail.

3.1 Current clinical practice

The foremost goal of cancer radiotherapy is to achieve tumor control (i.e. locally destroying all tumor cells). Hence, safety margins around the clinical target volume are introduced to avoid tumor under-dosage arising from range uncertainties (Paganetti 2012), deliberately accepting overdosage of healthy tissue. An overview over the margin recipes used at different particle therapy sites is shown in Figure 3.1. The figure also shows the distribution of tumor depths relative to all treated cases (Dal Bello 2020). As can be seen, most often, the tumor depth is between 100 mm and 150 mm, for which then margins of up to $\sim$8 mm are added (e.g. at MD Anderson, Houston, TX, USA). In addition, treatment directions aimed directly at OARs are generally avoided, and multi-field or patched field solutions are preferred where the spread-out Bragg peak distal falloff is placed more in the center of the target volume (Knopf & Lomax 2013). For such fields, range uncertainty results in a reduction of dose homogeneity within the target.

Range uncertainty stems from various sources some being systematic, some stochastic in nature. Stochastic uncertainties include for example the daily patient positioning. As the treatment is usually divided in several so-called fractions delivered independently, stochastic sources of uncertainty may average

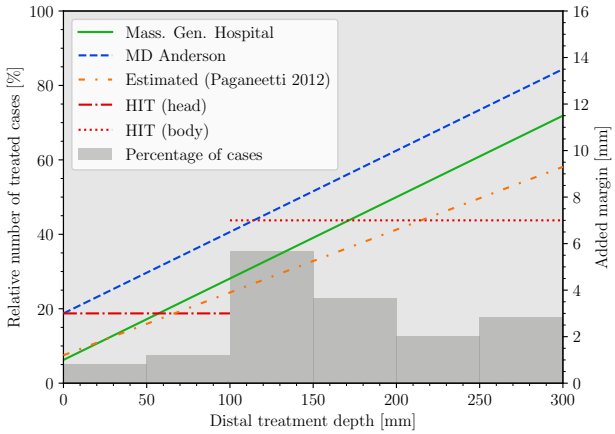

Figure 3.1: Margin recipes used at different particle therapy treatment facilities in comparison to the frequency of the respective treatment depth. The range margin recipes were obtained from Paganetti (2012). The estimated range uncertainty corresponds to the estimation of physical range uncertainties given by Paganetti in his table 1, where the contribution of biological uncertainties and lateral heterogeneities was not considered. Reproduced from Dal Bello (2020).

out in the physical dose to the target over the course of the fractionated treatment (Lomax 2020).

Systematic uncertainties, on the other hand, are not mitigated through the fractionated treatment. Systematic uncertainties include for example the beam commissioning and dose calculation in treatment planning. For the latter, a major source of uncertainty stems from the accurate representation of the patient tissue as seen by the treatment ion beam. This can either be the tissue chemical composition for Monte Carlo based treatment planning, or the Relative Stopping Power (RSP) for analytical treatment planning. As analytical treatment planning systems currently still represent the most common systems used (Nystrom et al. 2020), the improved acquisition of the patient specific RSP map is a main target for developments in particle therapy image guidance.

In current clinical practice, the RSP information is extracted from the HU measured in a treatment planning Single-Energy x-ray CT (SECT) through a scanner specific calibration. The most commonly applied method to retrieve the HU to RSP calibration curve is the stochiometric calibration proposed by Schneider et al. (1996). For this method, first, a scan is acquired of a Gammex RMI-467 (Gammex, Middleton, WI, USA) calibration phantom using the same scan protocol as used for the patient treatment planning. The Gammex is a cylindrical plastic phantom of 330 mm diameter which contains 17 plastic inserts (each with a diameter of 28 mm) modeling different patient tissues from lung (LN-300) to dense bone (SB3 Cortical Bone). The accurate knowledge of the density and composition of these inserts is then used to obtain the scanner-specific parameters of the photon attenuation coefficient contained in the CT scan HU information. The relevant formulas are given as Equation 3.1 and

(a) Gammex RMI-467

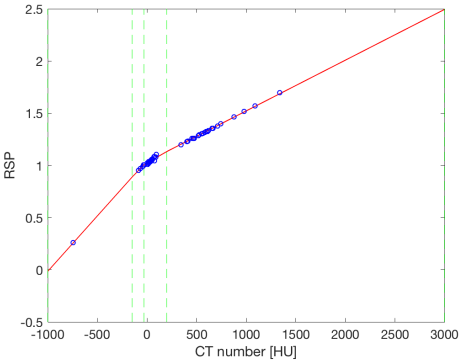

(b) HU to RSP calibration curve

Figure 3.2: a) Gammex RMI-467 (Gammex, Middleton, WI, USA) calibration phantom with tissue equivalent plastic and true water inserts. b) Hounsfield Unit (HU) to RSP calibration curve derived for SECT with the German Cancer Research Center (DKFZ) Somatom Definition Flash x-ray CT scanner (Siemens Healthineers, Forchheim, GER). The calibration was acquired by E. Bär (UCL, London, UK) through the stoichiometric calibration method. The green vertical lines indicate the regions used for the individual linear fits.

Equation 3.2.

$$HU = 1000 \times \frac{\mu - \mu_{water}}{\mu_{water}} \tag{3.1}$$

$$\mu = \rho_e \left[K^{ph} \hat{Z}^{3.26} + K^{coh} \hat{Z}^{1.86} + K^{KN} \right], \tag{3.2}$$

where μ is the total photon attenuation coefficient, ρ_e is the relative electron density. K^{ph} is the cross section of the photo-electric effect, K^{coh} that of coherent scattering and K^{KN} the Klein-Nishina cross section describing Compton scattering, where all parameters are averaged over the photon energy spectrum of the scanner. $\hat{Z}$ is the effective atomic number of the material. K^{ph}, K^{coh} and K^{KN} in Equation 3.2 can be retrieved through a least-squares fit to the measured HUs for the different tissue equivalent plastic inserts of the Gammex calibration phantom. The knowledge of these scanner specific parameters then enables to calculate the theoretical HUs for a list of human tissues with tabulated chemical composition (Woodard & White 1986, White et al. 1987). For these tissues, the theoretical RSPs are computed by evaluating the Bethe formula, using the Bragg additivity rule to compute the tissue I-value (Bär et al. 2018a). Finally, the HU to RSP calibration is obtained by piece-wise linear fitting of the so obtained calibration points.

This HU to RSP conversion is not based on any physical principle, due to the fundamentally different interactions of photons and ions with matter.

Therefore, the relationship between HU and RSP is not bijective: different materials having the same HU can have different RSP values and vice versa. As such, the conversion from the treatment planning SECT to the patient specific RSP map is uncertainty prone, with the mean absolute RSP error for different tissues being in the order of ∼3% (Yang et al. 2010, Bär et al. 2018b, Möhler et al. 2018, Taasti et al. 2017). This conversion uncertainty is a major cause of range uncertainty in therapy, up to an estimated 1.6% of the ions' range (Paganetti 2012). A significant part of that stems from the uncertainty in the material I-value used to calculate the RSP (Doolan et al. 2016, Bär et al. 2018a). Even for water, several different I-values are reported in the literature (Tanabashi et al. 2018). In addition, different particle therapy centers apply different protocols to acquire the HU to RSP conversion, and inter-center variation in proton range prediction has recently been reported to be as high as 2.9% for typical prostate treatment fields (Wohlfahrt & Richter 2020).

3.2 Dual-Energy x-ray CT

In order to improve upon the current state of the art, Dual-Energy x-ray CT (DECT) has been proposed and developed by several groups over the last decade (Yang et al. 2010, Yang et al. 2012, Hünemohr et al. 2014a, Möhler et al. 2018, Bär et al. 2017, Bär et al. 2018b, Taasti et al. 2017). A recent review highlighting the use of DECT in particle therapy can be found in Wohlfahrt & Richter (2020).

DECT represents the combination of two CT scans acquired at distinct photon energy spectra (different x-ray tube voltages) to more accurately determine the tissue specific quantities (Torikoshi et al. 2003, Bazalova et al. 2008, Yang et al. 2010). As the attenuation coefficient given in Equation 3.2 depends on two unknown tissue-specific variables, ρ_e and $\hat{Z}$, two independent measurements of the photon attenuation coefficient μ allow to extract them accurately. The two photon spectra used in the DECT scan contain partly complementary information, where a larger spectral separation of the two scans results in better information on the tissue (Wohlfahrt & Richter 2020). DECT therefore has been used for obtaining the tissue elemental composition (Landry et al. 2013, Hünemohr et al. 2014b, Lalonde & Bouchard 2016, Saito & Sagara 2017), and for improved determination of the RSP (Yang et al. 2010, Hünemohr et al. 2014a, Bourque et al. 2014, Möhler et al. 2016, Taasti et al. 2016) amongst other applications. In recent experimental studies using fresh animal tissue samples, different groups demonstrated the capability of DECT to predict RSP values with mean absolute errors below 1% (Taasti et al. 2017, Möhler et al. 2018, Bär et al. 2018b). With strong evidence of the benefit achievable with DECT for RSP determination, it is currently in the phase of clinical implementation with first commercial RSP determination solutions available (Wohlfahrt & Richter 2020). In addition to RSP prediction, the capability of DECT to extract elemental tissue composition is valuable for treatment planning based on Monte Carlo simulation which is advantageous over analytical treatment planning solutions

in terms of dose calculation (Paganetti 2012). The use of more than two distinct photon energy spectra (multi-energy CT) could even further improve tissue decomposition and range prediction (Lalonde & Bouchard 2016, Lalonde et al. 2018).

3.3 Treatment monitoring

Even if the dose calculation were based on ideal image data, uncertainties in the beam range in the patient would remain. These can stem, for example, from uncertainties in the planning algorithm itself, the beam delivery system, inter-treatment anatomical changes or intra-treatment motion. As such, it would be highly desirable to get on-line and in-vivo feedback on the Bragg peak position relative to the treated anatomy within the patient (Parodi & Polf 2018a).

A substantial effort in on-line treatment monitoring has been placed in exploring the secondary radiation produced in nuclear interactions. Secondary radiation is inevitably produced along the beam path, and hence available "for free", i.e. without any setbacks for the patient. Especially interesting for dose monitoring is secondary γ radiation. The γ radiation produced by the primary beam can be divided into a prompt and a delayed component. The delayed γ signal is produced in electron-positron annihilation after the β^+ decay of isotopes or excited states produced in nuclear interactions. The former is the basis of Positron Emission Tomography (PET) beam monitoring. β^+ emitting isotopes may be either target fragments or – in case of particle therapy with $z_p > 5$ – projectile fragments. The decay time of the produced β^+ emitters ranges from few hundred μs to several minutes (e.g. $t_{1/2} = 20\,\text{min}$ for ^{11}C). Hence, PET beam monitoring may be either in-beam (quasi on-line) (Bisogni et al. 2017, Ferrero et al. 2018) or after treatment (offline) (Handrack et al. 2017). For offline PET, the precision of the range monitoring is limited to a few mm, where the main limiting factors is the biological washout of the isotopes (Handrack et al. 2017). For in-beam PET, biological washout is less problematic, however, specialized PET detectors are needed and the shorter scan duration paired with the increased radiation background during the spill compromises the signal-to-noise ratio (Bisogni et al. 2017). A general limitation of in-beam PET is that the information for single pencil beams is not easily accessible — the produced long-lived isotopes result in an increasing background signal with every irradiated pencil beam.

As a promising method for fast on-line range monitoring, the prompt γ signal has been investigated (Parodi & Polf 2018a). The prompt γ component originates from the de-excitation of excited nuclear states of either target or projectile. The decay time of these states is on the sub-nanosecond scale, hence the designation as "prompt". Different approaches to measuring the prompt γ signal and relating it to the Bragg peak position can be found in the literature. An informative overview over these approaches and their respective technological advance can be found in Dal Bello (2020). For example, prompt γ enables relative range verification using a collimated detector placed next to the patient with aperture orthogonal to the beam (Min et al. 2012). As the nuclear

cross section drop to zero when the particle kinetic energy is not anymore sufficient to cross the Coulomb barrier of the target nuclei, so does the prompt γ yield. For protons, the prompt γ signal measured in the detector therefore ceases shortly before the Bragg peak. For heavier ions, in addition, the prompt γ yield of longer-range secondaries needs to be taken into account. For measuring absolute range changes, prompt γ spectroscopy has been proposed (Verburg et al. 2012) and recently a first clinical prototype has been demonstrated (Hueso-González et al. 2018). Prompt γ spectroscopy exploits the energy dependence of the prompt γ production cross sections for different decay channels of elements abundant in the human body. With an optimized prompt γ spectroscopy system, absolute range changes in the order of 2 mm may be detectable for particle therapy at synchrotron facilities (Dal Bello et al. 2020).

Other techniques exploiting nuclear interactions involve the detection of charged secondaries or neutrons. For example, Félix-Bautista et al. (2019) have successfully demonstrated the feasibility of monitoring the lateral beam position from secondary particles produced in carbon ion therapy. However, most projectile fragments are produced in beam direction and then provide only little information on the Bragg peak position. With increasing angular position of the measurement device relative to the beam direction, it becomes more feasible to infer the Bragg peak position from the secondary particle production. On the other hand, the measurement precision suffers from the decreasing number of secondaries emitted with large angles to the beam.

A setback of techniques monitoring secondary radiation is the missing information on the treated anatomy. For example, an under or overshoot relative to a fixed prompt γ detector position might not necessarily indicate a change of the Bragg peak position within the patient considering the patient may simply be positioned closer or farther from the isocenter. On the other hand, anatomical motion of soft tissue may leave the Bragg peak unchanged or only slightly shifted, if it is not associated with a significant difference in the RSP. Still, this would produce a misplacement of the dose compared to the prescription, but it would not be picked up by current range monitoring techniques. In order to monitor also the treated anatomy, an on-line imaging system would be desirable.

One possibility for anatomy monitoring would be Magnetic Resonance Imaging (MRI) guided particle therapy (Hoffmann et al. 2020). MRI would offer the feasibility for non-invasive monitoring of the treated anatomy, and possibly even to track the anatomy in quasi real-time. However, MRI does not provide information on the Bragg peak position and methods to infer RSPs from MRI scans are still sparse. In addition, integrating an MRI scanner into a particle therapy beam line is a challenging task (Schellhammer et al. 2018). Especially since the static field of the MRI system results in a bend of the treatment beam which has to be taken into account in the treatment planning algorithm. Still, MRI guided particle therapy is a promising technology for tackling the challenge of anatomical motion.

The ideal on-line treatment monitoring system would yield both accurate range information and an image of the treated anatomy at the same time, while inflicting little to no additional dose. Particle imaging in principle would be a

suitable candidate for that task (Han et al. 2011). However, only little attention has been given to on-line particle imaging so far. A key issue is the fast switch between therapy and imaging beam needed for on-line treatment monitoring. In publication P.VII (Section 5.5), we therefore investigate the potential of a mixed helium/carbon ion beam for simultaneous treatment and imaging.

3.4 Particle imaging

In the following we will give an overview over the techniques used in particle imaging, where the measured quantity is the integrated energy loss of the ions passing through the patient/object, i.e. the object's WET. The central problem of particle imaging, formulated in Equation 2.8, relates the WET to the line integral over the voxelized RSP information. Hence, a Particle Computed Tomography (PCT) can be used to reconstruct the RSP information. Due to the avoidance of a conversion from one physical quantity to another, particle imaging is widely accepted as the theoretically most accurate method for RSP prediction (Yang et al. 2010). In principle, PCT should yield a mean absolute RSP error well below 1% (Poludniowski et al. 2015). This would especially also hold true for cases with metal implants which result in major artifacts in x-ray imaging (Ordoñez et al. 2017, Oancea et al. 2018). In addition, Particle Radiography (PRad) enables pre-treatment patient alignment (Palaniappan et al. 2019) and verification in treatment position and from beams eye view. Moreover, combining few particle imaging projections with a treatment planning SECT can be used to optimize the HU to RSP calibration (Schneider et al. 2005, Doolan et al. 2015b, Collins-Fekete et al. 2017a, Krah et al. 2019).

Historical overviews over the development of particle imaging, initiated with the seminal paper by Cormack (1963) and first experimental studies by Koehler (1968), can be found in Poludniowski et al. (2015) and Johnson (2017). As do most efforts in particle imaging, this thesis focuses on the particles' energy loss as contrast giving quantity. However, it is noteworthy that particle imaging also provides other quantities useful for generating the image contrast. Scattering particle imaging for example measures the angular or lateral displacement of the ions after passing through the object (Bopp et al. 2013, Taylor et al. 2016).

3.4.1 Integration mode particle imaging

The WET projection can be obtained either by integrating over a large number of ions, or by measuring each ion individually. The former method, referred to as *integration mode* particle imaging, relies on measuring the range shift of individual pencil beams (Krah et al. 2015, Hammi et al. 2017, Meyer et al. 2017, Deffet et al. 2020, Kopp et al. 2020) or the cumulative dose shift of a broad beam (Zygmanski et al. 2000, Seco et al. 2013, Testa et al. 2013b, Doolan et al. 2015a, Doolan et al. 2019, Darne et al. 2019) in order to infer the WET of the object. As single particles do not need to be resolved, integration mode devices are cost-efficient, can be used with clinical particle beam settings, and therefore

would be easy to handle in clinical practice. However, the major drawback of integrated mode particle imaging is the lack of spatial resolution (Krah et al. 2018). Hence, many efforts in integration mode imaging have focused on the use of heavier ions exploiting the decreased MCS with increased ion mass at the same range. Most recently, Kopp et al. (2020) have compared the use of protons, helium ions and carbon ions for integrated mode particle imaging with an Ionization Chamber (IC) stack. They demonstrate that carbon ions are most favorable in terms of image quality with such a system.

While greatly improved image quality has been demonstrated with recently advanced image reconstruction techniques relying on scanned pencil beams (Krah et al. 2015, Meyer et al. 2017, Hammi et al. 2017, Deffet et al. 2020), measuring individual particles still offers increased spatial resolution and better dose efficiency compared to integration mode setups. Except for the study on on-line treatment monitoring from particle imaging (publication P.VII; Section 5.5), where fast spot-by-spot range information is required, this thesis therefore focuses on particle imaging from individually measured events. This form of particle imaging will be explained in more detail in the following.

3.4.2 Single-event particle imaging

In order to improve the spatial resolution, in *single-event* particle imaging (also referred to as list-mode or tracking imaging), position and energy loss information are acquired for each individual particle. As such, Equation 2.8 can be reformulated for a single event, where we substitute the WET with the Water Equivalent Path Length (WEPL), the water equivalent length of the particle's trajectory through the object.

$$WEPL = \int_{\Gamma} RSP \mathrm{d}\Gamma \tag{3.3}$$

Here, Γ refers to the particle's scattered trajectory through the object. The key idea of single-event imaging is to utilize an estimate of Γ for optimized image reconstruction. The proposed, so called Most Likely Path (MLP) estimates rely either on probabilistic inference of the particle's position inside the object based on the Fermi-Eyges approximation to MCS (Schneider & Pedroni 1994, Williams 2004, Schulte et al. 2008, Collins-Fekete et al. 2017d, Krah et al. 2018), or on a phenomenological approach based on Hermite splines (Li et al. 2006, Wang et al. 2012, Hansen et al. 2014b, Collins-Fekete et al. 2015). Both will be explained in detail in Section 3.4.2 below. A schematic depiction of a typical single-event detector system is given in Figure 3.3. It comprises two tracking detectors, one before and one after the patient, to infer the particles trajectory through the object, as well as a residual energy/range detector in order to determine the particle's WEPL.

Path estimation

The first MLP estimate has been proposed by Schneider & Pedroni (1994) who estimated the position of a proton within the object given its entrance and exit

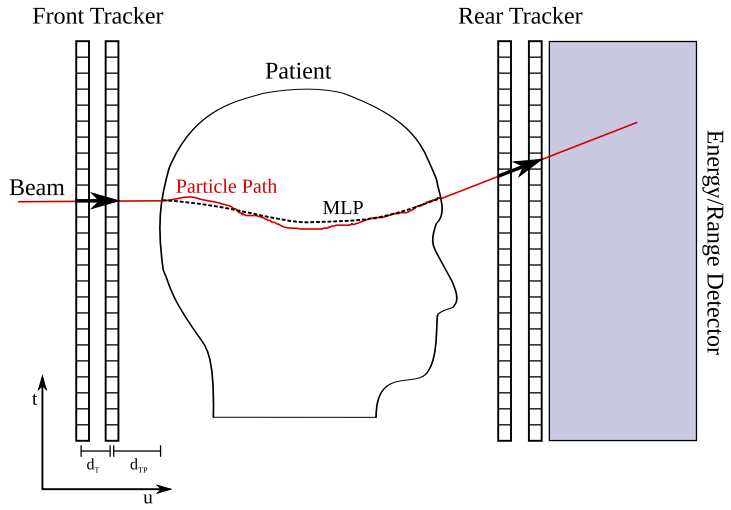

Figure 3.3: Schematic depiction (not to scale) of a single-event particle imaging system. The position/direction of each individual ion is measured by a set of position sensitive detectors placed upstream and downstream of the patient. These measurements can be used to compute the MLP (dotted black curve), an estimate of the scattered proton path (red curve). For better visibility, the scattering is largely exaggerated compared to the other components shown in the figure. The residual energy/range of each particle is measured using an energy/range detector downstream of the last tracking plane.

position. Williams (2004) further developed the most likely path algorithm, by including also the particles' entrance and exit direction into the expression of the MLP. The formalism was revisited by Schulte et al. (2008) who employed Bayesian statistics to derive the MLP. While mathematically equivalent to what was proposed by Williams (2004), the closed-form matrix expression provided by Schulte et al. (2008) is to-date still the most used MLP formalism in single-event particle imaging.

In their MLP formalism, Schulte et al. (2008) combine the lateral position t and angular displacement θ of a particle at depth u into the 2D parameter vector $Y(u)$

$$Y(u) = \begin{pmatrix} t(u) \\ \theta(u) \end{pmatrix}, \tag{3.4}$$

where the position/direction vector at the object entrance u_0 is $Y_0(u_0) = (t_0, \theta_0)^T$ and the one at the object exit at u_2 is denoted $Y_2(u_2) = (t_2, \theta_2)^T$.

The likelihood of finding a particle at depth u with a parameter vector $Y(u)$ given the entrance measurement is then obtained from Fermi-Eyges theory (Equation 2.14) in matrix notation as

$$\mathcal{L}(Y|Y_0) \propto \exp\left(-\frac{1}{2}(Y^T - Y_0^T R_0^T)\Sigma_0^{-1}(Y - R_0 Y_0)\right), \tag{3.5}$$

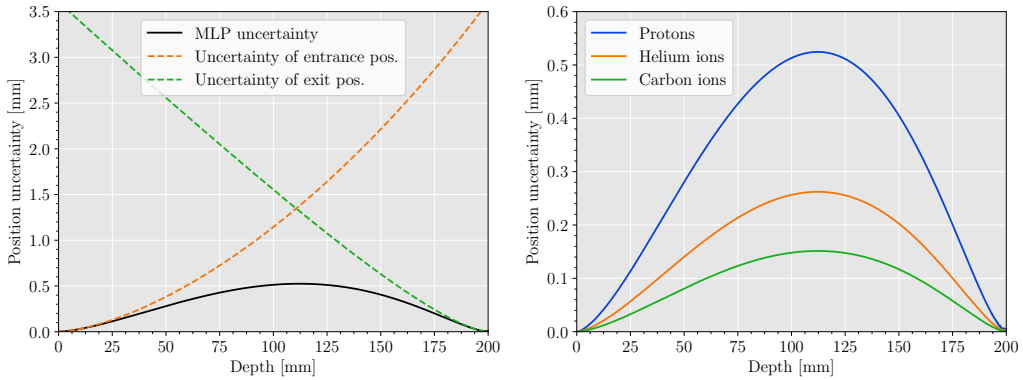

(a) **(b)**

Figure 3.4: (a) Uncertainty of a protons lateral position at depth u inferred from only the entrance position ($A_2(u, u_0)$; dashed orange), only the exit position ($A_2(u_2, u)$; dashed green) and the MLP (solid black). The calculation of the uncertainty matrix elements was performed for protons with an initial energy of 200 MeV crossing a 200 mm thick homogeneous water absorber. (b) The MLP uncertainty calculated for protons, helium and carbon ions at the same range (RW=260 mm). Ideal (uncertainty free) position/direction measurements were assumed.

where the co-variance matrix Σ_0 is defined from the scattering uncertainty of a particle scattering from the entrance to depth u:

$$\Sigma_0 = \begin{pmatrix} A_2(u, u_0) & A_1(u, u_0) \\ A_1(u, u_0) & A_0(u, u_0) \end{pmatrix} \tag{3.6}$$

The matrix elements A_n are defined using the generalized highland scattering power as in Equation 2.18. $R_0 Y_0$ represents the forward projection of the entrance measurement onto the depth u along the particle's initial direction using the small angle approximation. The translation matrix R_0 is given as

$$R_0 = \begin{pmatrix} 1 & u - u_0 \\ 0 & 1 \end{pmatrix}. \tag{3.7}$$

The uncertainty of the entrance position propagated to depth u ($A_2(u, u_0)$) is shown as dashed orange curve in Figure 3.4(a).

Similar, the likelihood of the parameter vector $Y(u)$ given the exit measurement is

$$\mathcal{L}(Y|Y_2) \propto \exp\left(-\frac{1}{2}(Y_2^T - Y^T R_2^T)\Sigma_2^{-1}(Y_2 - R_2 Y)\right), \tag{3.8}$$

Where Σ_2 is defined in the same way as Σ_0 from the scattering moments, but evaluating them as $A_n(u_2, u)$. The matrix R_2 presents the propagation of the parameter vector Y onto the exit depth. The uncertainty of the exit position ($A_2(u_2, u)$) propagated to depth u is shown as dashed green curve in Figure 3.4(a).

The combined likelihood of finding the particle with a parameter vector Y given both entrance and exit position/direction measurements is then

$$\mathcal{L}(Y|Y_0, Y_2) = \mathcal{L}(Y|Y_0)\mathcal{L}(Y|Y_2) \tag{3.9}$$

Due to Equation 3.9 being a multiplication of Gaussians, the result is again a Gaussian distribution. This means, the maximum likelihood inference can be done using a χ^2 minimization technique. This gives

$$Y_{MLP} = 2\epsilon^{-1}(\Sigma_0^{-1}R_0Y_0 + R_2^T\Sigma_2^{-1}Y_2). \tag{3.10}$$

Here, $\epsilon = 2(\Sigma_1^{-1} + R_2^T\Sigma_2^{-1}R_2)^{-1}$ is the error matrix, where $\epsilon_{1,1}$ denotes the variance in lateral displacement. This uncertainty is plotted as the solid black curve in Figure 3.4(a). The sought most likely path is given as the first (the lateral) component of the Y_{MLP} vector (t_{MLP}), while the second component is the most likely angular displacement.

In general, before image reconstruction, a hull projection algorithm is performed: The particles are projected from their measured positions along their direction in a straight line onto the contour of the object, following the reasoning that scattering in air is negligible. The object hull is obtained either through prior information or estimated from an initial low quality reconstruction. Hull projections have been shown to significantly improve the path estimation accuracy (Schultze et al. 2014, Collins-Fekete et al. 2017b). The path estimation accuracy shown in Figure 3.4 assumes ideal position and direction information on the front and rear trackers. However, the precision limit of real tracking systems paired with the scattering in the tracker itself, limits the accuracy of the hull projection and overall path estimation accuracy (Bopp et al. 2014). Recently, Krah et al. (2018) have extended the MLP formalism to also account for the uncertainty of the entrance and exit measurements. They start with the assumption of a Gaussian uncertainty on the tracker measurements stemming from both the tracker resolution and the scattering in the tracker material. Denoting the measured parameter vectors $\hat{Y}_0$ and $\hat{Y}_2$, and their uncertainty co-variance matrices projected onto the hull of the object $S_{in}\Sigma_{in}S_{in}^T$ and $S_{out}\Sigma_{out}S_{out}^{-1}$, Krah et al. (2018) arrive at

$$Y_{MLP} = C_2(C_1 + C_2)^{-1}R_0S_{in}\hat{Y}_0 + C_1(C_1 + C_2)^{-1}R_1^{-1}S_{out}^{-1}\hat{Y}_2, \tag{3.11}$$

where the matrices C_1 and C_2 are defined from the scattering co-variance and measurement co-variance matrices as

$$C1 = R_0S_{in}\Sigma_{in}S_{in}^TR_0^T + \Sigma_1 \tag{3.12}$$

$$C2 = R_1^{-1}S_{out}^{-1}\Sigma_{out}(S_{out}^{-1})^T(R_1^{-1})^T + R_1^{-1}\Sigma_2(R_1^{-1})^T. \tag{3.13}$$

This formalism opens up the possibility of employing the information of the pencil beam scanning system instead of a front tracker: The front tracker measurement is replaced with the pencil beam mean position, and the uncertainty matrix of the front tracker measurement with the known pencil beam spatial/angular co-variance matrix. The image quality achievable with such a

system is explored in publication P.VI.

As a fast alternative to the MLP formalism, Li et al. (2006) have proposed a Hermite cubic spline path estimate based on the measured entrance position and direction vectors. Hansen et al. (2014b) later improved the formalism by scaling the normalized entrance and exit direction vectors by the distance travelled by the particle through the object ($|u_2 - u_0|$), to account for different object thicknesses. Observing that the scattering inside the object should not only be a function of distance travelled, but also depend on the initial energy and energy loss of the particles, Collins-Fekete et al. (2015) further introduced phenomenological weighting factors Λ_0 and Λ_2 to the measured entrance and exit directions.

$$\Lambda_0 = 1.01 + 0.43 \left(\frac{WEPL}{RW} \right)^2 \tag{3.14}$$

$$\Lambda_2 = 0.99 - 0.46 \left(\frac{WEPL}{RW} \right)^2 . \tag{3.15}$$

Using the small angle approximation, their optimized Cubic Spline Path (CSP) formalism reads

$$\begin{aligned} t_{CSP} = {} & (2\nu^3 - 3\nu^2 + 1)t_0 + (\nu^3 - 2\nu^2 + \nu)\Lambda_0 \left| u_2 - u_0 \right| \theta_0 \\ & + (-2\nu^3 + 3\nu^2)t_2 + (\nu^3 - \nu^2)\Lambda_2 \left| u_2 - u_0 \right| \theta_2. \end{aligned} \tag{3.16}$$

Collins-Fekete et al. (2015) demonstrated that this formalism yields equivalent accuracy to the full MLP. Its major strength is the reduction of computation time over the MLP due to the lower number of floating point operations needed. In a recent work, Collins-Fekete et al. (2017d) revisited the MLP formalism, demonstrating its inherent connection to the CSP formalism. In addition, they demonstrated this equivalence to also hold for different ion species.

Image reconstruction

PRad can be computed from single projections either by binning the particles by their measured position on the front or rear tracker, or by redistributing their information based on the MLP. The latter can be achieved, for example, by selecting a depth of interest in the object and using the MLP lateral position at that depth to bin the particles (Schneider & Pedroni 1994, Rit et al. 2013, Gehrke et al. 2018). As of now, this requires prior knowledge on the depth of the object to achieve a spatial resolution subject only to the MLP accuracy. Another option to compute radiographs from the MLP, is to redistribute the particles WEPL into pixel according to the length of the particles' MLP in pixel channels through the object (Collins-Fekete et al. 2016, Gehrke et al. 2018). While not relying on prior information, the image quality is limited due to the projection of the scattered particle paths onto a single reconstruction plane. An in-depth theoretical investigation of the spatial resolution achievable with these algorithms is provided in publication P.IV. Since a thorough explanation of these algorithms is provided in that publication (Section 5.1), the details of the binning algorithms are omitted here.

Direct reconstruction techniques proposed for PCT image reconstruction combine similar binning strategies as used for PRad with filtered back projection methods applied in conventional x-ray CT. For example, optimized particle radiographs can be computed from the projection data by binning the particle histories on the front or rear tracker, or from the maximum-likelihood method by Collins-Fekete et al. (2016) and a conventional Feldkamp-David-Kress filtered backprojection can be applied. Rit et al. (2013) have proposed a more sophisticated distance-driven-binning filtered back projection algorithm. For each projection, the WEPL the particles is backprojected into the image voxels based on their MLP estimate. The voxel-wise WEPL distributions are filtered and weighted as in the Feldkamp-David-Kress method, with the difference being that the filtering is now performed in 3D. A voxel-vise summation over the filtered and weighted distributions from different projections then yields an estimate of the RSP. The algorithm has been shown to yield improved spatial resolution compared to the methods based on optimized radiographs (Rit et al. 2013, Khellaf et al. 2020a) and provides highly accurate RSP (Hansen et al. 2016, Dedes et al. 2019).

Aside from direct reconstruction techniques, iterative image reconstruction techniques have been developed for improved image reconstruction of pCT data (Penfold 2010, Penfold & Censor 2015, Hansen et al. 2016, Ordoñez et al. 2017, Schultze et al. 2018). The single-event PCT reconstruction problem can be formulated in matrix notation as

$$\mathbf{A}\mathbf{x} = \mathbf{b}. \tag{3.17}$$

$\mathbf{A}$ is the system matrix, where $\mathbf{A}_{i,j}$ is the length particle i traversed in voxel j. $\mathbf{x}$ is the sought vector containing the RSP information of each voxel. $\mathbf{b}$ is a vector containing the measured WEPL traversed by each particle. For PCT, both $\mathbf{A}$ and $\mathbf{b}$ are connected to uncertainties stemming from the path estimation, the energy/range straggling and the detector resolution. Solving for $\mathbf{x}$, aside from direct analytical methods, can be accomplished through iterative feasibility seeking algorithms. Such algorithms provide an estimate of the most feasible image solution given the measured uncertain projection data and are therefore especially useful for PCT. In this thesis, all PCT reconstructions have been made using the diagonally relaxed orthogonal row (DROP) ordered-subset iterative reconstruction algorithm with interleaved superiorization of the total variation norm (TVS) (Penfold et al. 2010). In DROP, the data are divided into optimization blocks which are optimized sequentially. Each optimization yields an updated estimate of $\mathbf{x}$ which is then used as the starting point for the optimization of the next block. The TVS is performed at each optimization block and regularises the convergence of the algorithm in the presence of noise. As starting point for the iterative solver and for computing the convex hull, a fast Feldkamp-David-Kress filtered backprojection based on a straight-line path assumption is used.

Prior to image reconstruction, data filters are applied to remove events with unusually large WEPL (for example from nuclear interactions or energy straggling) or large angular displacement (produced through single large angle scattering or nuclear interactions). In most contemporary applications, these

data filters act on the standard deviation of the recorded WEPL and angular distribution in a pixel, following the work by Schulte et al. (2005) and Schulte et al. (2008). However, the non-gaussian tails of both angular and WEPL distribution can largely affect the calculation distribution standard deviation if not considered carefully. In publication P.XI, it is demonstrated how nuclear interactions inside the energy detector can have a major effect on the standard deviation based WEPL filtering.

Instrumentation for single-event particle imaging

Single-event particle imaging requires sophisticated detectors in order to resolve the particle track and energy information on a single-event basis (Schulte et al. 2004). As an example, in Figure 3.5 the prototype detector developed by the US pCT collaboration (Johnson et al. 2016, Sadrozinski et al. 2016, Bashkirov et al. 2016a) is depicted, where the top figure shows a detailed Monte Carlo implementation of the system (Piersimoni et al. 2017) and the bottom a picture of the system installed at the HIT facility.

Optimal path estimation requires precise measurements of each particles position and direction before and after the patient (Krah et al. 2018). At least 4 independent measurement planes are necessary for the highest path estimation accuracy. However, it has been proposed in several studies, including this work (publication P.VI), to reduce the number of tracking planes. This would have the main benefit of reduced cost of the overall system and simpler implementation at a clinical beam line. For example, Schneider & Pedroni (1994) and (Schneider et al. 2012) based their radiography system on only two position sensitive detectors, placed before and after the patient. Without the information on the direction of the particles, this only allows for a straight-line path assumption between the measurement points. However, if pencil beam scanning is used and the beam has only a small angular divergence, the pencil beam mean direction may be used as the entrance direction measurement. This has been employed, for example, in the recent prototype by ProtonVDA inc. (Chicago, Il, USA) (Welsh et al. 2017, Ordoñez et al. 2019).

For the tracking detectors employed in the system described in Johnson et al. (2016), which was also used for the helium and proton imaging experiments in this thesis, in total 8 Silicon Strip Detector (SSD) planes are used (each measuring 1D position). The SSDs are placed together in pairs at a 2 mm distance between the planes, forming a tracker layer that enables 2D position measurements. For inference of the particle direction, two such layers are grouped as tracker module (henceforth simply denoted tracker), where the distance between the tracker layers is 50 mm (Sadrozinski et al. 2013). Aside from SSDs, scintillating fibres have also been used as front trackers (Uzunyan et al. 2015).

High accuracy and precision requirements are especially placed on the energy/range detector of the single-event system, as it directly influences the quality of RSP prediction. For highest RSP precision, the energy/range detector should provide a WEPL resolution close to the particles range straggling (Bashkirov et al. 2016a). As cost-efficient option for the energy/range detector, scintillator calorimeters composed of a single or multiple scintillator stages

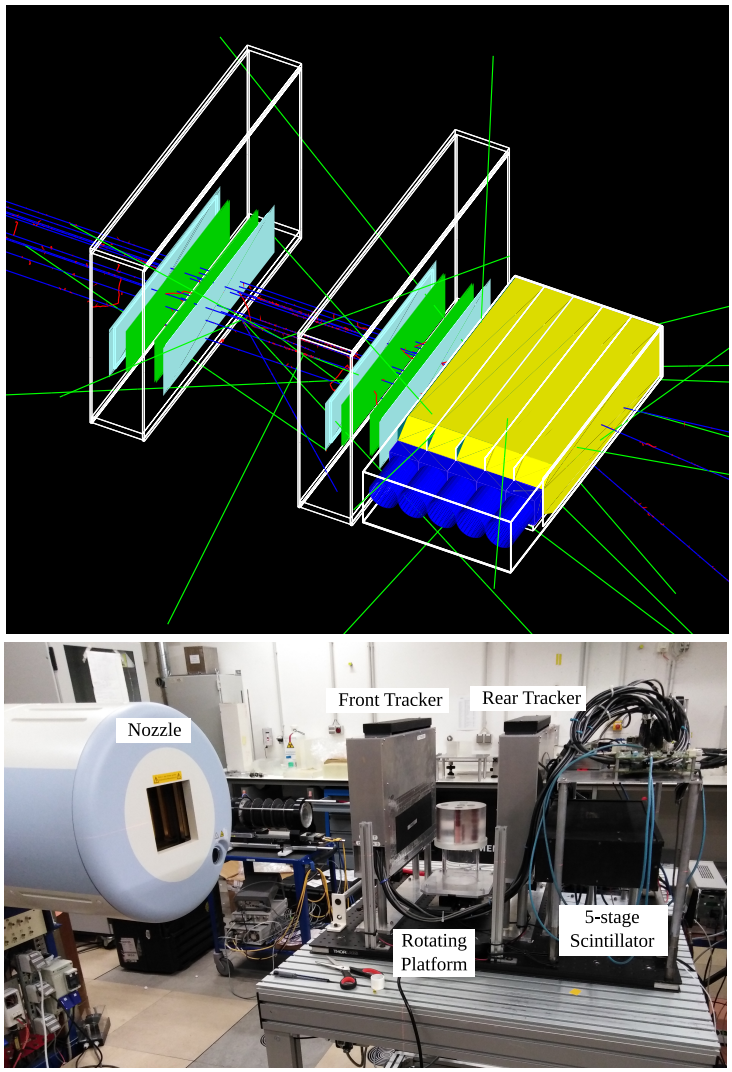

Figure 3.5: The US pCT collaboration pre-clinical head scanner prototype. Top: The scanner as implemented in theTOPAS simulation toolkit for publication P.XII and P.XI. The figure shows the two tracking detectors, and the 5-stage scintillator energy/range detector. Bottom: The prototype installed at the HIT.

have been investigated (Bashkirov et al. 2007, Sadrozinski et al. 2013, Bashkirov et al. 2016b). The rationale behind segmented energy detector designs is that the thickness of each stage traversed completely by the particles directly contributes to the range measurement. Only in the final stage reached by the particles, the energy deposit has to be determined. This relaxes the precision requirement on the energy measurement in each individual stage. Currently, the benchmark for accuracy in proton CT is set by the 5-stage scintillator developed by the US pCT collaboration (Bashkirov et al. 2016a, Sadrozinski et al. 2016, Johnson et al. 2016). With this detector, mean absolute RSP accuracy better than 1% and especially also better than that of a contemporary Dual-Energy x-ray CT has been demonstrated for tissue equivalent plastic materials in pCT experiments (Dedes et al. 2019).

Gehrke et al. (2018) have proposed a single-event imaging system which measures the particles energy loss in a single silicon pixel sensor placed behind the last tracker plane. By selecting the initial energy of the particles such that they reach the detector just before the end of their range, the steep gradient in energy loss per unit length at the rise of the Bragg peak can be utilized to generate the image contrast. The main benefit of this system is the low cost and setup complexity, but it is limited in terms of dynamic WEPL range (Amato et al. 2020). So far, this system is the only system available developed directly for single-event helium ion imaging (Gehrke et al. 2017).

Several groups have investigated range counters for direct measurement of the particles residual range. A range counter consists of a stack of thin detector slabs and the particle range is obtained from the detector WET between entrance and the last slab where a signal above noise is measured. Range counters have been proposed in the form of stacks of thin scintillator slabs read out by SiPMs (Sadrozinski et al. 2013, Uzunyan et al. 2015) or stacks of silicon strip/pixel sensors (Pettersen et al. 2017, Esposito et al. 2018). The former comes at the benefit of a low cost. The main advantage of the latter is that the fine spatial resolution of the position sensitive detectors used enables simultaneous measurement of a large multiplicity of incident ions simultaneously (Pettersen et al. 2017). Tracking the individual detector hits then enables to resolve single-events in data processing (Pettersen et al. 2019b). However, a disadvantage of such a detector design is the relatively large overall cost, and the readout complexity. In Pettersen et al. (2019a) (publication P.IX, not presented as part of this thesis), the optimization of a range telescope for proton imaging based on the ALPIDE (Mager 2016) silicon pixel sensors is investigated. A Bragg-peak fit to the energy deposit, inferred from the size of the produced pixel clusters around a particle hit, is performed to improve the range accuracy. The performance of the optimized detector design for helium ion imaging is further explored in publication P.III.

As alternative to energy/range detectors that require the particles to come to a (near) stop, the residual energy of the helium ions could be measured using either time-of-flight (TOF) detectors or magnetic spectrometers. The size of suitable magnetic spectrometers, however, prohibits their use in a clinical environment (Johnson 2017). In a TOF detector the particles' residual energy is measured from their travel time between two detector planes acting both es

energy detector and rear tracker. Worstell et al. (2019) have recently presented promising results using Large Area Picosecond Photon Detectors achieving a time resolution of 64 ps. The feasibility of such a design for helium imaging in terms of the achievable WEPL resolution is explored in Appendix A.

CHAPTER 4

Overview over the results

In this thesis, presented in the cumulative form, the potential of particle energy loss imaging at a synchrotron based therapy facility was investigated. With the ultimate goal of bringing particle imaging closer to clinical reality, this project was divided in three main parts:

1. Identification of limitations (and potential solutions) in particle imaging
2. Investigation of the ideal application of particle imaging
3. Investigating improved particle imaging systems

For the first part, theoretical limitations in the spatial resolution of proton and helium ion radiographic imaging are investigated based on a model of the scattering and path estimation uncertainty (publication P.IV). In that work, theoretical considerations are provided, aiming to strengthen the understanding of different radiography binning methods found in the literature. It is demonstrated that the projection of the scattered particle paths onto a single reconstruction plane will inevitably present a loss of information, i.e. a reduced spatial resolution beyond just the expectation of the path estimation uncertainty.

In the next work featured in this thesis, secondary fragments are identified as a major cause of image artifacts in helium imaging. As a solution, a novel technique for filtering nuclear interactions and fragments based on the well-known ΔE-E method for particle identification is proposed. Using this method, in collaboration with the US pCT collaboration (Prof. Reinhard W. Schulte, Prof. Robert P. Johnson and Assoc. Prof. Vladimir A. Bashkirov), the University College London (Dr. Charles-Antoine Collins-Fekete) and the HIT facility (Dr. Stephan Brons), the feasibility of high quality single-event HeCT with a pre-clinical proton CT detector was demonstrated yielding an RSP accuracy better than 0.5% in plastic samples (publication P.XII).
Extending the work on nuclear interactions to proton imaging, it is shown that contemporary filtering methods used to remove events with unusually large WEPL suffer in accuracy due to nuclear interactions inside the energy/range detector. The ΔE-E method is shown to also be valuable for proton imaging, as

it enables to effectively suppress the nuclear interaction contamination (publication P.XI). The main effect of the ΔE-E filter is to reduce uncertainties at the stage interfaces of the multistage scintillation detector employed in the pCT prototype.

Given the feasibility of high quality experimental helium ion imaging, the next step was to investigate the benefit of helium imaging for particle therapy in comparison to other existing modalities. For this, our group in collaboration with the US pCT collaboration was awarded with a project funding "Proof-of-principle for range uncertainty reduction with helium ion imaging" by the Particle Therapy Co-Operative Group (PTCOG). This enabled another series of beam tests with the US pCT collaboration pre-clinical prototype at the HIT facility. Working together with DECT and pCT experts from the University College London (Dr. Esther Bär and Dr. Charles-Antoine Collins-Fekete; London, United Kingdom), for the first time, a detailed experimental comparison between photon and particle imaging modalities in animal tissue samples was conducted. Preliminary results of the ongoing analysis of the acquired experimental data are provided in Section 5.4. While HeCT yielded a similar RSP accuracy to that of DECT, image artifacts are present for the particle imaging modalities reducing the image quality. Especially for pCT large ring artifacts were present in the reconstructions, exceeding those previously reported in the literature and their origin is not yet fully understood. A general limitation was the time uptake for a full PCT at a synchrotron facility.

Based on the experience with the limitations of particle imaging, as well as the needs for optimal RSP accuracy and image noise, we investigated different detector designs for helium ion imaging. The results are provided as Appendix A. For helium ion imaging, the necessity to filter out fragments limits the choice of detector equipment, if a ΔE-E filter is to be applied. However, multistage detectors are subject to ring artifacts due to uncertainties related arising at stage interfaces. In addition, the need to fully stop the particles results in an increased energy straggling and loss of primaries, compared to the ideal case. A Time-Of-Flight (TOF) detector system was investigated as potential alternative, as it does not require the particles to come to a complete stop and hence, results in less straggling and less loss of primary particles. However, the inference of the energy based on the TOF requires very high time resolution (<10ps), if a clinically relevant distance ($\sim$30 cm) between the TOF detector planes is assumed.

In publication P.VII, a novel concept for on-line particle imaging is evaluated: Helium ions offer the unique potential of online particle imaging during carbon ion therapy. Due to the magnetic rigidity of fully stripped helium and carbon ions being approximately equal (relative difference $\sim$0.065%), the two ion species may be accelerated simultaneously to the same energy per nucleon in a circular accelerator. Due to the factor 3 longer range of helium ions compared to that of the carbon ions at the same energy per nucleon, this opens up the possibility to utilize a small helium ion contamination in a carbon ion therapy beam for online feedback on the treatment (Mazzucconi et al. (2018), as well as conference contribution C.XI and publication P.VII). In publication

P.VII, the clinical potential of this promising modality is investigated experimentally in collaboration with the GSI Helmholtzzentrum für Schwerionenforschung GmbH (Dr. Christian Graeff; Darmstadt, Germany), the University College London (Assoc. Prof. Simon Jolly, Dr. Raffaella Radogna and Laurent Kelleter; London, United Kingdom). These proof-of-concept experiments have been conducted using separately irradiated helium and carbon ion beams, as a real mixed beam was not yet available at the HIT facility. An integration mode detector was used for the proof-of-concept study, since the system needs to cope with the high rate of carbon ion fragments produced during therapy. Due to its simple setup and high range resolution, the scintillator stack range telescope developed in the PhD thesis of Mr. Laurent Kelleter (Kelleter 2020) was chosen to monitor the residual helium ion range and the carbon ion fragments produced during carbon ion therapy. It is demonstrated that, for a 1/10 ratio between primary helium and carbon ions, the helium/carbon method enables to resolve relative range changes of only 1 mm that affect less than a quarter of the helium ions in the pencil beam — despite the signal contamination with the carbon fragments. Further, the method is investigated for the use in prostate cancer therapy using two anthropomorphic pelvis phantoms. A promising potential of the helium/carbon mixing for detecting patient rotations and rectal gassing is demonstrated. This study therefore sets a strong reasoning for further investigating the acceleration of a mixed helium/carbon ion beam. In addition, in these beam tests, a full experimental characterization of the novel scintillator stack range telescope has been conducted with proton and light ion beams, the results of which are published in publication P.V (not featured in this thesis).

To enable the full potential of online helium ion imaging in a mixed helium carbon beam, namely to resolve highly accurate 2D WET images of the patient anatomy as seen by the treating beam, it would be desirable to resolve the single-event information. However, due to the expected event rate, especially of secondary fragments produced during carbon ion beam therapy (the highest used clinical rate at the HIT is 80 MHz), a true single-event measuring detector is infeasible. Rather, the idea would be to use a hybrid detector, capable of measuring a high rate of simultaneously impinging particles in a mixed radiation field, and then resolve the single-event information only in data processing. Currently, a group from the University of Bergen (Bergen, Norway) is developing a suitable detector prototype (Pettersen et al. 2017, Pettersen et al. 2019b). The envisioned system is based on the ALPIDE CMOS MAPS sensor chips originally intended for CERN's ALICE experiment inner tracking system upgrade (Mager 2016). The pCT system design has recently been optimized for proton imaging (publication P.IX, not featured in this thesis). It consists of 40 layers of ALPIDE chips interleaved with aluminum plates used both as beam degrader and to hold the chips. The system will measure a multiplicity of particles simultaneously per read-out frame. The fine pixelization of the ALPIDE chips then enables to track individual particles in data processing, regaining the single-event information (Pettersen et al. 2019b). In order to improve the range resolution, a Bragg-peak fit to the energy deposit

in each detector layer is performed. Since the ALPIDE sensor does not measure energy directly, the energy deposit is obtained from the size of the pixel clusters produced around a hit due to charge diffusion. In collaboration with the University of Bergen pCT group, first tests with the ALPIDE sensors for their use in proton, helium and carbon ion beams have been performed at the HIT facility. From these tests, the cluster size to energy relationship has been derived. The results are featured in publication P.VIII (not presented as part of this thesis) and publication P.II (not presented in this thesis).

For the operation in a mixed helium/carbon ion beam, the usual front tracker pair used with a single-event system becomes impractical for a clinical realization. Additional material in the beam line in front of the patient is usually tried to be reduced to a minimum, to avoid additional fragmentation and scattering before the patient. In addition, if a large number of particles are measured simultaneously per detector read-out frame, the scattering inside the object would make it difficult to connect front and rear tracker measurements accurately. Hence, in a conjoined project with Mr. Jarle R. Sølie (University of Bergen, Bergen, Norway), the feasibility of utilizing the pencil beam scanning information as substitute for the front tracker has been investigated (publication P.VI). The recently extended MLP formalism by Krah et al. (2018) was utilized in combination with the uncertainty matrix of the pencil beam. It is demonstrated that the use of this path estimate is superior over the use of only the pencil beam mean position in conjunction with a conventional MLP algorithm. Simulated Proton Radiographies (pRads) and pCTs for a system with and without front tracker are presented. Further, a comparison is made between ideal and realistic material budget of the tracking detectors. An overall reduction of the spatial resolution for the setup without front trackers is observed. However, the difference between setups with and without front trackers is reduced when considering realistic tracker properties, compared to the decrease in image quality observed when assuming an ideal tracking system. Uncertainties associated with realistic trackers affect the setup with front trackers more than they do the setup without front trackers.

The lower scattering of helium ions compared to that of protons would be especially beneficial for a single sided system. Not only does the lower scattering improve the path estimation, it also results in smaller achievable pencil beam spot sizes due to the reduced scattering in the nozzle. In the final publication presented as part of this thesis (publication P.III), the feasibility and limits of helium imaging with the University of Bergen setup are therefore assessed in simulation (principal author Dr. Helge E. S. Pettersen (Haukeland University Hospital, Bergen, Norway)). Since secondary particles have previously been demonstrated in publication P.XII to be detrimental for the image accuracy, different filtering approaches to remove secondary particles inside the silicon pixel sensor telescope are investigated. It is shown that filtering based on the charge cluster size measured in the ALPIDE chips can reduce the fragment contamination effectively. In addition, the optimal degrader material between the sensitive layers of the detector is studied, pointing towards the aluminum degrader already planned for the final detector to be optimal also for helium ion imaging in terms of loss of primaries compared to carbon

based degrader materials. However, the WET of the degrader as optimized for proton imaging, is shown to be too thick for helium ions resulting in systematic artifacts in the images from sampling gaps in the WEPL distribution. Still, despite the systematic fluctuations, for Helium ion radiography (HeRad) of an anthropomorphic head phantom a high WET accuracy was achieved, benefiting from the reduced scattering of the helium ions.

Simulations presented in this thesis have been carried out with the Geant4 Monte Carlo simulation toolkit (Agostinelli et al. 2003, Allison et al. 2006, Allison et al. 2016) and the TOPAS toolkit, where the specific version is indicated in the publications. Geant4 is a powerful tool for particle transport simulation, and provides a high level of control over the simulation and scoring, enabling highly detailed modelling of experimental setups. Its various physics lists have been tested against experimental data in several papers found in the literature. The TOPAS toolkit is a wrapper of Geant4 targeted directly for medical physics. The concept of TOPAS is to rely on simple parameter files, rather than C++ code, in order to make the simulation toolkit more approachable and user friendly. The default physics classes enabled in the TOPAS toolkit have been validated experimentally for proton therapy (Testa et al. 2013a). In this thesis, a pre-existing TOPAS implemented model of the US pCT collaboration prototype scanner (Piersimoni et al. 2017) has been utilized in publication P.XII and publication P.XI. For the two publications in collaboration with the University of Bergen where the simulations have been implemented mainly by Mr. Jarle R. Sølie and Dr. Helge E. S. Pettersen, the Gate (Jan et al. 2011, Grevillot et al. 2010) Geant4 wrapping toolkit is utilized. All data analysis presented have been conducted using self-written analysis software written in the python (`www.python.org`) and C++ (`www.cplusplus.org`) programming languages.

CHAPTER 5

Publications

This thesis is presented as an accumulation of manuscripts published from the thesis research, in accordance with the regulations of the Department of Physics and Astronomy of Heidelberg University. Over the course of the thesis project, the author of this thesis has contributed to nine articles published in internationally acclaimed peer-reviewed journals, two articles currently under revision, and one in preparation. In this thesis, seven of these manuscripts are featured, where the author of this thesis is either the principal (first) author (publications P.XII, P.XI, P.VII, P.IV, P.I) or principal co-author (publications P.VI, P.III). As such, the cumulative work presented here was predominantly performed by the author of this thesis. Detailed author contribution statements precede each publication. As required by the regulations for cumulative dissertations, two of the first author publications in particular publication P.XII and publication P.IV, are not and will not be used in any other dissertation. The content of the publications has not been altered. The formatting has been edited to be conform with the rest of the thesis.

5.1 P.IV: Spatial resolution of particle radiographic imaging

Title : Theoretical considerations on the spatial resolution of single-event particle radiography

Authors : L. Volz, C.-A. Collins-Fekete, J. Sølie and J. Seco

Status : Published

Journal : Biomedical Physics and Engineering Express

DOI : doi.org/10.1088/2057-1976/ab9c3f

Contributions : The principal author, LV, conceptualized the work, developed the theoretical models and wrote the software to generate and analyze the data under the supervising guidance of JS. CACF contributed to the development of the theoretical formalism, especially for the maximum likelihood radiography algorithm, and discussion of the results. JRS aided in the conceptualization of the work and contributed with discussions on the understanding of the observations made. JS coordinated the research and ensured its scientific rigor and relevance. LV finalized the results, produced the plots shown and wrote the manuscript. All authors contributed to the review process of the manuscript draft.

5.2 P.XII: Feasibility study for high quality helium ion imaging

Title : The impact of secondary fragments on the image quality of helium ion imaging

Authors : L. Volz, P. Piersimoni, V. A. Bashkriov, S. Brons, C.-A. Collins-Fekete, R. P. Johnson, R. W. Schulte and J. Seco

Status : Published

Journal : Physics in Medicine and Biology

DOI : doi.org/10.1088/1361-6560/aadf25

Contributions : The principal author, LV had the idea for and implemented the dE-E filtering technique to identify and remove secondary fragments before image reconstruction, conducted the processing of the experimental data, the HeCT image reconstruction and wrote the software for the analysis of the image quality. JS supervised the research, coordinated the project between institutions and ensured the relevance and rigor of the investigations. LV, PP, CACF, RPJ and RWS directly participated in the experiments at the Heidelberg Ion-Beam Therapy Center. CACF contributed to the conceptualization of the work. RPJ provided technical support on the detector prototype, and together with VAB and RWS provided support on the calibration and pre-processing software for the detector. LV, PP and RPJ together modified the calibration software to enable the processing of helium ion data. LV together with SB developed the low intensity helium ion raster scanning plans to fit the detector specifications. PP conducted the simulations presented in the work. This included a detailed investigation on the energy deposit of individual secondary fragment species, which aided in the understanding of the observed detector signals. LV finalized the research, produced all plots shown in the manuscript and, with significant input from PP, wrote the manuscript draft. The contribution by PP was acknowledged by a shared first author position on the manuscript. All authors contributed to the review process of the manuscript.

Abstract

Single-event ion imaging enables the direct reconstruction of the relative stopping power (RSP) information required for ion-beam therapy. Helium ions were recently hypothesized to be the optimal species for such technique. The purpose of this work is to investigate the effect of secondary fragments on the image quality of helium CT (HeCT) and to assess the performance of a prototype proton CT (pCT) scanner when operated with helium beams in Monte Carlo simulations and experiment.

Experiments were conducted installing the U.S. pCT consortium prototype scanner at the Heidelberg Ion-Beam Therapy Center (HIT). Simulations were performed with the scanner using the TOPAS toolkit. HeCT images were reconstructed for a cylindrical water phantom, the CTP404 (sensitometry), and the CTP528 (line-pair) Catphan® modules. To identify and remove individual events caused by fragmentation, the multistage energy detector of the scanner was adapted to function as a $\Delta E - E$ telescope.

The use of the developed filter eliminated the otherwise arising ring artifacts in the HeCT reconstructed images. For the HeCT reconstructed images of a water phantom, the maximum RSP error was improved by almost a factor 8 with respect to unfiltered images in the simulation and a factor 10 in the experiment. Similarly, for the CTP404 module, the mean RSP accuracy improved by a factor 6 in both the simulation and the experiment when the filter was applied (mean relative error 0.40 % in simulation, 0.45 % in experiment). In the evaluation of the spatial resolution through the CTP528 module, the main effect of the filter was noise reduction. For both simulated and experimental images the spatial resolution was $\sim 4\,\mathrm{lp/cm}$.

In conclusion, the novel filter developed for secondary fragments proved to be effective in improving the visual quality and RSP accuracy of the reconstructed images. With the filter, the pCT scanner is capable of accurate HeCT imaging.

Introduction

Ion imaging was first proposed conceptually by Cormack (1963) in the form of proton computed tomography (pCT). The first experimentally acquired proton radiography (pRad) was published just a few years later (Koehler 1968). Studies on heavy ion imaging (atomic number $Z > 1$) followed shortly after (cf. Benton et al. (1973)). However, due to the need for large accelerators to produce ions of sufficient energy for imaging, this imaging modality was impractical for diagnostic use. Only with the advent of proton and ion radiotherapy, ion imaging gained increasing interest in the medical community.

Ion radiotherapy makes use of the favorable depth dose profile of ions, the *Bragg peak*, for a highly localized dose deposition in the patient. To maximize the treatment accuracy, knowledge of the position of the Bragg-peak distal fall-off within the patient is crucial. The distance from beam entry to a specified relative dose point on the distal slope of the fall-off (e.g., 90 % of the peak dose)

which is related to the range of the ions can be obtained from the Bethe-Bloch stopping power formula (Bethe & Ashkin 1953, Doolan et al. 2016). In current clinical practice, the stopping power information within the patient is retrieved by converting Hounsfield Units (HUs) from a X-ray planning CT to relative stopping power (RSP) (Schneider et al. 1996), defined as the stopping power of a material relative to that of water. The conversion from HU to RSP introduces range uncertainties (Yang et al. 2012) which have to be accounted for in clinical treatment planning, for example, by adding a 3.5 % plus a 3 mm margin (Paganetti 2012). Dual energy X-ray CT allows a better separation between electron density and atomic number effects on HU than single-energy CT, and should, therefore, improve the range uncertainty associated with the use of X-ray CT in treatment planning (Zhu & Penfold 2016, Bär et al. 2017, Wohlfahrt et al. 2017a). This has been evaluated in animal tissues with promising results (Taasti et al. 2017, Möhler et al. 2018, Bär et al. 2018b).

Ion imaging, on the other hand, can provide the direct reconstruction of the voxelized RSP information (Zygmanski et al. 2000). Moreover, ion imaging is expected to provide a better signal-to-noise ratio and higher density resolution at a lower dose level compared to conventional X-ray CT (Schulte et al. 2005, Depauw & Seco 2011). Finally, it does not suffer from beam hardening or metal artifacts (Depauw & Seco 2011, Ordoñez et al. 2017).
However, the spatial resolution of ion imaging suffers from multiple Coulomb scattering (MCS) which leads to non-linear ion trajectories. In single-event ion imaging this problem is addressed by the individual reconstruction of each ion path through the object. Various path estimation techniques have been developed among which the most likely path (MLP) algorithm is the most commonly used (Williams 2004, Li et al. 2006, Schulte et al. 2008, Erdelyi 2009, Collins-Fekete et al. 2017d). The MLP algorithm requires the knowledge of position and direction before and after the object of each projectile particle, as well as its residual energy. Therefore, ion imaging requires sophisticated detector systems, capable of measuring particle track information and residual energy/range on a single-event basis (Schulte et al. 2008). To date, several different prototype systems have been developed (Bashkirov et al. 2009, Seco & Depauw 2011, Talamonti et al. 2012, Uzunyan et al. 2015, Bashkirov et al. 2016a, Price 2016, Pettersen et al. 2017, Gehrke et al. 2017).

Additionally, current investigations in the field of single-event ion imaging focus on the choice of the optimal ion species to generate images. Whereas until now most studies have been based on protons, recently helium ions were identified to have a great potential especially in terms of spatial resolution (Hansen et al. 2014a, Collins-Fekete et al. 2017d, Gehrke et al. 2018, Piersimoni et al. 2018).
In 2016, a collaboration between the German Cancer Research Center (DKFZ)

and the U.S. pCT consortium[1] was established to investigate helium single-event radiography (HeRad) and tomography (HeCT). The U.S. pCT consortium prototype scanner (Bashkirov et al. 2016b, Johnson et al. 2016) that is capable of high quality pCT imaging (Plautz et al. 2016, Giacometti et al. 2017a, Piersimoni et al. 2017, Johnson et al. 2017) was tested for the operation with helium beams at the Heidelberg Ion-Beam Therapy Center (HIT). However, while preliminary results reported in Volz et al. (2017) and Collins-Fekete et al. (2017c) confirmed the expected increase in spatial resolution between pRad and HeRad, ring artifacts and a relatively low RSP accuracy were present for HeCT. This may be attributed to the projectile fragmentation processes of helium ions that are not present for protons. Fragments, both arriving from the object and generated inside the detector, have to be carefully identified and separated from the primary particle histories for accurate image reconstruction.

In this work, the effect of fragments in helium ion imaging with the pCT consortium prototype both in Monte Carlo (MC) simulation and experiment was investigated. A filtering method was developed using the multistage design of the pCT scanner energy/range detector as a $\Delta E - E$ telescope to efficiently remove all secondary particles before image reconstruction.

Theory

Fragmentation Processes for Helium Ions

In traversing the object and the detector material ions can undergo nuclear interactions with the target nuclei. Both elastic nuclear interactions and mass / charge changing inelastic interactions are possible, the latter resulting in the production of secondary particles.

Secondary particles from nuclear interactions can be grouped into "target" and "projectile" fragments. Target fragments can have a large atomic number, but are usually produced with only a small energy/range (Loveland et al. 1986, Zeitlin & La Tessa 2016) and, therefore, have no significant impact on ion imaging other than depositing unwanted dose to the object. Projectile fragments, on the other hand, are lower charge/mass remnants of primary ions that underwent nuclear break up in collision with a target nucleus. They usually undergo only a minor change of velocity and direction relative to the original projectile (Goldhaber 1974, Wilson 1983, Morrissey 1989, Morrissey 1993, Zeitlin & La Tessa 2016, Rovituso et al. 2017). Helium ions, due to the especially strong bond of the helium nucleus, are less likely to fragment compared to heavier ions (Cucinotta et al. 1993, Mairani et al. 2016, Zeitlin & La Tessa 2016, Rovituso et al. 2017) and have only six fragmentation channels producing neutrons, protons (p), deuterons (d), tritons (t) and ^{3}He. The predominantly produced helium fragments are protons that have essentially the same residual range as

[1] Here, U.S. pCT consortium refers to the collaboration of Loma Linda University (LLU), University of California at Santa Cruz (UCSC) and California State University San Bernardino (CSUSB) (http://scipp.ucsc.edu/pCT/index.html).

the primary helium ions (Rovituso et al. 2017). The produced charged fragments are detected in ion imaging systems with single-event registration, but are not readily distinguished, leading to a mixing of the energy loss of primaries and the lower energy deposit of fragments. An effective filter of secondary fragments is, therefore, crucial for accurate helium ion imaging.

The $\Delta E - E$ Technique

The general principle of a conventional $\Delta E - E$ telescope is to measure the energy loss in a thin absorber (ΔE) and the total residual energy (E) in a thick absorber immediately following the thin absorber for each projectile particle crossing the system. Following the formalism by Tassan-Got (2002) for a particle with atomic number Z, atomic mass A and total kinetic energy $\mathcal{E} = E + \Delta E$, the Bethe-Bloch stopping power can be written in a simplified way as:

$$\frac{\mathrm{d}\mathcal{E}}{\mathrm{d}x} = \frac{Z^2}{f(\mathcal{E}/A)}. \tag{5.50}$$

Defining $F(x)$ as $\int_0^x f(t)\mathrm{d}t$, ΔE can be written as a function of E:

$$\Delta E = A\left[F^{-1}\left(F\left(\frac{E}{A}\right) + \frac{Z^2}{A}\Delta X\right) - \frac{E}{A}\right], \tag{5.51}$$

where ΔX is the thickness of a homogeneous ΔE detector. Due to the dependence on Z and A in equation 5.51, plotting E against ΔE for each event results in separated response curves for different particle species, consequently enabling particle identification in a mixed beam (Carboni et al. 2012).

Materials and Methods

The Prototype Scanner

For this study the prototype scanner built by the U.S. pCT consortium was used. The prototype was originally developed for proton beams and its design and operation have been described already elsewhere (Sadrozinski et al. 2013, Bashkirov et al. 2016b, Bashkirov et al. 2016a, Sadrozinski et al. 2016, Johnson et al. 2016, Johnson et al. 2017). Figure 5.15 shows the scanner installed at the HIT experimental beam line.

The residual energy/range of each particle is measured with a custom-designed 5-stage energy/range detector (Bashkirov et al. 2016b). Each stage is made of plastic scintillating material (polystyrene UPS-923A) and has a dimension of $375 \times 100 \times 50.8\,\mathrm{mm}^3$. The scintillation light is collected by Hamamatsu R3318 photomultiplier tubes (PMTs) and converted into digital values by custom readout electronics (Johnson et al. 2016). The scanner is able to resolve particle rates up to 1 MHz with less than 5 % event pile up for the setup investigated in Giacometti et al. (2017a) and a data acquisition dead time of less

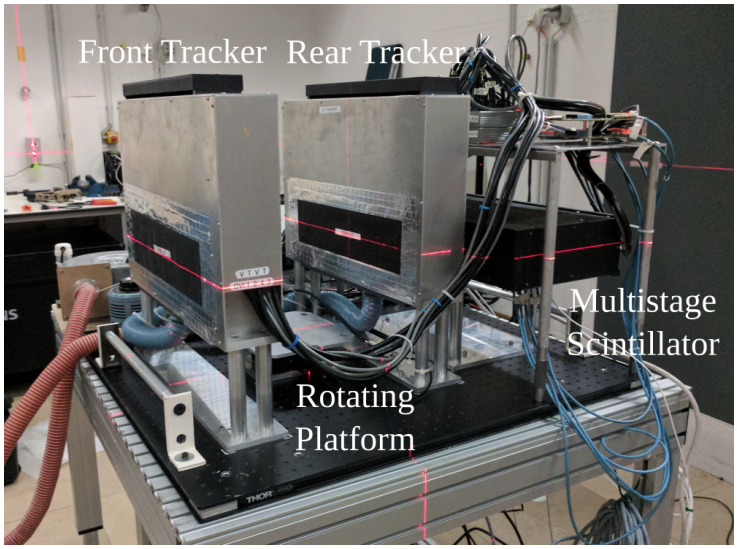

Figure 5.15: The U.S. pCT consortium prototype pCT scanner installed at the HIT facility. The detector consists of two tracking detectors, a multistage energy/range detector and a custom high-speed data acquisition board. For the prototype, a rotating platform enables full CT scans of various phantoms.

than 4 %. More details of the operation principle and performance of the scanner have been previously presented in Bashkirov et al. (2016a).

Calibration

Before the scanning experiment, the response of the energy/range detector was calibrated to water equivalent path length (WEPL) using a dedicated polystyrene object of known water equivalent thickness. The calibration procedure was originally developed by Bashkirov et al. (2016a). For the present work, the recently refined calibration procedure as given in Piersimoni et al. (2017) and Piersimoni et al. (2018) was followed. Two polystyrene wedges ($120 \times 120 \times 50.8\,\mathrm{mm}^3$) and 4 polystyrene degraders ($280 \times 120 \times 50.8\,\mathrm{mm}^3$) were used. The calibration was reproduced also in the simulations. The polystyrene material had a RSP$= 1.030 \pm 0.003$ for the experimental, and a RSP=1.043 for the simulated setup (Piersimoni et al. 2017, Piersimoni et al. 2018).

Simulation

MC simulations were performed using the simulation toolkit TOPAS (Perl et al. 2012) release 2.0 patch 3 with Geant4 (Agostinelli et al. 2003, Allison et al. 2006, Allison et al. 2016) version 10.01 patch 02. The default physics list was activated for the TOPAS application. This so-called "Modular Physics List" considers both electromagnetic and nuclear processes relevant for ion therapy (Testa et al. 2013a). In detail, it comprises the following Geant4 physics

lists: G4EmStandardPhysics_option4 for the most accurate electromagnetic interaction models available in standard and low energy categories, G4HadronPhysicsQGSP_BIC_HP, G4DecayPhysics, G4IonBinaryCascadePhysics and G4HadronElasticPhysicsHP for modeling nuclear interactions, and G4StoppingPhysics for nuclear capture at rest.

The simulated detector geometry presented in Piersimoni et al. (2017) was used for this work as well. A flat, ideal beam source was used for the simulations irradiating a $200 \times 100\,\mathrm{mm}^2$ field for phantom studies and $360 \times 90\,\mathrm{mm}^2$ for the calibration setups. Primary helium ions were simulated with an initial energy of 200 MeV/u. For each projection $2 \cdot 10^6$ particles were used. A full tomographic scan consisted of 90 projections at a 4° angular step, following the work-flow established by Plautz et al. (2016).

Experimental Setup at the Heidelberg Ion-Beam Therapy Center

Experiments were conducted at the HIT facility operating the U.S. pCT consortium scanner with helium beams.
The helium ion beams were delivered through the beam monitoring nozzle at the HIT beam line dedicated to experiments (Haberer et al. 2004). A $200 \times 100\,\mathrm{mm}^2$ field was irradiated using the HIT raster scanning with a spot size of 10.2 mm FWHM. The beam initial energy was set to 200.38 MeV/u (261.8 mm range in water). The particle rate was set to ~ 800 kHz to avoid event pile-up. Full tomographic scans were acquired in 90 individual projections in steps of 4°. Each projection consisted of $\sim 2.5 \cdot 10^6$ particles. For each calibration run $\sim 5 \cdot 10^6$ particles were used.

Investigated Phantoms

A cylindrical water phantom of 150 mm diameter and 40 mm height was investigated to disentangle the effect of fragments on HeCT from effects originating from the phantom geometry. The phantom container is made of a hollow plastic cylinder with 6.35 mm shell thickness that is filled with purified and degasified water (G4_WATER in simulation) and sealed by 6.35 mm thick plastic top and bottom plates.

The Catphan® QA modules (The Phantom Laboratory, Norfolk, Virginia, USA) were HeCT scanned in both simulation and experiment in order to analyze the impact of secondaries on RSP accuracy and spatial resolution. For the simulation, digital versions of both phantoms were based on the implementation by Giacometti et al. (2017a).

In detail, the CTP404 sensitometry module was used to evaluate the RSP reconstruction accuracy. The phantom is an epoxy cylinder of 150 mm diameter and 25 mm height. It contains six tube inserts (12.2 mm diameter) of different plastic materials. The RSP in the center of each material insert was measured in

a circular region of interest (ROI) with a radius of 3 mm and averaged over the 5 most central slices. The RSP of the epoxy material was measured at the same radial position as the inserts. The relative error of the reconstructed RSP was calculated by comparison to peakfinder (PTW, Freiburg, Germany) measurements (Giacometti et al. 2017a) for the experiment, and to the RSP calculated directly from the implemented material compositions in the simulation.

The CTP528 high resolution module was used to evaluate the spatial resolution of the acquired HeCT images. The phantom is a cylinder (40 mm height, 150 mm diameter) made of the same epoxy material as the CTP404 and containing aluminum line-pair inserts with increasing spatial frequency (1 - 21 lp/cm). The modulation transfer function (MTF) was calculated by comparing the maximum-to-minimum contrast at each line pair insert to the reference contrast:

$$MTF(x) = \frac{\langle \mathrm{RSP}_{max} - \mathrm{RSP}_{min} \rangle}{\mathrm{RSP}_{Al} - \mathrm{RSP}_{Epoxy}}, \quad x \in \{1\,\mathrm{lp/cm}, \ldots, 21\,\mathrm{lp/cm}\}\,. \tag{5.52}$$

The RSP of aluminum is 2.11, that of the Epoxy material 1.14 (Giacometti et al. 2017a). The $\mathrm{MTF}_{10\,\%}$, defined as the number of line pairs per cm resolved at 10 % of the contrast, was used to quantify the spatial resolution (Seco et al. 2013).

The Energy/Range Detector as a $\Delta E - E$ Telescope

The 5-stage structure of the energy detector was adapted to be used as a $\Delta E - E$ telescope. The concept is explained schematically in figure 5.16. The energy deposit measured in the stage where the ion stops (henceforth denoted *Bragg-peak stage*) was used as the residual energy E. ΔE was then defined as the energy deposited for the same event in the stage adjacent to the Bragg-peak stage in upstream direction (noted as ΔE *stage*).

For each stage (except stage 1) the $\Delta E - E$ spectrum was plotted using the detector response from the 5 calibration runs. In the simulation, the response curves were then identified by plotting the spectrum of each fragment species individually. In experiment, the individual response curves in the $\Delta E - E$ spectrum were identified by comparison with the simulation. The primary helium curve was parametrized with a second degree polynomial function which could subsequently be used as a filter for secondary fragments in the pre-processing of the image data.

Pre-Processing and Image Reconstruction

Image reconstructions were performed using 3 different pre-processing modalities: using all events without filtering secondary fragments, applying a standard threshold filter on the energy loss in each stage prior to the Bragg-peak stage, and applying the $\Delta E - E$ filter specifically developed.

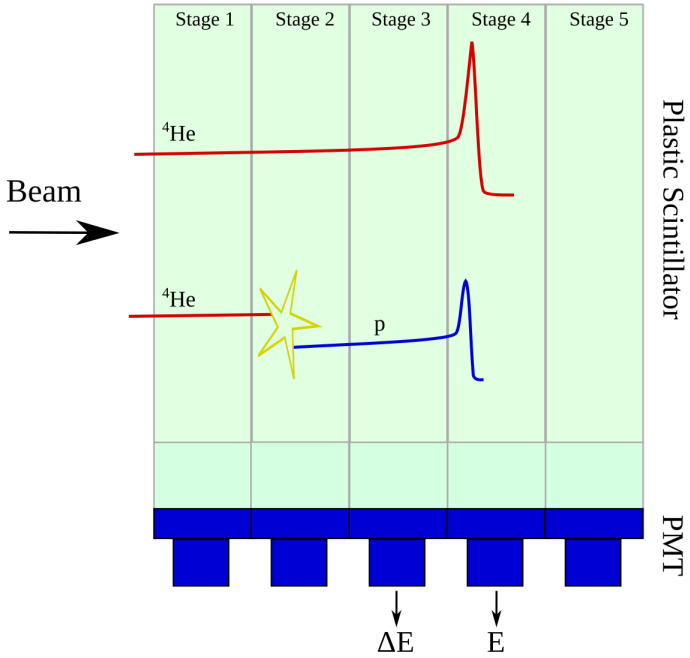

Figure 5.16: Drawing explaining how the $\Delta E - E$ technique was used with the U.S. pCT consortium prototype scanner. For each event, the residual energy E was taken as the energy deposit in the stage where the particle stopped, while ΔE was the energy deposited in the adjacent stage in upstream direction. Helium primaries and secondary fragments stemming from the object to be imaged or from nuclear interactions inside the detector geometry (as depicted by the yellow star) were distinguished by their individual correlation between E and ΔE.

The standard threshold filter removed all events with energy deposition lower than the lower bound energy deposit in each stage prior to the Bragg-peak stage based on a simulated helium depth dose curve when no phantom was placed in the beam line (within 5σ deviation). The same threshold filter has also been used for proton imaging with the device.

The $\Delta E - E$ filter was based on comparing the relationship between the energy deposit in the Bragg-peak stage of an event and the respective ΔE stage to the parameterization of the helium response curve derived for these stages during the calibration. The events for which the $\Delta E - E$ relationship was not compatible with the parameterized helium curve within a certain margin based on the relative occurrence frequency (see figure 5.18) were discarded for the image reconstruction.

Before the image reconstruction, also a 3σ cut was applied to the angular displacement and WEPL to filter out large angle scattering and unusually large energy losses for all setups.

The particle trajectories were estimated using the MLP algorithm by Schulte et al. (2008) that was recently shown to be also applicable for helium ions (Collins-Fekete et al. 2017d). Images were reconstructed using the diagonally relaxed orthogonal projection (DROP) iterative reconstruction technique with superiorization of the total variation norm (TVS), here denoted as DROP-TVS algorithm (Penfold et al. 2010). The Feldkamp-David-Kress (FDK) algorithm was used to generate the starting iteration for the algorithm (Giacometti et al. 2017a) and to perform a hull projection as described in Schultze et al. (2015). The DROP-TVS algorithm was run for 8 iterations and using 40 reconstruction blocks to allow a comparison with the experimental pCT results presented in Giacometti et al. (2017a). A recent study (Schultze et al. 2018) showed that a higher number of iterations would increase the spatial resolution and RSP accuracy, but would also enhance noise.

Results

$\Delta E - E$ Spectrum of the Detector

Figure 5.17 shows the individual $\Delta E - E$ spectrum for relevant secondary particles from a simulated calibration run with the 2 wedges and 2 degraders, so that most particles stop in stage 3. The spectrum was acquired by plotting the energy loss in stage 3 of all particles stopping in that stage, against their energy deposit in stage 2. Figures 5.17(a), (b), (c), (d), (e), and (f) show, respectively, the plots for protons, deuterons, tritons, ^{3}He, secondary and primary ^{4}He. The depicted spectra are overall very similar to the experimental measurements by Rovituso et al. (2017).

With the same setup, the total energy deposited by all particles stopping in

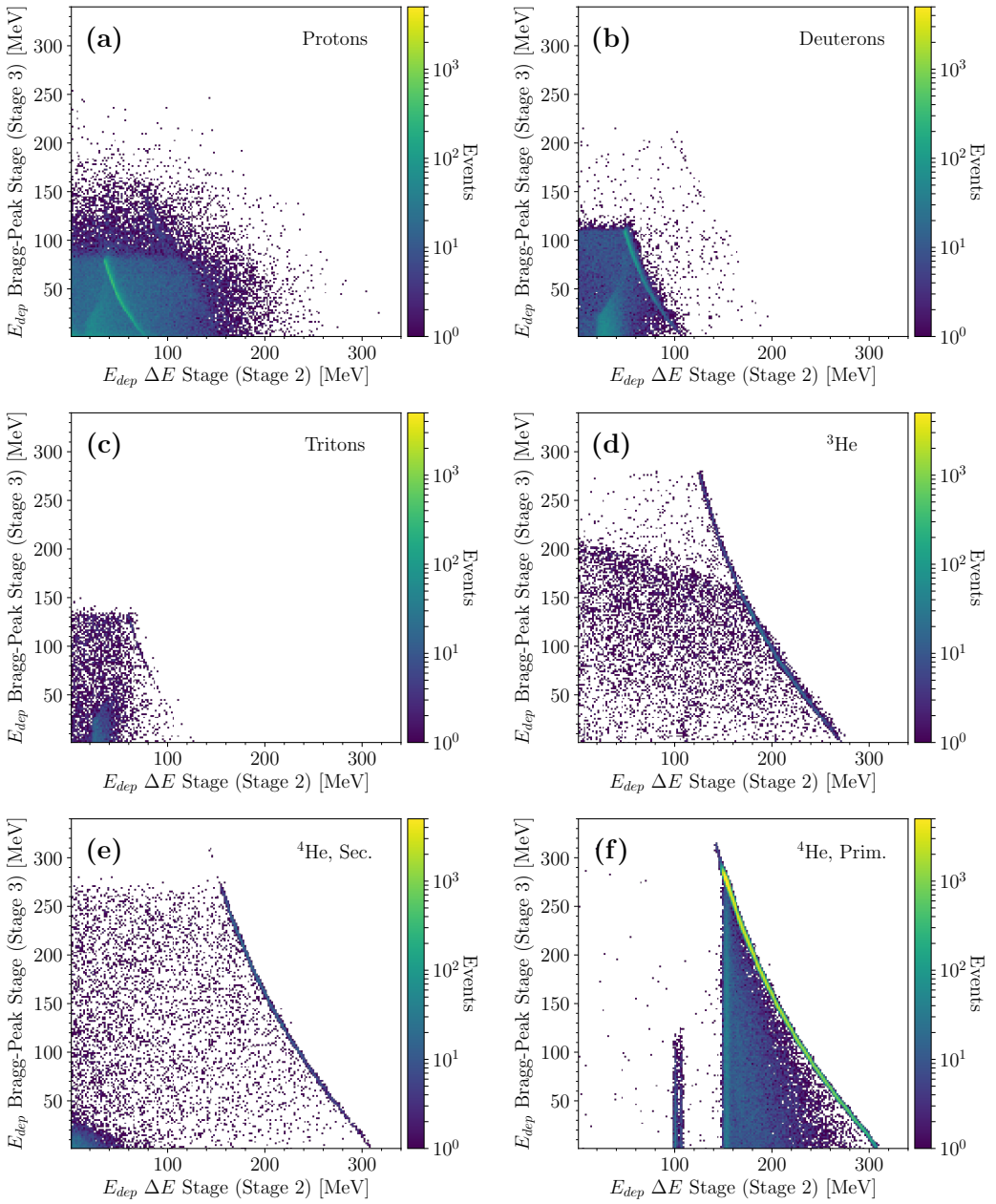

Figure 5.17: Simulated $\Delta E - E$ spectrum acquired for a calibration run with the two polystyrene wedges and two polystyrene degraders in the scanner. The energy loss of particles stopping in stage 3 (Bragg-peak stage) was plotted against their respective energy loss in stage 2 (ΔE stage). The plots refer to different particles, as indicated.

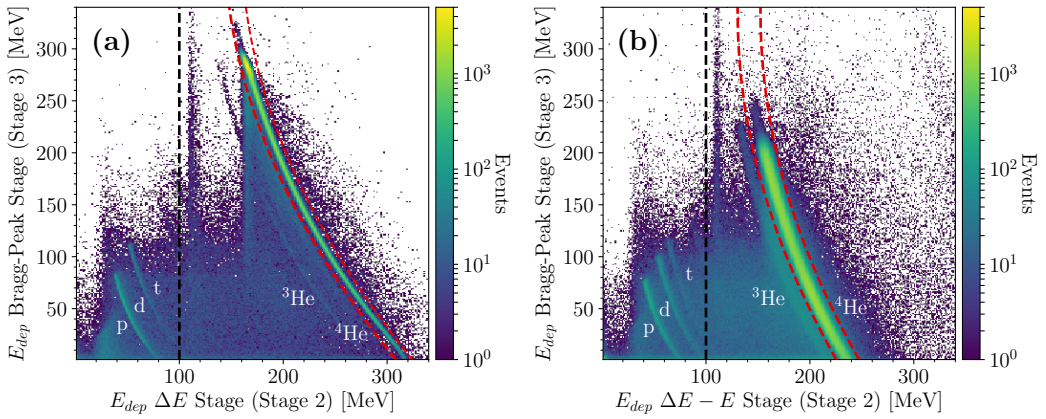

Figure 5.18: $\Delta E - E$ spectrum acquired for a calibration run with the two polystyrene wedges and two polystyrene degraders in the scanner. The plot was acquired following the procedure in figure 5.17 for **(a)** TOPAS simulated data, and **(b)** experimental data. The labels indicate the response curves of individual fragments as found through comparison with figure 5.17. The dashed red lines and the dashed black line are the $\Delta E - E$ filter and the threshold filter, respectively.

stage 3 was plotted against the energy deposited in stage 2, for both simulation (figure 5.18(a)) and experiment (figure 5.18(b)). The response curves in the spectra were identified by comparison with figure 5.17.

The noise visible in the spectra corresponds to particles stopping in stage 3 before reaching the Bragg-peak region due to nuclear interaction or scattering events. Especially noteworthy is the vertical pattern at approximately 110 MeV energy deposit in stage 2 visible in both figures 5.17(f) and figure 5.18. The pattern is located around an energy deposit in stage 2 expected for ^{4}He primaries that should stop in stage 5 (i.e. having crossed little to no WEPL). Hence, this pattern was likely caused by projectile particles that missed the phantom, but stopped in stage 3 before reaching their Bragg-peak region.

The dashed black line depicts the standard threshold that filters out most of the proton, deuteron and triton contamination, as seen by comparison with figure 5.17. However, the ^{3}He contamination was not affected by this filter. The margins of the $\Delta E - E$ filter are indicated by the dashed red lines in figure 5.18. The $\Delta E - E$ filter separated ^{4}He from noise and ^{3}He fragments.

In the experiment, approximately 38 % of the events were removed by the $\Delta E - E$ filter compared to the data without filtering fragments for the setup investigated here. In simulation, this number was slightly higher with $\sim$ 43 % of events cut.

Notably, the experimentally acquired and simulated spectra in figure 5.18 differ from each other. This effect will be discussed in more detail in section 5.2.

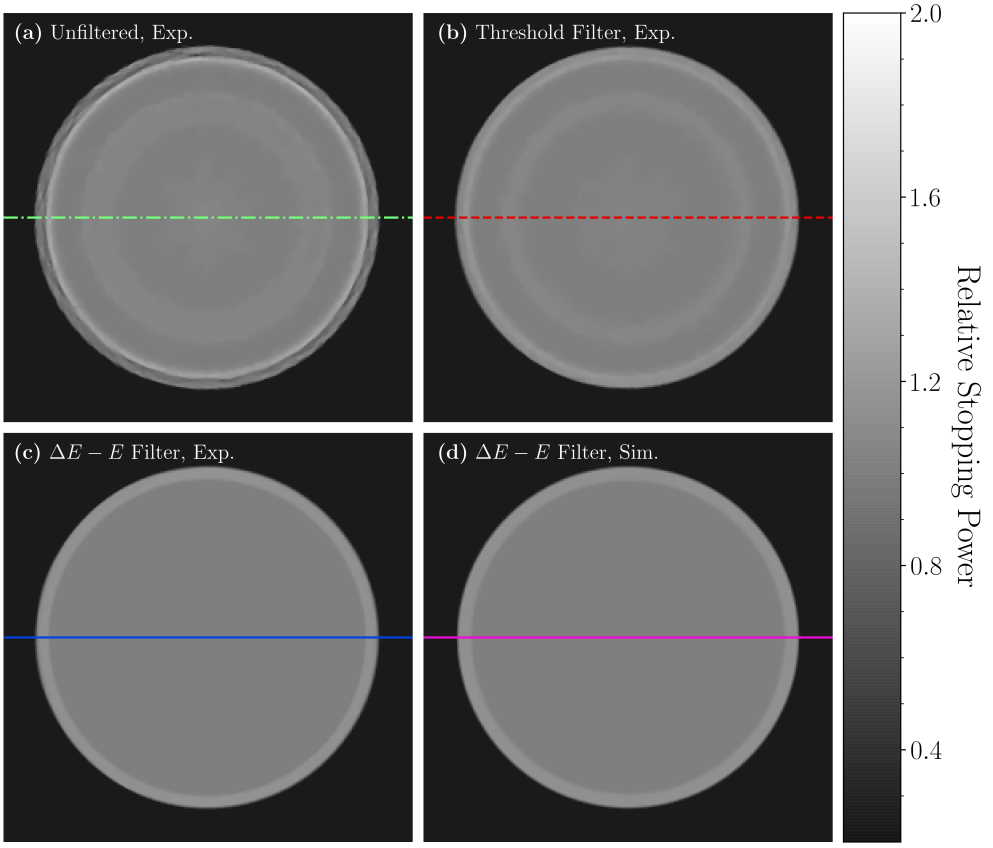

Figure 5.19: Transverse slice of the HeCT reconstructed images of the water cylinder. **(a)** Experimental data without filtering of secondaries. **(b)** Same slice with application of the standard threshold filter. **(c)** Same slice with the new $\Delta E - E$ filter. **(d)** Simulated data with the $\Delta E - E$ filter for comparison. All images were reconstructed with 256×256 pixel per slice (0.7 mm pixel size) and slice thickness of 2.5 mm.

HeCT Reconstructed Images of the Water Phantom

Figure 5.19 shows HeCT reconstructed images of the water phantom. In figures 5.19(a), 5.19(b), and 5.19(c), are shown, respectively, an experimentally acquired HeCT reconstructed image with no filtering of secondaries, a reconstructed image with the standard threshold filter, and a reconstructed image with the $\Delta E - E$ filter applied. Figure 5.19(d) shows a simulated HeCT reconstructed image with the $\Delta E - E$ filter for comparison. Strong ring artifacts are visible for the reconstructions of the unfiltered and the threshold filtered events.

Transverse profiles along the lines in figure 5.19 through the HeCT reconstructed images are shown in figure 5.20(a) and figure 5.20(b) for simulated and experimental data, respectively. The ring artifacts visible in figure 5.19(a) and (b) are reflected by significant fluctuations in the profiles of the unfiltered

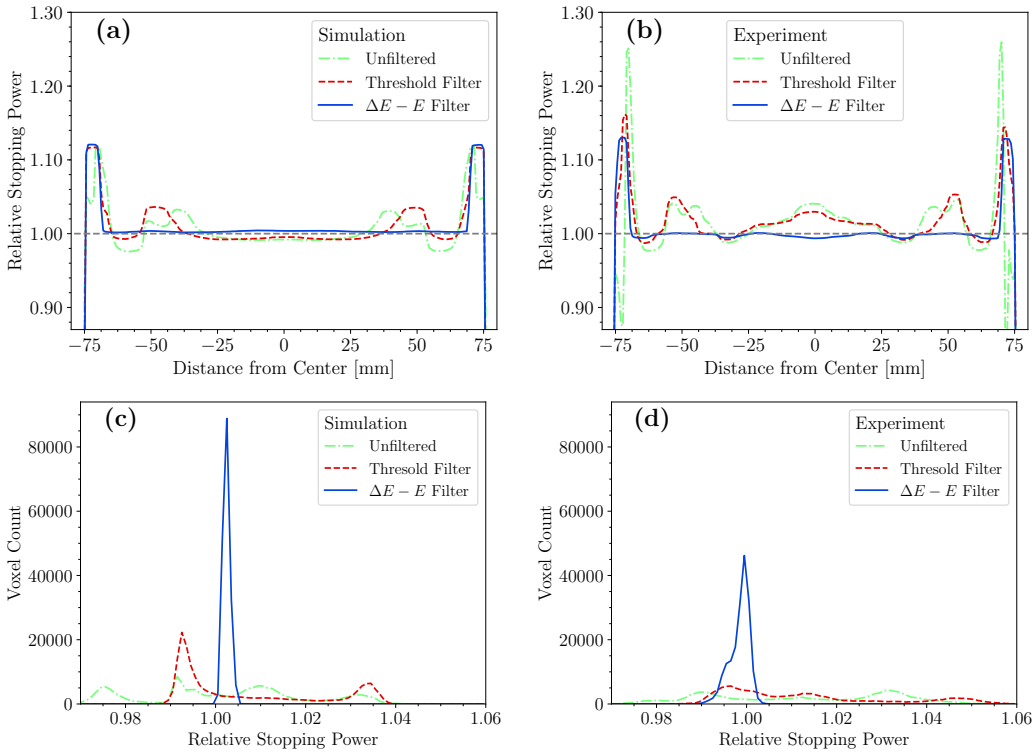

Figure 5.20: Quantitative analysis of the simulated and experimental HeCTs of the water cylinder reconstructed with different settings. **(a)** - **(b)** Traverse profiles along a diameter through the simulated and experimental HeCT reconstructed images, respectively. The dashed green line refers to the reconstruction without filter on fragments, the dashed red line to the reconstruction where a threshold filter was applied, and the solid blue line the reconstruction with the $\Delta E - E$ filter. **(c)** - **(d)** Distribution of the reconstructed RSP values in a cylindrical ROI (radius 60 mm) in the center of the HeCT reconstructed images for simulated and experimental HeCT, respectively.

and threshold filtered HeCT reconstructed images. For the unfiltered HeCT, edge effects were present at the radial position of the phantom plastic shell. In the center, the ring artifacts in the unfiltered HeCT resulted in fluctuations above 4 % compared to the mean value for the simulation, and above 6.5 % for the experiment. With the threshold filter, the ring artifacts were only slightly reduced and still resulted in deviations of $\sim$ 4 % from the mean for the simulation, and $\sim$ 6% for the experiment. With the $\Delta E - E$ filter fluctuations in the HeCT reconstructed images of the simulated data were reduced to less than 0.2 % with respect to the mean. For the experimental data, the $\Delta E - E$ filtered HeCT reconstructed images presented fluctuations of less than 0.5 % with respect to the mean value.

Figure 5.20(c) and figure 5.20(d) depict the distribution of the voxelized RSP

values in a ROI of 60 mm radius in the center of the reconstructions accumulated over the 9 most central slices for simulated and experimental HeCT reconstructed images, respectively. Both in the simulation and the experiment, the RSP values for the unfiltered and threshold filtered HeCT reconstructed images are spread over a range of several percent relative error without following a clear distribution. The maximum relative error was 4.24 % for the unfiltered and 4.01 % for the threshold filtered HeCT in the simulation. In the experiment, the unfiltered HeCT presented a maximum relative error of 7.83 % and the threshold filtered HeCT a maximum of 6.35 %. Conversely, with the $\Delta E - E$ filter, the reconstructed RSP values followed a sharp distribution. In the simulation, the mean relative RSP error of the $\Delta E - E$ filtered HeCT reconstructed images was (0.24 ± 0.07) %. In the experiment, the mean relative error was (0.15 ± 0.22) %. The experimental distribution was broader compared to the simulated and presented a shoulder for smaller RSP values.

Relative Stopping Power Accuracy

Figure 5.21 depicts 4 HeCT reconstructions of the CTP404 sensitometry module with different settings. In figure 5.21(a)-(c) experimental data are reported, while figure 5.21(d) shows the simulated HeCT for comparison. Figure 5.21(a) and 5.21(b) show, respectively, an unfiltered HeCT reconstructed image and one with the standard threshold filter applied. Figure 5.21(b) appears similarly in a previous publication (Volz et al. 2017). Figures 5.21(c) and 5.21(d) show reconstructed HeCT images using the $\Delta E - E$ filter for an experimental and a simulated scan, respectively. The images were reconstructed using 256×256 pixels per slice (0.7 mm pixel size) and a slice thickness of 2.5 mm similar to treatment planning voxel sizes.

Again, ring artifacts visible in figures 5.21(a) and 5.21(b) were not present for the $\Delta E - E$ filtered images. As is indicated by the horizontal lines in the images on figure 5.21, traverse profiles along a diameter through each pair of opposing material inserts were plotted and are shown in figure 5.22. Similarly to the reconstructions of the water phantom, the unfiltered HeCT of the CTP404 module yielded strong edge effects. The threshold filter reduced the artifacts, particularly on the edge of the phantom, while in the center the unfiltered and threshold filtered images showed a similar trend. The fluctuations in the profile were greatly reduced when the $\Delta E - E$ filter was applied. Simulated and experimental reconstructions with the new filter were similarly smooth. The small deviations between the experimental and simulated RSP values for the inserts stemmed from a slight difference in the simulated compared to the real material composition.

The RSP accuracy of the HeCT reconstructed images was evaluated and compared to reference values (peakfinder measurements for experiment, calculated values from the implemented material composition for simulation). The mean relative error of the RSP values reconstructed for the plastic inserts and the epoxy material was (2.39 ± 0.58) % for the unfiltered, and (2.90 ± 0.48) %

for the threshold filtered experimental HeCT, where the given error is the standard error of the mean. Moreover, the RSP values for both the unfiltered and threshold filtered reconstructions were subject to large noise, resulting in standard deviations of the reconstructed RSP values ranging up to $\sim 2\,\%$.

When the $\Delta E - E$ filter was applied, the mean relative error was $(0.40 \pm 0.19)\,\%$ and $(0.45 \pm 0.22)\,\%$ for simulated and experimental HeCT, respectively. The relative error and respective standard deviation of the $\Delta E - E$ filtered HeCT reconstructed values for each insert are shown in figure 5.23. For comparison, figure 5.23 also shows the accuracy of pCT acquired with the system (Giacometti et al. 2017a).

In the experiment, the highest relative error was seen for PMP at $(0.99 \pm 0.43)\,\%$. In the simulation, only for LDPE the relative error was above the clinically acceptable limit at $(1.01 \pm 0.12)\,\%$. Similar results have been previously presented for experimentally acquired pCT with the same scanner (mean relative

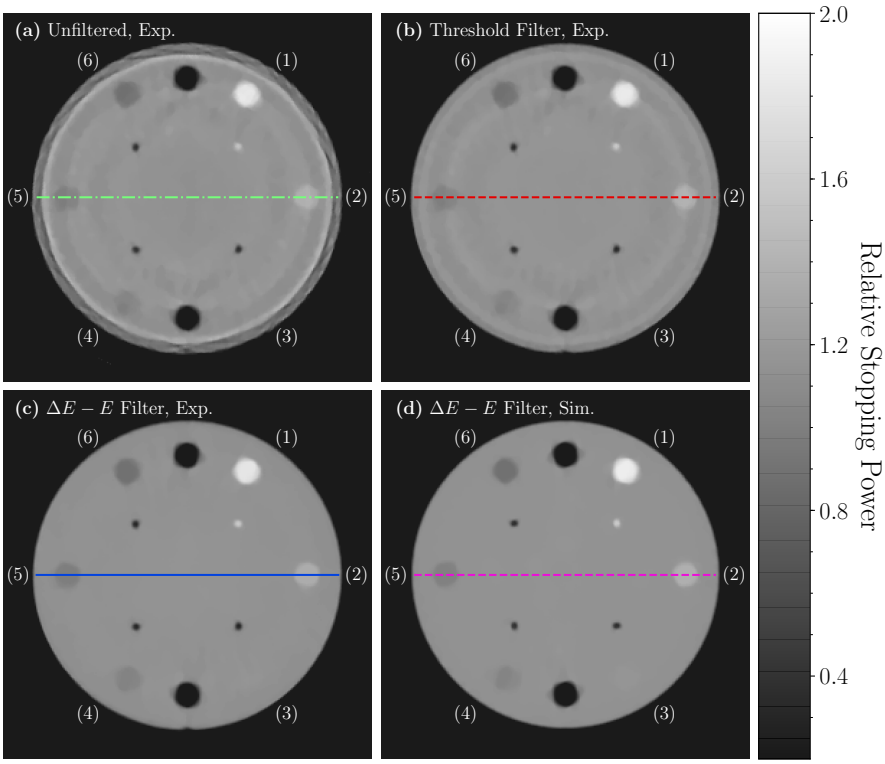

Figure 5.21: Experimental HeCT transverse slices of the CTP404 sensitometry module reconstructed with: **(a)** no filtering of secondary fragments; **(b)** standard threshold filter; **(c)** the developed $\Delta E - E$ filter. **(d)** Transverse slice of a simulated HeCT scan for the same phantom reconstructed applying the $\Delta E - E$ filter for comparison. The images were reconstructed with 256×256 pixels per slice (0.7 mm pixel size) and slice thickness of 2.5 mm. The insert materials are (1) Teflon, (2) delrin, (3) PMMA, (4) polystyrene, (5) LDPE and (6) PMP.

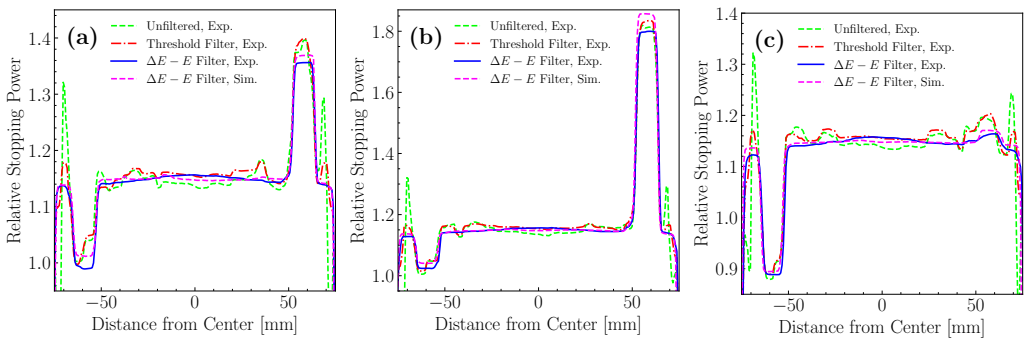

Figure 5.22: Traverse profiles through each pair of opposing inserts in the HeCT of the CTP404 module as indicated for LDPE and delrin **(a)** by the horizontal lines in figure 5.21. Similarly, the profiles were plotted for **(b)** polystyrene and Teflon, and **(c)** PMP and PMMA. The red dashed line refers to the experimental HeCT without filter on fragments, the dashed green line with the standard threshold filter, and the solid blue line with the $\Delta E - E$ filter. The dashed magenta line corresponds to the $\Delta E - E$ filtered simulated HeCT.

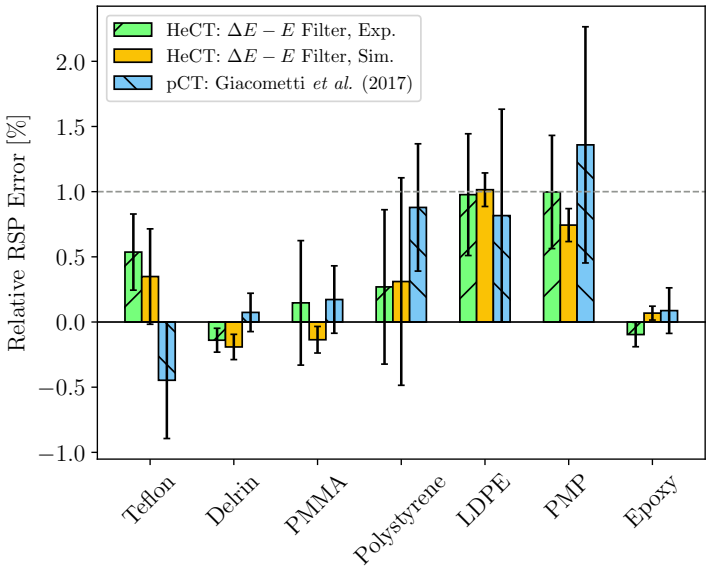

Figure 5.23: Relative error of the reconstructed RSP values for the material inserts of the CTP404 sensitometry module and the epoxy material. The dashed green bars are the experimental, the yellow bars the TOPAS simulated reconstruction. For both the $\Delta E - E$ filter was applied. The dashed blue bars are experimental pCT data acquired with the same detector (Giacometti et al. 2017a).

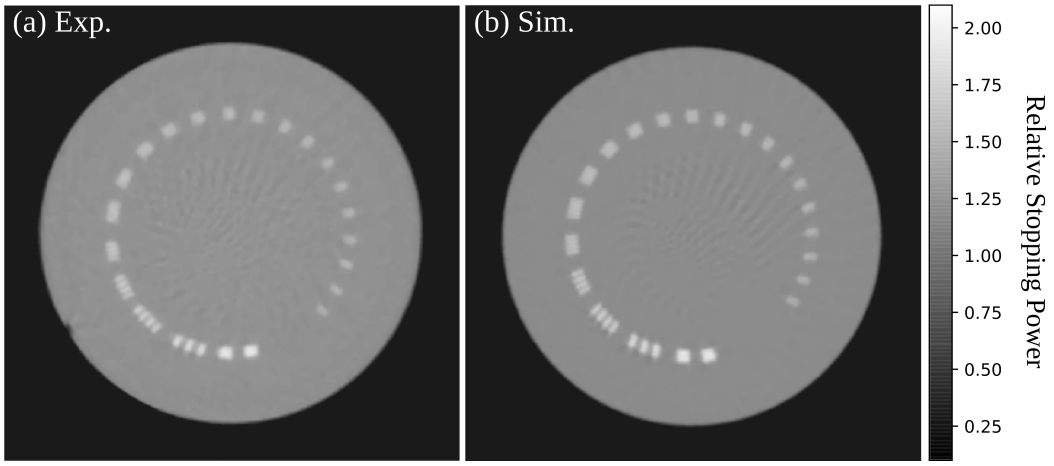

Figure 5.24: Traverse slice of the HeCT reconstruction for the CTP528 module where the $\Delta E - E$ filter was applied before image reconstruction. **(a)** Experimental, **(b)** simulated data. The images were reconstructed with 512×512 pixels per slice (0.35 mm pixel size) and 1.25 mm slice thickness.

error 0.43 %, relative error 1.36 % for PMP and 0.81 % for LDPE).

Spatial Resolution

Figure 5.24(a) and figure 5.24(b) show, respectively, an experimental and a simulated HeCT transverse slice of the CTP528 module. Ring artifacts, similar to the ones observed for the other phantoms discussed above, were removed by applying the $\Delta E - E$ filter. Streak artifacts in the center of the reconstructions are visible. The MTF of the system was evaluated using the aluminum line pairs and the result is shown in figure 5.25. A sigmoid fit was performed to yield the MTF over the whole spatial frequency range (Seco et al. 2013).

The MTF of both the simulated and experimentally acquired HeCT are very similar, with variations compatible within one standard deviation. The spatial resolution is only slightly lower if secondary fragments are not filtered before reconstruction as shown by the dashed gray line in figure 5.25. The unfiltered experimental HeCT yields an $\mathrm{MTF}_{10\,\%}$ of 3.7 lp/cm. The $\mathrm{MTF}_{10\,\%}$ for the $\Delta E - E$ filtered HeCT is 3.8 lp/cm in experiment and 3.7 lp/cm in simulation.

Discussion

The Effect of Fragments and the $\Delta E - E$ Filter

In this study, the effect of secondary fragments on HeCT imaging was investigated both for MC simulation and experiment. The ring artifacts and low RSP accuracy visible in HeCT images acquired with the U.S. pCT consortium prototype scanner (Volz et al. 2017) were shown to be caused by secondary

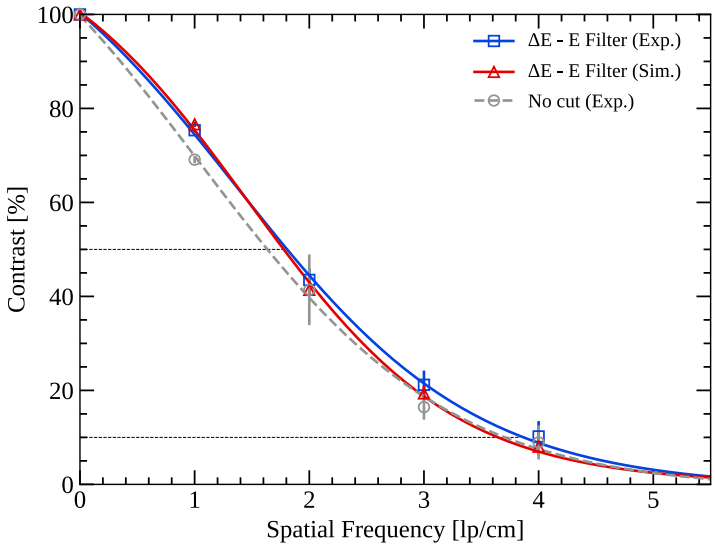

Figure 5.25: MTF of the experimentally acquired (blue) and simulated (red) HeCT of the CTP528 module with the $\Delta E - E$ filter applied. The dashed gray line shows the MTF of the experimentally acquired HeCT without filtering secondaries before reconstruction. The error bars mark the standard deviation of the measured contrast. A sigmoid fit has been performed to yield the MTF over the whole spatial frequency range. The dashed lines indicate the $MTF_{50\,\%}$ and $MTF_{10\,\%}$, respectively.

fragments produced inside the the multistage energy/range detector. In general, fragments introduced additional errors to the reconstructed WEPL. The largest errors were seen at stage interfaces of the multistage detector, where fragments can stop in an adjacent stage compared to the primaries.

The effect of fragmentation in single-event helium imaging has been recently investigated for radiography with a CMOS active pixel setup by Gehrke et al. (2017). In that work, a threshold based on the much lower energy deposit of protons compared to primary helium ions was used to filter out fragments, showing an improvement of the image quality. The present work showed that with a similar threshold filter, able to remove most of the proton, deuteron and triton contamination, the HeCT reconstructed images still presented reduced RSP accuracy and significant fluctuations. Conversely, with the $\Delta E - E$ filter which was able to distinguish also ^{3}He fragments images with high RSP accuracy and without large ring artifacts were obtained. Despite the fact that ^{3}He fragments only represented a small percentage of the overall secondary yield, their effect on the reconstruction accuracy was relatively large.

As shown in figures 5.19 and 5.20, with the $\Delta E - E$ filter, fluctuations were reduced to less than 0.2 % compared to the mean RSP value in simulation, and to less than 0.5 % in the experiment. Similar fluctuations have also been observed for pCT with the detector (Piersimoni et al. 2017, Giacometti et al. 2017a) and were attributed to the detector calibration procedure rather than secondary

fragments. Further improvement of the detector calibration is under investigation.

The $\Delta E - E$ filtered reconstructions of the Catphan CTP404 module yielded a RSP uncertainty better than the clinically acceptable limit of 1 % for most inserts. Especially, the $\Delta E - E$ filter improved the mean RSP accuracy by a factor 6 compared to the unfiltered and threshold filtered reconstructions. A comparable RSP accuracy for experimental pCT data to that of the $\Delta E - E$ filtered HeCT is reported in Giacometti et al. (2017a).

The MTF evaluated through the line pairs in the CTP528 module was not significantly affected by secondary fragments. Both the simulated and experimentally acquired HeCT images of the CTP528 module yielded similar MTFs with an $\mathrm{MTF}_{10\,\%}$ of $\sim 4\,\mathrm{lp/cm}$. An initial energy higher than the 200 MeV/u used in the present study would lead to an increase in spatial resolution due to reduced MCS (Seco et al. 2013), but the contrast-to-noise ratio would be expected to decrease and the increased range straggling (Schulte et al. 2005, Amato et al. 2018). Additionally, in the relevant energy range, the nuclear fragmentation cross sections for helium ions are energy dependent and increase for kinetic energies above 280 MeV/u, see, e.g., figure 6 in Horst et al. (2017). Therefore, in future studies, the optimal initial energy for helium imaging of different body sites should be investigated.

A drawback of the filtering is the loss of approximately 38 % of the events in experiment and 43 % in simulation compared to the event histories when no filtering of fragments is applied, as calculated for a calibration run with two bricks and the two wedges. The higher number in simulation might be a result from the slight difference in implemented and real density of the degrader material and the uncertainty of the Geant4 physics modeling classes regarding nuclear fragmentation. The latter has been investigated for carbon ions (Böhlen et al. 2010, Dudouet et al. 2014, Bolst et al. 2017) and found to be of the order of tens of percent; similar uncertainties are expected to be present for the simulation of helium beams, but no experimental results are yet available. Both simulated and experimental numbers are comparable to the loss of primaries shown by Rovituso et al. (2017) for helium ions with initial energy of 200 MeV crossing 200 mm of water. However, Gehrke et al. (2018) and Piersimoni et al. (2018) have shown that the quality of helium imaging would not be affected when the number of events used in reconstruction is reduced to 25 % with respect to that used for proton imaging.

For the investigated prototype, the $\Delta E - E$ filter could not be applied for particles stopping in the very first energy detector stage. However, for an initial energy of 200 MeV/u, primary helium ions stopping in the first detector stage correspond to a WEPL of 21 cm or more. Hence, the first stage would only become relevant for relatively thick objects. In order to also filter secondary fragments stopping in the first stage, a rear tracker unit capable to measure energy loss on top of position could be used to function as a thin $\Delta E - E$ stage.

The strength of the $\Delta E - E$ filter lies within its generality. It adds only little computational cost when reconstructing the images. Additionally, to enable the technique, only a longitudinally segmented detector measuring the particles energy loss is necessary alongside the requirement that the particles stop within the detector geometry. Finally, as the relationship given by Eq. 5.51 is applicable for all charged particles, the method could also be extended to other ion species.

Detector Performance

As can be noticed comparing figure 5.18(a) and figure 5.18(b), the response curves in the $\Delta E - E$ spectra were different for the simulated compared to the experimentally acquired detector response. Moreover, in experiment the acquired $\Delta E - E$ spectra also varied among each pair of adjacent detector stages. This dissimilarity could most likely be attributed to a non-linear stage response at high energy depositions. In experiment, the digitized scintillation light output was converted into a numerical energy value using a calibration run with no phantom in the scanner. This method used only one energy calibration point per stage and thus, a linear stage response was necessary for a correct conversion of the digitized light output to energy over the whole range of possible energy deposits.
However, individual energy depositions were mapped directly to the known WEPL crossed by the particles in the calibration procedure. For this, the numerical energy value was used only as an index to retrieve a WEPL value from the acquired WEPL versus energy map. Therefore, the correct numerical energy in MeV is not important for accurate WEPL reconstructions as long as the values are consistent and no saturation occurs. This was confirmed by the high RSP accuracy achieved in this work. Still, in follow up studies, the linear region of the stage response should be increased to optimize the detector accuracy for HeCT.

For HeCT, 90 projections for a full scan limited the reconstruction accuracy as can be seen by the streak artifacts visible in the reconstructions shown in figure 5.24. Considering the Nyquist-Shannon (Shannon 1948) sampling theorem, such streak artifacts were a result of sparse view tomographies and an under-sampled system matrix. This was also shown recently in Piersimoni et al. (2018). This work hence did not reflect the full potential of HeCT. A complete comparison of HeCT and pCT was beyond the scope of this work.

Overall, considering the achieved quality of HeCT reconstructed images in this work, the prototype proton detector could be operated with helium beams without altering the design. As the above filter could be adapted for other ion species as well, this renders the pCT consortium prototype design a powerful tool for ion imaging in general.

Conclusions

In this work, the effect of projectile fragments on the image reconstruction in ion imaging with a prototype detector was presented. By adapting the $\Delta E - E$ technique to the image reconstruction, a method to filter out secondaries in ion CT imaging was developed. As shown in the HeCT reconstructions presented in this work, applying this filtering resulted in a notable improvement of the image quality both in simulation and experiment, removing almost completely the strong ring artifacts otherwise arising. This can be considered a general result, since secondary fragments can affect the WEPL evaluation in any particle CT scanner system, independent of the detector design.

The developed $\Delta E - E$ method could be applied for imaging with other ion species, or different detector setups as long as the energy detector is longitudinally segmented. The promising spatial resolution and high RSP accuracy achieved both in simulation and experiment affirm the opportunity of further investigating helium ions in single-event imaging, possibly using a larger number of projection angles, to fully exploit the potential of HeCT.

In conclusion, the U.S. pCT consortium prototype pCT scanner was proven to produce high quality HeCT images, when a filter on secondary fragments, in particular, ^{3}He fragments, is applied. Future investigations will therefore focus on identifying/designing the ideal scanner for helium imaging, possibly with an energy detector optimized for helium ions. Under such conditions, a full comparison of HeCT, pCT, and X-ray imaging modalities could be possible.

Acknowledgements

The authors want to acknowledge the Heidelberg Ion-Beam Therapy Center (HIT) for providing beam time as well as the HIT engineers for their excellent help in planning and conducting the experiments. The authors want to thank Bruce Faddegon and José Ramos-Mendéz for helping with the TOPAS simulations and providing server time. This work was partially supported by grants from the National Institute of Biomedical Imaging and Engineering and the National Science Foundation (NSF) (R01EB013118), the National Cancer Institute (NCI) (1P20CA183640-A101), and the United States - Israel Binational Science Foundation (BSF) (2009012 and 2013003).

5.3 P.XI: Improving proton imaging

Title : Improving single-event proton CT by removing nuclear interactions within the energy/range telescope

Authors : L. Volz, P. Piersimoni, R. P. Johnson, V. A. Bashkirov, R. W. Schulte and J. Seco

Status : Published

Journal : Physics in Medicine and Biology

DOI : doi.org/10.1088/1361-6560/ab2671

Contributions : The principal author, LV conceptualized the work, conducted all simulations presented and wrote the necessary analysis software to acquire the results presented under the supervising guidance of JS. PP aided in the simulation of the CT scans and originally implemented the detector simulations. RPJ, VAB and RWS provided technical support regarding the calibration procedure of the detector and aided with valuable discussions. JS ensured the scientific rigor and relevance of the research. LV wrote the software to export the plots shown in the work, finalized the results and wrote the manuscript draft.

Abstract

Data filtering is crucial for accurate relative stopping power (RSP) reconstruction in proton CT (pCT). In this work, we assess different filters and their performance for the US pCT collaboration prototype pCT system in Monte Carlo (MC) simulations. The potential of using the recently proposed ΔE-E filter for removing nuclear interactions that occurred in the energy/range detector of the pCT system is investigated.

Full pCT scans were acquired with the TOPAS MC simulated version of the prototype scanner that comprises two tracking detectors and a 5 stage energy/range detector. An ideal water cylinder and a water cylinder with 5 tissue inserts were investigated. Before image reconstruction, a 3σ WEPL filter was applied as the only filter, or in addition to filters acting on the energy deposit in each of the energy detector stages, as done currently with the prototype. The potential of the ΔE-E filter that was recently proposed for helium imaging was assessed. The results were compared to simulations for which nuclear interactions were disabled representing ground truth.

The 3σ WEPL filter alone was not sufficient to filter out all nuclear interaction events and systematic fluctuations in the form of ring artifacts were present in the pCT reconstructed images. Applying energy filters currently used with the device prior to the 3σ WEPL filter only slightly improved the image quality. A 2σ WEPL filter improved the mean RSP accuracy, but could not fully remove the systematic fluctuations. The ΔE-E filter in addition to the current reconstruction procedure efficiently removed the systematic fluctuations and the achieved RSP accuracy closely matched the simulation without nuclear interactions.

This study demonstrates the dependence of the accuracy of the usual 3σ WEPL filter on uncertainties arising within the energy detector. By enabling to remove such uncertainties, the ΔE-E method proved to yield some potential for improving the accuracy of pCT.

Introduction

Proton imaging has gained increasing interest over the last decades. The main advantage of proton CT (pCT) over conventional X-ray CT is the more accurate reconstruction of the voxelized relative stopping power (RSP) information (Hansen et al. 2015) that is crucial for accurate ion beam radiotherapy treatment planning (Paganetti 2012).

While pCT exhibits other benefits (Schulte et al. 2005, Depauw & Seco 2011, Oancea et al. 2018), the achievable spatial resolution is limited due to multiple Coulomb scattering (MCS). To reduce the uncertainty introduced by MCS, in single-event pCT, the trajectory of each proton through the object is estimated during image reconstruction (Williams 2004, Li et al. 2006, Schulte et al. 2008, Erdelyi 2009, Collins-Fekete et al. 2015, Collins-Fekete et al. 2017d, Krah et al. 2018). The use of path reconstruction techniques requires sophisticated detector systems capable of acquiring the proton track information before and

after the object to be imaged, as well as the residual energy/range on a single-event basis (Schulte et al. 2004, Schulte et al. 2008, Sadrozinski et al. 2013). Additionally, a high precision requirement is placed on the energy/range detector of such a system to ensure accurate RSP reconstruction (Bashkirov et al. 2016b).

However, energy straggling as well as nuclear interactions inside the object to be imaged result in events with an unusually large energy loss and the production of secondary protons that consequently increase the image noise and compromise the RSP accuracy if included in the image reconstruction procedure (Schulte et al. 2005) - see also (Rädler et al. 2018) for a comprehensive analysis of image noise in proton imaging. In order to ensure high quality pCT images, data filters have to be implemented that accurately identify and remove such events from the recorded particle histories. In most contemporary studies, therefore a $3\,\sigma$ filter on the water equivalent path length (WEPL) crossed by each proton is applied as was proposed by Schulte et al. (2005). Additionally, since the path reconstruction algorithms are based on a Gaussian approximation to MCS, a $3\,\sigma$ filter on the angular displacement of the particles is used to exclude single large angle scattering events (Schulte et al. 2008).

The $3\,\sigma$ WEPL filtering was suggested based on the straggling theory given by Tschalär (1968) and assuming an ideal energy detector (Schulte et al. 2005). However, for energy detectors that require the particles to stop within the detector, nuclear interactions and particles that scatter outside the detector sensitive area increase the weight of the straggling distribution tail compared to the purely electromagnetic expectation. This can largely affect the calculation of the distribution standard deviation, as already pointed out by Tschalär & Maccabee (1970). Hence, while representing relatively few events, nuclear interactions and scattering inside the energy detector could compromise the accuracy of the $3\,\sigma$ WEPL filter and, consequently, the achievable RSP accuracy of the reconstructed image.

The goal of this work was to investigate the effect of such events on the accuracy of pCT with the prototype detector developed by the US pCT collaboration (Bashkirov et al. 2016a, Johnson et al. 2016, Johnson et al. 2017) in Monte Carlo simulations. We investigate the performance of the usual $3\,\sigma$ WEPL filter and assess the potential of using the ΔE-E filtering technique recently proposed to identify nuclear fragmentation events in helium ion CT (HeCT) with the scanner energy/range detector (Volz et al. 2018) to identify nuclear interaction events in pCT.

Materials and Methods

TOPAS simulation setup

The TOPAS simulation toolkit (Perl et al. 2012) release 2.0 patch 3 with Geant4 (Agostinelli et al. 2003, Allison et al. 2006, Allison et al. 2016) version 10.01 patch 02 was used for the Monte Carlo simulations presented in this work. The default "Modular Physics List" of the TOPAS application was activated that has been verified experimentally (Testa et al. 2013a). It includes the following

physics lists: G4HadronPhysicsQGSP_BIC_HP, G4DecayPhysics, G4StoppingPhysics for nuclear capture at rest, G4IonBinaryCascadePhysics and G4HadronElasticPhysicsHP for modelling nuclear interactions, as well as G4EmStandardPhysics_option4 for electromagnetic interactions.

The TOPAS simulated version of the US pCT prototype scanner presented in Piersimoni et al. (2017) was used to acquire full pCT scans of two phantoms. The scanner consisted of four position sensitive detector planes, two preceding (front tracker) and two following (rear tracker) the object to be imaged, and a 5-stage energy/range detector. Each of the position sensitive tracker planes comprised two silicon layers ($349 \times 86 \times 0.4\,\mathrm{mm}^3$) used to measure the particle position in vertical and horizontal direction, respectively. Each stage of the energy/range detector consisted of $375 \times 100 \times 50.8\,\mathrm{mm}^3$ blocks of UPS-923A polystyrene scintillator material (simulated using the polystyrene material composition given by the NIST database (Berger et al. 2005)), as well as 65 μm of PMMA wrapping material around each stage (Piersimoni et al. 2017). More details of the pCT prototype scanner design and operation have already been published elsewhere (Bashkirov et al. 2016b, Bashkirov et al. 2016a, Sadrozinski et al. 2016, Johnson et al. 2016, Giacometti et al. 2017a, Piersimoni et al. 2017, Johnson et al. 2017).

To investigate the accuracy of the data filters in eliminating nuclear interaction events, we compared the image accuracy to simulations where only electromagnetic interactions were enabled (i.e. activating only G4EmStandardPhysics_option4 in the physics list).

Primaries were generated with an initial energy of 200 MeV and delivered through an ideal flat-field beam configuration (200 mm width, 100 mm height). Full tomographic scans were acquired in 90 individual projections at a 4° angular step as established by Plautz et al. (2016). For each projection, 2×10^6 primary protons were simulated.

To closely model the experimental operation principle, for the different setups the energy output was calibrated to WEPL using a dedicated polystyrene phantom setup. The calibration procedure was originally developed by Bashkirov et al. (2016a); in the present work, the "wedge" calibration procedure described in detail for configuration C in Piersimoni et al. (2017) was followed. The calibration was performed in 5 individual runs: for the first run, two polystyrene wedges (RSP=1.043) providing a continuous thickness variation between 0 and 50.8 mm were placed between the front and rear tracker. In the subsequent runs, 50.8 mm thick blocks of the same polystyrene were added one after another enabling the calibration of the detector over the full range of the particles. During the calibration procedure, the particles were binned in a 2D array according to their WEPL and energy deposit to the farthest detector stage in downstream direction they reached into. For each energy bin, the most likely WEPL was computed as the mean within the FWHM bounds of the corresponding WEPL distribution. This resulted in a 340 element vector for each stage that connected the energy deposit in steps of 0.25 MeV from 0 to 85 MeV to the respective most likely WEPL crossed by the particle.

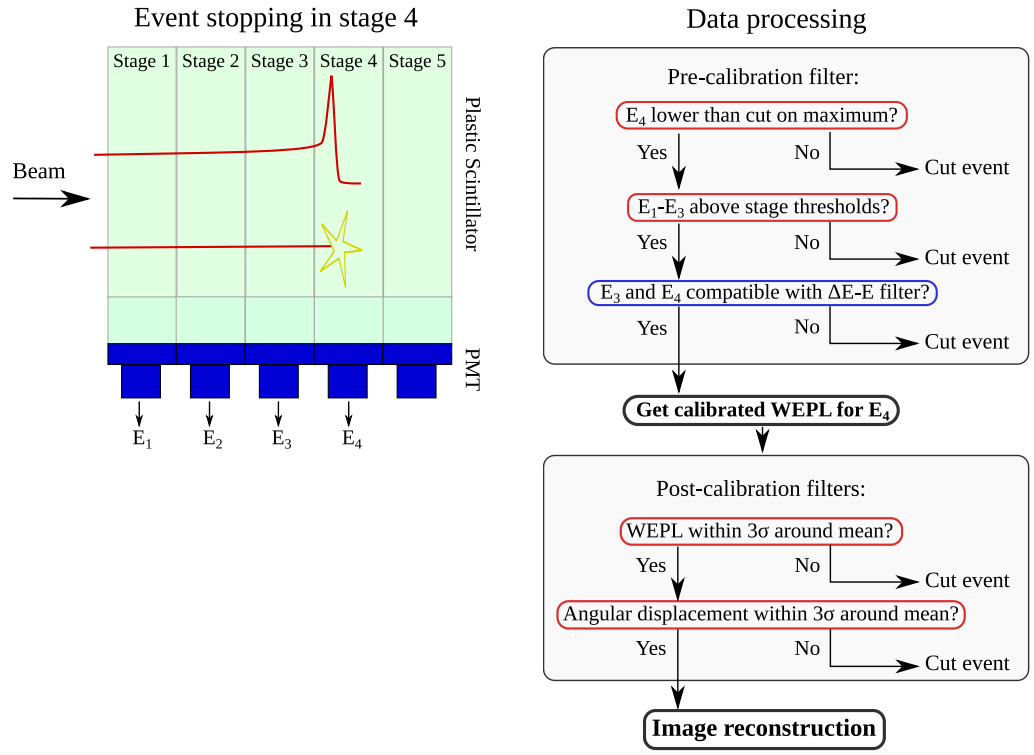

Figure 5.26: Schematic depiction of the energy/range detector and flowchart of the filtering processes used in this work. The processes outlined in red are used in the current reconstruction procedure for the device. In this work, additionally the recently proposed ΔE-E filter (highlighted in blue) was used to identify such events that suffered a nuclear interaction inside the detector or scattered outside the detector sensitive area (as indicated by the yellow star).

Image reconstruction and data filtering

Several filters are involved in the current data processing procedure for the prototype detector underlying the investigation in this note. They can be divided into filters that act on the energy loss measurement in the multistage detector before the conversion of the energy loss to WEPL through the derived WEPL calibration (in the following referred to as pre-calibration filters) and filters that act on the calibrated output of the detector (post-calibration filters). The different data filtering processes are explained in figure 5.26, where the filters currently used with the device are highlighted in red.

Pre-calibration filters For the prototype, first the stage where the particle stopped (henceforth denoted Bragg-peak stage) was determined as the last stage in beam direction in that an energy deposit above 1 MeV was measured. As is implemented in the current pre-processing procedure for the investigated prototype, events with a higher energy deposit in the Bragg-peak stage than transferable by a single proton were removed. Additionally, in the current procedure, an energy threshold filter is implemented, that acts on the energy

deposit in each stage leading up to the Bragg-peak stage. For a run without phantom (i.e. a run for that most particles reach into the last detector stage), the mean and standard deviation of the energy deposit in each stage was computed, and the mean minus 5σ was set as the stage threshold. Events with a lower energy deposit in any stage leading up to the Bragg-peak stage compared to the respective stage threshold were removed by the filter.

The data filters mentioned above (threshold energy filter and maximum energy cut) will be referred to as "current" pre-calibration filters throughout this work. However, this refers only to the investigated prototype and does not reflect the reconstruction procedure for other imaging devices.

In order to improve upon the current setup, the recently proposed ΔE-E filtering mode of the detector (Volz et al. 2018) was investigated for its use in proton imaging. For the method, the energy deposit in the Bragg-peak stage was defined as residual energy E and the energy deposit in the stage adjacent in upstream direction as ΔE. Particles that scattered outside the detector sensitive area or those that stopped due to a nuclear interaction could then be identified by comparing the measured ΔE-E relationship with the one expected for protons that stopped in a stage "correctly": In the detector calibration procedure, the ΔE-E response pattern of protons that did not undergo nuclear interactions was parametrized by a second order polynomial. Events for that the ΔE-E relationship was not compatible with the parametrization within certain margins could then be removed before image reconstruction (compare figure 5.27).

Image reconstruction and post-calibration filters For each event not removed by the pre-calibration filters, the energy deposit in the Bragg-peak stage was then converted to WEPL using the energy vs. WEPL calibration curves derived in the detector calibration (Piersimoni et al. 2017).

Images were reconstructed using the DROP algebraic reconstruction technique with superiorization of the total variation norm (TVS) (Penfold et al. 2010). The algorithm was run with 40 blocks and stopped after 8 iterations. Proton paths were estimated using the optimized cubic spline path formalism by Collins-Fekete et al. (2015) that was recently shown to be equivalent to the probabilistic most likely path formalism (Collins-Fekete et al. 2017d). All images were reconstructed with a slice thickness of 2.5 mm and 256×256 pixel per slice (0.7 mm pixel size). The Feldkamp-David-Kress (FDK) algorithm was used to generate the starting image for the iterative reconstruction. This initial estimate was also used to project the start and end-point of the cubic spline path onto the object hull as described in Schultze et al. (2014).

Within the DROP-TVS algorithm the 3σ WEPL filtering was performed. First, the particle histories were binned based on projection angle (4° bins) and midpoint of the straight line connection between their entrance and exit positions of the reconstruction volume into equal intervals in lateral (1 mm bins) and vertical (2.5 mm bins) coordinates. For each bin, the mode WEPL was identified as the maximum of the WEPL distribution (the maximum with smallest WEPL value should more than one WEPL value contain the maximum number of events). Then, the mean and standard deviation of the WEPL distribution for the bin were computed within $\pm 30\,\%$ around the mode WEPL

Material	Element(Weight[%])	RSP
Brain tissue	H(8.17);C(53.62);N(1.53);O(26.51);Mg(9.98);Cl(0.19)	1.049
Trabec. bone	H(8.4);C(59.66);N(1.56);O(21.43);Mg(1.46);P(2.33);Cl(0.12);Ca(5.04)	1.112
Cort. bone	H(4.13);C(29.70);N(0.85);O(34.12);Mg(3.11);P(7.57);Cl(0.04);Ca(20.48)	1.591
T. enamel	H(2.77);C(21.81);N(0.82);O(34.02);P(12.33);S(0.31);Cl(0.03);Ca(26.60);Ba(1.31)	1.794
T. dentin	H(4.51);C(35.36);N(1.23);O(29.41);P(9.20);S(0.08);Cl(0.04);Ca(19.84);Ba(0.33)	1.518

Table 5.1: Material composition for the insert phantom as used in the simulation. The RSP was calculated directly from the stopping power tables used in the simulation with G4_WATER as reference. The elemental composition was implemented as given in Piersimoni et al. (2017).

value. For image reconstruction, only events with a WEPL within $\pm 3\,\sigma$ of their bin mean WEPL were considered. Additionally, in each bin, a $3\,\sigma$ filter on the angular deflection of the particles was applied. In the case where nuclear interactions were disabled in the simulation, only the post-calibration filters were applied.

Investigation of filter efficiency Additionally to comparing the results to a simulation without nuclear interactions, we counted the events that underwent a inelastic/non-elastic nuclear interaction before and after the filtering. This was achieved using the "filtering scorer" framework provided by the TOPAS toolkit: a filtering scorer was added to the energy/range detector that recorded the energy deposit to the energy/range detector only for particles that originated from inelastic/non-elastic nuclear interactions processes. In processing of the data, a boolean was assigned to each event that was set true, if any energy deposit in any stage was measured for the event with the implemented filtering scorer.

Simulated Phantoms

First, an ideal water cylinder was investigated, so that the effect of filter uncertainties could be disentangled from the phantom geometry. The cylinder was 150 mm in diameter, 80 mm high and composed of G4_WATER.

To investigate the stopping power accuracy, the insert phantom IP1 presented in Piersimoni et al. (2017) was used. The phantom was a water cylinder (G4_WATER) of 150 mm diameter and 80 mm height with five different tissue inserts of 15 mm radius and 80 mm height: tooth dentin, tooth enamel, cortical bone, trabecular bone and brain tissue, see table 5.1 for the material composition and reference RSP. To yield an estimate of the RSP accuracy, the mean RSP value was computed in a region-of-interest of 10 mm radius in the center of each insert averaged over the 5 most central slices, and compared to the reference values.

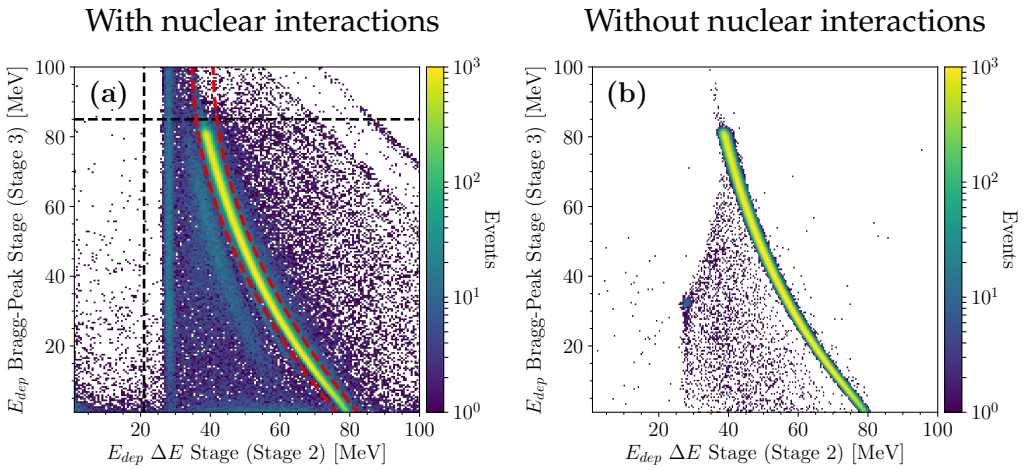

Figure 5.27: The ΔE-E spectrum for one projection of the ideal water cylinder. **(a)** The energy deposit to stage 3 of all particles stopping in that stage was plotted against their respective energy deposit to stage 2. **(b)** The equivalent for a simulation for that nuclear interactions were disabled. No data filtering was used in acquiring the spectra. The vertical dashed black lines indicate the threshold filter, the horizontal dashed black lines the cut on the maximum transferable energy as used in the current reconstruction procedure with the investigated prototype. The red dashed lines indicate the margins used for the ΔE-E filter.

Results

ΔE-E spectra

Figure 5.27 shows two ΔE-E spectra acquired using a pCT projection of the ideal water cylinder. In figure 5.27(a), the energy deposition (E_{dep}) to stage 3 was plotted against the energy deposited to stage 2 for all particles stopping in stage 3. For comparison, in figure 5.27(b), the equivalent was plotted for a simulation without nuclear interactions.
The dashed black lines in figure 5.27 indicate the currently used pre-calibration filters (energy threshold and cut on maximum energy). The dashed red lines depict the margins used for the ΔE-E filter. The protons that stopped in stage 3 "correctly", i.e. did not suffer nuclear interactions or scattered outside the detector sensitive area, are seen as the high occurrence pattern. The vertical pattern at $\Delta E \sim 30\,\text{MeV}$ in figure 5.27(a) corresponded to particles which had crossed a small amount of material or no material at all, and, hence, should have stopped in the last detector stage, but stopped already in stage 3 due to nuclear interactions or scattering. In figure 5.27(b), the residual noise around the proton occurrence pattern could be removed by excluding particles close to the vertical boundaries of the detector. Therefore, the conclusion was drawn that the residual noise was attributed to events scattering outside the detector sensitive area.

WEPL calibration curves

In deriving the WEPL calibration curves for each of the 5 stages of the energy/range detector, the effect of the ΔE-E filter was negligible. In the following, therefore, the calibration curves derived with the current calibration procedure of the detector was used for preprocessing all simulations where the full physics list was active. For the simulation where only G4EmStandardPhysics_option4 was active, a separate set of calibration curves was derived and used for the WEPL conversion. Due to the missing elastic nuclear interactions (*hadElastic* physics processes) both in the calibration phantom and inside the detector and the attributed on average slightly lower energy loss of the particles, the calibration curve for the simulation without nuclear interactions was shifted to slightly larger WEPL values at the same energy deposit in the Bragg-peak stage (mean difference $\leqslant$0.22 mm).

Data filter performance

The effect of the different pre-calibration filters is demonstrated in figure 5.28. The figure shows the distribution of the converted WEPL crossed by protons that entered the ideal water cylinder in a central region of 5 mm width and 60 mm height (depicted by the drawing on the right side of the figure), i.e. particles that crossed a water equivalent thickness of $\sim$ 150 mm. We note that the so obtained distribution does not correspond directly to the WEPL distributions used for the 3σ WEPL filtering in the DROP-TVS algorithm, where the particles are binned using a finer binning grid as explained above. Different pre-calibration filters were applied before the WEPL conversion: no pre-calibration filtering (blue triangles), the pre-calibration filters currently used with the prototype (green squares) and the ΔE-E filter in addition to the previous (red, circles). For comparison, the figure also shows the equivalent WEPL distribution acquired in a simulation where only electromagnetic interactions were active. At a WEPL of $\sim$ 145 mm, there was a stage interface and consequently, events below or above this value correspond to events that stopped in different stages (stage 2 and 3). This caused the fluctuations observed at the peak of the distribution in Figure 5.28.

The bottom part of the figure shows the 3σ region around the mean where the different filter setups correspond to the same colors as above. The mean and standard deviations for each distribution are listed in table 5.2. The WEPL distribution tail was larger for the cases without pre-calibration and the pre-calibration filters currently used with the prototype, when compared to the distribution without nuclear interactions. The ΔE-E filter effectively reduced the tail, which is reflected in the 3σ region: without the ΔE-E filter, the 3σ region still includes events with an unusually large WEPL.

To visualize the nuclear interaction contamination in the final set of events used for image reconstruction, figure 5.29 shows the resulting ΔE-E spectra for the setup in figure 5.27(a) after the post-calibration filters were applied in addition to the different pre-calibration filters. In particular, figure 5.29(a) shows the spectrum after the currently used pre- and post-calibration filters were applied – the threshold filter on the particle energy deposit in the detector stages

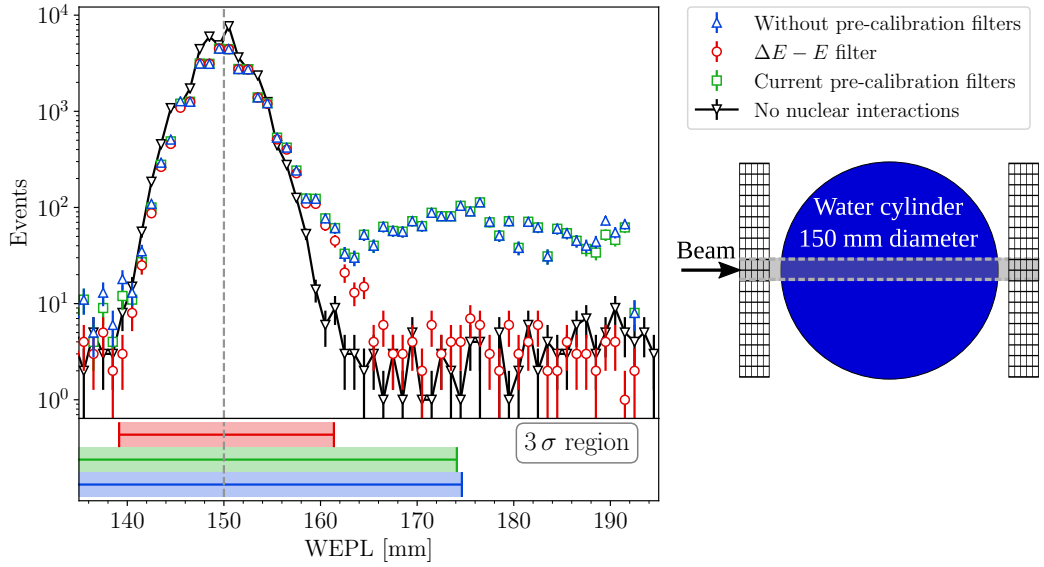

Figure 5.28: Distribution of WEPL crossed by particles that entered the water phantom in a central region of 5 mm width and 60 mm height indicated by the gray-shaded area in the drawing on the right (not to scale). The blue triangles, the green squares and the red circles mark respectively, the WEPL distribution without pre-calibration filters, the distribution where the current pre-calibration filters were applied, and the distribution after the ΔE-E filter was added to the current pre-calibration filters. The black triangles are the WEPL distribution obtained for a simulation without nuclear interactions. The bottom part of the graph indicates the $3\,\sigma$ regions for the ΔE-E filter (red), for the current pre-calibration filters (green), and the distribution without pre-calibration filters (blue). The errors indicate the standard deviation of the counts. The dashed grey line in the plot depicts the diameter of the water phantom, i.e. the approximate water equivalent thickness crossed by the selected protons.

WEPL distribution	Mean [mm]	Std. dev. [mm]
No pre-calibration filters	151.8	7.6
Current pre-calibration filters	151.9	7.5
Add. ΔE-E filter	150.3	3.5
No nuclear interactions	149.9	3.1

Table 5.2: Mean and standard deviation for the WEPL distributions indicated in figure 5.28.

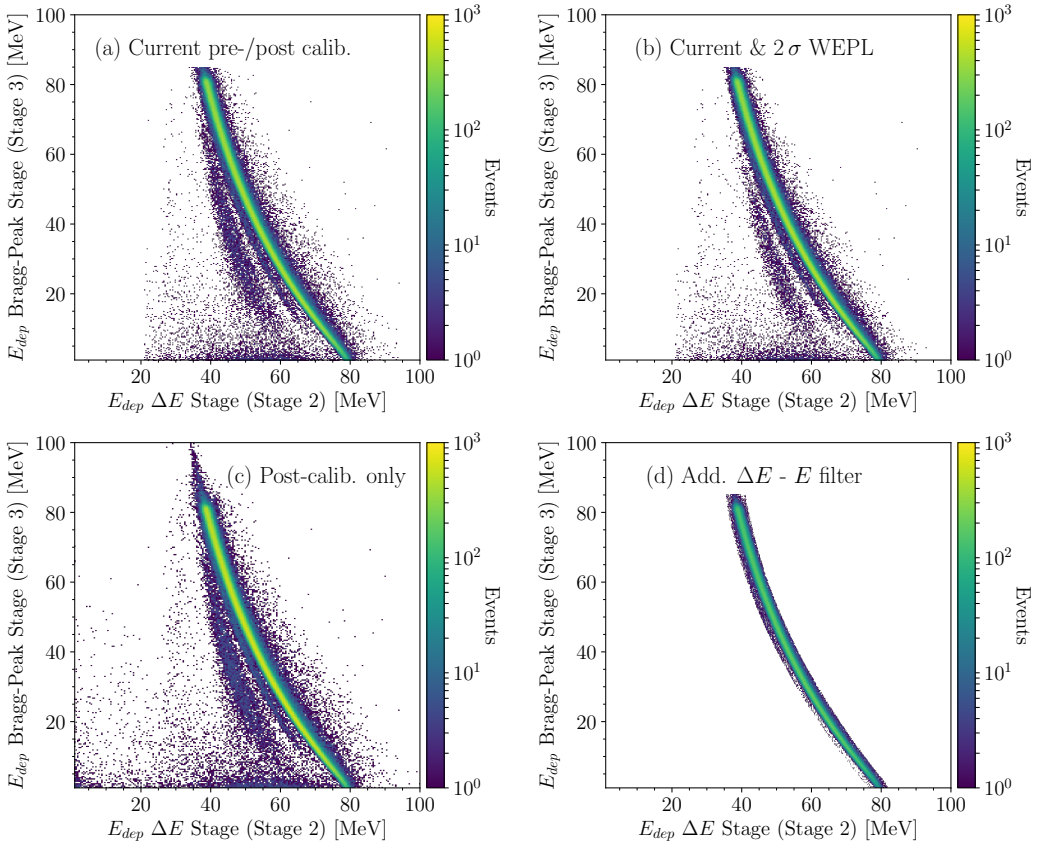

Figure 5.29: ΔE-E spectrum as shown in figure 5.27(a) after different data filtering procedures were applied. **(a)** ΔE-E spectrum after the current pre- and post-calibration filtering. **(b)** After the current pre-calibration filters, but using a $2\,\sigma$ WEPL filter in the post-calibration filters. **(c)** Only using the post-calibration filters. **(d)** ΔE-E filter added to the current pre-calibration filters.

	Filter	True pos.	False pos.	True neg.	False neg.
Pre-calib.	Curr. filters	83 %	14 %	3 %	< 1 %
	Add. ΔE-E	80 %	4 %	13 %	3 %
Pre- and post-calib.	Curr. filters ($3\,\sigma$ WEPL)	72 %	3 %	13 %	12 %
	Curr. filters ($2\,\sigma$ WEPL)	71 %	2 %	14 %	13 %
	ΔE-E ($3\,\sigma$ WEPL)	71 %	1 %	15 %	13 %

Table 5.3: Number of events that underwent a inelastic/non-elastic nuclear interaction and were removed/not removed by the current setup of pre- and post-calibration filters, as well as the ΔE-E filter added to the current pre-calibration filters. The values were acquired for one projection of the ideal water cylinder and are relative to the total number of particles that entered the reconstruction field-of-view in that projection.

and the cut on maximum transferable energy, as well as the $3\,\sigma$ filters on both angular displacement and WEPL. The currently used filters were not able to remove all nuclear interaction events. For figure 5.29(b), the same pre-calibration filters as in (a) were applied, but in the post-calibration filters, the $3\,\sigma$ WEPL filter was replaced by a $2\,\sigma$ WEPL filter. While an improvement compared to the current procedure filters was observed, still some nuclear interaction events were left for image reconstruction. In figure 5.29(c), the post-calibration filters were applied without pre-calibration filters. An increase in nuclear interaction events left for image reconstruction was seen especially at lower ΔE values and also at higher E values, which were previously removed by the threshold filter and maximum cut. Finally, in figure 5.29(d) the ΔE-E filter was added to the pre-calibration filters. Most nuclear interactions were removed with this setup.
To further quantify the efficiency of the filters, we counted the events that underwent inelastic / non-elastic nuclear interactions for one projection of the ideal water phantom after different filters were applied. The results are listed in table 5.3. A true positive was defined as an event that remained after filtering and that did not undergo an inelastic / non-elastic nuclear interaction (see section 5.3); a false positive an event that remained but underwent a inelastic/non-elastic nuclear interaction. True/false negatives are equivalently defined for particles that were removed by the filtering.

While the effect of the ΔE-E filter is small relative to the overall number of particles that entered the reconstruction volume, it is important to note, that the filtered events were not evenly distributed in terms of their WEPL. Rather, the number of particles removed by the ΔE-E filter with respect to those used for image reconstruction after the current pre- and post-calibration filters were applied peaked at WEPL values that correspond to stage interfaces.

Accuracy of the reconstructed pCT images

As example reconstructions, figure 5.30(a) shows the central slice of the pCT current procedure reconstructed image of the ideal water cylinder and figure

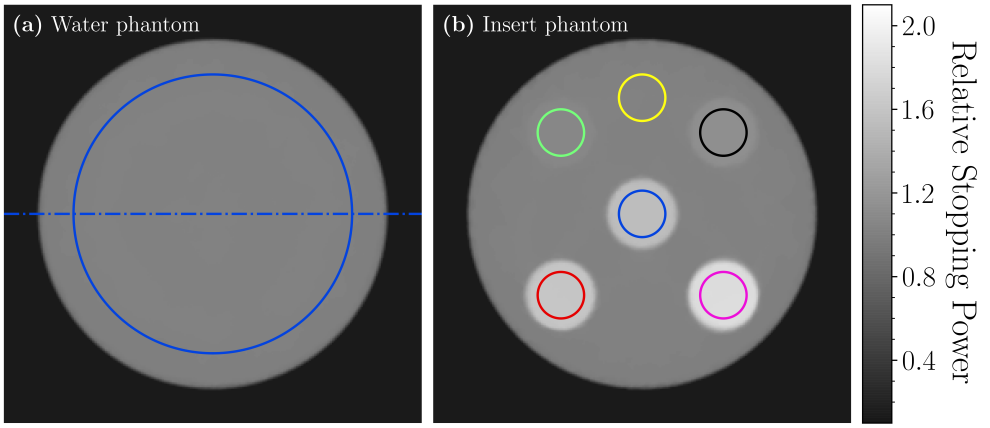

Figure 5.30: Central slice through the current procedure reconstructed pCT of **(a)** the ideal water phantom and **(b)** the water cylinder with plastic inserts (insert phantom). The blue circle and the dashed blue line in **(a)** show the region-of-interest and line-of-interest used for the acquisition of figure 5.31, respectively. The circles in **(b)** depict the region-of-interest used for assessing the RSP accuracy (blue: tooth dentine, magenta: tooth enamel, green: brain tissue, red: cortical bone, black: trabecular bone, yellow: water).

5.30(b) that of the water phantom with different tissue inserts. The effect of different data filters is presented in more detail in the following.

Ideal water phantom

Figure 5.31(a) shows transverse profiles through the pCT images of the water phantom reconstructed with different filtering setups. In the profile of the reconstruction where only the post-calibration filters were used, systematic fluctuations in the form of ring artifacts were present extending to an amplitude of $\sim$ 0.5% relative to the mean. Using the current pre-calibration filters, these fluctuations were reduced to $\sim$ 0.3 % relative to the mean, however, a bias towards overestimated RSP values was present. Note, that these fluctuations are not visible in figure 5.30 due to the RSP scale which was chosen to cover all materials of the insert phantom. A $2\,\sigma$ WEPL filter reduced this bias, but did not fully eliminate the systematic fluctuations. The ΔE-E filtering in addition to the currently used filters was able to remove the systematic fluctuations completely. This was the case, even when a more relaxed $4\,\sigma$ WEPL filter was applied.

In figure 5.31(b) the distribution of reconstructed RSP values in each voxel in a central region of interest of 60 mm radius is shown. The reconstruction in which only the post-calibration filtering was applied yielded a maximum relative error of 1.7 % and the reconstructed RSP values followed no clear trend. Adding the current pre-calibration filters yielded a mean relative error of (0.53 ± 0.23) %, where the given uncertainty is the distribution standard

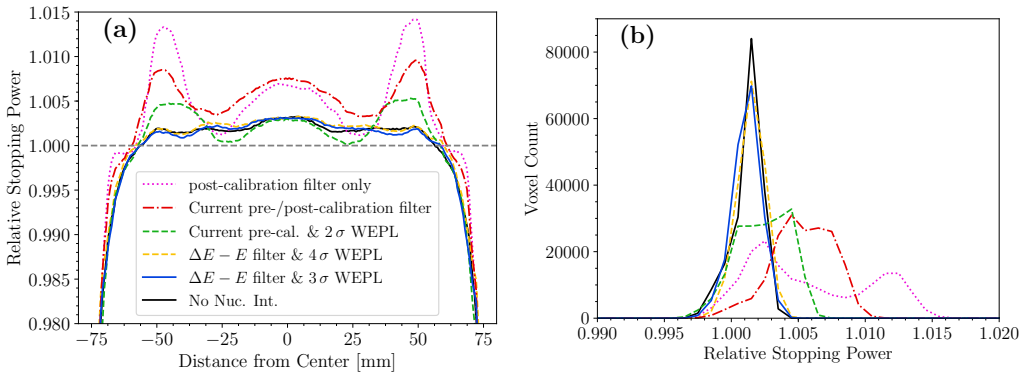

Figure 5.31: **(a)** Transverse profiles through the pCT reconstructed images of the ideal water cylinder. **(b)** RSP distribution accumulated for every voxel in a central region of interest of 6 cm radius over the 9 most central slices. Different data filtering methods were used to acquire the images: the current pre- and post-calibration filters (dash-dot, red), the current pre-calibration filters with a $2\,\sigma$ WEPL filter (dashed, green), using only post-calibration filters (dotted, magenta), the ΔE-E filter added to the current pre-calibration filters (solid, blue), and the same with a more relaxed $4\,\sigma$ WEPL filter (dashed, yellow). For comparison, the simulation without nuclear interactions is shown (solid, black).

deviation. Using a $2\,\sigma$ WEPL filter in the post-calibration filter setup, the distribution of reconstructed RSP values improved to a mean relative error of $(0.24 \pm 0.20)\,\%$. When the ΔE-E filter was applied in addition to the current pre-calibration filters, the distribution of reconstructed RSP values was much sharper and yielded a mean relative error of $(0.11 \pm 0.10)\,\%$. The ΔE-E method with a more relaxed $4\,\sigma$ WEPL filter yielded similar results with a mean relative error of $(0.15 \pm 0.10)\,\%$. With the ΔE-E filter a similar reconstruction accuracy was achieved as for the simulation without nuclear interactions.

Insert phantom

In figure 5.32 the relative errors for each of the tissue inserts of the insert phantom are shown for different filtering setups used with the 5 stage energy/range detector. Again, the results are compared against a simulation without nuclear interactions. The mean absolute RSP error resulting from the reconstructions performed using the different filter setups are listed in table 5.4.

The mean RSP accuracy was lowest for the current procedure data filter setup. A post-calibration filtering with a more strict $2\,\sigma$ WEPL filter in conjunction with the current pre-calibration filters improved the RSP accuracy. The ΔE-E filtering in addition to the current pre-calibration filters improved the RSP accuracy towards the accuracy achieved in a simulation for that nuclear interactions were disabled. Using a more relaxed $4\,\sigma$ WEPL filter in conjunction with the ΔE-E filtering lowered the RSP accuracy again, especially for the denser material inserts. On the other hand, using the additional ΔE-E filter together with a $2\,\sigma$ WEPL post-calibration filter resulted in the highest mean RSP

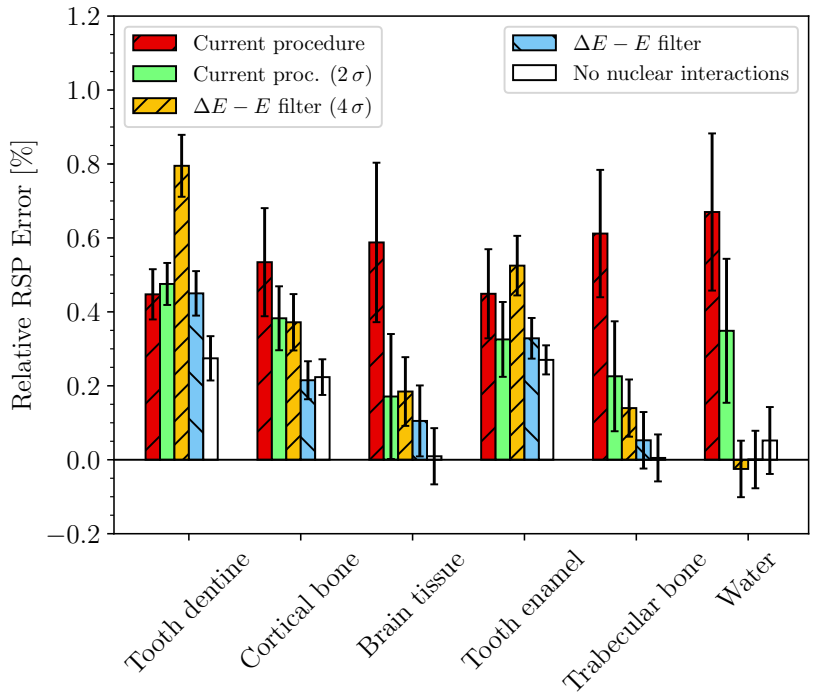

Figure 5.32: Relative error of the pCT reconstructed RSP values for each tissue insert of the insert phantom for different data filtering modalities. The dashed red bars are the reconstruction with the current pre- and post-calibration filters, the green bars the current reconstruction with a $2\,\sigma$ WEPL filter, the dashed blue bars are the ΔE-E filtered reconstruction and the dashed yellow bars are the ΔE-E filtered reconstruction with a more relaxed $4\,\sigma$ WEPL filter applied. The white bars are the RSP accuracy achieved in a simulation without nuclear interactions. The error bars show the standard deviation.

accuracy. For all data filtering methods, the relative error of the reconstructed RSP was better than the clinically acceptable 1 %.

Filter setup	MAE [%]
Current pre-cal. ($3\,\sigma$ WEPL)	0.55 ± 0.05
Current pre-cal.. ($2\,\sigma$ WEPL)	0.32 ± 0.05
Add. ΔE-E filter ($3\,\sigma$ WEPL)	$\mathbf{0.19 \pm 0.09}$
Add. ΔE-E filter ($4\,\sigma$ WEPL)	0.34 ± 0.14
Add. ΔE-E filter ($2\,\sigma$ WEPL)	0.10 ± 0.06
No nuc. int. ($3\,\sigma$ WEPL)	$\mathbf{0.14 \pm 0.07}$

Table 5.4: Mean absolute error (MAE) of the reconstructed RSP for the inserts of the insert phantom when different filtering modalities were applied before image reconstruction. The given uncertainty is the standard error of the mean. In parentheses the deviation of the particle WEPL from its mean accepted by the respective post-calibration WEPL filters is indicated.

Discussion

In this note, the accuracy of different data filtering setups in removing nuclear interaction events from the primary histories was assessed based on the U.S. pCT collaboration pre-clinical pCT prototype. The benefit the recently developed ΔE-E filter could bring to pCT was investigated.

Calibration procedure

In acquiring the WEPL calibration curves for the system following the procedure given for configuration C in Piersimoni et al. (2017), applying the ΔE-E filter did not have a significant impact. As explained in section 5.3, during the calibration procedure of the detector, the particle histories are binned according to their WEPL and energy deposit to the Bragg-peak stage. The calibration for each stage is then found by computing the most likely WEPL for each energy bin. For protons, the number of events contained in the energy loss distribution tail is much smaller compared to the distribution central part. Hence, WEPL values for that only the energy loss distribution tail overlaps with a given energy bin do not influence the most likely WEPL corresponding to that energy bin, given that all WEPL bins contain a similar number of events. However, the ΔE-E filter by construction acts only on the tail of the energy loss distribution. Therefore, the calibration curves were expected not to be affected much by the ΔE-E filter.

Image reconstruction

In reconstructing the pCT images, it was seen that the presence of nuclear interactions leads to a larger standard deviation of the WEPL distribution compared to the purely electromagnetic distribution, due to nuclear interaction

events increasing the weight of the WEPL distribution tail. Consequently, the post-calibration filters ($3\,\sigma$ WEPL and angular displacement filter) alone were not sufficient in removing events with an unusually large WEPL. This resulted in a reduced RSP accuracy of the pCT reconstructed image. The effect was seen most prominently as systematic fluctuations in the form of ring artifacts arising at stage interfaces, where events stopping in a different stage due to a nuclear interaction can introduce a systematic shift in the WEPL conversion (Bashkirov et al. 2016b). Applying filters on the particle energy deposit measured in the multistage detector as used currently with the investigated prototype only slightly reduced these fluctuations. A $2\,\sigma$ WEPL filter in addition to the current pre-calibration filters improved the image quality, but could not completely remove the systematic fluctuations. Conversely, with the ΔE-E filter applied in addition to the current pre-calibration filters, the tail of the WEPL distribution was reduced towards the distribution where nuclear interactions were disabled in the simulation, thus resulting in a smaller standard deviation and a more effective filtering of events with an unusually large energy loss. With the ΔE-E filter, the systematic fluctuations in the pCT reconstructed images of the ideal water phantom were removed even when a more relaxed $4\,\sigma$ WEPL filter was used. The obtained results closely matched the reconstructed pCT for that nuclear interactions were disabled in the simulation.

Similar results were obtained for the RSP accuracy studied with the insert phantom: the ΔE-E filter added to the current pre-calibration filters improved the RSP accuracy towards the reference value with no nuclear interactions. However, here, a more relaxed $4\,\sigma$ WEPL filter in addition to the ΔE-E filter resulted in a reduced RSP accuracy, especially for the denser material inserts, where nuclear interactions are more likely to occur. This highlights how the ΔE-E filter cannot replace the $3\,\sigma$ filter, since it cannot remove uncertainties stemming from within the object, but only those arising within the energy/range detector. Not using the $3\,\sigma$ filter in addition to the ΔE-E filtering still results in the issues outlined by Schulte et al. (2005). Using a $2\,\sigma$ WEPL filter together with the ΔE-E filter further improved the accuracy, but also led to the removal of $\sim 7\,\%$ events more compared to the current pre- and post-calibration filter setup. On the other hand, removing the threshold filter from the pre-calibration filters did not degrade the image quality if the ΔE-E filter was used.

For the water phantom, the ΔE-E filter in addition to the pre- and post-calibration filters removed about $4\,\%$ events more with respect to the number of events used in the reconstruction with the current filter setup; a $2\,\sigma$ WEPL filter removed $3\,\%$ events more. The number of particles filtered by the ΔE-E filter with respect to that used with the $2\,\sigma$ WEPL post-calibration filter is not evenly distributed over the full WEPL range, but rather peaks at WEPL values corresponding to stage interfaces of the multistage energy/range detector. On the other hand, for the cylindrical water phantom investigated, the WEPL ranges corresponding to stage interfaces do not correspond to a large fraction of the primary fluence explaining how a low number of events filtered more with the ΔE-E filter can have a noticeable impact on the image quality. We note, that the effect of different filters on the image quality also depends on the

reconstruction algorithm used, but the comparison of different reconstruction algorithms was beyond the scope of this work.

ΔE-E filter

As the the ΔE-E filter was originally proposed for helium imaging with the device, the filtering was performed using only the last two stages the particle reached into which is sufficient to identify helium ions that did not undergo nuclear fragmentation along their path. On the other hand, the more conventional approach to a ΔE-E telescope would be to use the first stage in upstream direction as the ΔE stage and summing up the energy deposits measured in the remaining stages to form E. This, however, could result in a somewhat reduced efficiency of the filter for particles reaching farther into the detector, due to the lower variation of their energy deposit in the first detector stage.

In proton imaging, the main effect of the ΔE-E filter is to remove events that stopped in a stage due to a nuclear interaction within the energy detector or scattered outside the detector sensitive area. Still, the ΔE-E filter acts only on the last two stages a particle reached into and can hence not remove secondary protons with a range sufficient to traverse more than one detector stage, as these would fall together with the primary proton ΔE-E spectrum. In order to improve upon the current filter setup, additional ΔE-ΔE filters based on the information of the earlier stages could be implemented. However, the results of this work indicate that the potential benefit of this would be minor, as with the current filter setup, already satisfying accuracy was achieved – close to the reference acquired through simulations where nuclear interactions were disabled entirely.

The impact of nuclear interactions

The key observation in this work is that the calculation of the WEPL standard deviation is sensitive to nuclear interaction events occurring within the energy detector. While the effect on the image quality will be different for other detector designs, the general issue is not limited to the prototype detector investigated here. For energy/range detectors that require the particle to come to a stop within the detector, but provide no longitudinal segmentation (e.g. a one-stage scintillator), filtering out the nuclear interaction contamination stemming from within the energy/range detector would be a more difficult task due to the lack of information. This would also be the case for a classical range telescope, i.e. a stack of thin detector layers providing neither energy nor spatial information, where the range is computed simply from the farthest detector layer the particle reached into. However, the results obtained in this work suggest that for a single stage detector design a 2σ WEPL filter could be a sufficient workaround, as uncertainties remaining after the 2σ WEPL filter were mainly connected to the stage interfaces of the multistage energy/range detector hybrid. Potentially, the optimum would be to implement smart filters, either employing probability measures that correlate the tracker

information and the measured WEPL (as e.g. proposed by Collins-Fekete & Romano (2018)) or using machine learning algorithms.

For segmented energy/range hybrid detectors, the ΔE-E filter developed for helium ion imaging was shown to improve also pCT. By removing uncertainties arising from the detector segmentation, the ΔE-E filter potentially further adds to the benefits of using segmented energy/range hybrid detectors outlined by Bashkirov et al. (2016b). However, while nuclear interactions are one cause of uncertainty, for the full experimental setup, additional effects connected to the detector readout and calibration would have to be taken into account[2]. The modeling and evaluation of such effects, however, was beyond the scope of this work and will be subject to further investigations.

Conclusion

In this work, it was demonstrated that for the prototype system developed by the US pCT collaboration the $3\,\sigma$ filtering alone is not sufficient in removing unusually large energy losses and nuclear interaction events prior to image reconstruction. This resulted in reduced RSP accuracy and systematic fluctuations in the reconstructed images. In general, nuclear interactions inside the energy/range detector influence the calculation of the standard deviation of the WEPL distribution and can reduce the filter efficiency. In this context, the ΔE-E filtering mode was shown to yield some potential for pCT as well, since it enables the identification and effective filtering of nuclear interaction events that occurred within the detector. For single stage detectors, a more strict $2\,\sigma$ filter could potentially act as a workaround. In future studies, the results of this work should be verified in experiment and investigated also for other detector designs.

Acknowledgements

The authors acknowledge Jannis Dickmann for fruitful exchanges regarding the preprocessing procedure of the detector. The authors would like to thank Guillaume Landry and Georgios Dedes for useful discussions. We also thank Lucas Burigo for helpful insights regarding the TOPAS simulation framework. This work was partially supported by grants from the National Institute of Biomedical Imaging and Engineering and the National Science Foundation (NSF) (R01EB013118), the National Cancer Institute (NCI) (1P20183640-01A1), and the United States - Israel Binational Science Foundation (BSF) (2009012 and 2013003).

[2]Such effects can be observed also in Volz et al. (2018) where systematic fluctuations remained in the HeCT reconstructions, even after the ΔE-E filter was applied.

5.4 P.I: Stopping power acquisition from particle CT versus x-ray CT

Title : Experimental comparison of proton CT and helium ion CT with single- and dual-energy x-ray CT in heterogeneous biological tissue samples

Authors : L. Volz, E. Bär, C.-A. Collins-Fekete, V. A. Bashkirov, S. Brons, R. P. Johnson, A. Runz, C. Sarosiek, R. W. Schulte and J. Seco

Status : In Preparation

Journal : N/A

DOI : N/A

Copyright : N/A

Contributions : LV under the supervising guidance of JS planned the overall project, prepared the experiments and organized the installation of the US pCT collaboration scanner at the HIT facility. LV and EB jointly conceptualized and prepared the study concerning the biological tissue samples. AR and LV designed and constructed the custom phantoms. EB, LV, and AR prepared the biological tissue samples. EB, CACF, LV, RPJ and CS directly participated in the beam tests at the HIT facility. RPJ, RWS and VAB provided technical support on the pCT scanner prototype and the data acquisition and pre-processing software. LV together with SB prepared the low intensity pencil beam scanning plans for the PCT acquisition. SB provided technical support on the HIT accelerator complex and the peakfinder reference RSP measurements. CS aided with the Gafchromic®EBT-XD measurements and directly contributed to preparation measurements with the tissue samples. EB and LV acquired the SECT and DECT scans. EB conducted the RSP calibration and evaluation of the SECT and DECT scans, processed the peakfinder RSP reference measurements, and finalized the results concerning modality comparison for the homogeneous tissue samples. CACF significantly contributed to the finalization of the measurement plan, and, together with LV, optimized the pre-processing and calibration procedure of the detector. LV, finalized the results on the detector calibration, conducted the pre-processing and image reconstruction for all PCT data, and wrote the chapter.

Abstract

Given the feasibility of high quality helium ion imaging demonstrated in publication P.XII and the potential improvement of proton imaging with the ΔE-E filter suggested in the simulation study presented in publication P.XI, the next step in this research was to experimentally explore the potential of these imaging modalities for the clinics. In 2019, to continue this research, our group together with the US pCT collaboration was awarded with project funding by the Particle Therapy Co-Operative Group (PTCOG). This enabled another series of experiments with the US pCT collaboration prototype scanner installed at the HIT facility between end of 2019 and early 2020. The overall aim of this project was to investigate the reduction of range uncertainty in particle therapy achievable through helium ion and proton imaging compared to the current clinical practice. For comparison, we considered both SECT and DECT as the latter can be considered the current gold standard for RSP acquisition in terms of accuracy and clinical maturity. To ensure an unbiased comparison, we used both homogeneous and heterogeneous fresh animal tissue samples (porcine and bovine). This enabled a direct comparison between the RSP accuracy and image quality achievable with the different methods. In-tissue range reference measurements performed for the heterogeneous tissue sample will further enable the assessment of the achievable range accuracy with the different modalities. In the following, preliminary results from our ongoing investigations are presented.

Introduction

Accurate analytical treatment planning in particle therapy requires accurate voxelized information of the relative stopping power (RSP) within the patient (Paganetti 2012). In current clinical practice, the RSP map is acquired with a treatment planning Single-Energy x-ray CT (SECT) through a calibrated conversion from the measured photon absorption coefficient (Hounsfield Units, HU). The HU-RSP conversion curve can be obtained either empirically, by measuring both the HU and RSP for tissue surrogate plastic materials, or based on the stochiometric calibration method by Schneider et al. (1996). The former method generally suffers in accuracy due to the poor representation of human tissues offered by the tissue surrogates (Wohlfahrt & Richter 2020). For the latter, the tissue surrogate materials are only used to obtain scanner specific parameters for calculating theoretical HUs for a list of human tissues with tabulated chemical composition (Woodard & White 1986, White et al. 1987). RSPs of these tissues are calculated by evaluating the Bethe formula (Bär et al. 2018a). Both the empirical and stochiometric methods result in a set of discrete calibration points. The calibration is extended to the whole HU range through piece wise linear fitting (Wohlfahrt & Richter 2020). The HU-RSP conversion is not based on physical principles, due to the fundamentally different interactions of photons and particles with matter. Hence, the HU-RSP relationship is not bijective and tissues with the same HU can have different RSP or vice versa.

As such, the HU-RSP conversion is a key uncertainty factor when computing the particles range inside the patient (Paganetti 2012, Lomax 2020). Already Schaffner & Pedroni (1998) have shown the HU-RSP conversion to cause uncertainties in the range calculation up to 1.5%. In order to ensure tumor dose coverage, safety margins are therefore added around the target volume in current clinical practice of up to 3.5%+3 mm (Paganetti 2012).

As means to improve the current clinical practice, in recent years methods for RSP acquisition from Dual-Energy x-ray CT (DECT) have been proposed (Yang et al. 2010, Hünemohr et al. 2013, Bourque et al. 2014, Möhler et al. 2016, Taasti et al. 2016, Wohlfahrt et al. 2017b). DECT uses two different photon energy spectra providing partially complementary information which enables a more accurate determination of tissue specific parameters (Wohlfahrt & Richter 2020). In recent extensive theoretical studies and experimental campaigns, methods for RSP determination from DECT have been shown to yield an RSP accuracy better than 1% and, consequently, can improve the achievable range accuracy (Bär et al. 2017, Bär et al. 2018b, Möhler et al. 2018, Taasti et al. 2017, Almeida et al. 2018). Given the potential of DECT, it is now at the forefront of reaching widespread clinical application (Wohlfahrt & Richter 2020). Still, RSP estimation from DECT represents an indirect conversion subject to the calibration materials and method applied, and especially, will return larger RSP errors in non-tissue materials.

Particle imaging has been proposed as a more direct alternative for RSP estimation in clinical practice. By measuring the water equivalent path length (WEPL) traversed by particles through the patient, the RSP can be resolved through particle Computed Tomography. In addition, the treatment planning x-ray CT HU to RSP conversion can be optimized with a small number of particle imaging projections (Schneider et al. 2005, Doolan et al. 2015b, Collins-Fekete et al. 2017a, Krah et al. 2019, Gianoli et al. 2020). Particle radiographs could also be used for patient anatomy verification and alignment in treatment position and from beams-eye view (Palaniappan et al. 2019). Moreover, particle imaging does not suffer from metal artifacts that can compromise the image accuracy for x-ray CT based methods (Ordoñez et al. 2017, Oancea et al. 2018). At the same time, since only the dose plateau of the particles depth dose profile lies within the patient, particle imaging also comes at a distinct dose advantage when compared to SECT at the same image noise level (Schulte et al. 2005, Depauw & Seco 2011, Collins-Fekete et al. 2020). Generally, image quality in particle CT suffers from the multiple coulomb scattering (MCS) of the particles. Current particle CT prototype systems therefore individually measure each particle's position and direction before and after the patient. During image reconstruction, this information is used to estimate the particle's Most Likely Path (MLP) through the patient, enabling a more accurate back-projection of the WEPL (Li et al. 2006, Rit et al. 2013).

Already Hansen et al. (2015) have demonstrated an advantage in RSP accuracy for pCT compared to DECT in a simulation study. This was corroborated in the recent experimental study by Dedes et al. (2019) who investigated the RSP accuracy for 13 different tissue equivalent plastic materials demonstrating a mean absolute percentage error (MAPE) of 0.55% for pCT, whereas

(a) (b)

Figure 5.33: The "competitors" for investigating the RSP acquisition for particle therapy treatment planning in this study. (a) The DKFZ Siemens Somatom Definition Flash (Siemens Healthineers, Forchheim, Germany) dual-source x-ray CT scanner. (b) The US pCT collaboration particle CT prototype installed at the HIT.

DECT yielded 0.67%. They observed that pCT could be further improved if the ring artifacts arising in pCT with the investigated prototype particle CT scanner could be solved. However, a full assessment of the RSP accuracy of both techniques in animal tissue samples has not yet been performed. In addition, HeCT could offer further advantage over pCT due to the reduced scattering and range straggling of helium ions (Hansen et al. 2014a, Collins-Fekete et al. 2017d, Gehrke et al. 2018, Piersimoni et al. 2018). Moreover, helium ions are especially tight bound (Cucinotta et al. 1993), resulting in less fragmentation when compared to other light ions heavier than protons. Still, the fragments create large uncertainties in the image, if they are not removed before image reconstruction (Gehrke et al. 2017, Volz et al. 2018). Using a ΔE-E technique with the prototype particle CT scanner developed by the US pCT collaboration, Volz et al. (2018) demonstrated experimental helium CT (HeCT) with a RSP mean absolute percentage error (MAPE) $<$0.5%.

Given the feasibility of high quality helium ion imaging, and the potential improvement of proton imaging with the ΔE-E filter suggested in Volz et al. (2019), the overall aim of this project was to experimentally explore the potential of pCT and HeCT for improving range accuracy in particle therapy. In 2019, to continue this research, our group together with the US pCT collaboration was awarded project funding by the Particle Therapy Co-Operative Group (PTCOG). This enabled another series of experiments with the US pCT collaboration prototype scanner (Figure 5.33(a)) installed at the HIT facility between end of 2019 and early 2020. For comparison, we considered both SECT and DECT as the latter can be considered the current gold standard for RSP acquisition in terms of accuracy and clinical maturity. The SECT and DECT treatment planning CTs were acquired using the DKFZ Siemens Somatom Definition Flash dual-source (Siemens Healthineers, Forchheim, Germany) x-ray

Machine (Figure 5.33(b)). HeCTs, pCTs, SECTs and DECTs, as well as HeRads and Proton Radiography (pRad) of various plastic quality assurance phantoms were acquired. For an unbiased comparison between the modalities, we custom-designed two phantoms comprising fresh animal tissue samples. The first one (named Meatphan1; MP1) aims at a direct comparison of the RSP accuracy between the different CT modalities based on homogeneous tissue samples. The second (Meatphan2; MP2) comprises a heterogeneous pig-head sample, enabling the assessment of the image quality for a clinically realistic case. In the following, preliminary results from the ongoing evaluation of the acquired data are presented.

Materials and Methods

The prototype particle CT scanner

Full tomographic scans of various phantoms were acquired using the preclinical prototype particle CT scanner developed by the US pCT collaboration (Johnson et al. 2017, Sadrozinski et al. 2016). The scanner comprises two tracking detectors, one preceding and one following the object to be imaged, that measure each particle's position and direction.

Each of the tracking detectors comprises 4 layers of silicon strip detectors (strip pitch 0.228 μm). The measurement of 2D position information is achieved by pairing two layers with horizontal and vertical strip direction, respectively. Two layer pairs spaced 50 mm to each other together form a tracker module enabling measurement also of the entrance and exit direction. A detailed description of the tracking system is provided in Sadrozinski et al. (2013).

To measure the residual energy of the particles, the system relies on a 5-stage scintillator, where the stages are individually read out by PMTs. Each of the five scintillator stages has a dimension of 50.8 mm$\times$100 mm$\times$375 mm (T$\times$H$\times$W) and is made of UPS923A polystyrene plastic scintillator (Artikov et al. 2005). The segmentation of the energy detector reduces the precision requirement on the energy measurement in each stage for achieving a certain WET resolution (Bashkirov et al. 2016a).

For helium ion runs, the data acquisition settings of the detector were modified slightly compared to those used usually for proton runs: A low-gain setting was used for the tracking detectors, and for the energy detector the PMT high voltage was lowered to 760 kV compared to the usually used 800 kV to avoid saturation.

Detector calibration

The energy detector measures quenched scintillation light output which shows a non-negligible variation across the lateral face of the detector (Bashkirov et al. 2009). Prior to the scanning experiments, the energy detector response is therefore first flattened across the detector aperture, and then a calibration of the energy output to WEPL is performed.

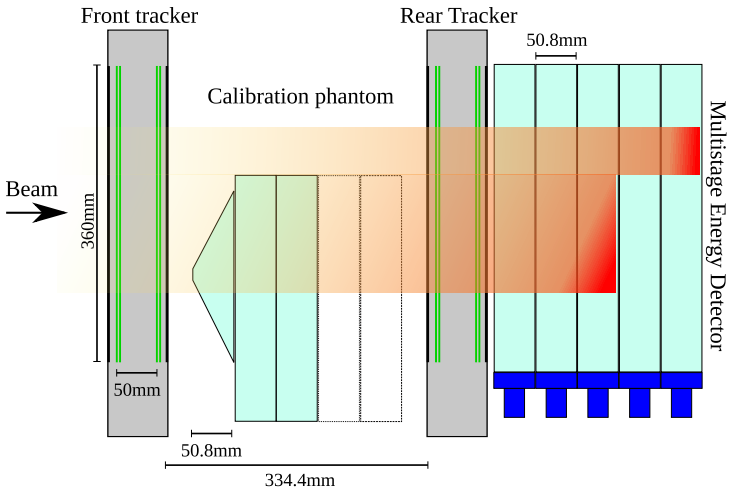

Figure 5.34: Schematic depiction of the calibration scheme for the detector (to scale). First a run without phantom between the trackers (empty run) is performed to calibrate the detector energy output. In a second run, two polystyrene wedges are placed between the front and rear tracker, in order to create a continuous thickness variation between 0 mm and 50.8 mm. In subsequent runs, 50.8 mm thick blocks of polystyrene are added one by one such that the full WET range of the detector is covered. In data processing, the physical path length traced by each particle through the calibration phantom is related to the energy loss measured in the stage where the particle stopped.

To calibrate the lateral dependence of the detector response, a run without phantom in between the tracker planes is acquired. From these data, 2D histograms of the measured ADC output as function of the lateral position at the stage entrance were created for each of the 5 scintillator stages. The particles position at the stage entrance were thereby estimated through a forward projection of the rear tracker measurements. Comparing the peak ADC value after subtraction of the stage noise pedestal to the expected peak energy response in the stage for an empty run as computed through a detailed Monte Carlo simulation (Giacometti et al. 2017b) then returns a 2D matrix of ADC-to-energy correction factors (here denoted lateral correction; LC).

To calibrate the energy output to WEPL we followed the procedure detailed as "configuration C" in Piersimoni et al. (2017). A schematic depiction of the calibration procedure is shown in Figure 5.34. First, data is taken with two polystyrene wedges of known geometry (50.8 mm thickness, 104.75 mm width and 100 mm height) and known RSP of 1.030 ± 0.003 (Giacometti et al. 2017a) placed in between the trackers. In 4 subsequent runs, 4 bricks of 50.8 mm thickness made of the same material as the wedges are added to the setup one-by-one. In total, the five runs provide a smooth thickness variation over the full dynamic WEPL range of the detector. Since the irradiation field lateral width (200 mm) did not cover the full width of the two wedges (209.5 mm), the setup was shifted by 50.8 mm compared to the beam center. While this effectively

leaves only one of the wedges for calibration, the two wedge halves are anyways redundant in the calibration process. Hence, it is not expected for this to causes a reduction in accuracy. To avoid calibration uncertainties arising from particles scattering out of the phantom, the end of the bricks was shifted by $\sim$20 mm with respect to the end of the wedge. The empty region irradiated next to the phantom was used for online re-calibration of the PMT gain, which can vary with particle rate (or more precisely the intensity of the produced scintillation photons), temperature and fluctuations in the high voltage supply (Bashkirov et al. 2016a).

In processing of the calibration data, the WEPL for each event is estimated as the Euclidean distance between the front and rear tracker measurements projected onto the calibration phantom contour, scaled by the known RSP of the setup. The WEPL is then related to the energy deposit measured in the stage where the particle stopped (stopping stage), and filled into a 2D histogram. The stopping stage is thereby estimated as the last stage in beam direction where an energy deposit above a 1 MeV noise threshold was measured. A superposition of the so-created energy-to-WEPL histograms is shown in Figure 5.35(a) for protons and Figure 5.35(b) for helium ions. Each high occurrence line in the figures represents the response of one of the 5-stage scintillator stages for particles stopping in that stage (left last stage, right first stage in beam direction). Evaluating the peak WEPL in row-wise projections of the energy-to-WEPL histograms of each individual stage then returns a calibration from energy deposit to most likely WEPL. Examples of the resulting calibration curves for the second stage in beam direction for protons and helium ions are shown in Figure 5.35(c).

This method of detector calibration, of course, requires the calibration phantom to be well aligned with the geometry defined in the calibration code. However, we observed a small lateral misalignment between the tracker position and the wedges (Figure 5.36(b)). This misalignment caused systematic effects in the image reconstruction. Especially, a lateral shift of the wedges causes systematic effects at WEPL values corresponding to integer multiples of the brick thickness, due to particles crossing the flat brick regions next to the wedge break points being assumed to have crossed the wedge slope and vice versa (compare Figure 5.34). Notably, this cause of artifacts is not specific to the detector used, but only the calibration procedure.

In order to realign the wedges, from the 5 calibration runs we created a 2D histogram of the particles' lateral position at the entrance of the wedge (estimated from the front tracker measurement) and the total energy deposit measured in the detector (Figure 5.36(a)). Investigating the total energy output rather than the WEPL avoids additional uncertainties arising from the WEPL calibration. As the wedge calibration phantom consists of two identical wedge halves, the small gap in between the halves could be used to realign the calibration phantom with the trackers. In that way, the lateral misalignment between the actual and expected position of the calibration phantom was identified as 0.9 ± 0.1 mm (Figure 5.36(b)), where half of the strip pitch is assumed as uncertainty. The same misalignment was observed between independent beam tests during the experimental phase at HIT and for both helium and proton

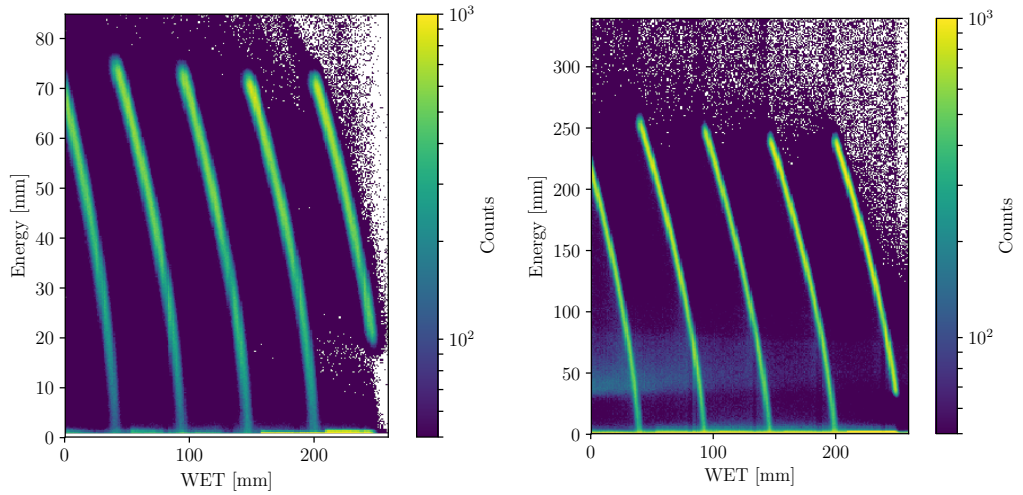

(a) Protons

(b) Helium ions

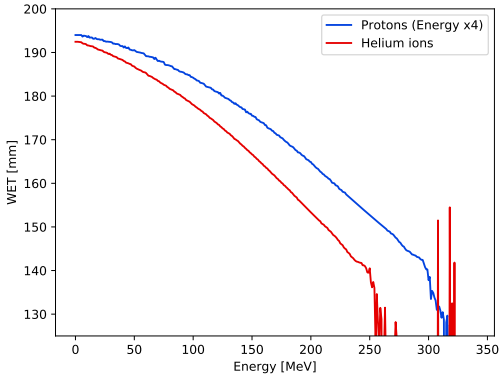

(c) Example calibration curves (second stage)

Figure 5.35: Energy response of each of the 5 scintillator stages as function of the WET traversed by the events stopping in the stage during the calibration runs. (a) Protons and (b) helium ions. Each high occurrence pattern corresponds thereby to the response of one of the stages. The curve for the first stage in beam direction does not reach 0 MeV, as it is used to trigger the data acquisition (threshold of 20 MeV). The calibration curves for each stage are obtained by evaluating the peak of the response patterns. Example proton (blue) and helium (red) calibration curves for the second stage in beam direction are shown in (c). The proton calibration curve x-axis was multiplied by 4 to enable better comparison.

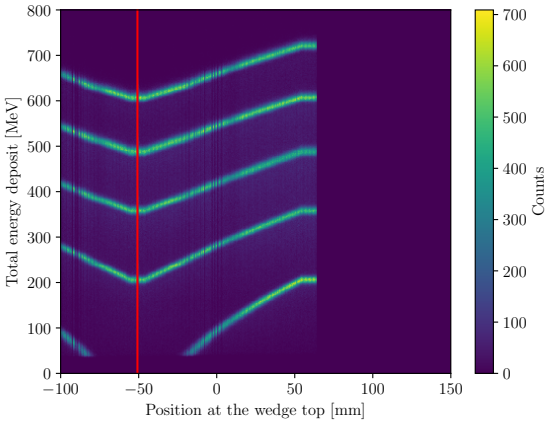

(a) Superimposed energy profiles of the 5 wedge calibration runs

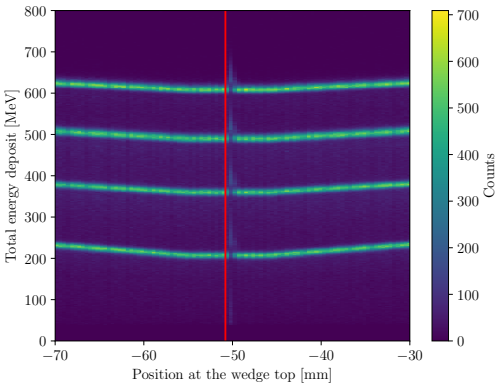

(b) Misaligned wedges

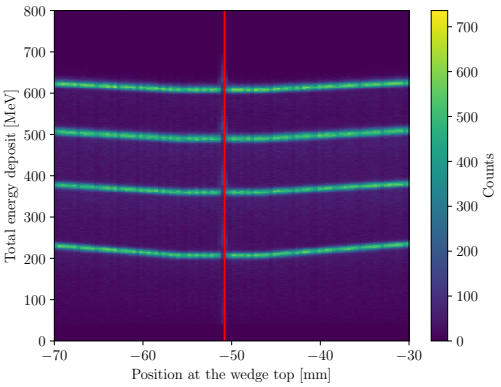

(c) Aligned wedges

Figure 5.36: 2D histogram of the total energy deposit in the detector (sum of the energy output to each of the 5 stages) versus the particle's position at the entrance of the wedge phantom for the five calibration runs. a) The full response for the 5 wedge calibration runs. From top to bottom the high occurrence response lines indicate the run with only the wedges and no additional brick (particles stopping in the last detector stage) to the run with five bricks (particles stopping in the first stage/not reaching the detector anymore). The red vertical line indicates the expected center of the wedges. b) Zoom in on the gap between the two wedge halves in the phantom center, showing the misalignment. c) Zoom in on the gap between the wedge halves after realignment of trackers and wedge.

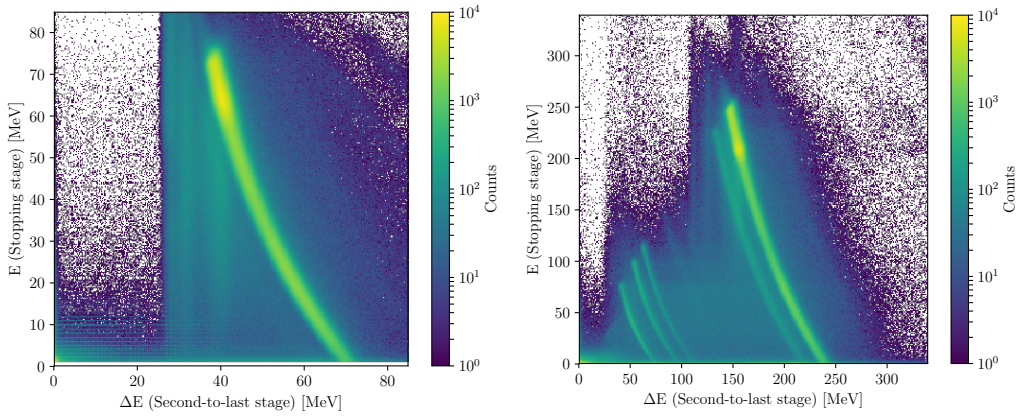

(a) Protons **(b)** Helium ions

Figure 5.37: ΔE-E spectra for (a) protons and (b) helium ions acquired during the calibration of the detector for events stopping in the second stage in beam direction.

runs. The observed shift in the wedge position was used to correct the alignment of the trackers and the wedge (Figure 5.36(c)).

Data processing and image reconstruction

During data processing of imaging runs, for each event the stopping stage was determined in the same way as for the calibration run. The ADC output measured in that stage was then converted to energy using the LC. To remove secondary fragments and nuclear interaction events, a ΔE-E filter was applied to the data (Volz et al. 2018, Volz et al. 2019). This filter is based on the unique relationship between the energy deposit in the stopping stage and that in the immediately adjacent stage in upstream direction for a particle with given mass and charge. Comparing the measured ΔE-E response of an event to that expected for primary particles enables accurate particle identification, and, hence, filtering of events that would otherwise cause image degradation. Examples for the ΔE-E response patterns for protons and helium ions are given in Figure 5.37. The ΔE-E filter margins were computed based on the ΔE-E spectra of each stage in the calibration runs: gaussian fitting the peak response in row-wise projections of the ΔE-E spectrum returned the peak ΔE-E response curve of primary particles and the connected standard deviation envelope. Only if the measured ΔE-E response for an event agreed with the expected response for primary particles within 2.5σ, the event was used for image reconstruction.

In addition to the ΔE-E filter, a cut on the maximum energy deposit in a stage (75 MeV for protons; 300 MeV for helium ions) and energy thresholds to the stages leading up to the stopping stage were applied (see Volz et al. (2019) for more details on the filtering procedure). For events surviving the data filters, the energy deposit measured in the stopping stage was converted to WEPL using the respective energy-to-WEPL calibration curve.

Images were reconstructed using the diagonally relaxed iterative row projection (DROP) iterative algorithm with total variation superiorization (TVS) (Penfold et al. 2010). This algorithm has been used broadly with the investigated prototype (Giacometti et al. 2017a, Plautz et al. 2016, Piersimoni et al. 2017, Volz et al. 2018, Volz et al. 2019). Prior to the iterative solver, 3σ filters acting on the angular displacement and WEPL of the particles were applied: The particles were re-binned based on the midpoint position and angle of a straight line path between their entrance and exit positions. For each bin the standard deviations of the angular displacement and WEPL distribution were computed. Events with angular displacement or WEPL outside a 3σ region around the maximum were discarded.

A Feldkamp-David-Kress (FDK) analytical filtered backprojection reconstruction was used as starting estimate for the iterative solver and to estimate the objects contour for a hull projection algorithm (Schultze et al. 2014). Inside the object, particle paths were estimated with the optimized cubic spline path formalism by Collins-Fekete et al. (2015). For the DROP-TVS iterative reconstruction, the data were divided in 40 optimization blocks and the relaxation parameter was set to 0.1. The iterative algorithm was stopped after eight iterations. This choice of parameters was based on what had been used in previous publications with the algorithm (Giacometti et al. 2017a, Piersimoni et al. 2017, Piersimoni et al. 2018, Volz et al. 2018, Volz et al. 2019, Sølie et al. 2020). However, due to the algorithm convergence being subject to the imaged object as well as the noise in the data, an optimization of the reconstruction parameters for this study is ongoing and will likely result in improved image accuracy.

Beam settings at the Heidelberg Ion-Beam Therapy Center

To deliver the proton and helium ion imaging fields, the HIT raster scanning method was employed. The beam nominal initial energy was 200.11 MeV for protons ans 200.38 MeV/u for helium ions. The pencil beam size was 12.8 mm for protons and 10.2 mm for helium ions, corresponding to the largest spot sizes available at the investigated energy. The spot centers were spaced 3 mm in both lateral directions to achieve a homogeneous field coverage. The scanning field had 100 mm vertical, and 200 mm horizontal extent. As the detector is capable of a maximum particle detection rate of $\sim$1 MHz, the beam intensity had to be lowered compared to the clinical settings. For helium ions, the rate was set to $\sim$680 kHz similar to previous studies with the detector (Volz et al. 2018), i.e. roughly 30 times lower than the lowest clinically available intensity setting. For protons, the intensity was $\sim$1.35 MHz, $\sim$60 times lower than the lowest clinically available setting at HIT. While, in principle, lowering the beam intensity for protons further would be feasible at HIT, raster scanning at lower beam intensities was not yet possible due to the sensitivity limit of the ionization chambers monitoring the dose per spot.

The trigger rate measured with the detector in a run without phantom in the beam line (empty run) is shown in Figure 5.38. Figure 5.38(a) shows a helium ion run and Figure 5.38(b) a proton run. In addition, the figure depicts the event rate, i.e. the rate at which events were saved for output. The relative

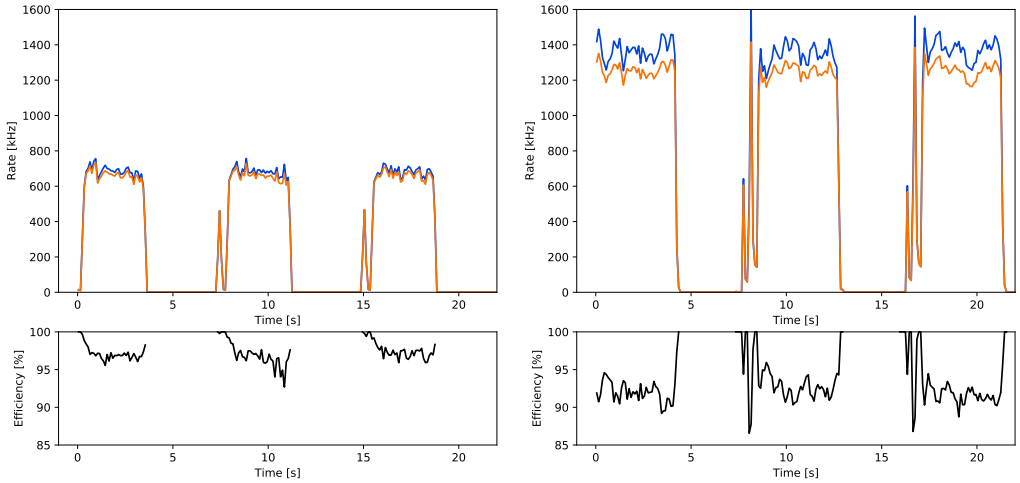

Figure 5.38: Low-intensity spill as used for the measurements with the detector for a) helium ions and b) protons, measured in a run without phantom in the beam line. The blue line indicates the trigger rate, the orange line indicates the event rate, i.e. the rate of events generated and saved by the event builder.

difference between trigger and event rate is shown to provide a quantitative analysis of the detector dead time. For helium ions, the dead time of the system was less than 4%. Notably, for the proton beam, the increased particle rate resulted in an decreased efficiency of ∼90%, i.e. a $\leq$10 % dead time. Despite the operation at intensities far lower than the clinically used, the particle rate within each spill was relatively stable with only short spikes at the beginning of the spill.

Photon imaging modalities

Single-energy CT

All CT images were obtained using the Somatom Definition Flash dual-source scanner (Siemens Healthineers, Forchheim, Germany) installed at the German Cancer Research Center (DKFZ). The machine is in daily patient operation and regularly maintained to ensure highest accuracy. To obtain single-energy CT images, we used a tube voltage of 120 kV, a tube current of 215 mAs and a field of view of 500 mm. Images were reconstructed using a H30s filtered back projection reconstruction kernel with a slice thickness of 2 mm and a pixel size of 0.977x0.977 mm^2. For the SECT to RSP conversion, we scanned the Gammex RMI 467 electron density phantom (Gammex Inc., Middleton, WY, USA) with tissue-equivalent materials, densities, mean excitation energies (I-values) and theoretically calculated RSP values as listed in table 5.5. Electron densities were obtained from the densities and elemental compositions of the materials given by the manufacturer. I-values were calculated using the Bragg additivity rule from elemental compositions and elemental I-values taken from Bär et al. (2018a). RSP values were calculated using the Bethe formula (Bethe & Ashkin 1953) with protons of an energy E = 195 MeV as projectile.

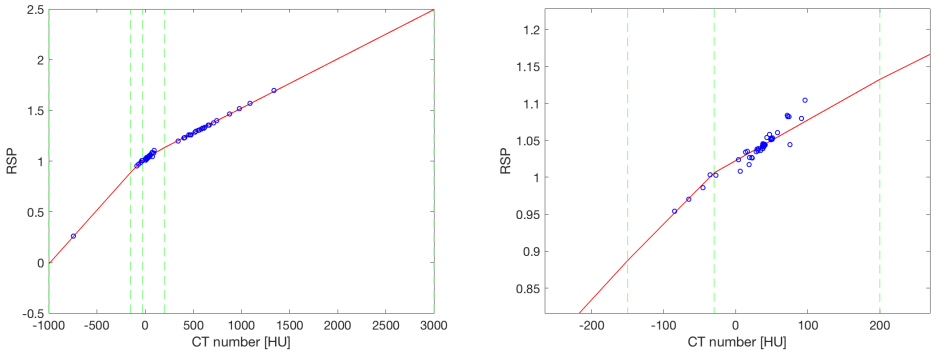

(a) (b)

Figure 5.39: Stoichiometric calibration from HU to RSP used in this work. The points represent the tabulated tissues of given densities and compositions, the solid line is the fitted curve, and the dotted lines represent the fit regions; a) shows the calibration curve over the whole CT range; b) shows a zoom into the soft tissue region.

To estimate RSP values from SECT images, the stoichiometric calibration by Schneider et al. (1996) was used. We first performed the energy calibration after Equation 8 in Schneider et al. (1996) to find the energy-dependent coefficients K^{ph}, K^{coh} and K^{KN} from the CT numbers (in Hounsfield units, HU) measured for the tissue-equivalent Gammex materials. These coefficients were then used to calculate the theoretical HUs for 70 tabulated human tissues (Woodard & White 1986, White et al. 1987). Finally, the calibration curve was obtained by plotting the RSP of these tissues calculated from the Bethe formula as in Bär et al. (2018a) against the calculated HU and performing a step-wise linear fit to the so obtained calibration points. For this work, we combined four linear fits to cover the the following regions: Lung (HU $<$ -150), adipose tissue (-150 $\leq$ HU $<$ -30), soft tissues (-30 $\leq$ HU $<$ 200), and bones (200 $\leq$ HU). The SECT calibration curve is shown in Figure 5.39(a), and a detailed view in the soft tissue region is provided in Figure 5.39(b).

Dual-energy CT

To obtain dual-energy CT images, we used tube voltages of 100 kV and 140 kV tin filtered, and a tube current of 174 mAs for both x-ray tubes. Reconstruction was done using an D34s filtered back projection reconstruction kernel with a slice thickness of 2 mm and a pixel size of 0.977x0.977 mm^2. The DECT stoichiometric calibration by Bourque et al. (2014) was applied to estimate the RSPs from DECT images. This image-based model uses two images acquired at different CT energies to estimate the electron density (ED) and effective atomic number (EAN) of the material in the image on a voxel-by-voxel basis. From the DECT images, the dual-energy ratio (DER) is calculated as the ratio of CT numbers taken from the low and high energy images. The DER in a voxel can be related to the EAN of the material within that voxel using a

Material	ρ_e	I-value	RSP
Water	1.00	78.73	1.00
LN450 Lung	0.44	77.47	0.44
AP6 Adipose	0.93	67.07	0.94
BR12 Breast	0.97	68.73	0.98
CT Solid Water	0.99	71.00	1.00
LV1 Liver	1.06	71.00	1.07
SR2 Brain	1.04	66.85	1.06
Muscle	1.02	71.01	1.03
CB2 - 30% CaCO3	1.27	86.51	1.25
CB2 - 50% CaCO3	1.46	99.95	1.42
SB3 Cortical Bone	1.68	113.79	1.61
B200 Mineral Bone	1.11	82.51	1.10
IB3 Inner Bone	1.10	82.41	1.09

Table 5.5: List of electron densities, I-values and theoretically calculated RSP of the materials used to calibrate the SECT and DECT stoichiometric methods.

5-th order polynomial. In a similar way, a relation can be established between the CT number within a voxel and the electron density. The parameters of the polynomials are found by least squares optimisation using a DECT scan of the Gammex RMI 467 electron density phantom with known elemental compositions and densities (listed in Table 5.5). Once the parameters are found, the model can be used to estimate the ED and EAN voxelwise from the DECT images of a phantom or patient scan. The EAN is then used to estimate the I-value per voxel via a parametric fit. The original paper from Bourque *et al.* suggests to perform the parametric fit on a data set of human reference tissues. We used this approach in this work, however modified it using the elemental I-values as suggested in Bär et al. (2018a). The EDs and I-values estimated from the DECT scan were then used to calculate the RSPs by evaluating the Bethe formula where we followed the procedure suggested by Bär et al. (2018a).

Investigated Phantoms

Over the duration of the experiments with the US pCT collaboration prototype, several plastic and tissue phantoms were studied. These will be used for an in-depth comparison between proton and helium ion imaging with the scanner in a future study. Here, only the results of the study based on the custom designed tissue sample phantoms described below are presented.

Meatphan 1 For the Meatphan 1 (MP1), shown in Figure 5.40, we collected porcine and bovine tissues from the local butcher's to prepare fresh tissue samples for RSP reference measurements. A total of 16 tissue samples was collected: porcine lung, porcine belly fat, porcine back fat, bovine bone marrow, porcine blood, porcine cheek muscle, two samples of porcine loin muscle,

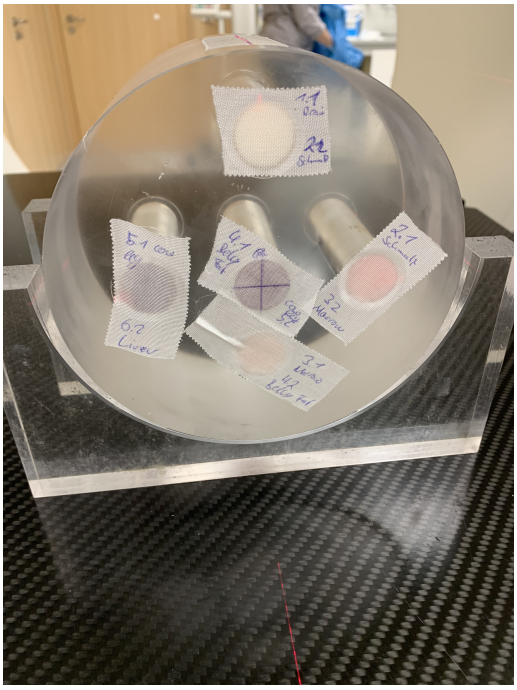

(a)

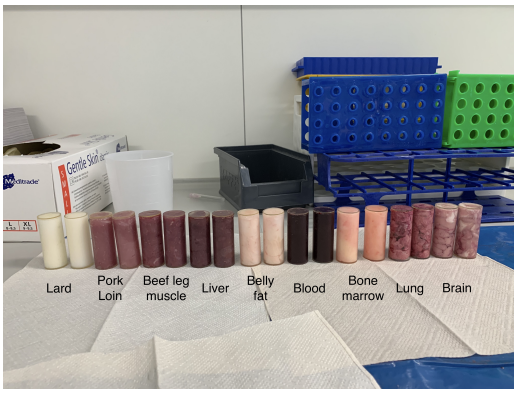

(b)

Figure 5.40: (a) photograph of the MP1 including 10 tissue inserts. The radial positions of the inserts are central, 30 mm, 40 mm (2) and 50 mm. (b) Photograph of individual sample cylinders. Not all tissues investigated are shown in this picture. Two samples per tissue were created, but not all were used in the analysis due to air enclosures or decay.

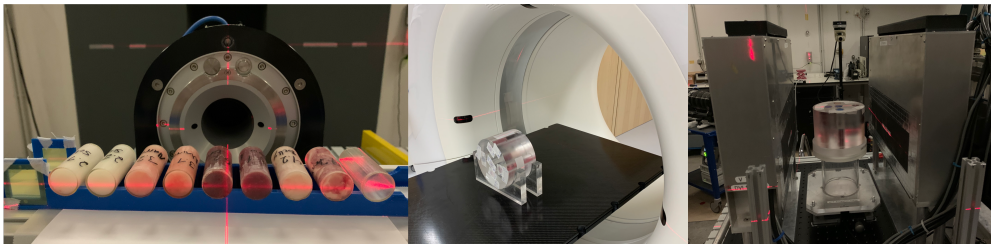

(a) (b) (c)

Figure 5.41: Pictures showing the measurement setups for a) reference measurement using the PTW peakfinder; b) photon CT scanning; c) particle CT imaging. For peakfinder reference measurement, the samples were positioned using a 3D-printed holder and placed on a remote controlled moving platform for efficiency. For photon and particle CT imaging, the samples were placed into an in-house designed cylindrical PMMA phantom.

bovine leg muscle, porcine brain, two samples of porcine kidney, two samples of porcine liver, porcine trabecular bone, bovine cortical bone. Soft and adipose tissues were cut into small pieces and filled into 3D-printed cylindrical containers (d = 2 cm, h = 5 cm, wall thickness = 1 mm) made of VeroClear epoxy (Sculpteo, Villejuif, France). Lung, liver and kidney were finely minced and filled into the container. Trabecular and cortical bone pieces were taken from a single piece of bone, sawed into shape to exactly match the length of the container, then filled in. The containers were then closed and sealed. One cylinder was left empty to measure the WET of the container wall, another container was filled with distilled water for a consistency check. For CT scanning, the containers with the biological samples were inserted into an in-house designed cylindrical phantom made of PMMA material (d = 150 mm, h = 100 mm, density 1.19 g/cm^3), as shown in Figure 5.41(b). The inserts were located at different radial positions (central, 30 mm, 40 mm, and 50 mm) in order to reflect different beam hardening in the photon CTs, as well as different scattering and detector artifacts in the particle CTs. From the RSP maps obtained with the different CT methods, we estimated an average RSP and the corresponding standard deviation per sample by measuring the RSPs in a cylindrical volume of interest (VOI). The VOIs radius was chosen to match the the size (1σ) of the carbon beam used for the range-sift reference measurements (described in Section 5.4). The volume of the VOI was 682 mm^3. All samples were kept in the fridge in between preparation and measurements to avoid decay, and all measurements were performed within 24 hours of sample preparation. The measurement setup for this phantom in the different modalities is shown in Figure 5.41

Meatphan 2 Finally, to provide a fully realistic case, a pig head phantom was custom designed as shown in Figure 5.42. The phantom was a cylindrical, 3D printed container (150 mm diameter, 2 mm shell thickness) made from VeroClear epoxy (Sculpteo, Villejuif, France). A CAD drawing of the phantom

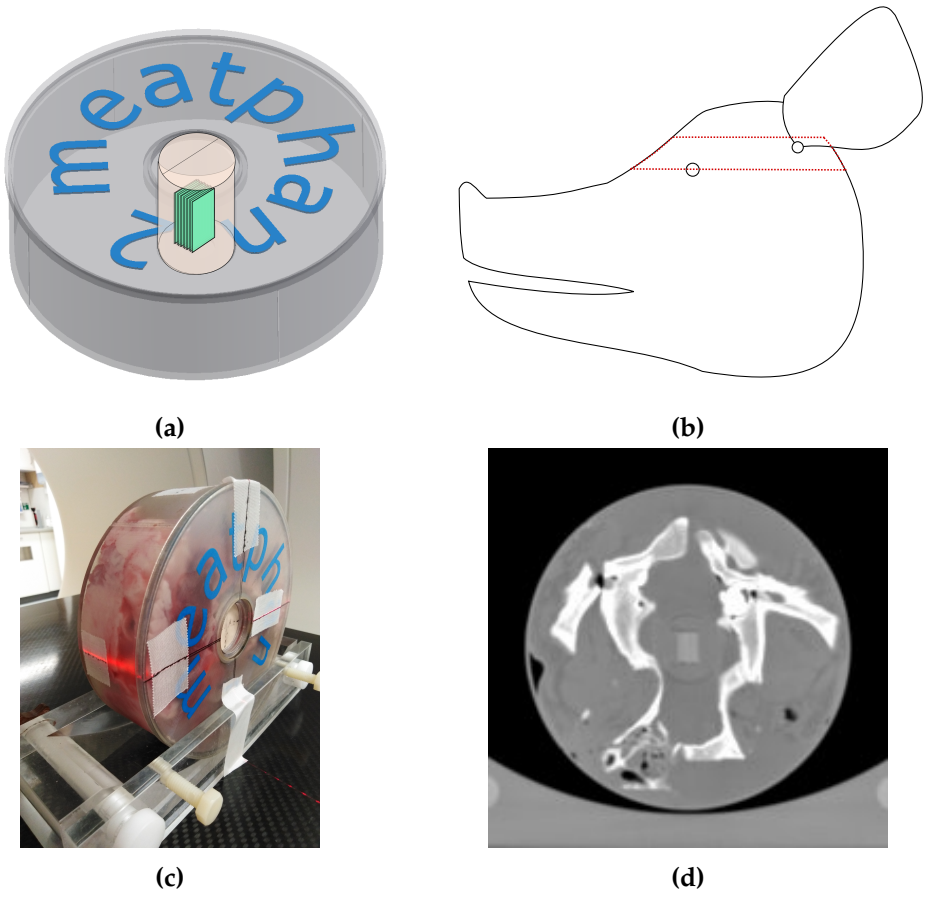

Figure 5.42: Custom-designed pig-head phantom (Meatphan2). (a) Drawing of the 3D-printed phantom container (150 mm diameter, 1 mm wall thickness). The outer cylinder compartment held the tissue, which was then enclosed in a 2% agarose-water mixture. A dosimetry insert (height 40 radius 30 mm) made of brain equivalent plastic (CIRS, Norfolk, VI, USA) was placed in the central bore of the phantom. The dosimetry insert featured a rectangular cavity holding 36 Gafchromic EBT-XD films (0.26×15×30 mm; T×W×H). (b) Shows the approximate cut through the pig head chosen as heterogeneous sample for the study. (c) Shows the finished phantom, including the brain insert with EBT-XD films, at the DKFZ DECT machine. (d) Presents a SECT HU reconstruction of the phantom (C=0 HU, W=2000 HU). In the image, the pig nose points downwards.

container is shown in Figure 5.42(a). The phantom had a central cylindrical bore of 30 mm diameter for holding a dosimetry insert. A pair of fresh pig head halves was obtained from a local butchery on the day before the measurement. From the half pig heads 40 mm thick slices around the brain cavity were cut out and trimmed to fit the phantom container dimensions. The brain had been removed by the butchery. The schematic position of the slice is shown in Figure 5.42(b). The two slices from the two half heads were placed in the phantom container such that the central bore of the phantom was positioned in the brain cavity of the cranium. The halves were then held in place using a $\sim$2 % agarose water mixture which is similar in HU and RSP to soft tissue (Niebuhr et al. 2019, Volz et al. 2017). Inside the central bore, a 30 mm diameter cylindrical insert was placed which was manufactured by CIRS (Norfolk, Virginia, USA) and made of the same plastic material as the brain of the anthropomorphic head phantoms offered by the company. The insert itself had a rectangular cavity ($\sim$15$\times$15$\times$30 mm^3; T$\times$W$\times$H) for holding 36 Gafchromic®EBT-XD dosimetry films. The films were used for evaluation of the range prediction accuracy from the different imaging modalities which will be detailed in a future work to be brought forward by our group. The final phantom is shown in Figure 5.42(c). A slice through the single-energy x-ray CT of the phantom is shown in Figure 5.42(d).

Reference RSP acquisition the MP1 inserts

To obtain a reference value for the RSP values of the inserts of the MP1, we performed range-shift measurements with a peakfinder (PTW, Freiburg, Germany) and a clinical carbon beam (E=200.3 MeV/u for soft tissues, 250.1 MeV/u for bones; beam width = 6.7 mm and 4.3 mm, respectively). A picture of the setup is shown in 5.41(a). The samples were positioned with a custom 3D printed holder on top of a moving platform. Prior to the measurement, the pencil beam position was determined using Gafchromic®EBT-XD film (seen on the very left in Figure 5.41(a)), and the sample position was adjusted such that the pencil beam center was placed approximately in the center of the cylinders. The moving platform was remotely operated from the control room, accelerating the reference measurement acquisition (Möhler et al. 2018).
The step size of the peakfinder measurement was set to 0.1 mm, interpolation between measurement points was done using a spline interpolation method as suggested in Möhler et al. (2018). From the interpolated peak, the position of the 80% proximal and distal dose were found for all samples and the empty container. The WET of the samples (excluding the container) was calculated as the difference in the positions of the 80% distal dose (R_{80}) of the empty container and the sample

$$\mathrm{WET}_{\mathrm{sample}} = R_{80,\mathrm{emptycontainer}} - R_{80,\mathrm{sample}}. \tag{5.53}$$

The average RSP of each sample was obtained as

$$\mathrm{RSP}_{\mathrm{sample,ref}} = \frac{\mathrm{WET}_{\mathrm{sample}}}{t}, \tag{5.54}$$

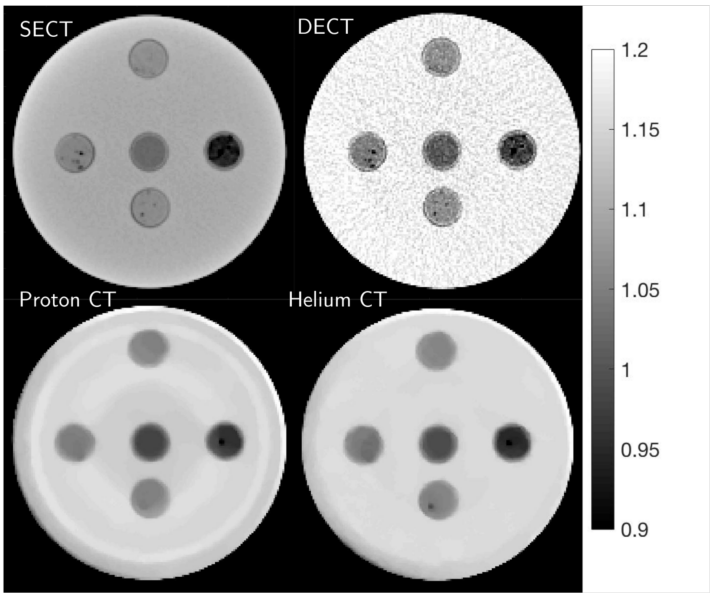

Figure 5.43: Example slice through reconstructions of the MP1 from the different modalities. (a) SECT, (b) DECT, (c) pCT, (d) HeCT. In all cases, the slice thickness was 2 mm, and the pixel size was 0.977 mm.

where t is the sample thickness of 48 mm. The so found average RSP values serve as reference RSPs in this study. Uncertainties for these measurements are calculated by assuming that the increase in range straggling between an empty measurement and a measurement with sample in place is induced by the presence of the RSP heterogeneity within the sample. In this work, we define range straggling as the distance between the distal ($R_{80,\text{distal}}$) and proximal ($R_{80,\text{proximal}}$) 80% fall-off of the Bragg peak. The uncertainty of the reference measurement can hence be approximated as

$$\sigma_{\text{stragg.}} = \frac{(R_{80,\text{distal}}) - (R_{80,\text{proximal}})}{t} \tag{5.55}$$

$$\sigma_{\text{RSP,ref}} = \sigma_{\text{stragg.,empty}} - \sigma_{\text{stragg,sample}} \tag{5.56}$$

Results

Meatphan 1

Figure 5.43 shows the reconstruction of the MP1 from the different photon and particle imaging modalities. The DECT reconstruction shows an increased noise compared to SECT which is related to the lower tube current used per photon energy spectrum for DECT. The pCT and HeCT reconstructions exhibit ring artifacts. These ring artifacts have an amplitude of ∼0.5% in RSP values compared to the mean for HeCT. For pCT, the rings are more pronounced, exceeding 1% in amplitude compared to the mean. A preliminary RSP analysis for the different tissue inserts is shown in Figure 5.44 and given in detail in

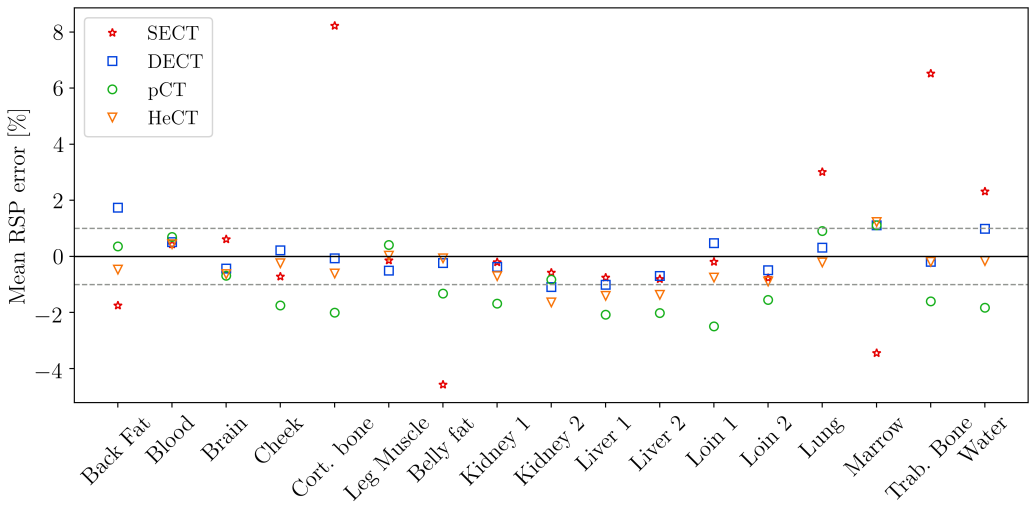

Figure 5.44: Mean RSP accuracy of SECT, DECT, pCT and HeCT for the different tissue samples. The uncertainty bars were omitted for better visibility, but are listed in Table 5.6

Table 5.6. The RSP accuracy was best for DECT, at a mean absolute percentage error (MAPE) of only 0.65%. HeCT performed similar at a MAPE of 0.69%. Due to the systematic uncertainties present in the pCT reconstructions, the pCT RSP accuracy at 1.46% MAPE was significantly lower to what has been reported in the literature with the same detector (compare Giacometti et al. (2017a) and Dedes et al. (2019)). Identifying the reason for these uncertainties is the main subject of the ongoing investigations in this project. Still, despite these uncertainties pCT outperformed SECT for which the MAPE was only 2.19%.

The uncertainty reported with the relative errors for the different CT modalities given in Table 5.6 were defined as percentage ratio between the standard deviation of the reconstructed RSP values in the VOI's and the reference RSP of the sample. The large uncertainties across modalities observed for some samples is likely caused by increased heterogeneity. Overall, DECT and SECT seem to be associated with a larger uncertainty than the values obtained from pCT and HeCT.

Meatphan 2

Figure 2 shows example slices from the SECT, DECT pCT and HeCT reconstruction of the MP2, where SECT and DECT are converted to RSPs as mentioned in section 5.4 and Section 5.4. Visibly, the DECT is more noisy compared to the other imaging modalities as also observed for the MP1. HeCT qualitatively seems to provide a better spatial resolution compared to pCT. However, it is important to mention, that in both cases, the spatial resolution is subject to the total variation superiorization employed in the DROP-TVS algorithm, and

Type	Sample	Reference RSP	SECT	DECT	pCT	HeCT
Muscle	Loin1	1.059 ± 0.004	-0.20 ± 2.14	0.47 ± 3.55	-2.50 ± 0.99	-0.75 ± 1.33
	Loin2	1.064 ± 0.004	-0.77 ± 1.46	-0.49 ± 2.75	-1.55 ± 0.70	-0.89 ± 0.90
	Leg (bov.)	1.049 ± 0.007	-0.14 ± 1.51	-0.50 ± 2.69	0.41 ± 0.60	0.03 ± 0.83
	Cheek	1.054 ± 0.006	-0.72 ± 1.36	0.22 ± 2.89	-1.75 ± 0.79	-0.24 ± 1.00
Adipose	Back fat	0.970 ± 0.008	-1.75 ± 1.79	1.74 ± 3.19	0.36 ± 0.67	-0.4 ± 0.53
	Belly fat	0.997 ± 0.005	-4.57 ± 3.31	-0.24 ± 4.21	-1.32 ± 1.01	-0.07 ± 1.22
Organs	Kidney1	1.050 ± 0.003	-0.20 ± 3.24	-0.37 ± 3.81	-1.69 ± 1.00	-0.70 ± 1.04
	Kidney2	1.040 ± 0.005	-0.58 ± 4.88	-1.09 ± 6.25	-0.83 ± 2.21	-1.64 ± 3.30
	Blood	1.050 ± 0.001	0.43 ± 0.28	0.51 ± 1.94	0.69 ± 0.20	0.43 ± 0.16
	Liver1	1.061 ± 0.004	-0.75 ± 4.59	-1.01 ± 5.21	-2.08 ± 1.11	-1.41 ± 1.36
	Liver2	1.06 ± 0.003	-0.80 ± 6.30	-0.69 ± 6.89	-2.02 ± 4.63	-1.37 ± 5.33
	Lung	0.900 ± 0.040	3.01 ± 10.03	1.11 ± 9.88	1.11 ± 4.56	1.23 ± 5.51
	Brain	1.035 ± 0.002	0.61 ± 0.81	-0.43 ± 2.12	-0.69 ± 0.30	-0.63 ± 0.46
Bones	Cortical (bov.)	1.783 ± 0.027	8.22 ± 4.78	0.07 ± 4.62	-2.00 ± 1.46	-0.60 ± 1.33
	Trabecular	1.194 ± 0.062	6.52 ± 4.05	-0.19 ± 4.10	-1.60 ± 3.08	-0.188 ± 3.43
	Marrow (bov.)	0.932 ± 0.024	-3.44 ± 4.84	1.11 ± 6.05	1.11 ± 2.12	1.23 ± 2.44
Ref.	Water	0.9965 ± 0.0003	2.31 ± 0.31	0.98 ± 2.30	-1.83 ± 0.66	-0.16 ± 0.25
Mean			**0.45**	**0.02**	**−1.02**	**−0.48**
MAPE			**2.19**	**0.65**	**1.46**	**0.69**

Table 5.6: Reference RSP, and relative error of the RSP estimation from SECT, DECT, pCT and HeCT for the different tissue samples investigated in this work. The samples are porcine tissue, or bovine tissue (as indicated).

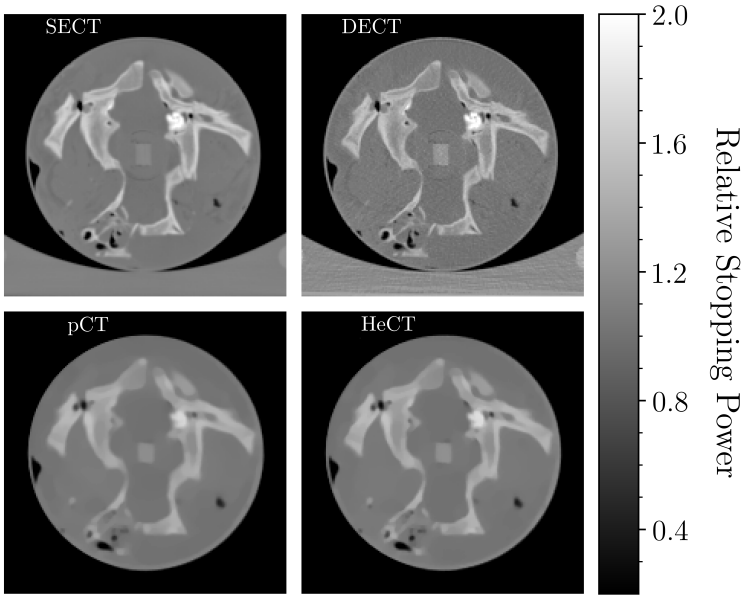

Figure 5.45: Example slice through the reconstructed CT scans of the MP2 from a) SECT, b) DECT, c) pCT and d) HeCT. In all cases, th eslice thickness was 2 mm and the pixel size was 0.977 mm

the number of iterations (8) used to obtain the reconstructions. Direct reconstruction algorithms would enable a more resilient comparison of the spatial resolution between modalities. It also has to be mentioned that the different CTs are not co-registered yet, such that the shown slices do not perfectly match.

Discussion

In this work, the current progress of the analysis of the experimental data acquired with the US pCT collaboration prototype scanner at the HIT facility in the final year of this PhD project was shown. In several beam tests, particle and photon CT scans of different plastic and tissue phantoms were acquired. With these experiments a full experimental comparison between photon and particle imaging modalities in fresh tissue samples has been conducted and in this manuscript preliminary results were provided. In the following the project is briefly discussed.

Particle CT detector calibration

The energy calibration of the detector was based on comparing the peak light output measured in an empty run to pre-calculated values from a Monte Carlo simulation. As this utilized only two calibration points per stage – the second one given by the noise pedestal corresponding to 0 MeV energy – it would require the signal output to be linear over the whole energy range. However, due to the scintillation light quenching (Birk's effect), the energy output is depended on the linear energy transfer (LET) of the particles. As a result of using a single empty run for the calibration, different regions of the particles' depth dose profile are used for the ADC-to-energy calibration of each scintillator stage, i.e. the calibration point is subject to different levels of quenching. This results in different calibrated energy output for each of the stages. This is especially the case for the last detector stage which is the stopping stage of the particles in the empty run and as such, the conversion is most affected by the scintillation light quenching. This could be overcome either by modeling the scintillation light quenching or creating an ADC-to-energy calibration from multiple measurements at different energies — either by setting the beam energy or using the calibration phantom bricks without the wedges to have the beam stop in the different stages. On the other hand, the detector energy output is anyways only used to identify the most probably WET of the particles, and hence an improved ADC-to-energy conversion may not be needed.
The scintillation light quenching is also the reason why the calibration curves for helium ions and protons shown in Figure 5.35 differ significantly. At the same initial range, protons and helium ions traversing the same WET retain approximately the same residual kinetic energy per nucleon, and, hence, the same residual range. As such, the peak energy deposit to the stopping stage normalized to the number of nucleons also should be approximately the same. Therefore, if the energy axis of the calibration curve for protons is multiplied by four, in principle, it should approximate the calibration curve for helium ions. The observed difference in Figure 5.35(c) can be directly attributed to the

larger energy quenching present for helium ions. Similar, the primary proton response pattern in the ΔE-E spectrum for proton runs (Figure 5.37(a)) and the proton fragment response pattern in the ΔE-E spectrum for helium ion runs (Figure 5.37(b)) should be the same, if no energy quenching would be present. However, especially here, the different scintillation light quenching for protons and helium ions results in the proton ΔE-E response to differ between helium ion and proton runs.

In deriving the calibration curves, only particles passing through the slope of the wedge were considered, and particles crossing the flat brick regions were discared. The larger number of particles crossing the flat brick regions compared to the number of particles contained in other thickness intervals otherwise creates issues when finding the most likely WEPL for a given energy, resulting in a step ("kink") in the calibration curves (compare Dickmann et al. (2019)). Instead of finding the most likely WEPL for a given energy, computing the most likely energy for a given WEPL would be more robust against the number of events measured in each WEPL bin. However, the truncation of the energy distribution at stage interfaces of the multistage detector would then need to be considered to avoid a systematic shift in the computed most likely energy. This can be accomplished, for example, by deriving the calibration from the total energy deposit near stage interfaces, instead of the energy output of just the stopping stage.

A misalignment between the trackers and the calibration wedge phantom was observed and caused major artifacts before correction. The origin of this misalignment is not fully understood yet, as both the wedge phantom and the trackers were fixated into position. In case of the wedge phantom, the positioning was performed through small positioning pins on the calibration table which itself was positioned on the optical bench that holds the pre-clinical scanner setup. The trackers were positioned inside the tracker housing with positioning pins, and the housing was also mounted on the optical bench. Correcting for this misalignment, however, was possible by investigating the lateral position of features of the wedge in a plot of the energy profile of the particles. This reduced the amplitude of the ring artifacts in the reconstruction to 0.5% amplitude around the mean for a HeCT reconstruction of a water phantom (results not shown in this work), comparable to what had previously been observed for HeCT with the setup (Volz et al. 2018).

For pCT, despite re-alignment of the wedge phantom in data processing, major rings were present in the reconstructions. These rings exhibited an increased amplitude (exceeding 1% compared to the mean) compared to what has been reported in previous studies with the scanner. Reducing these ring artifacts is the subject of our ongoing investigations in this project. A possible reason for these artifacts could lie in the comparatively high particle rate used for pCT in this work. The particle rate and pencil beam focus are the only conceivable differences compared to previously published studies with the detector (see Dedes et al. (2019)), and therefore main focus of our current investigation.

Scan acquisition time

One important aspect of this study is the overall time necessary for completing a full PCT scan. At the HIT facility, the scan duration was largely dominated by the spill structure, and the fact that we used a step-and-shoot method acquiring a single projection per spill. The spill duration was $\sim$4 s to $\sim$5 s, for helium ions and protons respectively, with a pause between spills of $\sim$4 s. Hence, the PCTs from 180 projections took a minimum of 24 minutes to acquire. Improvement of the scan duration would require to prolong the spill relative to the spill pause and to acquire multiple projections within a single spill. At HIT, a spill of 12 s duration is possible in experimental mode. However, as of now, beam scanning was not available in this mode.

Dose

For the SECT scan, the CTDIvol was reported as 59.76 mGy by the scanner, while for DECT it was reported at 59.65 mGy for the MP1 phantom. To provide an estimate for the dose in the PCT modalities, we conducted a TOPAS simulation utilizing the simulated detector geometry presented in (Piersimoni et al. 2017). In order to estimate the dose to the MP1 phantom, we scored the dose in a PMMA cylinder (density and chemical components as given for PMMA in Piersimoni et al. (2017)) of the same dimension as the MP1, neglecting the different sample inserts. For 2×10^6 initial protons at 200 MeV initial energy irradiated in a homogeneous $100\times200\,\mathrm{mm}^2$ (V$\times$H) field, we find the dose to the phantom to be 8.5 μGy. For helium ions at 200 MeV/u, the dose was found to be 31.98 μGy. For each proton projection, $\sim 6.2\times10^6$ primaries were irradiated as estimated from the trigger rate. Hence, we find the dose per projection to be 26.35 μGy. For helium ions, $\sim 2.8\times10^6$ primaries were irradiated, giving 44.77 μGy. In total, the pCT from 180 projections presented here delivered 4.74 mGy, while the HeCT delivered 8.06 mGy. This is considerably larger than what has been used in previous studies on pCT (Dedes et al. 2019), and is a result of the step-and-shoot operation with a relatively high dose per projection. For pCT the dose could be reduced significantly, if the beam intensity could be lowered further. Similar, for helium ions, Gehrke et al. (2018) have suggested that an equal dose compared to that of protons could result in the same image quality. While in their work, the loss of helium primaries is neglected, the relative fluence loss of protons and helium ions at 200 MeV/u (approximately 50% for helium ions and 25% for protons) can be incorporated into their theoretical considerations. We find that for a homogeneous phantom, a factor $\sim$1.5 higher dose for helium ions (see Chapter 6) would result in the same image noise. For heterogeneous objects, the reduced scattering of helium ions could benefit the mean image noise (compare Dickmann et al. (2019)). The dose to noise ratio will be explicitly studied based on the MP2 in future work.

Reconstruction algorithm

To reconstruct the PCTs in this work, we used the DROP-TVS ordered subset iterative algorithm developed by Penfold et al. (2010). The performance of this iterative algorithm is sensitive to several parameters as outlined in Schultze et al. (2018). These include, the number of optimization blocks used, the relaxation parameter, the superiorization of the total variation, and not least, the total number of iterations. Schultze et al. (2018) note that a large number of iterations leads to the amplification of uncertainties in the image data. That being said, here, we have used the same parameters as in previous studies with the detector (Giacometti et al. 2017b, Piersimoni et al. 2017), including our previous works on helium ion imaging (Piersimoni et al. 2018, Volz et al. 2018). An optimization of the reconstruction parameters for this work is currently ongoing.

Similarly, also for the SECT and DECT reconstruction the outcome is subject to the reconstruction algorithm. The here used H30s reconstruction kernel for SECT and the D34s filtered back projection reconstruction kernel correspond to the standard used with the x-ray CT machine also for patients. In addition, several different methods for RSP reconstruction from the DECT data can be found in the literature. Their respective advantage/disadvantage has been studied in Bär et al. (2017).

Sample preparation and reference measurements

The major difficulty in the preparation of the samples for the MP1 was the tight packing of the tissues in the sample containers. Small air enclosures could not be avoided, and some of the prepared and scanned samples had to be discarded due to large volume air enclosures. We characterized the uncertainty of the reference measurements of the sample RSP through the width of the carbon ion Bragg peak observed for the reference measurements with the PTW peakfinder. Heterogeneity within the samples results in a broadening of the peak due to range mixing, and therefore an increased uncertainty for the sample reference RSP in Table 5.6. Especially for lung, the measured carbon peak was quite broadened compared to the reference measurement due to the large heterogeneity present in the lung tissue. This is also reflected in an increased standard deviation of the RSP measured with the other modalities. In principle, multiple cylinders with the same sample would offer a statistically more significant estimate for the RSP accuracy of the different modalities. However, due to limited beam time, and the need to perform the peakfinder reference measurements, as well as full HeCTs and pCTs in the same night shift together with the corresponding setup change has limited the number of samples that could be scanned in this work.

The MP2 phantom was designed to hold a central dosimetry insert for range verification in a situation that most closely resembles a real patient case, but remains controllable and reproducible. As tissue sample, we chose a pig head as it resembles a human head in tissue composition. Especially, the highly heterogeneous geometry comprising adipose tissue, skin, muscle and bone enabled to investigate the feasibility of resolving small features with the different

modalities. The agarose-water mixture chosen to keep the tissue in place has the benefit of being almost tissue equivalent in both HU (Niebuhr et al. 2016) and RSP (Volz et al. 2017), ensuring the overall clinical relevance of the study. For the in-tissue range reference measurements, we chose Gafchromic® EBT-XD films as the detection method because they are easy to handle, provide a high spatial resolution and have a high saturation dose. However, in principle, the phantom design can also be used for other dosimetry methods, like 3D gel dosimetry or micro-dosimetry based on silicon pixel detectors. Hence, this simple design could prove useful also for other future studies. In a follow up work by our group, the range prediction with the different CT modalities for the MP2 will be compared against the reference acquired with the Grafchromic® EBT-XD films for a proton pencil beam stopping in the dosimetry insert inside the phantom. This will provide a first estimate of the range accuracy achievable with pCT and HeCT in heterogeneous samples.

Comparison between modalities

In this work, we have taken the data for the first-ever comparison between SECT, DECT, pCT and HeCT in fresh animal tissue samples. As of now, the RSP accuracy was similar for DECT (MAPE of 0.65%) and HeCT (MAPE of 0.69%). Due to elevated ring artifacts compared to what has previously been demonstrated with the detector (Dedes et al. 2019), in this work, pCT yielded a substantially lower RSP accuracy than HeCT and DECT with a MAPE of 1.46%. Both pCT and HeCT showed a bias towards underestimated RSPs with the mean RSP error being -1.02% and -0.48%, respectively. SECT returned the overall lowest accuracy, at a MAPE of 2.19% and also exhibited an overestimation bias at a mean error of 0.45%. Noteworthy, the uncertainty of the RSP accuracy was increased for the photon modalities, especially DECT, compared to the PCT modalities. At the same time, the spatial resolution of the PCT modalities is visibly lower than that of the x-ray modalities. However, it has yet to be determined how much this result is influenced by the choice of reconstruction parameters for PCT.

As the outcome of the RSP accuracy for the PCT modalities depends on the parameters of the iterative algorithm, we currently investigate the optimal imaging parameters for our study. In addition, it would be interesting to reconstruct the images from DROP without TVS, or from a direct reconstruction algorithm, for example the distance-driven-binning developed by Rit et al. (2013). The letter would enable to draw conclusions that are more dominated by the underlying data, rather than parameters set in the iterative reconstruction. Moreover, the pCT images currently suffer from increased ring artifacts the origin of which has yet to be determined. As these artifacts are larger compared to those observed with the scanner at the Chicago Proton Center (Dedes et al. 2019), they might stem from the higher beam intensity at the HIT facility. Our current efforts focus on improving the image quality for the acquired pCT scans. As such, the results presented in this work are preliminary and subject to further improvements.

Conclusion

In this work, the first-ever comparison of SECT, DECT pCT and HeCT based RSP estimation in fresh animal tissue samples has been performed. Preliminary results indicate a similar RSP accuracy for HeCT and DECT. As of now, pCTs acquired at the HIT facility suffer from greatly increased ring artifacts compared to previously published studies with the detector. Despite the comparatively low accuracy of the pCT scans presented here, both pCT and HeCT greatly outperformed SECT in terms of RSP accuracy. In terms of noise, pCT and HeCT seem to outperform DECT and SECT, albeit a more in depth investigation is needed in regards of the contribution of the PCT reconstruction algorithm chosen. HeCT offered a qualitatively improved spatial resolution over pCT, however, for both modalities it was visibly lower than that of DECT and SECT. HeCT. Optimization of the reconstruction parameters in the iterative algorithm used for the PCTs reconstructions is ongoing and expected to improve the image quality of pCT and HeCT. After optimization of the image reconstruction algorithm, range information recorded for a proton beam with Gafchromic® EBT-XD films placed in the center of the MP2 will enable to compare the range accuracy achievable with the different modalities.

5.5 P.VII: Using helium ion imaging as on-line monitor

Title : Experimental exploration of a mixed helium/carbon beam for online range monitoring inn carbon ion-beam therapy

Authors : L. Volz, L. Kelleter, S. Brons, L. Burigo, C. Graeff, N. Niebuhr, R. Radogna, S. Scheloske, C. Schömers, S. Jolly and J. Seco

Status : Published

Journal : Physics in Medicine and Biology

DOI : doi.org/10.1088/1361-6560/ab6e52

Contributions : The principal author of this work, LV conceptualized the project and prepared the experiments under the supervising guidance of JS. This included prior tests at the DKFZ x-ray CT machine on the use of a rectal balloon in the pelvis phantoms, generation of carbon ion beam treatment plans, selection of interesting scenarios and water equivalent thickness reference measurements for the used PMMA degraders. LV implemented/conducted all simulations presented in this work with additional support from LB on the realistic implementation of the beam nozzle. LK, RR and SJ provided the detector used for the experiments. LV, LK, RR, SJ and NN directly participated in the experiments and significantly contributed to the finalization of the measurement plan. LK operated the detector during the experiment campaigns and conducted the calibration and processing of the measured data. This included the determination of the scintillator quenching factor which was crucial to ensure the accuracy of the simulation. NN contributed to the handling of the pelvis phantoms prior and during experiments. CS and SS prepared the experimental high energy helium ion accelerator settings, and together with SB provided technical support regarding the HIT accelerator complex. CG provided the initial idea for the helium/carbon mixing and aided in valuable discussions on its clinical relevance. JS and SJ ensured the scientific rigor of the study and coordinated the project between the institutions. LV produced and finalized the plots shown in the manuscript. LV and LK equally shared writing the manuscript and elaboration of the acquired results. The contribution by LK is acknowledged in a shared first author position on the manuscript.

Abstract

Recently, it has been proposed that a mixed helium/carbon beam could be used for online monitoring in carbon ion beam therapy. Fully stripped, the two ion species exhibit approximately the same mass/charge ratio and hence could potentially be accelerated simultaneously in a synchrotron to the same energy per nucleon. At the same energy per nucleon, helium ions have about three times the range of carbon ions, which could allow for simultaneous use of the carbon ion beam for treatment and the helium ion beam for imaging. In this work, measurements and simulations of PMMA phantoms as well as anthropomorphic phantoms irradiated sequentially with a helium ion and a carbon ion beam at equal energy per nucleon are presented. The range of the primary helium ion beam and the fragment tail of the carbon ion beam exiting the phantoms were detected using a novel range telescope made of thin plastic scintillator sheets read out by a flat-panel CMOS sensor. A 10:1 carbon to helium mixing ratio is used, generating a helium signal well above the carbon fragment background while adding little to the dose delivered to the patient. The range modulation of a narrow air gap of 1 mm thickness in the PMMA phantom that affects less than a quarter of the particles in a pencil beam were detected, demonstrating the achievable relative sensitivity of the presented method. Using two anthropomorphic pelvis phantoms it is shown that small rotations of the phantom as well as simulated bowel gas movements cause detectable changes in the helium/carbon beam exiting the phantom. The future prospects and limitations of the helium-carbon mixing as well as its technical feasibility are discussed.

Introduction

The advantage of carbon-beam therapy over conventional photon radiotherapy lies in the ion's highly localised depth-dose deposition, with a low entrance dose increasing to a maximum — the Bragg peak — beyond which there is a sharp reduction in dose deposition. However, the steep dose gradient at the end of the particle range in matter makes ion beam therapy sensitive to range uncertainties arising, for example, from inter- and intra-fractional anatomical changes, uncertainties at the treatment planning stage as well as the patient setup. In current clinical practice, range uncertainties are accounted for by adding safety margins around the tumour volume (Paganetti 2012) and by avoiding beam directions corresponding to the ions stopping directly in front of an organ at risk (OAR). However, even with safety margins, intra-fractional motion can lead to severe target dose deterioration and/or overdosage of healthy tissue (Bert et al. 2008, Seco et al. 2009, Dolde et al. 2018).
In order to exploit the full potential of ion beam radiotherapy, therefore, improved methods for inter- and intra-fractional treatment verification are needed. Several methods for treatment verification have been proposed of which prompt gamma imaging (Hueso-González et al. 2018) and in-beam PET imaging (Ferrero

et al. 2018) are promising candidates. A detailed overview can be found in Parodi & Polf (2018a).

Recently, it has been proposed that a small percentage of helium ions could be added to a carbon ion treatment beam for online treatment monitoring (Graeff et al. 2018, Mazzucconi et al. 2018). The approximately equal mass / charge ratio of fully stripped helium and carbon ions (relative difference $\approx 0.065\,\%$), could enable their simultaneous acceleration in a synchrotron accelerator to the same velocity (same energy per nucleon). Due to the helium ions' $\sim$3 times larger range compared to that of carbon ions at the same velocity, treatment with a carbon ion beam and simultaneous treatment monitoring with helium ions could be possible. In fact, the similarity in accelerator settings for the delivery of a mixed helium/carbon beam ($^{12}C^{4+}$ with $^{3}He^{+}$) has been reported already in Kanai et al. (1997) for a cyclotron facility for the purpose of treatment with beams of mixed relative biological effectiveness (RBE) but without consideration for online treatment monitoring. Recently, Graeff et al. (2018) have shown the potential of using a mixed helium/carbon beam as a range probe for carbon ion treatment investigating lung patient cases using based on 4D treatment planning. Assuming a fixed helium contamination in the primary carbon ion beam during the plan optimisation, they showed that the additional RBE dose stemming from a 10 % helium contamination in the primary beam would make up less than 0.5 % of the target RBE dose. This stems from the physical dose difference between the plateau region of the helium ion depth dose profile and the carbon Bragg peak, as well as the difference in RBE. Moreover, the dose deposited in the patient distal to the tumor stemming from the additional helium contamination was also smaller compared to that deposited by the carbon fragments. The idea of a mixed beam for treatment monitoring was first explored experimentally in the study presented recently by Mazzucconi et al. (2018). In their proof-of-concept work, they demonstrated that for a 10 % mix of helium ions in the carbon beam, the helium residual range could be detected in a scintillation detector despite the signal contamination with carbon fragments. However, all experimental tests presented were conducted using protons in place of helium ions and no anthropomorphic cases were investigated.

The aim of this work was therefore to experimentally corroborate the results by Graeff et al. (2018) and Mazzucconi et al. (2018) using sequentially irradiated beams of helium and carbon ions at the Heidelberg Ion-Beam Therapy Centre (HIT). The beam was monitored using a novel range telescope developed at University College London (UCL). First, the system's sensitivity was assessed with simple PMMA degraders with differently sized air gaps. For assessing more clinically relevant scenarios, prostate cancer treatments were investigated. With the ADAM pelvis phantom (Niebuhr et al. 2019), the feasibility of using a mixed helium/carbon beam to detect rectal gassing/bowel gas movements was investigated. The recently developed ADAM-PETer pelvis phantom (Homolka et al. 2019) was used to simulate small patient rotations. The acquired data allow to draw conclusions on the clinical application and the limitations of the helium/carbon beam mixing method.

Materials and Methods

Range telescope

The range of the primary helium ions and the fragments produced by the carbon ion beam were monitored using a novel range telescope developed at UCL for proton range quality assurance. This detector will be detailed in a separate publication currently under preparation. The prototype detector consisted of a stack of 49 polystyrene-based plastic scintillator sheets of 2-3 mm thickness, covered an area of $10\times10\,cm^2$, and had a relative stopping power (RSP) of 1.025. The detector covered a total water equivalent thickness (WET) range of $\sim$127 mm. Each sheet was painted black in order to avoid light contamination into neighbouring sheets. The resulting thickness of paint was taken into account in the calculation of the absolute WET.

A large-area CMOS sensor with an active area of $150\times100\,mm^2$ and a pixel size of 100 µm was used for the readout of the scintillation light. The detector readout frame rate was 25 Hz (40 ms exposure time). The detector was placed in a light-tight enclosure with two beam entrance/exit windows made of aluminum coated Mylar polyester foil on both ends of the scintillator stack.
Before the measurements, the detector was calibrated by shooting high-energy beams of carbon ions (E=430 MeV/u) as well as helium ions (E=220 MeV/u) through the scintillator stack from both sides of the detector. In data processing, these shoot-through measurements were then used to correct for non-uniformity in the light output of each individual detector sheet for each ion species. Additionally, a background measurement was acquired to determine the signal in the absence of scintillation light.

It is important to note that the range telescope measures scintillation light and not dose. The plastic scintillator used in the range telescope exhibits quenching effects that can be described by Birks' law (Birks 1951). The measured depth-light curves presented in this work were not corrected for quenching: however, the simulated energy deposits were converted to depth-light curves using Birks' law (see section 5.5). Additionally, the measured light output of the detector depends on the lateral position at which the beam enters the detector. In this work, the detector position relative to the beam was not changed between measurements.

Investigated phantoms

Three different phantom setups were investigated in this study. The sensitivity and limitation of the method was assessed quantitatively using simple PMMA phantoms. For qualitatively investigating the use of a mixed helium/carbon beam in clinically relevant scenarios, different motion scenarios were explored using two anthropomorphic phantoms. Treatment planning X-ray CT scans of the anthropomorphic phantoms were acquired at the Siemens Somatom Definition Flash scanner of the German Cancer Research Centre (DKFZ, Heidelberg).

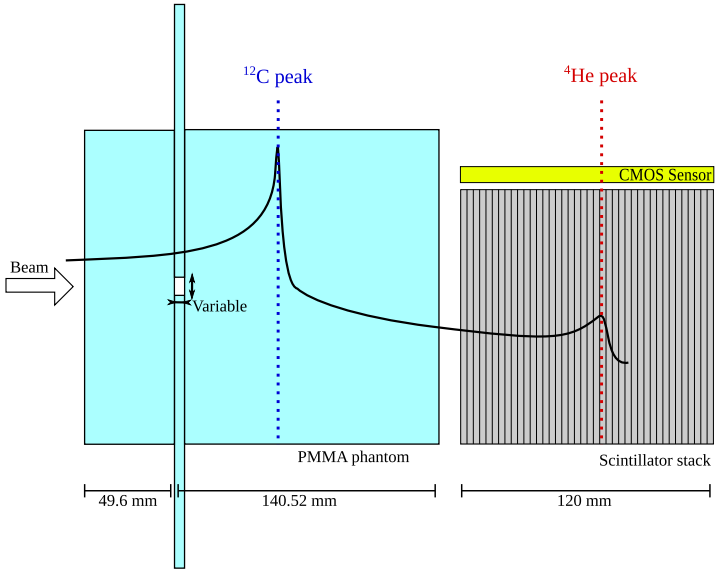

Figure 5.46: Schematic depiction of the PMMA setup used to investigate the sensitivity of the helium/carbon beam mixing method (not to scale). The total thickness of the PMMA setup was 190.12 mm (219.59 mm WET), the PMMA blocks had a width and height of 150 mm. Two PMMA slabs of equal thickness were used to create a vertical slit of variable width/thickness at a depth of 49.6 mm in the setup. For the investigated energy in this work, the carbon peak was located at a water equivalent depth of ∼99 mm, with the helium peak was located at 305 mm water equivalent depth.

PMMA phantom: First, several PMMA slabs were arranged upstream of the range telescope to quantify the sensitivity of the method in a controlled setting. Accurate WET values for each of the slabs were available from PTW Peakfinder measurements (Arico 2016). In order to create a range shift in the beam, two thin PMMA slabs of similar WET were placed at a depth of 49.6 mm PMMA (57.64 mm WET) such that they formed a vertical slit of adjustable opening width (2-5 mm). Different PMMA slabs were used to create variable gap thicknesses (1-5 mm). The total WET of the setup (without gap) was 219.59 mm for all measurements. The schematic setup is shown in figure 5.46.

ADAM phantom: The ADAM (Anthropomorphic Deformable And Multimodal) Pelvis Phantom (Niebuhr et al. 2019) was used to demonstrate the effect of rectal gassing/bowel gas movements on the helium range. The phantom consists of various tissue equivalent materials enclosed in an elliptical PMMA container (370 mm major, 220 mm minor axis) and closely models the anatomical structure of a male pelvis. The phantom features a fully deformable and movable prostate, an inflatable rectum and a deformable bladder, as well as the pelvic bone structures. To simulate rectal gassing/bowel gas movements, a rectal balloon was inserted into the phantom's rectum such that the

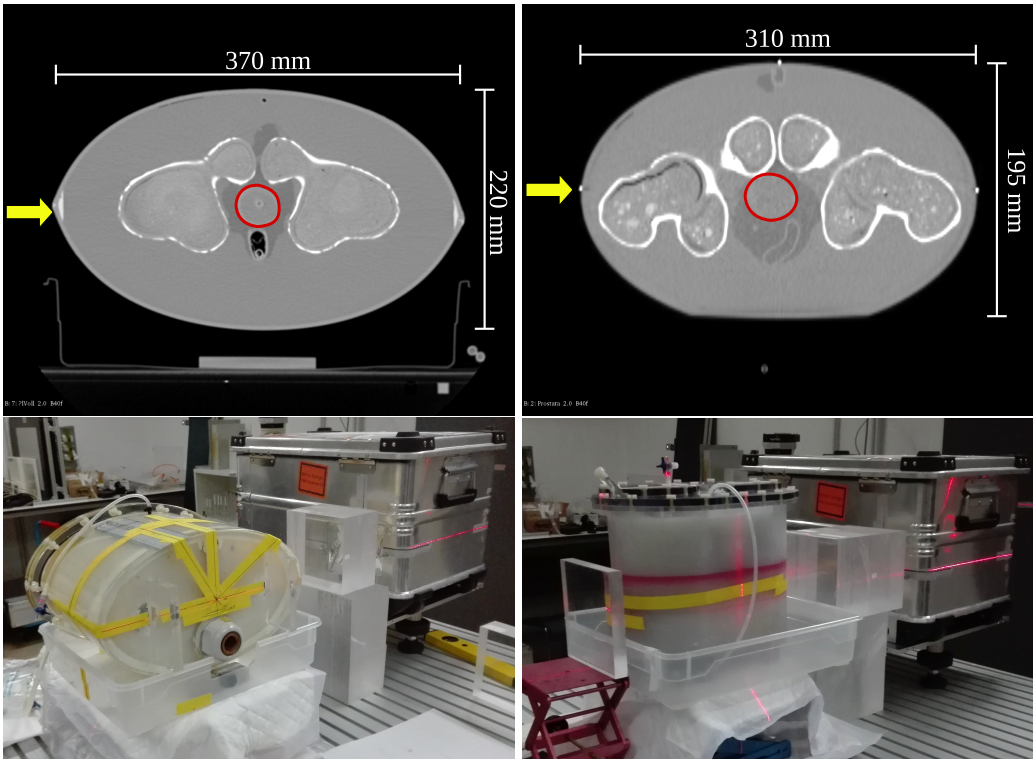

(a) (b)

Figure 5.47: Isocentrical axial slice through CT images of the used phantoms (top), and photographs of the experimental setup (bottom): a) ADAM phantom and b) ADAM-PETer phantom. The area outlined in red on the CT scans marks the target (prostate), the yellow arrow indicates the beam direction.

balloon was located next to the prostate. The balloon was inflated to air volumes of 30 ml, 45 ml and 60 ml. The uncertainty on the air volume was estimated to be ∼5 ml from the retained air volume after irradiation. Liquid fillings were not yet possible with the phantom and the rectum was not collapsed when the rectal balloon was not inflated, but retained a residual volume.

ADAM-PETer phantom: In order to investigate the effect of patient rotations, the recently developed second generation of the ADAM phantom, named ADAM-PETer (Homolka et al. 2019), was used. Compared to the ADAM phantom, the ADAM-PETer phantom has a smaller container (310 mm major, 195 mm minor axis), denser and more realistic bone structures as well as a 3D printed prostate. The reason for using both available ADAM phantoms in this study resides in their respective advantages/disadvantages. The ADAM phantom hull was made from two separate PMMA pieces that are glued together on both lateral sides (see figure 5.47). Additionally, the thickness gradient of the ADAM phantom hull is larger compared to that of the newer ADAM-PETer phantom. Hence, for investigation of patient rotations/motion, observed effects could stem from the glue or the phantom shape, rather than anatomical features which would not resemble a realistic scenario. However,

Phantom	Gantry Angle (°)	Min. E (MeV/u)	Max. E (MeV/u)
ADAM	[90, -90]	300	355
ADAM-PETer	[90, -90]	260	316

Table 5.7: Treatment plan minimum and maximum energies for the different phantoms. The 0° gantry angle refers to a vertical beam direction.

Setup	Energy (MeV/u)		Focus (mm)		Intensity (part./s)	
	^{12}C	^{4}He	^{12}C	^{4}He	^{12}C	^{4}He
PMMA phantom	219.8	220.5	8.5	8.1	8×10^{7}	8×10^{7}
ADAM/ADAM-PETer	324.26	324.26	8.0	7.0	8×10^{7}	7×10^{8}

Table 5.8: Beam settings for the different experimental setups investigated in this work. The beam focus is given as the beam FWHM at the isocentre.

the available version of the ADAM-PETer phantom did not feature a fully deformable/movable prostate and rectum, which would have been unfavourable for the investigation of rectal gassing.

Treatment planning: For the anthropomorphic pelvis phantoms, treatment plans were generated using the MatRad open source treatment planning platform (Wieser et al. 2017). A dose of 2 Gy RBE per fraction was planned for the target (whole prostate). The spot spacing was set to 3 mm. No OARs were considered and no margins were set around the target volume. The additional dose from the helium beam was not considered in the treatment optimization. The minimum and maximum beam energy in the plan as well as planned beam angles are listed in table 5.7. The prostate was positioned in the beam isocentre in all cases.

Beam settings

Experiments were conducted at the HIT experimental room (Haberer et al. 2004). Since a real mixed beam could not yet be delivered, the experiments were conducted with sequentially irradiated helium and carbon ion beams of similar energy/nucleon and similar spot size. The measurements from the sequentially irradiated beams were mixed offline which will be detailed in section 5.5. The generation of a mixed beam will be discussed in section 5.5. For all measurements, a 3 mm ripple filter was used following the common practice with carbon ion treatments at HIT. The detailed beam settings for the respective phantom setups are listed in table 5.8. The generation of a real mixed beam is further discussed in section 5.5.

Energies up to ∼220 MeV/u were available for both carbon and helium ions from the standard libraries of beam characteristics used at HIT (Kleffner et al. 2009). As no perfect match between helium and carbon ion beam settings

existed in these tables, the closest representation was chosen for the PMMA measurements. The highest clinically available beam intensity of 8×10^7 particles/second for carbon ions would — assuming a constant ratio of 10:1 between primary carbon and helium ions — correspond to an intensity of 8×10^6 particles/second for helium ions in the mixed beam. This is lower than the lowest helium intensity available from the standard settings. Since the runs were mixed off-line in data processing, the same intensity was therefore chosen for both ion types. The impact of this is discussed in section 5.5.
Due to the high carbon beam energy required for the treatment of the prostate targets within the pelvis phantoms, a helium beam with manual settings had to be used, since the corresponding high helium energies are not available from the standard beam libraries at HIT which cover a maximum range in water of 30 cm for the different ion species. However, since the HIT synchrotron was designed for the acceleration of carbon ions up to 430 MeV/u, the synchrotron has the potential to accelerate helium ions (and protons) to higher energies than those used clinically. Helium ion beams, with higher energies than needed for therapy, have recently been established at HIT in a preliminary version, for a few energies only and without scanning capability or position and intensity control. In this work, a helium beam at 326 MeV/u was used, with an intensity of 7×10^8 particles/second and a beam focus of 7 mm FWHM.

For the ADAM-PETer phantom, a 20 mm PMMA slab was added before the setup, as the available high helium energy would have been above the energies set by the treatment plan. With the PMMA slab, the beam energy was reduced to $\sim$303 MeV/u for carbon ions (value obtained from the simulation described below), corresponding to the high energy part of the respective treatment plan.

Monte Carlo simulation

In order to validate the acquired measurements and to further exploit the potential of the helium/carbon beam mixing technique, Monte Carlo simulations using Geant4 version 10.05.0 (Agostinelli et al. 2003, Allison et al. 2006, Allison et al. 2016) were conducted. In detail, the following physics lists were activated: G4DecayPhysics, G4StoppingPhysics for nuclear capture at rest, G4EmExtraPhysics and G4EmStandardPhysics_option4 for accurate modelling of low energy electromagnetic interactions, G4HadronElasticPhysics for modelling of elastic nuclear interactions. To model inelastic nuclear interactions the G4QMDReaction model was chosen for carbon ions as recommended by Böhlen et al. (2010) and Dudouet et al. (2014). For helium ions, G4BinaryLightIonReaction was activated together with the Tripathi cross section data (Tripathi et al. 1996) recently tuned by Horst et al. (2019) to accurately model the helium Bragg peak. The default production cuts (affecting electrons and photons) were set in the simulation to 1 mm. Within the range telescope a finer step limit and finer production cuts (both 0.05 mm) were set.

The helium and carbon energy spectra after the 3 mm ripple filter were modelled from the generic beam line presented in Wieser et al. (2017). The beam monitoring chambers were modelled in the generic beam line using a

water slab of 2.03 mm thickness. The distance between nozzle and isocentre was 1.02 m (air, RSP=0.001). Therefore, the WET the beam crossed before reaching the isocentre was 3.05 mm. The lateral beam profile was modelled with a 2D Gaussian spatial distribution with the FWHM set in the experiments. The initial beam divergence was neglected in the simulation.

The detector was modelled as a single $100 \times 100 \times 120\,\mathrm{mm}^3$ block of polystyrene using the polystyrene material composition from the NIST database (Berger et al. 2005) and modifying the density to match the known RSP of 1.025. Within the simulation, the energy deposit in the detector was binned along the condensed-history steps into a histogram for which the bins corresponded to the sheets of the prototype[3]. In order to accurately model the light output of the experimental measurement, the scintillation light quenching has been approximated using Birks' law (Birks 1951). The scintillation light output S is given as:

$$S \propto \int \frac{\mathrm{d}E/\mathrm{d}x}{1 + kB\mathrm{d}E/\mathrm{d}x}\mathrm{d}x \tag{5.57}$$

where Birks' constant was determined as $kB = 0.075 \pm 0.01\,\mathrm{mm/MeV}$ by comparing proton beam measurements with the detector and HIT base data proton depth dose curves (unpublished data). To accurately model the detector response across the transverse plane, S would need to be scaled by the scintillation light yield of the detector and an additional correction factor accounting for spatial variations in the detector response. The additional scaling factors that describe the light output of the detector are omitted here, as the signals were normalised in data processing.

The PMMA degrader slabs were simulated using the NIST PMMA material composition, setting the density such that the WET of the simulated slabs matched the WET of the experimental slabs. For the anthropomorphic phantoms, voxelised digital geometries were created from the treatment planning X-ray-CT scans. The phantom materials were implemented from their chemical composition using the material description in Niebuhr et al. (2019) and Niebuhr et al. (2016). See table 5.9 for a detailed list. First, for each Hounsfield unit (HU) in the CT scan, a material was assigned based on the thresholds listed in table 5.9. Then the relative electron density corresponding to the HU was calculated from the HU lookup table of the CT scanner used to produce the treatment planning CTs. The relative electron density was converted to physical density following equation 1 in Collins-Fekete et al. (2017a). This was then used to assign a material and density to each voxel of the CT scan. For all voxels with a HU below -160 the assigned material was air at density $1.155\,\mathrm{mg/cm}^3$.

For the anthropomorphic phantoms, additionally the dose deposit in each voxel was recorded in the simulation. The dose in lateral direction was then summed up to display the integral dose to the patient as function of the distance to the isocentre.

[3]The prototype features 2 mm, 2.6 mm as well as 3 mm sheets. In the simulation, a constant binning of 3 mm was used.

Material	HU	Element(weight(%))	Tissue
Peanut oil	-160	H(7.36);C(58.94);N(20.62);O(13.08)	Adipose
Agarose1	-30	H(10.57);C(0.94);O(84.49);Na(2.19);F(1.81)	Muscle
Agarose3	35	H(10.82);C(1.65);O(86.53);Na(0.55);F(0.45)	Prostate
Vaseline/ K_2HPO_4	80	H(5.52);C(64.6);N(5.02);O(9.19);P(4.45);K(11.22)	Inner bone
Gypsum	285	O(47.01);Ca(29.44);S(23.55)	Cortical bone

Table 5.9: Chemical composition of the different materials used the anthropomorphic phantoms as implemented in the simulation. The HUs mark the lower-bound thresholds used for assigning a given material to voxel in the CT scans. The corresponding modelled patient tissue is given for each material.

All simulation results shown in this work were generated using 10^6 primary carbon ions and 10^5 primary helium ions.

Data processing and offline beam mixing

In the experiment, helium and carbon beams were irradiated consecutively. The experimental results shown in this work always represent a "snapshot" of the beam: i.e. the sum of twenty-one image frames corresponding to a total acquisition time of 0.84 seconds. Depth-light curves were generated from the background-corrected images by summing up the light yield in a scintillator sheet and attributing it to the WET at the centre of the sheet. The light yield is calibrated with two shoot-through curves of the same ion taken from both sides of the range telescope in order to correct for the differences in the signal of the scintillator sheets. The depth-light curves of the helium and carbon beams were scaled according to a 10:1 carbon:helium ratio and summed up in order to produce the signal of a mixed beam. In the simulation, the recorded signals were simply summed as a factor 10 smaller number helium primaries compared to carbon had already been generated. Figure 5.48 shows the resulting depth-light curves of helium, carbon and the mixed helium/carbon beam. The curves were normalized to the combined helium/carbon signal in the first scintillator sheet. Small differences are due to the fluctuations in the measured carbon signal in the first couple of scintillator sheets.

Results

In this section, the results from the irradiation of the phantoms introduced in section 5.5 are presented. Both measurement and simulation results are presented side by side for comparison. The relative difference between the curve of interest $f(x)$ and a reference curve $g_{\text{ref}}(x)$ was chosen as a metric to quantify the change in the measured signal. It is defined as $[f(x) - g_{\text{ref}}(x)]/g_{\text{ref}}(x)$. This enables displaying very small differences between the curve of interest and the reference curve, emphasising the sensitivity of the helium/carbon beam mixing. In all plots, the horizontal axis represents the residual water equivalent

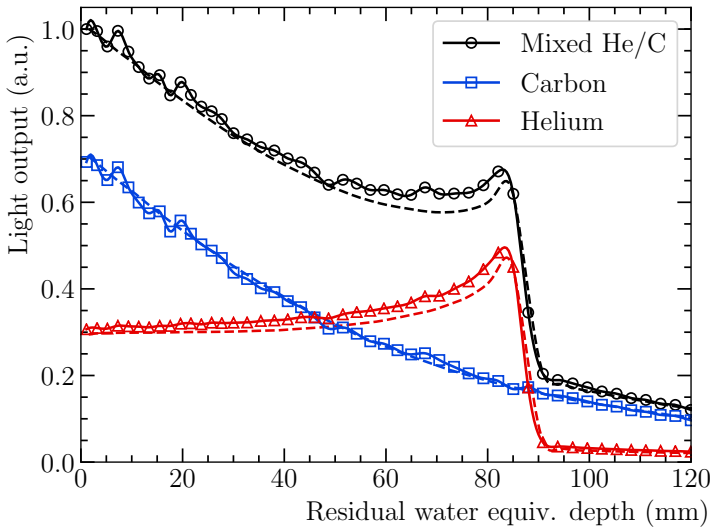

Figure 5.48: Example of helium (red) and carbon (blue) depth-light curves used for off-line helium-carbon beam mixing (black) at 220 MeV/u and the PMMA setup without gap: measurement (solid) and simulation (dashed). The measured signal for helium was scaled down to match a 10:1 ratio to the carbon primaries.

range of the beam measured in the scintillator stack. The depth-light curves were normalised to the signal in the first scintillator sheet of the reference measurement in order to enable easier comparison between experiment and simulation.

PMMA phantom

In figure 5.49, the effect of air slits of variable width and thickness are shown. The 5 mm and 2 mm slit widths resulted in respective relative differences of 40% and 17%. This is expected since, with increasing slit width, a larger fraction of beam particles crosses the slit. For the 8 mm FWHM beam, approximately 55% of the beam particles cross the slit opened to 5 mm width, while only ∼22% of particles traverse the slit in the case of an opening width of 2 mm.

It can be seen in figure 5.49 (bottom) that the observed peak width in the relative difference is proportional to the slit thickness. However, this relation is perturbed by the finite slope of the helium peak and the limited spatial resolution of the range telescope. In all cases, the mixed depth-light curve changed only slightly with the introduction of the air gaps and those changes were only observable in the high-gradient region at the helium peak. In the case of a 1 mm thick, 2 mm wide slit the resulting maximum relative difference was 8%.

ADAM phantom

The ADAM phantom was irradiated at three different spots in the same isoenergy layer: the tumour isocentre, a spot close to the rectum according to the treatment planning system (vertical position: isocentre-18 mm; horizontal

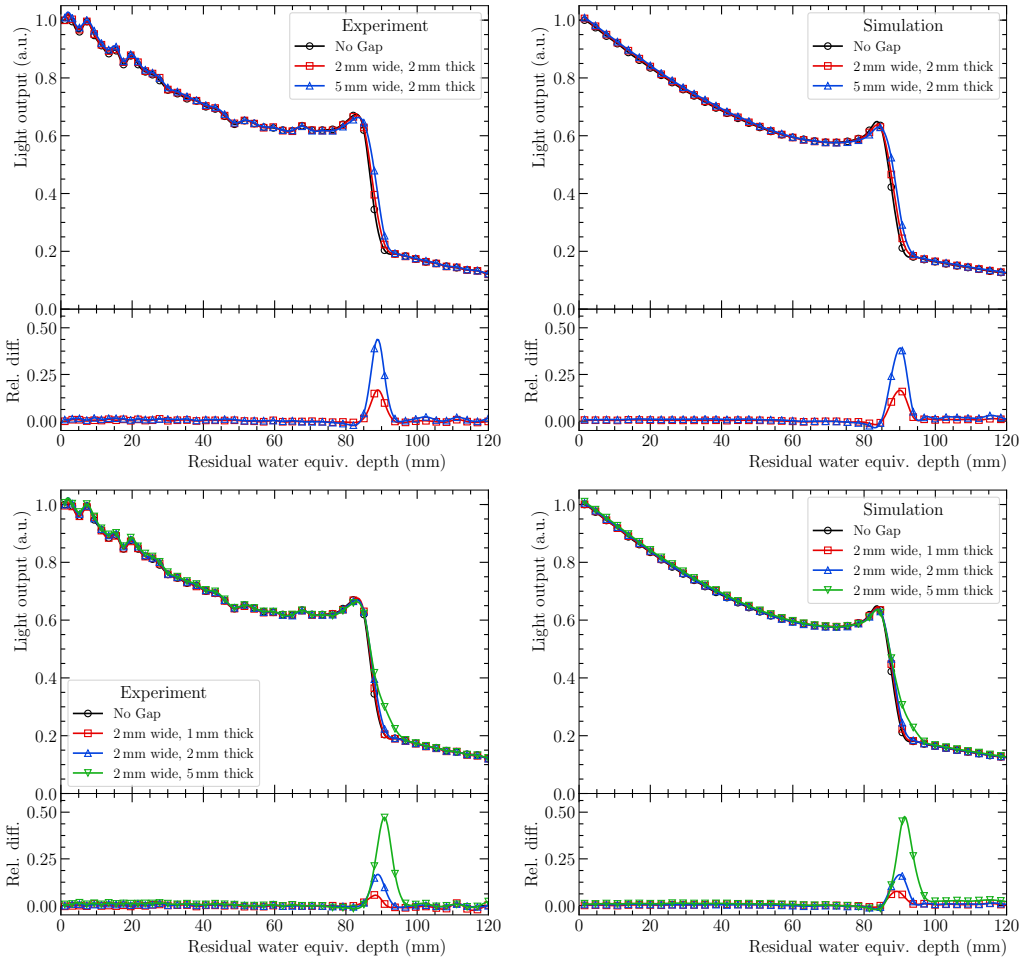

Figure 5.49: Result of introducing an air-filled slit of width 2 to 5 mm and thicknesses of 2 mm and 5 mm (top), as well as a fixed width of 2 mm and thickness of 1 mm to 5 mm (bottom) in the beam path: measurement (left) and simulation (right).

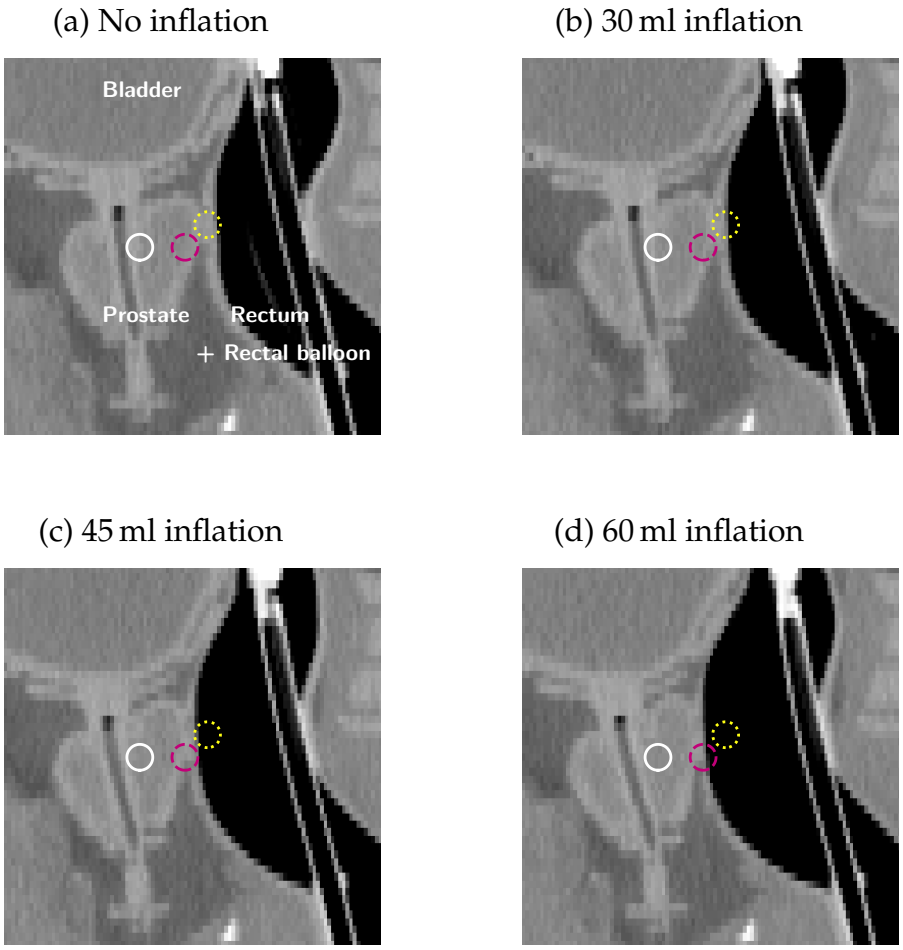

Figure 5.50: Sagittal plane of the ADAM phantom CT scans for different stages of inflation of the rectal balloon. The circles indicate the 2σ region of the irradiated carbon ion beam spots at the isocentre (white solid), close to the rectum (yellow dotted) and in between (magenta dashed).

position: isocentre+6 mm) and a spot in between the two (vertical position: isocentre-12 mm; horizontal position: isocentre). The spot positions and the different rectal fillings are shown in figure 5.50.

Figure 5.51 shows the artificially mixed helium/carbon signals. For the spot close to the rectum, a change in the helium range was observable even for the smallest air volume filled in the rectal balloon. Since the rectum did not collapse when the rectal balloon was not inflated, the lowest filling of the rectal balloon resulted only in a small change of the diameter of the rectum compared to the reference state. For larger fillings of the rectum, a drastic overshoot was observed in the helium range as the beam crossed into the rectum and the rectal gas. Similarly, for the spot located between isocentre and the rectal wall, the two larger rectal balloon fillings resulted in observable changes in the helium signal. For the spot in the isocentre, no significant change was observed for either air filling in the measurement. In the simulation, however, small changes

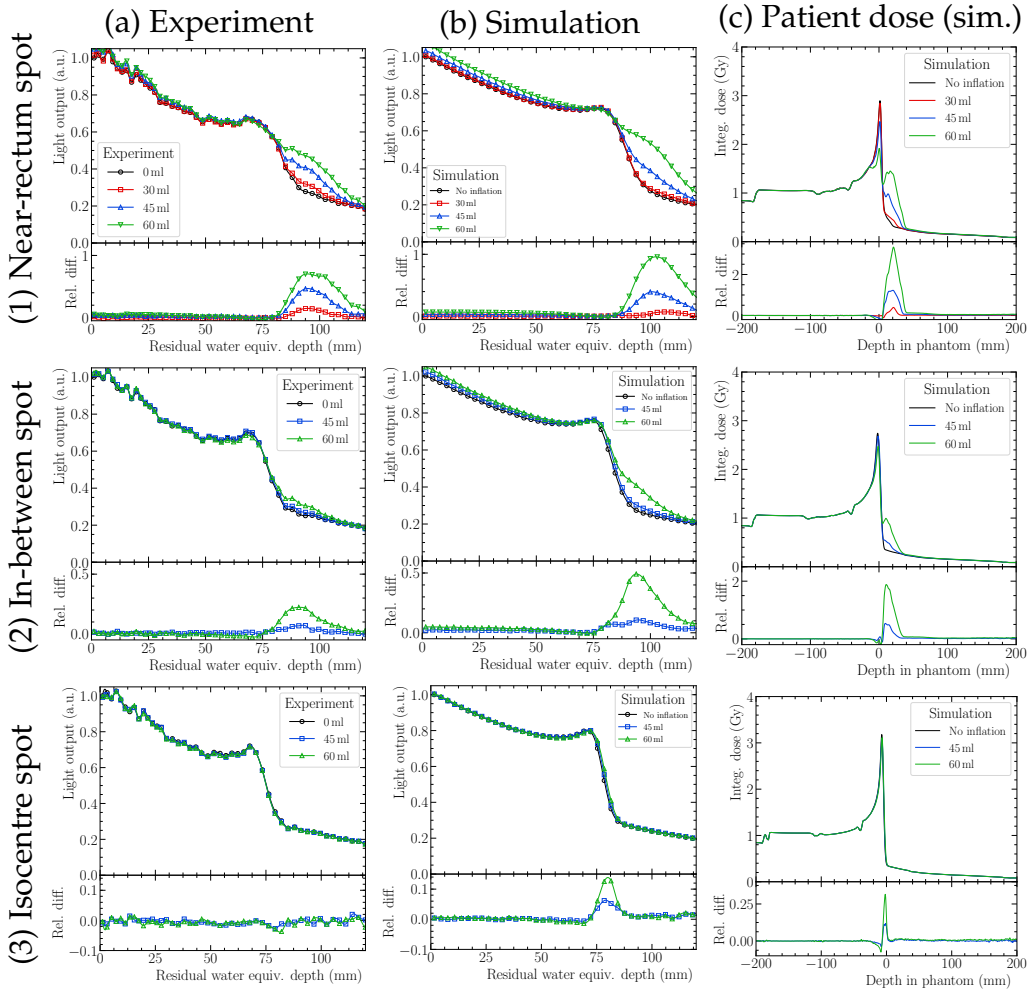

Figure 5.51: Detector response to different inflation stages of a rectal balloon placed in the rectum near the prostate for different beam spot positions: measured (left column) and simulated (middle column) helium/carbon beam signal in the detector. For comparison, the integrated dose to the phantom as a function of distance to the isocentre (right column) is shown. The dose considers both the helium and carbon beams.

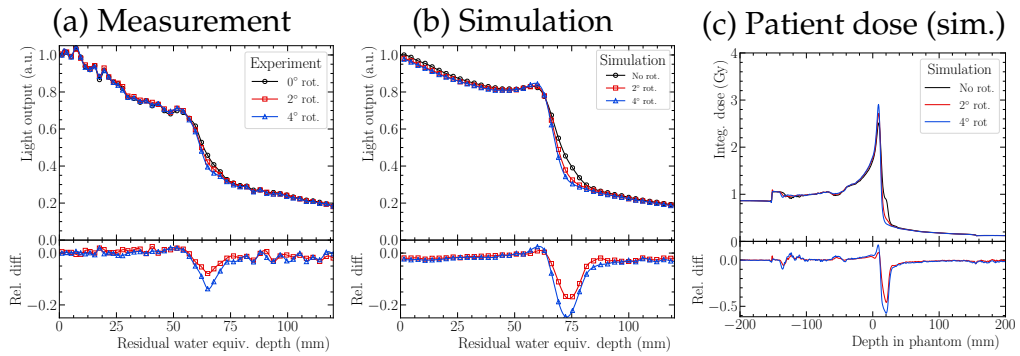

Figure 5.52: Result for different beam angles entering the phantom: measured (a) and simulated (b) helium/carbon signal in the detector. (c) shows the integrated dose to the patient as function of the distance to the isocentre. The dose considers both the helium and the carbon ion.

were observed for the two larger air fillings. This disagreement could likely be attributed to changes in the relative distance of the spot centre to the urethra stemming from position uncertainties and/or motion of the prostate between the treatment planning CT and the irradiation. In the phantom the urethra is modelled with a silicone pipe. As such, the rectal balloon filling pushing the pipe wall out of the beam might have caused the observed range change in the simulation (compare figure 5.50). The measurements of the other two spots qualitatively agree well with the simulation. Additionally, the simulation shows that the position of the helium peak in the detector correlates well with the changes in carbon dose in the patient (compare figure 5.51b and c). This correlation is essential for drawing conclusions on the carbon dose from the mixed helium/carbon beam signal in the detector.

ADAM-PETer phantom

In order to demonstrate the effect that a small patient rotation would have on the observed helium/carbon mixed signal, the ADAM-PETer phantom was used in its upright position, with the phantom rotated manually by 2° and 4° around the vertical axis. The results can be seen in figure 5.52. Both rotations lead to a noticeable change in the measured mixed beam signal. A similar, yet slightly larger effect can be observed in the simulation. In the depth-dose profile shown in figure 5.52(c), in addition to the range shift in the carbon peak, differences starting at the position corresponding to the entrance of the hip bone (at ∼135 mm upstream from the isocentre) can be seen. As such, it can be argued that the observed shift in the carbon range stems from the rotation of the hip bone.

Discussion

Uncertainty sources

Detector readout and data processing: Due to the high resolution of the CMOS sensor and the high light output of the scintillator, the statistical uncertainty on the light yield in a single sheet is low, <1% for carbon and helium.

However, the particle-specific calibration of the detector introduced a systematic uncertainty, which was the same for all recorded curves of the same particle. This uncertainty is estimated to be <3% by comparing the shoot-through curves for protons, helium and carbon ions.

Furthermore, the carbon depth-light curves were acquired at a very low beam intensity compared to the calibration shoot-through curves. This intensity mismatch is likely to be responsible for the fluctuations seen in the carbon signal (and therefore also in the mixed signal, see figure 5.48) close to the entrance of the scintillator stack. These fluctuations are consistently the same for all measured depth-light curves (see figures 5.49, 5.51 and 5.52). The magnitude of the systematic uncertainty in the low-intensity carbon signal is on the order of 5%.

Particle rate: The mixing of the sequentially irradiated helium and carbon beam in data processing required a stable particle rate to match a 10:1 ratio between the carbon and helium signal. While this was the case for the standard beam settings used, for the experimental beam parameters, fluctuations up to 15% were observed between spills. For the experimental helium settings, no spill regulation was active, likely causing these fluctuations. Hence, before adding the helium and carbon signals together, for the pelvis phantom measurements, the helium signals were scaled such that the signal in the first couple of sheets matched the reference measurement for each phantom. As this normalisation step can only cause an underestimation of signal changes, it does not affect the conclusion on the usefulness of the helium/carbon beam mixing method.

Beam parameters: There were slight differences in the beam parameters in the standard libraries used for the irradiation of the PMMA setup. The small mismatch between the beam energies of helium and carbon in the measurements with the PMMA phantoms leads to a sub-millimetre shift of the helium and carbon curves relative to each other compared to an actual mixed beam. This small shift has no qualitative effect on the reported results since the slope of the carbon curve beyond the Bragg peak is small and doesn't exhibit any prominent features. In the case of the pelvis phantoms, a smaller helium spot was used compared to the carbon spot, resulting in less range mixing (caused by lateral tissue inhomogeneities) as would have been observed for a real mixed beam.

Positioning uncertainty: Since the HIT experiment cave does not feature an in-room imaging system, a source of uncertainty was the correct positioning of

the phantoms relative to the beam, compared with the treatment planning and the simulation. For the PMMA setup, the slit was centered on the beam axis marked by the in-room laser positioning system by opening the two PMMA slabs symmetrically. In general a good agreement of simulation and measurement was observed here, suggesting an accurate phantom positioning for the measurement. For the ADAM phantom, the location of the target isocentre was marked on the phantom surface based on the treatment plan CT scan. This process already introduced some positioning uncertainty due to inaccuracies in the marking by hand. For the ADAM-PETer phantom, the target isocentre was already marked on the outside of the phantom with CT bead markers from an earlier experiment which can be seen as bright spots on the phantom contour in figure 5.47(b). The in-room positioning was then performed using the available laser positioning system. Nevertheless, for both pelvis phantoms, all investigated beam spots were more than 2 mm away from the treatment field edge. Therefore, it can be argued that despite positioning uncertainties, the results obtained still depict a realistic scenario.

In the ADAM-PETer measurements, an additional source of uncertainty was the manual rotation of the phantom, since no automatic rotation was available. Here, the angle relative to the isocentre position was manually drawn on the phantom and is therefore subject to the same uncertainties mentioned above. Nevertheless, the measurements serve to qualitatively demonstrate the feasibility of observing small patient rotations/movements with a mixed helium/carbon beam. It is important to mention that the CT bead markers were left on the ADAM-PETer phantom during irradiation as well as in the simulation. While being made from metal, they where spherical with a diameter of only 1.27 mm and are not expected to have affected the measurement.

Monte-Carlo simulation: The major uncertainty in the Monte-Carlo simulation was the modeling of the phantom materials. Especially, for the anthropomorphic phantoms, this introduced differences between the measured and the simulated helium range. Due to noise and beam hardening artefacts in the CT image as well as tissue substitute materials with overlapping Hounsfield unit range (Niebuhr et al. 2019), it was not possible to match the simulated and real composition perfectly with the method used in this work. For example, for the ADAM phantoms, the silicone organ shells were simulated as inner bone, due to the overlap in Hounsfield unit ranges for the two materials. Still, the observed signal variations introduced by the investigated changes in the treated geometry qualitatively agree well between simulation and experiment. However, when using Monte-Carlo as a basis for comparison to generate online treatment feedback (see discussion below), using more sophisticated methods to generate the Monte-Carlo material composition — e.g. using a Dual-Energy CT image as the basis (Hünemohr et al. 2014b, Lalonde & Bouchard 2016) — would be adequate. Implementing such methods, however, was beyond the scope of this work.

Using a mixed helium/carbon beam for treatment monitoring

This work highlights the potential of mixing a small amount of helium ions with a therapeutic carbon-ion beam for observing changes in the treated anatomy. This corroborates previous studies using treatment planning software (Graeff et al. 2018) and experimental investigations with protons in place of helium ions (Mazzucconi et al. 2018). Since the helium energies are fixed by the carbon energies from the treatment plan, the helium/carbon beam mixing technique is limited to treatment directions were the proximal target edge is located deeper than 1/3 of the patient WET in that direction. Otherwise, the helium ions would not have sufficient energy to fully cross the patient leading to the helium Bragg peak being located in healthy tissue. However, this limitation can potentially be overcome by selecting the treatment direction accordingly, if the gained additional information from the helium ions out-weights the drawback of a non-ideal beam direction. A thorough evaluation of patient data is needed to assess the applicability of the helium/carbon mixing method for different treatment sites.

A general drawback of the method is that the helium ions are not only sensitive to range changes that affect the carbon ions, but also to every change that occurs distal to the tumour. However, integrating the tissue properties over the whole thickness of the patient rather than just up to the tumour volume is true for any radiography-based system. For patient sites where there is known anatomical motion distal to the tumour, such as lung cases, a pre-treatment 4D-CT should be used to relate a given motion phase to the helium range including also the distal anatomy. For prostate cases, on the other hand, this is a less critical limitation. Here, the expected motion scenarios involve, for example, hip motion/rotation, bladder and rectum filling, as well as muscle contractions around the prostate (Langen et al. 2008), which should have an effect on both the helium and carbon range. Additionally, since the prostate lies centrally in the patient for lateral beam directions, all treatment plan energies should be sufficiently high for the helium ions to fully cross the patient. Moreover, prostate cases might benefit greatly from the helium/carbon mixing method: the irregularity and randomness of the motion patterns makes prostate motion hard to predict or mitigate in scanned ion-beam therapy (Ammazzalorso et al. 2014), which is why online treatment feedback would be highly advantageous. This is even more important when considering hypo-fractionated carbon-beam therapy.

The biggest advantage of the helium/carbon mixing method is the high sensitivity. With the system used in this work, range changes as small as 1 mm of less than a quarter particles in a pencil beam were observable. Furthermore, this sensitivity is achieved for a small number of incident particles per spot since only very few helium ions are required for a range measurement. It is important to note that for the measurements shown in this work a relatively large number of particles was integrated (21 readout frames summing up to $\sim 6.7 \times 10^7$ integrated particles for the PMMA phantom measurements) compared to the number of particles encountered in clinical pencil beams. This is due to the detector prototype used not being the ideal detection system for the helium/carbon beam mixing method, since it was developed as a quality

assurance device for proton beams. The amount of necessary particles could, however, be reduced by using a more sensitive photodetector. A fast-enough detector might even enable the acquisition of multiple range samples (snap shots) per beam spot (provided that the spot contains enough particles) in order to observe motion trends.

This work indicates that the previously suggested 10:1 ratio between primary carbon ions and helium ions is indeed useful for detecting changes in the treated anatomy. However, the optimal mixing ratio will depend on the detector used as well as on the technical aspects of the acceleration of the beam in the synchrotron. Furthermore, the sensitivity of the method also depends on the beam spot size, since with a smaller beam spot size small inhomogeneities would affect a larger portion of the pencil beam particles. However, for the range telescope used in this work, the lateral position of the artefact causing the observed range differences could not be determined with better precision than the pencil beam size without further processing. In order to achieve a better spatial resolution, the information of adjacent spots in the treatment plan could be matched (Hammi et al. 2017) or position sensitive detectors could be included to the setup (see for example Krah et al. (2018) for an overview over the spatial resolution of different particle imaging setups).

It is not trivial to quantify the observed changes in the helium range due to the strong range mixing in heterogeneous materials. A possible option would be to conduct a multi Bragg-peak fit similar to the methodology developed in Krah et al. (2015). In the work described here, the relative difference to a reference measurement was used to quantify range changes. This enables quantifying small changes compared to the expected signal without relying on a single point of reference and without the need to perform a fit to the signal. The latter feature could be of importance when using a mixed helium/carbon beam for generating online feedback during the treatment where computational speed is a necessity. On the other hand, using the relative difference compared to the expected signal as a metric requires generating a reference curve for every beam spot. This could potentially be accomplished using Monte Carlo simulations at the treatment planning stage that include an accurate description of the detector output (including spatial variations in the detector response/scintillation light quenching) and patient geometry, as has been suggested in Mazzucconi et al. (2018). As stated above, this would require sophisticated tissue decomposition methods, as well as accurate physics models in the simulation. Nevertheless, an accurate representation of the patient is crucial for treatment planning and, hence, an observed deviation from the expected signal would point towards a potential uncertainty in the treatment plan.

Finally, a mixed helium/carbon beam would offer the potential for post-treatment reconstruction of 2D images of the treated anatomy for each iso-energy slice using the techniques developed for particle radiographic imaging (cf. Parodi (2014), Krah et al. (2015)). This could be useful in post-treatment patient-specific quality assurance and dose accumulation.

However, whilst the presented results are indicative of the potential of a mixed beam, they can only serve as a conceptual assessment of the method

since they were produced with sequentially irradiated helium/carbon beams. Definitive statements of the usefulness of such a technique can only be made based on a real mixed beam.

Acceleration of a mixed helium/carbon beam

As also reported in Mazzucconi et al. (2018), the most straightforward way to generate a mixed beam would be to mix the two ions at the sources. However, at HIT, a reasonable current of $^{12}C^{6+}$ cannot be extracted from the sources. Hence, one would extract $^{12}C^{3+}$ and $^{4}He^{+}$ from a source running with methane[4] as the main gas and helium as the support gas. With a similar mass/charge ratio ($A/q \approx 4$), the partially stripped ions could pass the injection beam line together. However, the HIT LINAC pre-accelerator is optimised to accelerate ions with $A/q \leq 3$ and cannot accelerate ions with $A/q=4$. Therefore, a real mixed helium/carbon beam could not yet be delivered. A potential work-around to this issue could be to fully strip the ions before the LINAC instead of the current stripping after the LINAC, although this is usually avoided since the stripping efficiency decreases with decreasing beam energy (Bryant et al. 2000). Another possibility would be to achieve the beam mixing in the synchrotron by sequentially injecting the different ions. Since $^{16}O^{4+}$ could also pass the low energy beam transport together with $^{12}C^{3+}$ and $^{4}He^{+}$, mixing the beam inside the synchrotron might be preferable in order to avoid beam contamination with oxygen ions. The acceleration of a mixed beam will be the subject of further investigation. Nevertheless, since a great effort is usually made to avoid the contamination of the accelerated ion beams with ions of similar mass/charge ratio (cf. Winkelmann et al. (2008)), there is a strong reasoning that such a contamination could also be generated deliberately. If a mixed beam in the synchrotron can be generated, stable extraction, beam focusing and pencil beam scanning will add further complexity. Still, from the results presented in this work it is possible to conclude that the concept of a mixed beam for simultaneous treatment and imaging deserves further investigation.

Advantages of beam mixing versus sequential irradiation

Given the complexity of the acceleration of a mixed beam, the question arises if intra-fractional treatment monitoring could also be achievable with sequentially irradiated beams. Sequential beams come at the advantage of being easier to generate compared to a mixed beam. Moreover, the verification beam would not be limited by the parameters of the treatment plan. For patient sites subject to slow motion, sequential verification and treatment beams could provide useful information, if fast switching of ion sources or beam energy is technically feasible which is currently being investigated at HIT (Schömers et al. 2017). In that case, changes would be detected with a probably tolerable delay, depending on the rate of verification to treatment spills and the

[4] For the usually used CO_2 gas, the $^{12}C^{3+}$ peak in the source spectrum would overlap with the $^{16}O^{4+}$ peak.

time needed for switching sources/beam energy. Still, an online range estimate provided by a mixed beam would improve the potential for reduction of unwanted dose delivery and the accuracy of post hoc dose reconstruction for adaptive therapy.

For the treatment of moving targets, especially those with strong range changes such as lung tumors, a mixed beam would be most advantageous. Here, online motion information is most relevant, even if it is only used for dose reconstruction and possible adaptation of following fractions. An important aspect is also that with a mixed beam every spot in a treatment plan could be monitored without prolonging the treatment duration. This would be preferential for the clinical environment at an ion-beam therapy facility where short treatment duration is highly desired (Schömers et al. 2017). Nevertheless, in future studies, the usefulness of sequential beams for verification should also be further evaluated especially for static or non-periodically moving targets such as the prostate.

Conclusion

In this work the use of a mixed helium/carbon beam for monitoring intrafractional anatomical changes was investigated using a novel range telescope. It was demonstrated that with a mixed beam, range changes as small as 1 mm of only a fraction of the beam width could be observed with the system despite the presence of range mixing. Using two anthropomorphic phantoms, the method's use in more realistic clinical cases was investigated. Here, it was demonstrated that a mixed helium/carbon beam could be useful for observing bowel gas movements and small patient rotations. A limitation of the technique is that the helium energies are determined by the carbon treatment plan and thus might not have sufficient energy to cross the patient for all treatment fields/patient sites. Furthermore, the helium signal will integrate any uncertainty located distal to the carbon peak. Future studies should hence involve 4D patient data to identify patient sites that would benefit most from the technique. The generation of a real mixed helium/carbon beam at a synchrotron accelerator is a subject for further investigations.

Author contributions

LV was in charge of planning and preparing the experiments and carried out the simulations presented in this work. LK operated the detector during the experiment and conducted the processing of the experimental data. LV and LK equally shared the writing of the manuscript and the analysis/discussion of the acquired results. All authors contributed significantly to the presented work.

Acknowledgements

The authors would like to thank the Heidelberg Ion-Beam Therapy Centre (HIT) for providing the beam time and their excellent help in setting up the experiments. We thank Tim Winkelmann (HIT) for insightful discussions and exchanges regarding the HIT sources. Maria Martisikova (DKFZ) is acknowledged for initiating the implementation of the high helium beam energies. The authors thank Amit B. A. Bennan (DKFZ) for helping with the MatRad treatment planning software. The DKFZ phantom workshop is gratefully acknowledged for providing the phantoms used in this study. LV is funded by a scholarship of the Helmholtz International Graduate School (HIGS, Heidelberg, Germany). LK has received funding from the European Union's Horizon 2020 research and innovation programme under the Marie Sklodowska-Curie grant agreement No 675265, OMA – Optimization of Medical Accelerators.

5.6 P.VI: Investigation of a novel tracking detector approach

Title : Image quality of list-mode proton imaging without front trackers

Authors : J. R. Sølie, L. Volz, H. E. S. Pettersen, P. Piersimoni, O. H. Odland, D. Röhrich, Havard Helstrup1, T. Peitzmann, K. Ullaland, M. Varga-Kofarago, S. Mehendale, O. S. Grøttvik, V. N. Eikeland, I. Meric and J. Seco

Status : Published

Journal : Physics in Medicine and Biology

DOI : doi.org/10.1088/1361-6560/ab8ddb

Contributions : The principal author, JRS implemented and carried out the simulations shown in this work and was in charge of the project. LV and JRS together conceptualized the work, and shared writing the necessary software for reconstructing the pRad images and analyzing the image quality. HES aided in writing the software for the single-sided path estimation. PP aided in the CT reconstructions presented. IM, JS and DR coordinated the research between institutions and ensured the scientific rigor of the work by providing supervising guidance. JRS and LV together finalized the research, elaborated the results and equally shared writing the manuscript draft. The contribution of LV was acknowledged in a shared first author position on the manuscript. All other authors not mentioned contributed to conceptualization and discussion of the work and participated in the revision of the manuscript.

Abstract

List mode proton imaging relies on accurate reconstruction of the proton most likely path (MLP) through the patient. This typically requires two sets of position sensitive detector systems, one upstream (front) and one downstream (rear) of the patient. However, for a clinical implementation it can be preferable to omit the front trackers (single-sided proton imaging). For such a system, the MLP can be computed from information available through the beam delivery system and the remaining rear tracker set. In this work, we use Monte Carlo simulations to compare a conventional double-sided (using both front and rear detector systems) with a single-sided system (only rear detector system) by evaluating the spatial resolution of proton radiographs (pRad) and proton CT images (pCT) acquired with these set-ups. Both the pencil beam spot size, as well as the spacing between spots was also adjusted to identify the impact of these beam parameters on the image quality.

Relying only on the pencil beam central position for computing the MLP resulted in severe image artifacts both in pRad and pCT. Using the recently extended-MLP formalism that incorporate pencil beam uncertainty removed these image artifacts. However, using a more focused pencil beam with this algorithm induced image artifacts when the spot spacing was the same as the beam spot size. The spatial resolution tested with a sharp edge gradient technique was reduced by 40 % for single-sided ($MTF_{10\,\%}$ =3.0 lp/cm) compared to double-sided ($MTF_{10\,\%}$ =4.9 lp/cm) pRad with ideal tracking detectors. Using realistic trackers the difference decreased to 30 %, with $MTF_{10\,\%}$ of 4.0lp/cm for the realistic double-sided and 2.7 lp/cm for the realistic single-sided setup. When studying an anthropomorphic paediatric head phantom both single- and double-sided set-ups performed similarly where the difference between the two set-ups were less than 0.01 mm in homogeneous areas of the head. Larger discrepancies between the two set-ups were visible in high density gradients like the facial structures. A complete CT reconstruction of a Catphan® module was performed. Assuming ideal detectors, the obtained spatial resolution was 5.1 lp/cm for double-sided and 3.8 lp/cm for the single-sided setup. Double- and single-sided pRad with realistic tracker properties returned a spatial resolution of 3.8 lp/cm and 3.2 lp/cm, respectively. Future studies should investigate the development of dedicated reconstruction algorithms targeted for single-sided particle imaging.

Introduction

List-mode proton imaging, where individual protons are detected one-by-one, has gained increasing interest over the recent years as a promising candidate for improving range accuracy in particle therapy treatment planning (Poludniowski et al. 2015, Hansen et al. 2015, Dedes et al. 2019). The main advantage of proton imaging over conventional x-ray imaging modalities is the more accurate determination of the patient relative stopping power (RSP) from either particle computed tomography (pCT) (Hansen et al. 2015, Dedes

et al. 2019) or combining a small number of particle radiographs with a treatment planning x-ray CT (Schneider et al. 2005, Collins-Fekete et al. 2017a, Krah et al. 2019). A strong necessity in list-mode proton imaging is an accurate estimation of each proton's trajectory through the object in order to improve the spatial resolution deteriorated by multiple Coulomb scattering (MCS). An accurate estimate of the trajectory of each particle enables a more accurate distribution of the proton energy loss information, improving spatial resolution of reconstructed images (Li et al. 2006). Several different path estimation methods have been developed, of which the most widely used is the probabilistic most likely path (MLP) formalism that takes advantage of the Fermi-Eyges approximation of MCS (Schneider & Pedroni 1994, Williams 2004, Schulte et al. 2008, Erdelyi 2009, Collins-Fekete et al. 2017d, Krah et al. 2018). The MLP is usually computed from four input parameters — the particle's position and direction at the object entrance and exit. In practice, these parameters are obtained by integrating a set of position sensitive detector planes upstream (front tracker set) and downstream (rear tracker set) the object to be imaged (Poludniowski et al. 2015). Such a proton imaging set-up (in this work denoted double-sided) is illustrated in Figure 5.53a.

The accuracy of the MLP depends on the amount of scattering inside the patient, spatial uncertainty of the tracking detectors and their distance to the patient (Krah et al. 2018). However, for clinical implementation, a system that does not include a front tracker set (here denoted single-sided and illustrated in Figure 5.53b) might be more advantageous due to the reduced set-up complexity and reduced cost of the system. Additionally, for proton list-mode imaging at synchrotron facilities, a system using both front and rear trackers might be less practical for acquiring list-mode data at high particle rates: at a synchrotron, the beam typically is delivered in bunches lasting 20 to 50 ns spaced 100 to 200 ns apart (Krimmer et al. 2018). With increasing average particle rates, the probability of more than one particle being delivered per bunch increases and, hence, the effective particle rate impinging on the detector becomes much larger than the average rate set in the beam control. For list-mode particle imaging, the system would have to be either fast enough to assign a time stamp to every incident particle at the effective rate of the particles within each bunch, or measure a large multiplicity of particles simultaneously as for example proposed in Pettersen et al. (2019a). However, measuring a large multiplicity of particles in the same read-out frame compromises the feasibility of including a front tracker to the system, as the MCS in the object makes it difficult to accurately pair particle histories measured on the rear tracker with the measurements on the front tracker. Thus it is of interest to explore the possibility of using a single-sided set-up to avoid this pairing of particle histories. As has been shown by Krah et al. (2018) for active scanning beam delivery systems, the available treatment planning system (TPS) information (beam spot position/direction as well as spot size and beam divergence) can be included

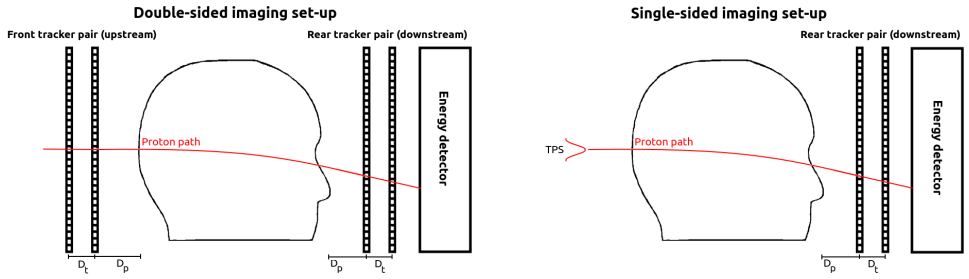

(a) Double-sided proton imaging set-up **(b)** Single-sided proton imaging set-up

Figure 5.53: Illustration comparing conventional double- (a) and single-sided (b) proton imaging set-ups. D_t is the distance between the position sensitive trackers in each tracker pair, and D_p is the distance between the inner tracking plane and phantom to be imaged. In Single-sided the front tracker pair is removed and pencil beam information (beam spot size, angle, and position) from the TPS is used instead.

in the derivation of the MLP. From their work it follows that the spatial resolution achievable with a single-sided set-up is limited compared to a double-sided set-up [5]. However, their work focused on the accuracy of the MLP without reconstructed images. The purpose of this work is hence to investigate the image quality of proton radiography (pRad) and proton CT (pCT) with a single-sided imaging system using Monte Carlo simulations. We assessed the effect of different pencil beam spot sizes and different lateral spacing between pencil beam spot center positions. A 200 mm thick water phantom with aluminium inserts at different depths was imaged to study the spatial resolution with respect to the MLP accuracy and object depth for reconstructed images from single- and double-sided set-ups. For comparing single-sided and double-sided imaging set-ups in a more clinically relevant scenario, pRad of a paediatric head phantom (Giacometti et al. 2017b) was performed. For investigating and comparing the spatial resolution between single- and double-sided set-ups in pCT, scans of a Catphan® (the Phantom Laboratories, Salem, NY, USA) CTP528 module was simulated and reconstructed. To investigate the image quality achievable with a single-sided setup in the ideal case, we first used ideal tracking planes having zero material budget and zero pixel pitch. In addition, we compared the results to those acquired with a realistic tracking system modeled after the current state-of-the-art prototype developed by the US pCT collaboration (Johnson et al. 2017). This study was done in the context of the Bergen pCT project, which is designed to work with clinical pencil beam scanning and a rear tracker set only, and whose detector components are currently under construction.

[5] While in their work, Krah et al. (2018) do not directly investigate a single-sided set-up where the rear tracker also measures the particle direction, it is straightforward to apply their methodology to such a case as well.

Materials and Methods

Monte Carlo simulations

All pRad and pCT data were simulated using the Geant4-wrapping GATE V8.2 Monte Carlo toolkit (Jan et al. 2004, Jan et al. 2011, Agostinelli et al. 2003, Allison et al. 2006). The reference physics list QGSP_BIC_EMZ, as recommended by the GATE Radiation Therapy and Dosimetry working group, was activated for the simulations and the ionization potential of water was manually set to 78 eV. The simulation world was filled with air and default step limits (1 mm) and production cuts (0.7 mm) were used in all simulations.

The tracker planes were implemented as ideal detector planes with zero material budget. For both the double-sided and the single-sided set-ups the distance between the inner tracking plane(s) of the tracker pair(s) to the phantom edge was set to 150 mm and the distance between tracking planes in each set was set to be 50 mm as based on the results from Krah et al. (2018) and Bopp et al. (2014). For studying the impact of tracker properties, a realistic tracking system was modeled after the Loma Linda prototype pCT scanner (Giacometti et al. 2017a, Johnson et al. 2016). The realistic tracking system comprises four 0.4 mm thick silicon strip detectors (SSD) each with a strip-pitch of 0.228 mm. Two tracker planes are used to form front and rear tracker sets respectively, with positioning of the trackers equivalent to that for the ideal setup. The proton residual energy was scored directly on the rear tracker and no residual energy uncertainty was modeled, this was done in order to limit the amount of image noise and focus solely on the effect of removing the front tracker pair.

To model a pencil beam scanning system, the GATE built-in treatment plan system (TPS) (Grevillot et al. 2010) was used. The pencil beam lateral full width at half maximum (FWHM) at the iso-centre was set to 7 mm to represent a clinically realistic beam. Additionally, 2 and 3 mm FWHM spot sizes were investigated. The initial beam energy was set to 230 MeV, representing the highest clinically available beam energy for most contemporary proton therapy facilities. The pencil beam characteristics underlying the investigations presented in this work are detailed in Table 5.10. Field sizes chosen to cover each investigated phantom in pRad were $3.0 \times 3.0\,\mathrm{cm}^2$ for the spot-phantom, $4.2 \times 4.2\,\mathrm{cm}^2$ for the step-phantom, and $20 \times 20\mathrm{cm}^2$ for the head-phantom. A total number of 2×10^6 protons were used to image the step-phantom and 12×10^6 protons to image the head-phantom. Proton CT scans were acquired from 360 projections separated by steps of 1° and containing 1×10^6 primary protons in each projection covering a $16.0 \times 5.0\,\mathrm{cm}^2$ field consisting of 705 beam spots with a spot FWHM of 7 mm and lateral spot spacing of 3.5 mm.

Phantoms

Five different phantom geometries were implemented in GATE to investigate the image quality for a single-sided imaging set-up combined with pencil beam scanning.

TPS source characteristics			
Energy	230 MeV		
Nozzle exit to iso-centre distance	500 mm		
Scanning magnet X to iso-centre distance	6600 mm		
Scanning magnet Y to iso-centre distance	6600 mm		
Beam characteristics	2 mm	3 mm	7 mm
Spot size in x (standard deviation) [mm]	0.85	1.3	3.0
Spot size in y (standard deviation) [mm]	0.85	1.3	3.0
Spot divergence theta [mrad]	2.4	2.8	2.8
Spot divergence phi [mrad]	2.4	2.8	2.8
Spot emittance theta [mm*mrad]	1.1	3.0	3.0
Spot emittance phi [mm*mrad]	1.1	3.0	3.0

Table 5.10: TPS set-up and 2, 3, and 7 mm FWHM pencil beam characteristics used to investigate image quality.

First, a water tank of 200 mm thickness was implemented to study the behaviour and quality of the MLP compared to the actual MC ground truth path.

The second phantom was a water tank of 200 mm thickness containing a $20\times20\times20\,\mathrm{mm}^3$ aluminium cube placed in the water tank's centre. This was used to study the impact of spot-spacing and beam spot size on the spatial resolution of reconstructed pRad. This phantom will be referred to as "spot-phantom" in this work.

The third phantom investigated was a water tank of 200 mm thickness where five $10\times10\times10\,\mathrm{mm}^3$ aluminium cubes were placed at five different depths inside (15 mm, 57.5 mm, 100 mm, 142.5 mm, 185 mm). This phantom is depicted in Figure 5.54 and will be referred to as "step-phantom" throughout this work. The cubes were slanted 5 degrees relative to the vertical image pixel direction to enable the evaluation of the modulation transfer function (MTF) from the edge spread of the cubes. This phantom enables the investigation of the spatial resolution as a function of object depth.

To represent a clinically relevant case, a digitised paediatric head phantom based on the CIRS model HN715 (Norfolk, Virginia, USA) was implemented in the simulations. The head is a high resolution ($0.1875\times0.1875\times1.25\,\mathrm{mm}^3$) voxelised geometry developed by Giacometti et al. (2017b). A ground truth pRad was reconstructed by integrating over the known RSP of every voxel of the head phantom and is used in evaluating radiography reconstruction errors.

The fifth and final phantom was a Catphan® CTP528 phantom module with the purpose of investigating the spatial resolution of a full proton CT scan. The phantom is an epoxy cylinder that contains small aluminium inserts at a fixed radial position with increasing spatial frequency (1–21 line pairs per cm – lp/cm). The phantom was implemented following the specifications in Piersimoni et al. (2018).

All phantoms were placed such that their center aligned with the iso-centre of the TPS. A complete list of all used material compositions, densities as well

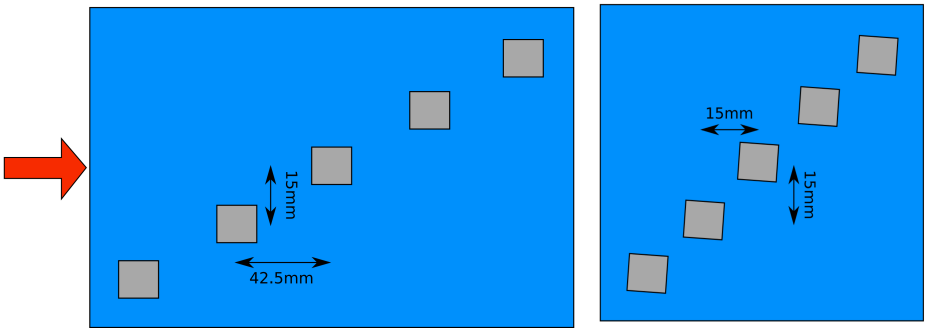

(a) Side-view of the step-phantom.

(b) Front/beam-view of the step-phantom.

Figure 5.54: Side (a) and front view (b) of the step-phantom. Five aluminium cubes of 10 mm edge length were slanted five degrees and placed at different depths in a water tank. The red arrow represents the beam direction and black arrows mark the distances between the centres of the aluminium inserts.

Material name	HU	H	C	N	O	Mg	Al	Si	Cl	Ca	P	S	Ba	Ar	ρ [g/cm^3]	RSP
Air	-998	-	0.01	75.53	23.18	-	-	-	-	-	-	-	-	1.28	0.001204	0.00114657
Water	-	11.20	-	-	88.80	-	-	-	-	-	-	-	-	-	1.00	1
Aluminium	-	-	-	-	-	-	100.0	-	-	-	-	-	-	-	2.7	2.12522
Silicon	-	-	-	-	-	-	-	100.0	-	-	-	-	-	-	2.33	1.88521
Epoxy	-	7.8	71.09	2.03	19.08	-	-	-	-	-	-	-	-	-	1.16	1.14341
Soft tissue	24	8.48	57.45	1.65	24.6	7.62	-	-	0.19	-	-	-	-	-	1.055	1.04063
Brain tissue	52	8.17	53.62	1.53	26.51	9.98	-	-	0.19	-	-	-	-	-	1.07	1.04918
Spinal disk	92	7.07	52.46	2.11	27.60	9.55	-	-	0.21	0.98	-	-	-	-	1.10	1.0631
Trabecular bone	197	8.39	59.65	1.55	21.42	1.46	-	-	0.12	5.03	2.33	-	-	-	1.13	1.11113
Cortical bone	923	4.13	29.70	0.85	34.12	3.11	-	-	0.04	20.48	7.57	-	- -		1.75	1.59127
Tooth dentin	1280	4.51	35.35	1.23	29.41	-	-	-	0.04	19.84	9.20	0.08	0.33	-	1.66	1.51866
Tooth enamel	2310	2.77	21.81	0.82	34.02	-	-	-	0.03	26.6	12.33	0.31	1.31	-	2.04	1.7955

Table 5.11: Hounsfield unit (HU), atomic composition (fraction of mass in %), density and RSP of materials used in Monte Carlo simulations.

as their reference relative stopping power (RSP) can be found in Table 5.11.

Spot-spacing and spot size

A smaller pencil beam lateral uncertainty and spread is expected to increase the spatial resolution following Krah et al. (2018). Hence, two pencil beam thicknesses of 7 and 3 mm FWHM were investigated. Smaller spacing in-between spots was also investigated following the rational that for the reconstruction algorithm from Collins-Fekete et al. (2016) the water equivalent thickness (WET) of each pixel is calculated as a weighted mean over all protons crossing into the pixel column through the object. Hence, a denser packing of protons corresponding to the center of the beam spot might increase the image accuracy. The spot spacing was set to 0.5 and 1 times the beam lateral FWHM of each beam. Additionally, for the 7 mm beam, a spot spacing of 1 mm was investigated.

Image reconstruction

In this work, the extended-MLP formalism developed by Krah et al. (2018) was employed to estimate the proton trajectory throughout the phantoms. In this formalism, the TPS parameters (mean beam position and beam direction) were used, and the uncertainty of these parameters was accounted for by including the beam co-variance matrix following section 2.6 in their work. The beam co-variance was obtained at the same position as the innermost front tracker plane in the corresponding double-sided set-up. A hull projection algorithm was applied to project the proton positions from the trackers along their directions and onto the phantom contour positions. This effectively improves the accuracy of the MLP and reconstruction as reported by Schultze et al. (2015) and Collins-Fekete et al. (2017b). The WET crossed by each proton was computed by integrating over the inverse stopping power in water ($(\mathrm{d}E/\mathrm{d}x)_{\mathrm{W}}$) as

$$\mathrm{WET} = \int_{E_{\mathrm{in}}}^{E_{\mathrm{out}}} \frac{1}{(\mathrm{d}E/\mathrm{d}x)_{\mathrm{W}}} \mathrm{d}E. \tag{5.58}$$

The required list of stopping power versus energy, via data tables covering the proton energy range of 1 to 330 MeV in steps of 0.01 MeV, was obtained directly from MC simulation. Before image reconstruction a $2.5\,\sigma$ filter on the proton angles was applied to filter out the large angle scattering not described by the scattering theory underlying the MLP (Schulte et al. 2008, Gottschalk 2012). A $3\,\sigma$ filter on the WET of the protons was applied to remove unusually large energy losses and nuclear interactions (Schulte et al. 2005).
Radiography image reconstruction was performed using the maximum likelihood image reconstruction method developed by Collins-Fekete et al. (2016). This algorithm offers a reconstructed pRad where the WET of each image pixel is calculated as a weighted mean over all protons crossing into pixel columns through the object. The pixel size for reconstructed pRad was $0.25\times0.25\,\mathrm{mm}^2$, except for the anthropomorphic head phantom where is was $0.1875\times1.25\,\mathrm{mm}^2$ to coincide with the digitised CT voxels of the phantom.

For pCT reconstructions we used the diagonally-relaxed orthogonal row projection (DROP) iterative reconstruction algorithm with superiorization of the total variation (TVS) (Penfold et al. 2010). As starting point for the iterative reconstruction and for obtaining the object hull, an analytical CT reconstruction based on the Feldkamp-David-Kress (FDK) algorithm was used. For computational efficiency, an optimised cubic spline path (Collins-Fekete et al. 2015) was used to interpolate between the particle entrance position/direction estimated from the extended-MLP algorithm and the measured rear tracker information, following the work by Pettersen et al. (2019c). This approximates the full extended-MLP while retaining the computational advantages of the fast cubic spline path. The DROP-TVS algorithm was run for 8 iterations each divided into 40 optimization blocks. The slice thickness was set to 1.25,mm and 455x455 pixels per slice (160 mm radius FOV; 0.35 mm pixel size) were set for the reconstruction.

Image metrics

The main difference between single-sided and double-sided imaging set-ups is the degradation of the MLP accuracy due to the missing set of front trackers (Krah et al. 2018, Plautz et al. 2016). This will result in a decrease in the spatial resolution of the acquired images. We compared the spatial resolution of pRad and pCT acquired with single- and double-sided list mode using the MTF. We computed the edge spread function (ESF) for every insert of the step-phantom and fitted them with an error function to suppress noise. The derivative of the fits yielded the line spread functions, and the MTF was finally obtained as their Fourier transform. As a metric for comparison we used the spatial frequency lp/cm at which the MTF drops below the 10 % level as has also been done in previous literature (Seco et al. 2013, Krah et al. 2018).

For pRad of the step-phantom, the contrast-to-noise ratio (CNR) of the inserts was evaluated using,

$$\mathrm{CNR} = \frac{\overline{\mathrm{WET}}_{\mathrm{AlCube}} - \overline{\mathrm{WET}}_{\mathrm{Water}}}{\sqrt{(\sigma_{\mathrm{AlCube}})^2 + (\sigma_{\mathrm{Water}})^2}}. \tag{5.59}$$

Where $\overline{\mathrm{WET}}_{\mathrm{AlCube}}$ and σ_{AlCube} are the mean and standard deviation, respectively, of WET values in the central area ($2.5 \times 2.5\,\mathrm{mm}^2$) of the aluminium insert. $\overline{\mathrm{WET}}_{\mathrm{Water}}$ and σ_{Water} are the mean and standard deviation of the reconstructed WET values of the homogeneous water tank. A total of 100 image pixels were used for calculating each mean and standard deviation.

The WET errors of the reconstructed pRad of the anthropomorphic head phantom were quantified using the difference between the reconstructed WET pRad and the ground truth pRad. Additionally, the noise in each image pixel was obtained as the standard error of the mean of the weighted WET distribution in that pixel, where the weights were the same ones used in the image reconstruction from the algorithm by Collins-Fekete et al. (2016).

For the pCT reconstructions of the Catphan® CTP528 line pair module, the visual MTF was assessed from the maximum-to-minimum contrast measured for each set of line pairs relative to the reference contrast. Following Piersimoni et al. (2018), a discrete MTF was then obtained from the contrast $C(f)$ between adjacent maxima and minima in a profile over the line pair inserts of the same spatial frequency f (lp/cm).

$$\mathrm{MTF}(f) = \frac{C(f)}{C(0)}, \tag{5.60}$$

where

$$C(f) = \left\langle \frac{\mathrm{RSP}_{max} - \mathrm{RSP}_{min}}{\mathrm{RSP}_{max} + \mathrm{RSP}_{min}} \right\rangle \tag{5.61}$$

For a robust estimate, the contrast was averaged over all pairs of adjacent maxima and minima corresponding to the same spatial frequency. The contrast at $f = 0$ was obtained as using the peak RSP value reconstructed for the 1 lp/cm aluminium insert and the RSP reconstructed for the epoxy material for the ideal double-sided reconstruction.

Results

MLP accuracy impact

The average deviation between the MLP and the MC ground truth path is shown in Figure 5.55a as a function of depth in a 200 mm thick water tank for protons with initial energy of 230 MeV. The MLP for the single-sided set-up has the highest deviation in the very beginning of the phantom and continually improves with decreasing distance to the rear trackers. Not taking into account the pencil beam uncertainty and co-variance matrix in the MLP derivation, the MLP deviation is as high as 2.4 mm at the object entrance for a 7 mm FWHM beam. This is improved by a factor 2 when using the extended-MLP formalism by Krah et al. (2018). The smaller and more focused 3 mm beam exhibits the same behaviour, albeit with a smaller benefit from the extended-MLP formalism due to the already small width of the incoming pencil beam. However, the single-sided MLP is still less accurate compared to the double-sided set-up. In Figure 5.55b, the effect realistic tracker properties for setup parameters based on the Loma Linda phase II prototype have on the MLP accuracy is compared to ideal trackers. Due to pixel pitch and scattering inside the trackers, the entrance and exit position accuracy are deteriorated and thus affecting the MLP negatively.

Spot spacing and spot size

Using only the TPS mean position/direction information as input to the MLP estimation by Schulte et al. (2008) resulted in considerable image deterioration in the form of sampling artifacts due to the systematic shift in the entrance positions of the particles. This is shown for some selected spot spacing values in Figure 5.56. These artifacts can be understood from Figure 5.57. Using the mean position/direction in the pencil beam as entrance position resulted in a systematic shift of the MLP, particularly in the beginning of the phantom. This results in under-sampling of the shaded object regions during image reconstruction with the algorithm by Collins-Fekete et al. (2016). The size of these empty areas, and therefore the observed sampling artifacts, are dependent on the spot size and similar artifacts were observed for all investigated pencil beam spot sizes and spot spacing. It is noted that a larger amount of proton histories (5×10^6 compared to the original 2×10^6) were used during the image reconstruction of spot-phantom pRad to more clearly visualise the patterns being induced by the image artifacts caused by the spot-spacing.

These artifacts disappear for the 7 mm beam when the initial position of the proton is estimated using the extended-MLP. No difference in spatial resolution nor noise was observed for any of the three investigated spot spacing for the 7 mm beam. For the double-sided set-up, the image quality was not affected by the spot size and the spacing between spots, as expected.

For the smaller 2 mm and 3 mm FWHM spots, however, artifacts were present in the reconstructed single-sided pRad when a 1 FWHM spot spacing was

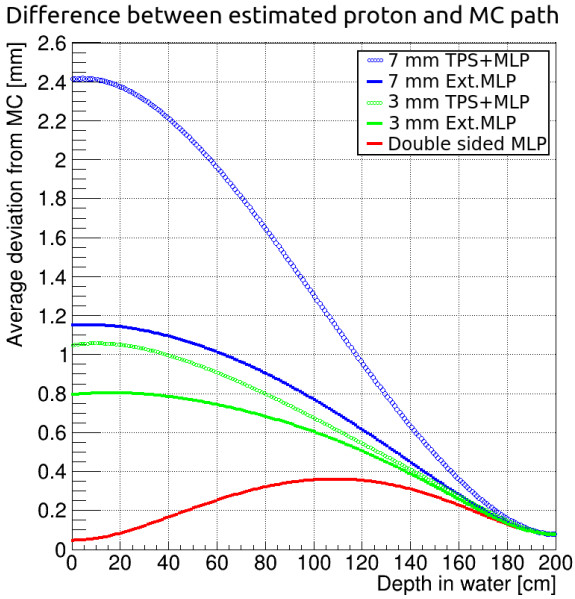

(a) The average deviation of the MLP path from the MC ground truth path. The blue curves denotes the 7 mm beam and the green curves the 3 mm beam: Dotted curves depict using TPS mean position and direction input, full curves refers to the extended-MLP formalism (Krah et al. 2018). The red curve is the MLP estimation with ideal front and rear trackers.

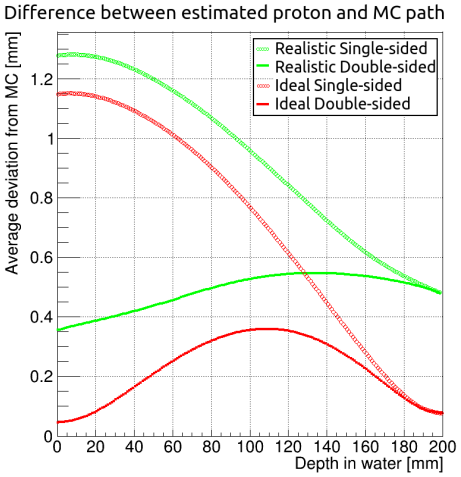

(b) Dotted curve is the single-sided set-up and full curve is the double-sided set-up. The red curves are the MLP estimation with ideal tracker pairs measurements, the green curves are the realistic Loma Linda tracker pairs.

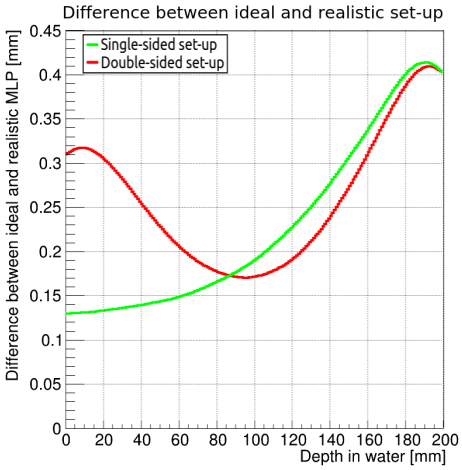

(c) The red curve is the difference between ideal and Loma Linda double-sided set-up. The green curve is the difference between ideal and Loma Linda in single-sided set-up.

Figure 5.55: The average deviation of the MLP path from the MC ground truth path inside a 20 cm water phantom.

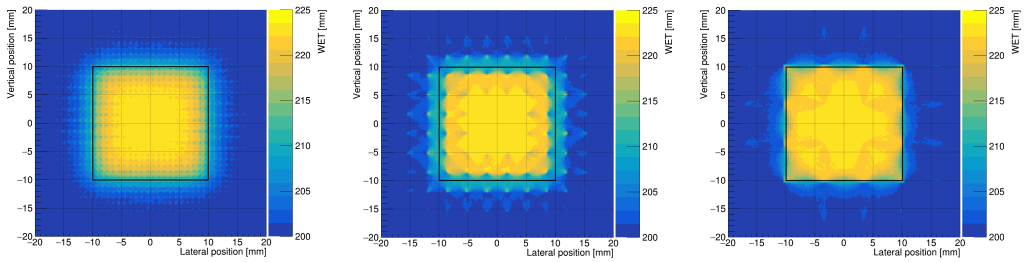

(a) 1 mm spot spacing. **(b)** 0.5 FWHM (3.5 mm) spot spacing. **(c)** 1 FWHM (7 mm) spot spacing.

Figure 5.56: The spot-phantom was scanned with 7 mm FWHM, 230 MeV proton beams at three different spot spacing settings. These pRads were reconstructed using only the TPS mean position/direction as input to the MLP. The black outline encases the actual edges of the aluminium cube.

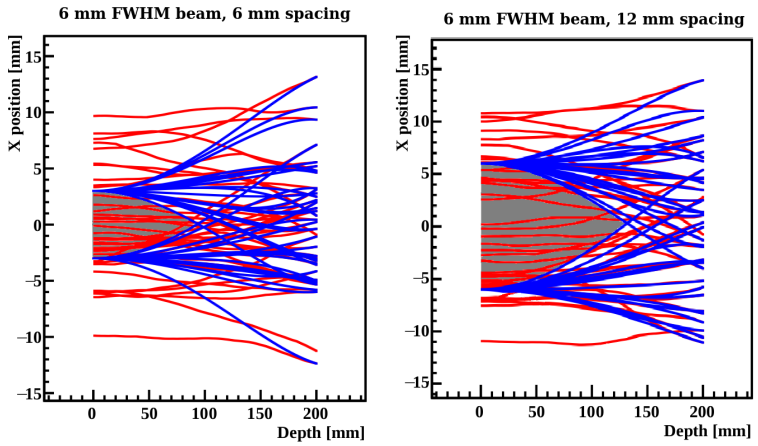

(a) 6 mm beam spot spacing **(b)** 12 mm beam spot spacing

Figure 5.57: Illustrating the loss of information that is located inside the shaded region caused by wrongly reconstructed proton paths. Red lines are the true MC proton paths and blue lines are the estimated proton paths assuming the beam central Gaussian position at entry. A beam spot size of 6 mm FWHM and spot spacing of a) 1 and b) 2 times its FWHM visually emphasises the effect on the shaded region.

Depth [mm]	Double-sided Ideal [lp/cm]	Single-sided Ideal [lp/cm]	Double-sided Realistic [lp/cm]	Single-sided Realistic [lp/cm]
15	7.2 (13.5)	2.6 (13.6)	4.7 (12.8)	2.4 (14.6)
57.5	5.9 (13.8)	2.7 (12.9)	4.7 (13.5)	2.4 (14.0)
100	4.8 (12.3)	3.1 (11.6)	4.1 (14.5)	3.0 (14.0)
142.5	3.6 (13.7)	3.7 (13.4)	3.5 (13.1)	3.0 (13.4)
185	2.9 (13.0)	2.9 (12.4)	2.9 (11.3)	2.5 (12.8)

Table 5.12: $MTF_{10\,\%}$ at five different depths inside a 200 mm thick water tank for both ideal and realistic single- and double-sided imaging set-ups. For each cube the corresponding CNR is given in parentheses.

used. This becomes apparent for the step-phantom as seen in Figure 5.58c. These artifacts stem from the the smaller corresponding uncertainty of the TPS mean position involved in the calculation of the extended-MLP (Krah et al. 2018): For a highly focused beam, the extended-MLP will effectively approach the pencil beam mean position and underestimate the spread of protons entering the phantom, as observed in Figure 5.58band 5.58d. The underestimated spread induces similar artifacts as in figure 5.56 which can be mitigated by a smaller spot spacing due to the overlapping of the proton distributions and preventing loss of information in gaps between pencil beam spots. For the 7 mm FWHM beam, the estimated pencil beam entrance distribution from the extended-MLP approaches the true distribution of the protons as shown in Figure 5.58f.

Spatial resolution

The step-phantom was irradiated with the 7 mm pencil beam and 0.5 FWHM spot spacing to evaluate the spatial resolution achievable with a clinically realistic beam. The $MTF_{10\,\%}$ together with their contrast-to-noise ratio (CNR) for each of the five aluminium inserts are presented in Table 5.12. The average resolution of the edges of the five cubes of the reconstructed step-phantom pRad in Figure 5.59 are 4.9 lp/cm for the double-sided set-up and 3.0 lp/cm for the single-sided set-up. For the realistic tracker set-ups the average resolution is 4.0 lp/cm for double-sided set-up and 2.7 lp/cm for single-sided.

Radiography of the paediatric head phantom

To investigate a clinically relevant scenario, the 7 mm and 3 mm beam with 0.5 FWHM spot spacing were used to image an anthropomorphic paediatric head phantom. The reconstructed WET from both the double- and single-sided pRad are compared to the ground truth integrated WET image in Figure 5.60. WET error profiles through different parts of the phantom are shown in Figures 5.60c - 5.60e for easier comparison of double- and single-sided set-ups.

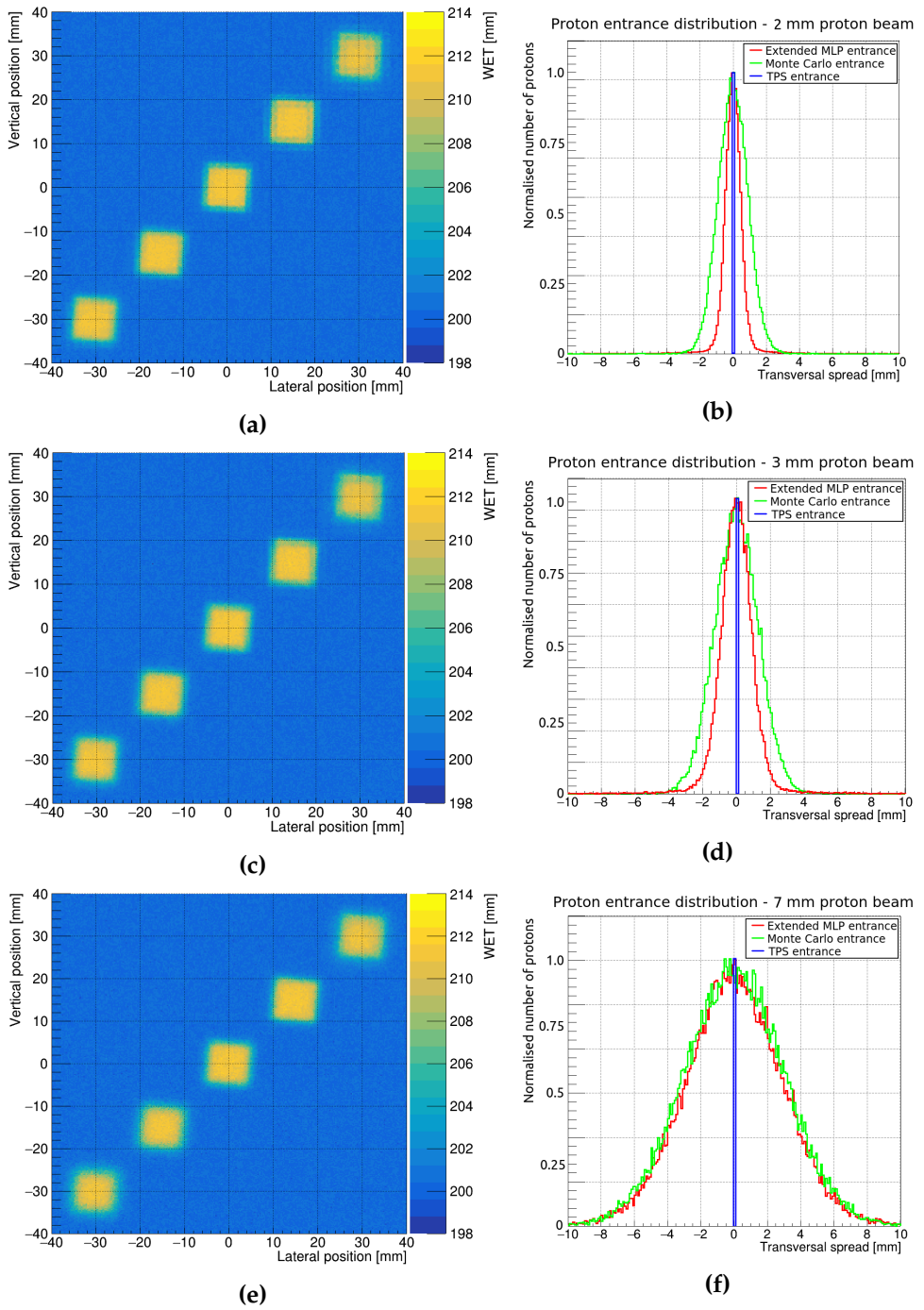

Figure 5.58: Reconstructed pRad of the step-phantom using 2, 3, and 7 mm FWHM beams with 1 FWHM spot spacing in a), c), and e) respectively. The three pencil beam proton entrance distributions in (b), (d), and (f) are normalised to the same height.

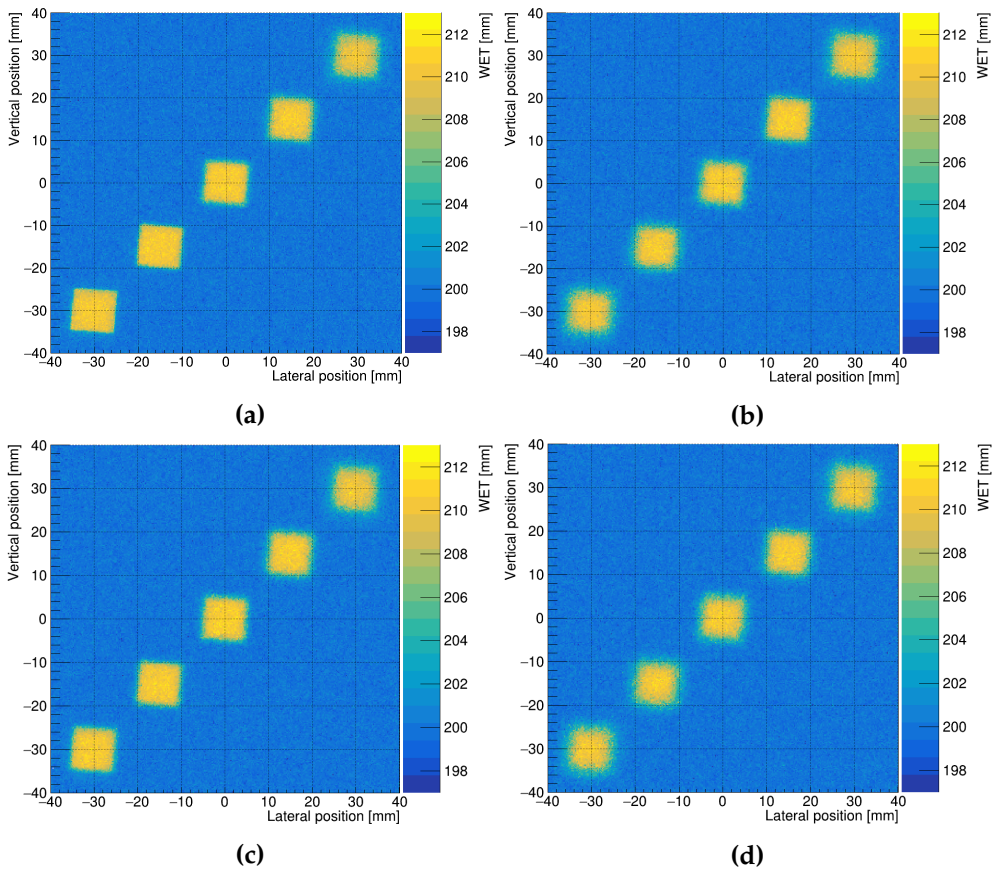

Figure 5.59: Ideal Double- (a) and Single-sided (b), and realistic Double- (c) and Single-sided (d) pRad of the step-phantom using the 7 mm FWHM beam.

Figure 5.61 shows the equivalent for reconstructions based on realistic tracker properties.

In Figure 5.60a and 5.60b, the single-sided pRad resulted in higher errors at high WET gradients, especially around the facial features like the nose cavity and mouth. Profiles through the homogeneous part of the brain (Figure 5.60c, between lateral position −40–40 mm) yielded a WET error for both set-ups that was better than 1% of the total WET in that region, while the facial structures in Figure 5.60d and 5.60e have WET errors between 1 % and up to 3 %. The average difference in reconstructed WET between double-sided and single-sided imaging in the homogeneous area of the brain was less than 0.01 mm. At high density gradient structures around the mouth, the difference between the two set-ups can reach over 1 mm. Similar results were observed in pRad with realistic trackers, albeit yielding larger errors at high WET gradients, reaching up to 5% of the WET in the facial structures. The difference between single- and double-sided set-ups in these regions was also larger, reaching up to 2 mm difference. This increased error originates from the more impaired MLP of realistic tracker properties. In homogeneous areas however, such as the brain, there is little to no difference between the imaging set-ups.

To quantify the image noise in both single- and double-sided pRad, the standard deviation of the reconstructed WET in each image pixel is shown in Figure 5.62, where the top row shows the ideal, and the bottom row the realistic tracker setup. Again, the single-sided reconstruction showed elevated noise levels compared to the double sided one at high WET gradients.

Spatial resolution of pCT

Figure 5.63 shows a central slice through the double-sided and single-sided pCT reconstructions of the Catphan® CTP528 line pair module. The single-sided pCT shows a reduced spatial resolution compared to the double-sided one. Figure 5.64 shows the $MTF_{10\,\%}$ computed from the maximum-to-minimum contrast for each set of line pairs relative to the reference contrast.

Overall, the MTF of double-sided pCT was above that of the single-sided reconstructions. For an ideal imaging setup, single-sided pCT had a $MTF_{10\,\%}$ of 3.8 lp/cm while that for double-sided pCT was 5.1 lp/cm. When realistic tracker properties were used in simulating the projection data, the $MTF_{10\,\%}$ was 3.2 lp/cm for the single-sided setup, while it was 3.9 lp/cm for the double sided setup.

Discussion

Choice of set-up parameters

In this work, we investigated the image quality achievable with a single-sided proton imaging set-up compared to a double-sided set-up. To this end, we focused our work on clinically realistic beam parameters, and also studied the effect of varying the spot spacing and pencil beam size. In order to demonstrate the potentially achievable image quality for single-sided imaging, an

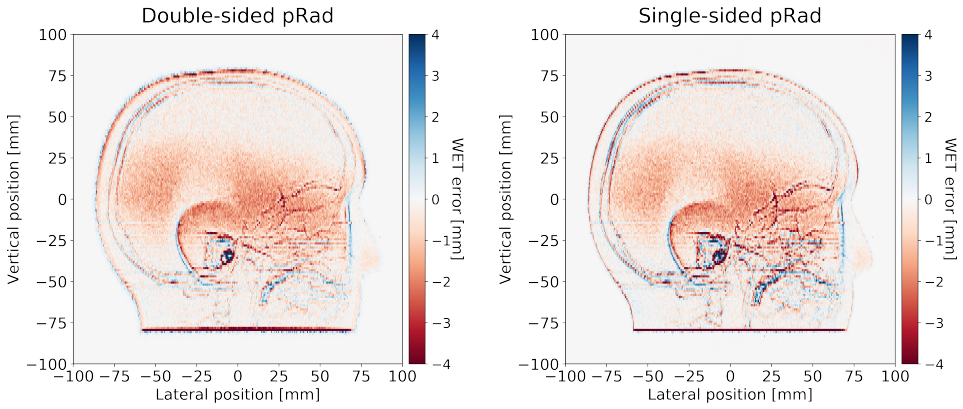

(a) **(b)**

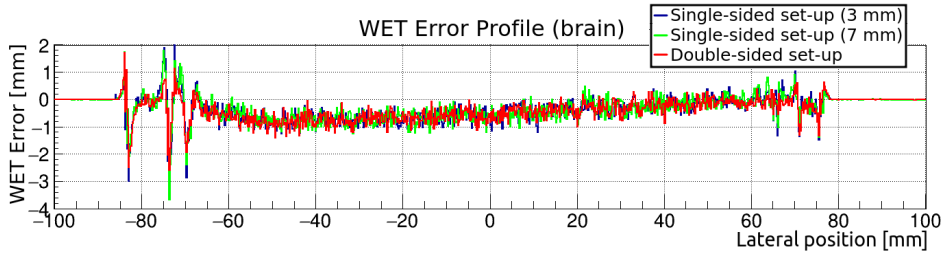

(c) WET error profile of the brain through vertical position 30 mm in (a) and (b).

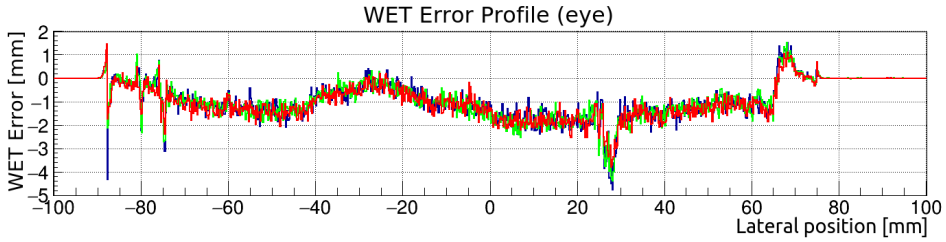

(d) WET error profile of the eye structures through vertical position 0 mm in (a) and (b).

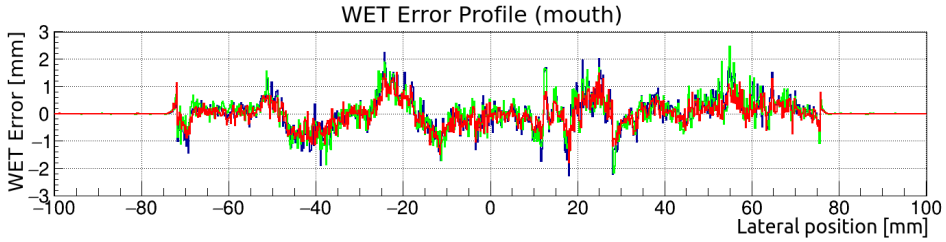

(e) WET error profile of the facial structures through vertical position -50 mm in (a) and (b).

Figure 5.60: Comparing double-sided and single-sided reconstructed WET error (a-b) with ideal trackers. Including three error profiles for detailed views of the brain, eye, and facial structures (c-e). Red curve is the double-sided image, blue curve is the single-sided image with the 7 mm beam, and green curve with the 3 mm beam.

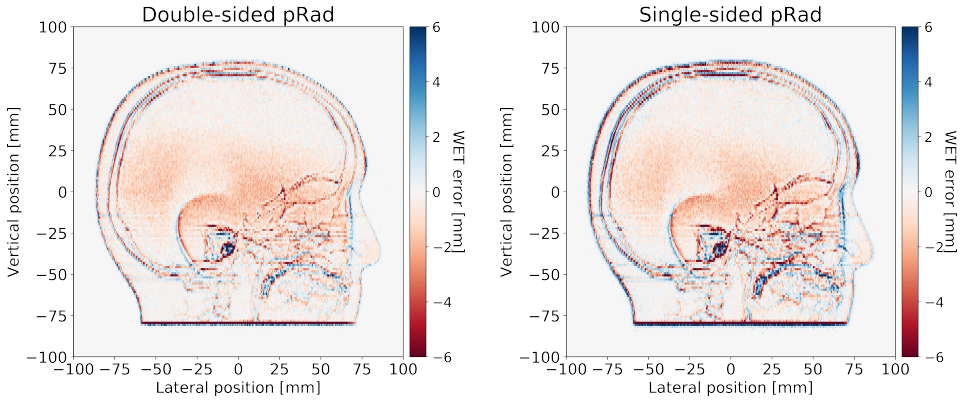

(a) **(b)**

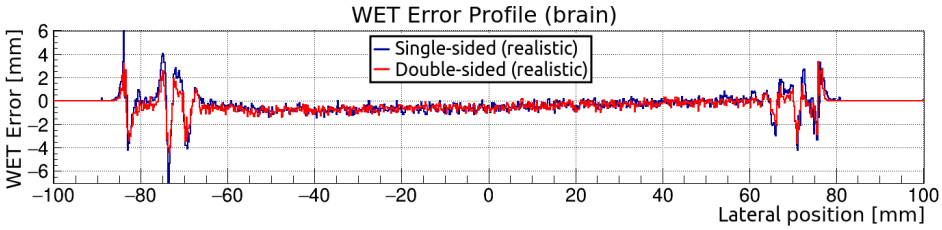

(c) WET error profile of the brain through vertical position 30 mm in (a) and (b).

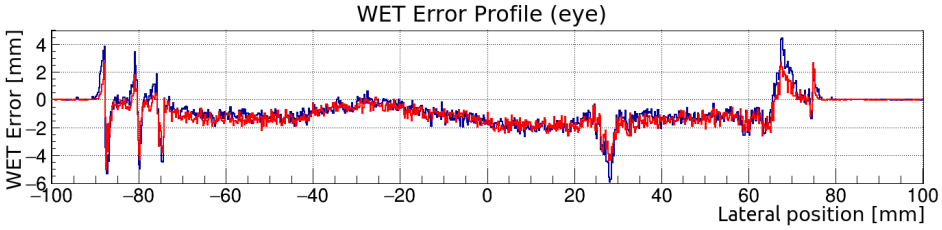

(d) WET error profile of the eye structures through vertical position 0 mm in (a) and (b).

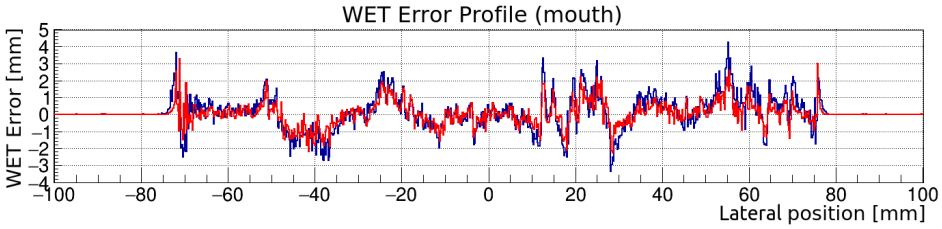

(e) WET error profile of the facial structures through vertical position -50 mm in (a) and (b).

Figure 5.61: Comparing double-sided and single-sided reconstructed WET error (a-b) with realistic trackers. Including three error profiles for detailed views of the brain, eye, and facial structures (c-e). Red curve is the double-sided image using ideal trackers, red curve is the double-sided image with realistic trackers, blue curve is the single-sided image with realistic trackers.

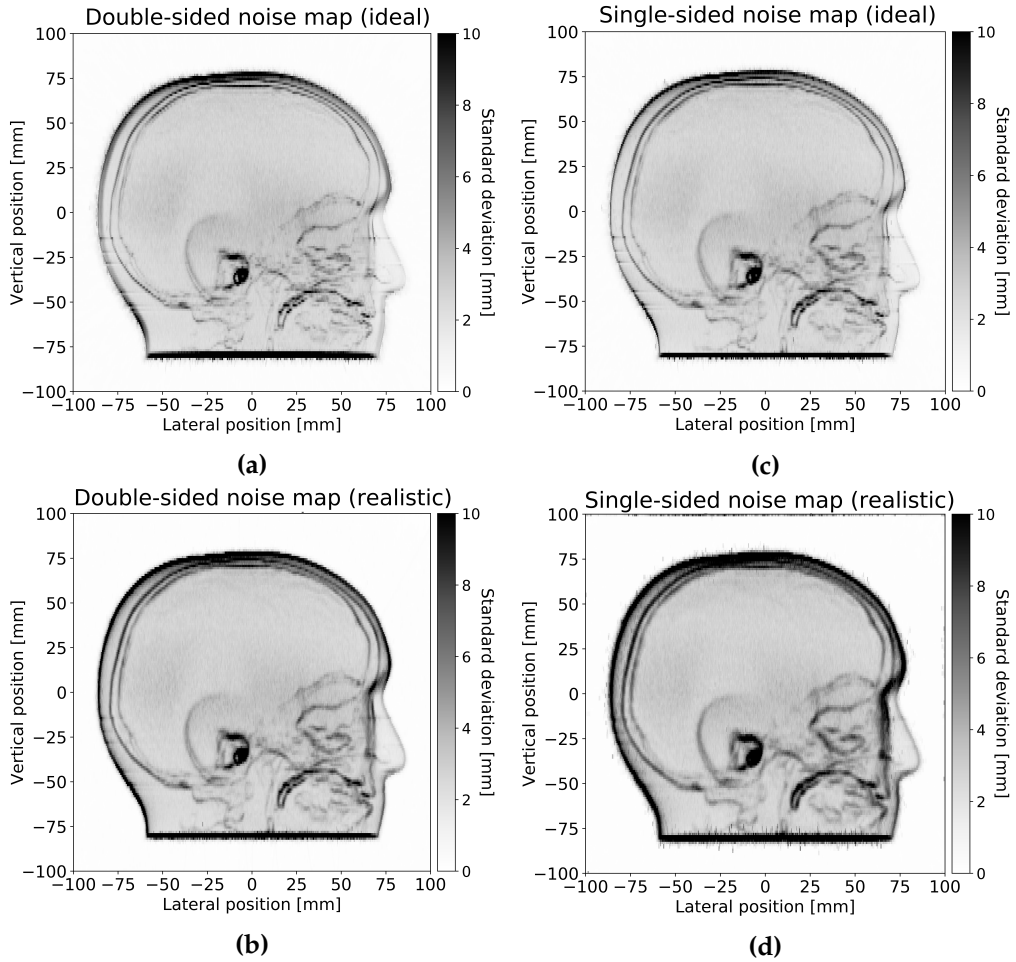

Figure 5.62: Comparing the WET noise per pixel (standard deviation of the weighted WET distribution in each pixel) for double- (a) and single-sided (c) pRad of the anthropomorphic paediatric head phantom with ideal trackers. Same for double sided (b) and single-sided (d) pRad using the Loma Linda trackers.

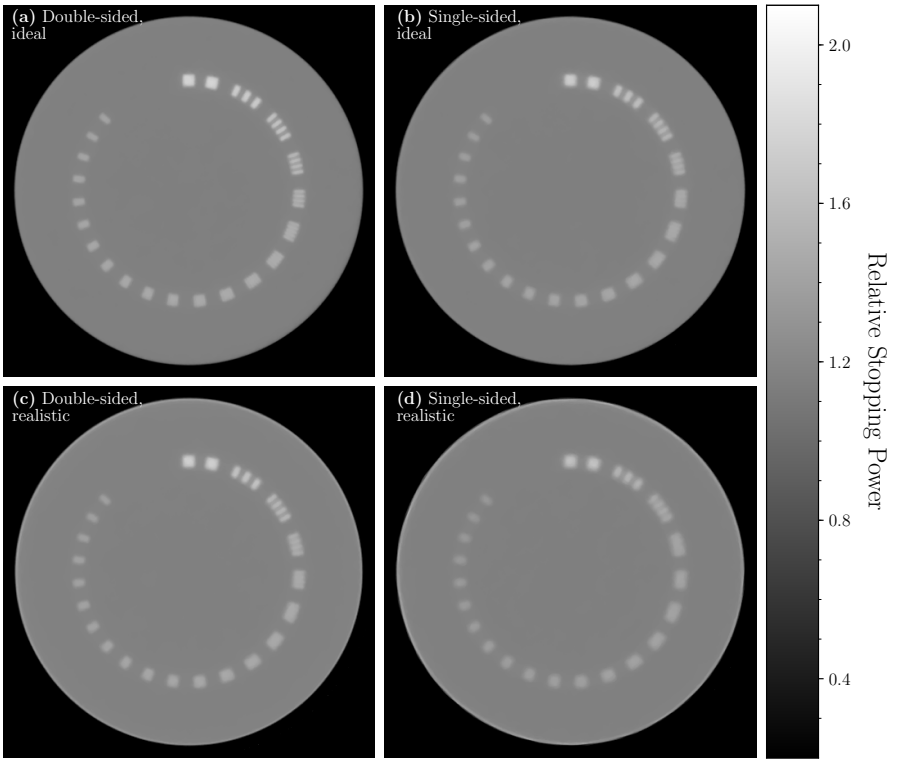

Figure 5.63: CT slice of the line-pair phantom (CTP528 phantom module). The ideal double-sided (a) and single-sided (b), as well as the realistic double-sided (c) and single-sided (d) setups.

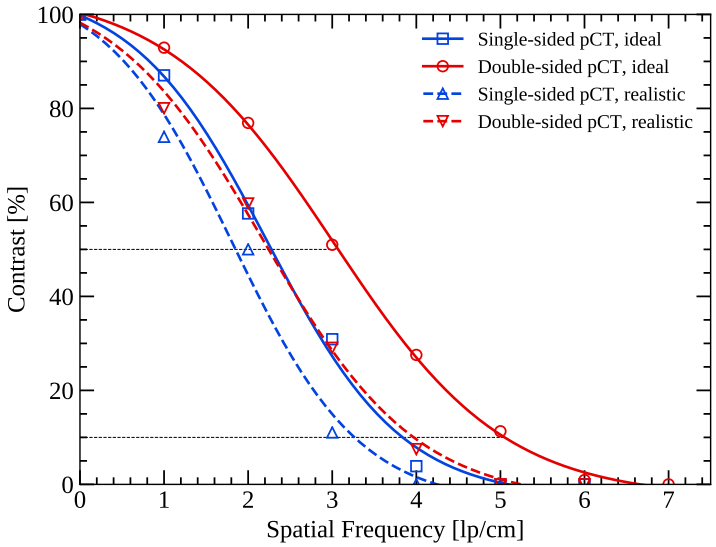

Figure 5.64: MTF of the Catphan® CTP528 line-pair module. A sigmoid fit has been performed to the data to extend the MTF over the whole frequency range. The MTF from the double-sided setup is shown in red, that of the single-sided setup is shown in blue. The solid lines depict the case of an ideal tracking system, dashed lines show the results for a realistic tracker system.

ideal imaging system was implemented. This enables to draw conclusions on the feasibility of single-sided imaging independent of the specific detector design and material budget. However, as shown already in Bopp et al. (2014) and Krah et al. (2018), a realistic tracking system deteriorates the MLP accuracy. Hence, in order to investigate the feasibility of single-sided imaging based on currently available technology, a realistic imaging system was modeled after the prototype pCT detector system developed by the US pCT collaboration. As expected, these realistic tracker properties had a negative effect on the MLP accuracy of both single- and double-sided setups (Figure 5.55). For the double-sided setup, a larger decrease in MLP accuracy was observed at the entrance region compared to the single sided setup (see Figure 5.55b). This is not surprising, as for the 200 mm water tank investigated, the uncertainty on the rear tracker measurement projected onto the phantom entrance is dominated by the scattering and therefore less influenced by the introduction of tracker uncertainties compared to the double-sided setup. Position sensitive detectors with lower material budget or smaller pixel pitch as envisioned in the design of the Bergen pCT system (Pettersen et al. 2019a) would improve the image quality for both single-and double sided reconstructions towards the ideal case (Krah et al. 2018). It has to be noted that although realistic position trackers are included in the analysis, no realistic energy detection is included as this would only serve to increase the total image noise compared to what is shown in Figure 5.62a to Figure 5.62d (see Dickmann et al. (2019) for an extensive investigation of the different noise sources of a realistic detector set-up).

A beam energy of 230 MeV was chosen, representing the highest energy setting commonly available at contemporary proton therapy facilities. A higher beam energy would improve the path estimation quality and the overall spatial resolution of the acquired images. However, for energy detection in particle imaging, where the beam is required to stop within the energy detector, choosing a higher beam energy would require a larger energy detector and hence, setting an arbitrarily high energy would not represent a clinically realistic case. In addition, with increasing energy, the noise due to range straggling would also increase (Collins-Fekete et al. 2020). On the other hand, choosing a lower beam energy than the one investigated here would lead to increased scattering and hence negatively affect the path estimation. Especially for single-sided imaging, the increased scattering would reduce the confidence in the remaining tracker information. In turn, the path estimation would depend more on the TPS information which can lead to systematic artifacts (see discussion below). It is also noted, that lowering initial energy would lead to an increase in the image noise due to the multiple Coulomb scattering (Collins-Fekete et al. 2020).

Image quality of single-sided proton imaging

Overall, the achievable image quality of single-sided proton imaging using contemporary image reconstruction techniques was lower compared to that of double-sided proton imaging, as expected. For pRad with ideal tracker planes, an average spatial resolution of 3.0 lp/cm was observed for single-sided pRad in contrast to the 4.9 lp/cm for double-sided pRad evaluated using a sharp edge gradient technique on the step-phantom inserts. For the reconstructions using realistic trackers, the spatial resolution decreased by 18 % to 4.0 lp/cm for the double-sided setup, whereas it only decreased by 10 % for the single-sided setup averaging at 2.7 lp/cm. For the single-sided setups, the spatial resolution was particularly deteriorated for the aluminium cubes located close to the entrance region when compared to the double-sided image, due to the lower path estimation quality in that region. It is also noteworthy that for both imaging set-ups, a decrease in spatial resolution was observed for the aluminium cubes close to the object exit, and that the spatial resolution constantly decreased with increasing depth for the double-sided pRad. This behavior of the spatial resolution with depth for the double-sided set-up is in contrast to the expected behavior when looking at the uncertainty of the MLP as a function of depth in Figure 5.55a. However, it is in-line with the observations made in the experimental work by Gehrke et al. (2018). This is connected to the maximum likelihood radiography reconstruction method and will be detailed in a further study to be brought forward by our group.

The pencil beam spot size as well as the distance between spots was varied to study the effect of these parameters on the image quality. In the double-sided imaging set-up, since every single proton position is measured both before and after the phantom, no adverse nor beneficial effect of smaller spot spacing or smaller FWHM pencil beam sizes was observed nor expected, given that the applied fluence field amply covers the phantom. For single-sided

imaging, all pencil beam sizes and lateral distances between spots induced sampling artifacts in the reconstructed images if only the pencil beam mean position/direction from the TPS was used as input to the path estimation. These were attributed to the systematic error in the proton entrance position and hence, systematic errors in the calculation of the weighted mean for each image pixel in the algorithm by Collins-Fekete et al. (2016).

When using the extended-MLP formalism by Krah et al. (2018) no spot spacing artifacts were observed for the 7 mm FWHM beam. However, the increased MLP accuracy associated with a thin pencil beam (2 and 3 mm FWHM) did not manifest as expected in the image quality. Instead, for the more focused 2 and 3 mm beam spot sizes the extended-MLP algorithm underestimated the spread of proton entrance positions, as can be seen in Figure 5.58b and Figure 5.58d. This resulted in sampling artifacts in the reconstructed pRad of the step-phantom similar to the ones observed when only the TPS mean position was used as input to the MLP estimation. For the two investigated beam widths, these artifacts could be removed by using a smaller spot spacing covering up the loss of information between the spots. The reason for these artifacts resides within the calculation of the MLP from Krah et al. (2018): The more certain the information provided by the pencil beam is compared to that of the rear tracker propagated to the object entrance, the less the rear tracker measurement will contribute to the estimation of the MLP at the entrance position. Hence, the entrance point of the protons will be systematically shifted closer to the TPS mean position/direction. Particularly, this depends on the rear tracker properties as well as on the scattering inside the object — and with that on the beam energy, object thickness and object material. In that regard, artifacts observed for the step-phantom were not observed for the anthropomorphic paediatric head phantom scanned with the 3 mm FWHM pencil beam, likely due to the lower WET of the phantom. To get the best possible image quality in single-sided list-mode proton imaging, the pencil beam size could be optimised as function of beam and set-up parameters in future investigations. It is important to note that a decreasing spot size and spot distance in the plan the minimum dose required to deliver the plan increases, depending on the minimum time required to irradiate a treatment spot (order of 1 ms (Schoemers et al. Sep 2015)).

For the paediatric head phantom investigated, the lower spatial resolution of single-sided pRad can be seen at the facial structures in the form of an increased WET error (Figure 5.59b) and increased pixel noise (Figure 5.62c) compared to double-sided reconstruction. Since the objective of taking a pRad for particle therapy would be pre-treatment patient alignment as well as potentially pre-treatment optimization of the Hounsfield Unit to relative stopping power lookup table (HLUT) (Collins-Fekete et al. 2017a, Krah et al. 2019), the impact of the lower spatial resolution in that context would need to be investigated. Especially for the optimization of the HLUT from the method by Collins-Fekete et al. (2017a), a reduced performance of the single-sided set-up would be expected due to the reduced path estimation accuracy. However, the WET error and noise for the homogeneous regions of the head phantom were

comparable for both single-sided and double-sided set-ups, albeit the realistic tracker properties increased the difference between the setups at heterogeneous regions. Since for the optimization of the HLUT, a smaller image area can be used (Krah et al. 2019), the feasibility of single-sided proton imaging for pre-treatment optimization would need to be systematically evaluated before definitive conclusions can be drawn.

For the simulated pCT of the CTP528 line pair module, the MTF was evaluated for both single-sided and double-sided set-ups acquired with the 7 mm FWHM scanned beam as above. With ideal trackers, the visual $MTF_{10\,\%}$ was 3.8 lp/cm for single-sided compared to 5.1 lp/cm for the double-sided pCT reconstruction, i.e. reduced by $\sim 25\,\%$. For realistic trackers, the difference between the two setups was 18 %, with $MTF_{10\,\%}$ of 3.2 lp/cm and 3.9 lp/mm for single- and double-sided setups, respectively. It has been argued in the work of Krah et al. (2018) that due to typical commercial TPS voxel size of 2 mm, the image resolution from pCT imaging should be no worse than 3 lp/cm to enable treatment planning. Following this argumentation, the single-sided set-up, in the realistic case, returned a spatial resolution just at the limit for clinical usefulness. Hence, future work should carefully investigate whether treatment planning with a single-sided pCT system would indeed be feasible.

Possible improvements of the spatial resolution of single-sided proton imaging set-ups are currently being investigated in our group. Especially, choosing helium ions to generate the images would improve the achievable image quality, due to the helium ions' reduced MCS compared to that of protons (Hansen et al. 2014a, Collins-Fekete et al. 2017d, Volz et al. 2017, Gehrke et al. 2018, Piersimoni et al. 2018). Future work will include the development of optimised image reconstruction techniques, targeted specifically for single-sided proton imaging.

Conclusion

In this work, we have compared single-sided and double-sided proton list-mode imaging. As expected, leaving out the front tracker and using the pencil beam information to reconstruct the protons paths during image reconstruction reduced the spatial resolution and increased the image noise. Using only the TPS mean position as input in conventional MLP estimation induced significant image artifacts and was ruled out for single-sided proton imaging. As of writing, the extended-MLP by Krah et al. (2018) is thus the only viable MLP estimation algorithm for use in single-sided proton imaging. When investigating the impact of the pencil beam properties on the image quality, we observed that by using the extended-MLP formalism, a smaller pencil beam spot size introduced sampling artifacts to the reconstructed image. This was shown to result from a systematic bias in the estimation of the proton paths towards the pencil beam spot's mean position. Since this shift in the estimated proton path is subject to the uncertainty of the rear tracker measurements as well as to the scattering of the protons inside the phantom, the optimal beam spot size and spot spacing should be evaluated as function of the detection system and object

properties. Single-sided pCT with a realistic rear tracker pair resulted in a spatial resolution just above what is suggested for accurate treatment planning. In future studies, the usefulness of single-sided pCT for treatment planning should to be carefully investigated based on different patient sites.

Acknowledgements

J. R. Sølie and I. Meric would like to acknowledge the financial support from Trond Mohn Foundation (Grant no. TMS2015PAR03). D. Röhrich would like to acknowledge the financial support from The Research Council of Norway (NFR) 250858.

5.7 P.III: Helium imaging in a digital tracking calorimeter

Title : Helium radiography with a digital tracking calorimeter—a Monte Carlo study for secondary track rejection

Authors : H. E. S. Pettersen, L. Volz, J. R. Sølie, J. Alme, G. G. Barnaföldi, R, Barthel, A. van den Brink, V. Borshchov, M. Chaar, V. Eikeland, G. Genov, O. Grøttvik, H. Helstrup, R. Keidel, C. Kobdaj, N. van der Kolk, S. Mehendale, I. Meric, O. H. Odland, G. Papp, T. Peitzmann, P. Piersimoni, M. Protsenko, A. U. Rehman, M. Richter, A. T. Samnøy, J. Seco, H. Shafiee, A. Songmoolnak, G. Tambave, I. Tymchuk, K. Ullaland, M. Varga-Kofarago, B. Wagner, R. Xiao, S. Yang, H. Yokoyama, D. Röhrich

Status : Under revision

Journal : Physics in Medicine and Biology

DOI : N/A

Copyright : N/A

Contributions : The principal author HESP conducted the simulations, wrote the analysis scripts for the results and finalized the plots shown in the work. LV is the principal co-author on the work and significantly contributed to the conceptualization of the work, the elaboration of the results and writing of the manuscript draft. LV and JRS wrote the software for the radiography images shown in the work. LV and HES implemented the extended MLP. DR and JS coordinated the work between the different institutions and ensured its scientific rigor. All other co-authors not mentioned contributed to the conceptualization of the work, especially the design of the digital tracking calorimeter, and reviewed the manuscript draft.

Abstract

Radiation therapy using protons and heavier ions is a fast-growing therapeutic option for cancer patients. A clinical system for particle imaging in particle therapy would enable online patient position verification, *in-vivo* measurements of the dose deposition and a reduction of uncertainties in the calculation of the relative stopping power of the patient.

Several prototype imaging modalities offer radiography and computed tomography using protons and heavy ions. A Digital Tracking Calorimeter (DTC), currently under construction, has been proposed as one such detector. In the DTC 43 longitudinal layers of laterally stacked ALPIDE CMOS monolithic active pixel sensor chips are able to reconstruct a large number of simultaneously recorded proton tracks.

In this study, we explored the capability of the DTC for helium imaging which offers favorable spatial resolution over proton imaging. Helium ions exhibit a larger cross section for inelastic nuclear interactions, increasing the number of produced secondaries in the imaged object and in the detector itself. To that end, a filtering process able to remove a large fraction of the secondaries was identified, and the track reconstruction process was adapted for helium ions.

By filtering on the energy loss along the tracks, on the incoming angle and on the particle ranges, 97.5% of the secondaries were removed. After passing through a 16 cm water phantom, 50.0% of the primary helium ions survived and their tracks were reconstructed; after the filtering 42.4% of them could be used for imaging. Helium track reconstruction leads to more confused track pairs when compared to proton track reconstruction, due to the increased focus strength of the helium beam. The helium range accuracy was approx. 0.5 mm WEPL in a water phantom, compared to the proton range accuracy of 0.25 mm WEPL. In an anthropomorphic head phantom, the WEPL accuracy was 0.9 mm WEPL for helium compared to 1.1 mm WEPL for protons. This accuracy is expected to be sufficient for helium imaging for pre-treatment verification purposes.

Introduction

Radiation therapy using protons and heavier ions is a fast-growing therapeutic option for cancer patients. However, the possibility of *in-vivo* verification of the dose distribution given to the patient is lacking compared to conventional radiation therapy using photons (Parodi & Polf 2018a), this is also true for online verification of the patient positioning (Hammi et al. 2018). In addition, there are uncertainties connected to the conversion of the measured X-ray mass attenuation of the planning CT to the Relative Stopping Power (RSP) needed during treatment planning in the order of 2%–3% (Paganetti 2012). Using Dual Energy CT, the uncertainty is further reduced by up to 1% (Bär et al. 2017, Almeida et al. 2018).

Direct measurement of the RSP prior to treatment as an input to or correction to the treatment planning system (TPS) using particle imaging is currently being explored (Johnson 2017). By measuring the energy loss of high-energy particles traversing the patient, it is possible to calculate the RSP along the particle's estimated path. In list-mode (non-integrated) particle Computed Tomography (PCT) two sets of particle trackers measure the position/direction of each particle, yielding their curved path through the patient (Li et al. 2006, Williams 2004, Schulte et al. 2008, Collins-Fekete et al. 2017d, Krah et al. 2018). A sufficient number of projections (180–360) is then acquired in order to reconstruct volumetric RSP images for use in dose calculation (Li et al. 2006, Plautz et al. 2016, Hansen et al. 2014a). Particle radiography (PRad) has been suggested for use in positioning and range verification by correction of the existing CT-based RSP map (Krah et al. 2019, Collins-Fekete et al. 2017a, Dias et al. 2019). So far, no PCT or PRad systems are clinically available.

Helium Imaging

Due to the more widespread availability of proton therapy centers compared to heavy ion therapy facilities, most research in the field of particle imaging so far has focused on protons as the particle species used to generate images. Recently, the possibility of using helium ions for imaging has been explored due to its reduced scattering power, leading to improved spatial resolution (Hansen et al. 2014a, Collins-Fekete et al. 2017d, Volz et al. 2017, Piersimoni et al. 2018, Gehrke et al. 2018), as well as its potential for on-line treatment monitoring (Volz et al. 2020b). So far, few studies on experimental helium list-mode imaging are available (Volz et al. 2017, Volz et al. 2018, Gehrke et al. 2018, Amato et al. 2020).

Compared to protons, helium has an increased probability of nuclear interactions leading to secondary particles inside the patient and the detector, especially due to the possibility of projectile fragmentation (Durante & Paganetti 2016, Gehrke et al. 2018, Volz et al. 2018). Any detection system (helium CT or helium radiography) must hence be able to effectively filter out secondary particles. In Volz et al. (2018) this additional fragmentation filter consists of a $\Delta E - E$ cut in the multistage scintillator of the US pCT consortium presented in Johnson et al. (2016). In Gehrke et al. (2018), a CMOS pixel sensor (TimePix) is used both as the tracking detector technology and as the energy detector. To suppress secondary particles they applied a threshold on the size of the charge clusters generated by the particles on the chip.

The Digital Tracking Calorimeter

Pettersen et al. (2017) showed that a Digital Tracking Calorimeter (DTC) consisting of a stack of silicon pixel sensors is able to individually reconstruct a large number of proton tracks measured simultaneously in a single read-out cycle. Subsequent design optimization and experimental measurements have shown promise in regards to proton imaging, as well as detection of heavier

ions (Pettersen et al. 2019a, Tambave et al. 2019). The DTC is currently under development and prototyping (Alme et al. 2020).

The final DTC concept is that of a 3D pixel matrix for reconstruction of a large number of simultaneously recorded particle trajectories, enabling PCT and PRad. It uses the high-granularity CMOS pixel chip ALPIDE of the ALICE-ITS upgrade at CERN (Rinella 2016). The ALPIDE pixel sensors have a pixel pitch of $29.24 \times 26.88\,\mu\text{m}^2$ and a fast readout cycle of 5 to 10 μs due to its binary readout (no energy discrimination above the activation threshold) and zero-suppression (no data transmitted from inactive pixels).

Especially, the simultaneous track reconstruction capabilities of the DTC are favorable in the context of particle imaging: the DTC might allow for higher particle rates at cyclotron and synchrotron accelerators compared to current detector designs despite the bunched beam structure with bunches typically lasting 20 to 50 ns and spaced 100 to 200 ns apart (Krimmer et al. 2018).

Other than most currently developed PRad and PCT systems that feature both a front and rear tracking system, the envisioned DTC will rely only on a rear tracker. The path estimation is then performed using the available pencil beam scanning system information to fill in the missing front tracker measurements. The reason for this lies in the simultaneous measurement of a high multiplicity of particle tracks. Due to the scattering in the phantom, correct matching of front and rear tracker vectors would be difficult. An evaluation of the image quality achievable with such a system (denoted single-sided in this work) is presented in the recent work by Sølie et al. (2020).

In that regard, the favorable scattering of helium ions is expected to be beneficial especially also for a single-sided system: The focus strength achievable at a clinical pencil beam scanning system is determined not only by the focusing in the beam line, but especially also from the scattering in the beam monitoring system and air drift between nozzle and patient. Hence, helium ions can be focused more compared to proton beams. For example at the Heidelberg Ion-Beam Therapy Center (HIT), the highest clinical focus strength for a proton beam has a full width at half maximum (FWHM) spot size of 7 mm, while for the helium beam a 4 mm FWHM is possible at the highest beam energy (Kleffner et al. 2009).

In this work, we are interested in studying the feasibility of the DTC in regards to helium imaging using Monte Carlo simulations. We aim at exploring several questions of relevance to helium beam imaging with a DTC. First, since the ALPIDE chips have binary readout, the energy deposited inside the ALPIDE by a traversing particle (E_{dep}) is calculated based on the size of the charge diffused area. Helium has a higher $\mathrm{d}E/\mathrm{d}z$ in the detector, and it will be of interest to evaluate how this will affect the E_{dep} resolution (impacting the range assessment and filtering of helium fragments) and cluster separation (impacting the track reconstruction). Second, compared to protons, the helium track reconstruction process is expected to be degraded by the increased cluster merging, the possibility of a thinner pencil beam (higher particle density) and the increased secondary production. On the other hand, the

tracking should be improved by the reduction of multiple Coulomb scattering. Hence, the tracking algorithm should be adapted for helium imaging and tested. Third, the DTC is planned to contain layers of 3.5 mm aluminum slabs for energy absorption. Due to the dependence of projectile fragmentation with the target atomic mass (Zeitlin & La Tessa 2016), it is of interest to investigate different absorber materials in terms of primary survival in the detector.

Secondary Particle Production

When helium ions traverse the imaged object and the detector, there is an increased probability of secondary production compared to protons. This is primarily due to the mass/charge ratio changing nuclear interactions leading to projectile fragmentation and an increased cross section for target fragmentation (Loveland et al. 1986, Zeitlin & La Tessa 2016). The secondaries from target fragmentation are isotopes of the target material, having low range and high linear energy transfer (LET).

The lighter fragments originating from projectile fragmentation have similar velocity and direction (and thus, residual range) compared to the initial helium particle (Zeitlin & La Tessa 2016, Rovituso et al. 2017). The fragment species are mainly protons, deuterons, tritons, neutrons and ^{3}He (Krämer et al. 2016).

In range telescope detectors such as the DTC, one could in principle think of including the secondary fragments in the image reconstruction process due to their similar residual range. However, for protons (which is the predominantly produced projectile fragment (Rovituso et al. 2017)), there are several competing production channels (Krämer et al. 2016) leading to shorter residual ranges such as inelastic scattering from the produced projectile fragments and neutron absorption (Rovituso et al. 2017). Hence, a model for the energy loss at the fragmentation process is necessary before recuperation of the excess dose given to the patient due to fragmentation would be possible.

Since the DTC reconstructs the tracks of 50–200 simultaneously recorded particles, any produced secondary may introduce confusion in the tracking process. The contribution of secondary particles has been shown to largely be suppressed with energy deposition-based filters (Volz et al. 2018, Gehrke et al. 2018), and hence similar filters will be explored in the following.

Methods

Detector Geometry

The detector consists of two low-mass tracker layers, followed by 41 calorimeter layers where the particles are stopped and tracked. The tracker layers are placed 5 cm apart from each other, and from the calorimeter layers (Sølie et al. 2020). A schematic design of one of the two tracker layers and one of the 41 calorimeter layers as implemented is shown in Figure 5.65.

The geometry as laid out in in Alme et al. (2020) was here implemented and simplified towards a representative *longitudinal* material distribution. In

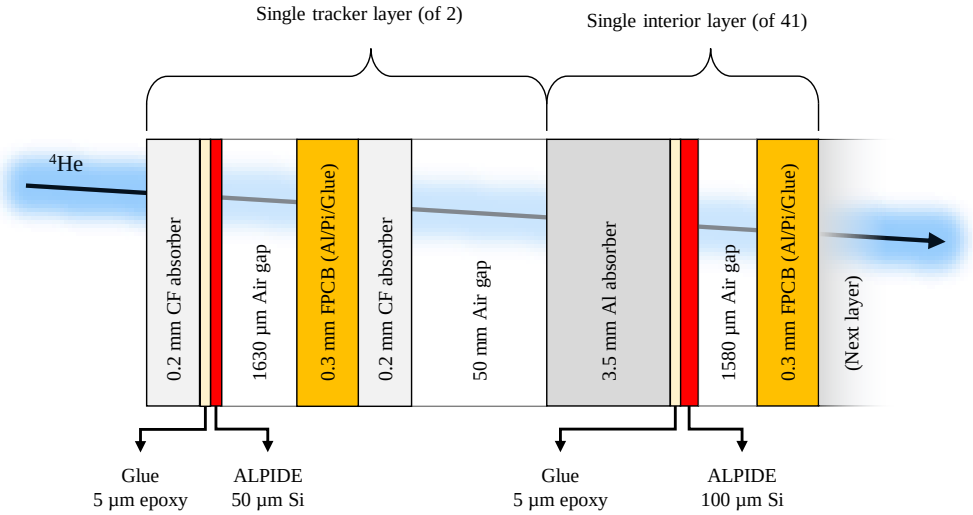

Figure 5.65: The materials and thicknesses of the different sub layers in the implemented design of the DTC: one tracker layer and one calorimeter layer are shown. CF: Carbon fiber, FPBC: Flexible printed circuit board, Pi: Polyimide.

short, a layer here consists of the flexible PCB (FPCB) glued onto an 3.5 mm aluminum absorber backing, with the ALPIDE glued on top of the absorber. A single calorimeter layer has a water-equivalent thickness of 8.2 mm. The first two layers which form the rear tracker of the device are mounted on $2\times200\mu$m carbon fiber (CF) absorbers for stabilization. This is done in order to reduce the amount of scattering when measuring the position and angle of the particle track, resulting in a layer-wise water-equivalent thickness of 1.8 mm. Finally, the WEPL of the detector is 33 cm, allowing for objects of up to $\sim$30 cm to be reconstructed: the primary ion must traverse three calorimeter layers for the track reconstruction to work properly.

Monte Carlo Simulations

In this study the Monte Carlo (MC) software GATE version 8.2 (Jan et al. 2004, Jan et al. 2011, Sarrut et al. 2014) and Geant4 version 10.5.1 (Agostinelli et al. 2003, Allison et al. 2016) were used. The physics list `QBBC_EMZ` with a mean ionization potential of water of 78 eV was applied. The step length was adjusted to a maximum of 1 mm to accurately track the helium through the imaged object (in the detector the step length is limited by the small slab thicknesses) and the production thresholds for $\gamma, e^{\pm}$ and protons were set to 10 μm inside the ALPIDE chip (keeping the default value of 0.7 mm outside the sensitive areas). This has been shown to yield sufficient accuracy (Pettersen et al. 2019a).

The helium beam was defined as a gaussian pencil beam with an FWHM of 4 mm with a divergence of 1 mrad (Schoemers et al. Sep 2015). The energy was 229.25 MeV/u, determined by having the same range in water as 230 MeV protons (32.9 cm) (Berger et al. 2005). For the analysis of track reconstruction and filter performance, 10^5 primary helium ions were simulated. The radiography

in Section 5.7 and the comparison of primary survival in Section 5.7 required improved statistics of, respectively, 5000 primaries/spot for 2150 pencil beam spots and 10^6 primaries per material.
The simulations used in the analysis were performed using only the ALPIDE chip slabs as sensitive detectors: the energy loss in each layer along a particle's path was fitted to the pristine Bragg-Kleeman depth-dose curve yielding the estimated WEPL of each track (Pettersen et al. 2017).

Charge Diffusion Model

A charged particle passing through the epitaxial (sensitive) layer of an ALPIDE chip will normally activate 5–30 pixels around its track. This is due to the lack of a reverse bias voltage across the sensitive layer, enabling charge diffusion of the released electron-hole pairs. This process was studied in Tambave et al. (2019) (including a library of 22000 measured cluster shapes) and modelled in Pettersen et al. (2019a). A power law between the number of activated pixels n and the E_{dep} (in keV/mum) was found to be

$$n = 4.23 \cdot E_{\text{dep}}^{0.65}. \tag{5.62}$$

For each hit in MC generated data, a discrete position was assigned corresponding to the center of the closest pixel. The charge diffusion process was then modelled by randomly choosing a cluster shape with the correct size from the cluster library according to Equation 5.62. In addition, for helium applications with high E_{dep}, there were several cases where the E_{dep} values were outside the bounds of the library (above $\sim$28 pixels/cluster, corresponding to $\sim$19 keV/μm). In these cases, a circular cluster shape was generated up to 70 pixels/cluster (75 keV/μm) according to Equation 5.62. Before applying the charge diffusion model, all particles contained within a single pixel (such as short range electrons) were binned together.

Close hits (with a lateral distance of $< 150\,\mu$m) could result in merged clusters. While the track reconstruction algorithm allows for a missing cluster in a single layer through further extrapolation, 3%–5% of the proton tracks were pairwise confused due to cluster merging in Pettersen et al. (2019a).

Helium Track Reconstruction

Using the 3D hit information throughout the DTC it is possible to reconstruct a high number of simultaneous particle tracks resulting from a single data readout cycle (in this study up to 150 primaries per bunch were considered). In Pettersen et al. (2019b) track reconstruction algorithms for the DTC were presented. In short, a track-following and track-splitting scheme (Strandlie & Frühwirth 2010) were applied starting at the distal end of the detector and moving to the front end.

For each seed hit in the last active layer, every nearby hit in the next-to-last active layer were identified. For each hit-pair, the track was extrapolated to the next layer, where the angular deviation to the closest match (or two) was calculated. When two similar matches were identified, both candidate tracks

were explored. This process was repeated until one of two conditions was met: Either the first layer was reached, or the total angular deviation along the track $S = \sqrt{\sum_{i=0}^{n}(\Delta\theta_i)^2}$ was larger than a pre-set value $S_{\max} = 275\,\text{mrad}$. To avoid discarding straight track segments, only tracks where new segments exceed $\Delta\theta_{i,\max} = 100\,\text{mrad}$ in addition to $S > S_{\max}$ were discarded. These values were previously found using a proton beam: For helium applications, due to less expected scattering of the primaries, it is expected that a tighter bound can be put on the $S_{\max}, \Delta\theta_{i,\max}$ parameters.

At the end, several tracks originated from a single seed in the last layer: the straightest track (lowest S) was kept, and the remaining hits were available for the next track candidate. This procedure was found to yield acceptable results for track reconstruction for both thick (Pettersen et al. 2017) and thin (Pettersen et al. 2019a) absorber layers. In addition, a forward (front-to-back) track-filling model was subsequently applied to identify unused clusters downstream to the reconstructed tracks. To consider a track correctly reconstructed it has to originate from the same primary, and must be completely reconstructed at its endpoints (detector front face and its last hit). Thus we can define the fraction of completely reconstructed tracks (FCR) as the number of correctly reconstructed tracks divided by the total number of tracks. The FCR is given after filtering is applied.

The reconstructed tracks could then be aggregated down to their essential values necessary for image reconstruction: The initial tracker vector (equivalent to the rear tracker position and direction information) and the WEPL of the track (see next section).

Range Calculations

The WEPL range of a single projectile was found by performing a model-fit of the $\mathrm{d}E/\mathrm{d}z$ to the Bragg-Kleeman depth-dose function along the projectile's track, as suggested in Pettersen et al. (2017). Then, a collection of projectiles give rise to the mean WEPL and the WEPL uncertainty (range straggling) by calculating the mean and standard deviation from a histogram over the individual WEPL values.

Detector Calibration

The detector was calibrated through MC simulations with increasing water phantom thicknesses, where the (MC truth) stopping position of the primaries inside the detector were recorded. The water-equivalent path length (WEPL) to each detector layer was stored and later interpolated using cubic splines. The imaged object's water-equivalent thickness is then the primary beam's range in water subtracted by the particles' reached detector depth.

WEPL Accuracy and Uncertainty

To quantify the WEPL accuracy and uncertainty in the detector calibration and in the radiographic images, we extracted statistics from, respectively, WEPL error look-up-tables and images.

For the detector calibration, each water phantom thickness yielded a nominal (MC truth) WEPL value. This difference between the reconstructed WEPL and the nominal WEPL is the WEPL accuracy. The accuracy was plotted as a function of object thickness. The mean and standard deviation of the accuracy across all water phantom thicknesses were calculated: the standard deviation of this distribution is the width of the distribution of WEPL errors, or the WEPL error envelope.

This procedure was repeated for the radiographic images: subtracting the "MC truth" image from the reconstructed image, we obtained a pixel-wise WEPL error map. The standard deviation of all WEPL errors is reported as the width of the distribution of pixel-wise WEPL errors.

Another metric is the WEPL uncertainty, or measured range straggling. It was observed in Pettersen et al. (2019a) that the number of layers covered by a range straggling distribution played an important role in the WEPL accuracy. This was because a broader distribution (or less distance between the layers) lead to more layers being involved in the calculation of the mean WEPL, reducing the width of the WEPL error distribution. In this work, using the detector calibration setup, we calculated the $\pm 2\,\sigma$ window of the simulated WEPL uncertainty as a proxy for the layer coverage.

Absorber Material Optimization

In Pettersen et al. (2019a) energy-degrading absorber layers of 3.5 mm aluminum were recommended for proton imaging using the DTC. It is of interest to explore whether alternative materials are favorable for helium imaging with regards to the depth-dependent survival of the primary particles.
Three different materials were considered for the absorber in each detector layer: the original aluminum ($\rho = 2.7\,\mathrm{g/cm^3}$), graphite ($\rho = 1.7\,\mathrm{g/cm^3}$), carbon foam ($\rho = 0.7\,\mathrm{g/cm^3}$) and PMMA ($\rho = 1.19\mathrm{g/cm^3}$): The thickness of the materials were scaled up to match the water equivalent thickness of 3.5 mm aluminum at 125 MeV/u, this to ensure that the beam ranges are equal in terms of the number of traversed layers. These thicknesses correspond to 4.86 mm, 11.79 mm and 6.37 mm for graphite, carbon foam and PMMA, respectively. A water phantom of 10 cm thickness was placed before the detector in this simulation. The number of primary particles was scored in each detector layer (note that, in order to reduce the uncertainties, track reconstruction was not applied here as only the primary hits were scored). Then the reduction of the number of primaries close to the Bragg peak relative to the number of primaries in the first layer was found for each material.

For this study, the inelastic nuclear-nuclear cross sections from Shen et al. (1989) were used in GATE, through the ^{4}He model `G4BinaryLightIonReaction` and dataset `G4IonsShenCrossSection`. This combination was recently verified for helium projectiles in the relevant energy range (Horst et al. 2019).

Filtering of Secondary Particles

The goal of the filtering process is to remove as many secondaries as possible while keeping the number of primaries more or less intact. In this section, we will explicate the criteria to decide upon which distributions should be used for filtering, and the cut values of the various filters after applying them successively. The threshold values were found by comparing the distributions of primary and secondary tracks.

In this study, a helium pencil beam as previously defined in Section 5.7 was impinging on a water phantom of depth 16 cm and lateral dimensions to match the detector, placed with an air gap of 14.5 cm between the phantom and the front tracker.

We define here a secondary particle as a track that either was a secondary particle, or one that at some stage produced a (hadronic) secondary particle (*i.e.* a primary helium ion producing a target fragment but staying intact itself). In addition, tracks that were incompletely reconstructed (thus containing no Bragg peak) were tagged as secondary particles as they should be removed by the filtering process.

Filtering on Small Pixel Clusters

A high number of low E_{dep} hadrons were usually seen in the simulated DTC data after a detector readout threshold of 0.1,keV/mum was applied in accordance with Tambave et al. (2019).

Before track reconstruction, a filter was applied on clusters of $<= 5$ pixels (corresponding to $E_{\text{dep}} < 1.3\,\text{keV}/mu\text{m}$). In Figure 5.66 (top) the cluster sizes of primary and secondary particles are shown. This filter simplifies the track reconstruction, however a conservative cut value was chosen as to minimize the number of removed primary particles used for the track reconstruction.

Filtering on Minimum Track Length

All tracks crossing fewer than five layers (including the two tracker layers) were removed—a Bragg peak occurring in this region would correspond to an imaged object size in excess of 30 cm WEPL which is currently outside of the scope of the DTC (Pettersen et al. 2019a), or to a secondary / incomplete tracked particle.

Filtering on the Deposited Energy

The E_{dep} is a powerful discriminatory tool for particle identification due both to the shape of a particle's depth dose-curve (leading to rejection of incorrectly reconstructed and disappearing tracks) and to the large differences in $\mathrm{d}E/\mathrm{d}z$ between different particles (leading to particle identification).

The DTC yields an estimate of the E_{dep} in each traversed layer along a particle's track, and hence we defined two filters: one for the Bragg peak region and one for the plateau region.

First, for a primary particle we required that the deposited energy in its last tracked layer (downstream) be at least $8\,\text{keV}/mu\text{m}$. This filter is shown

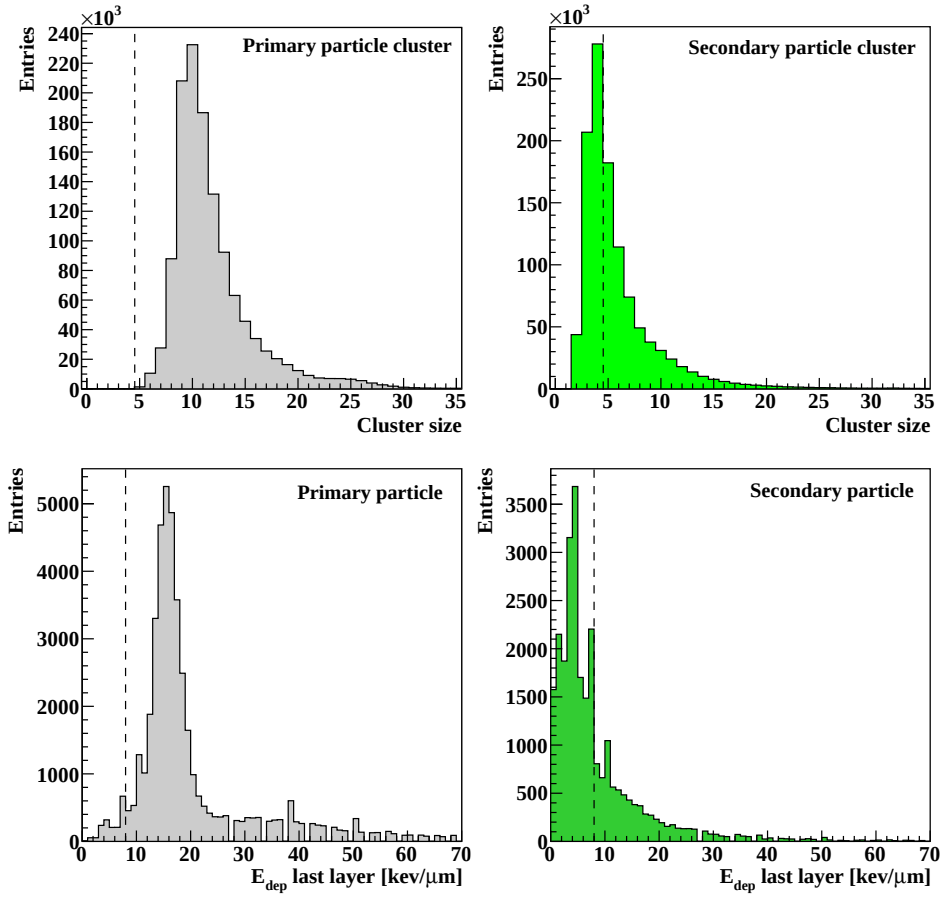

Figure 5.66: Top: The cluster size distribution of primary and secondary hits in the detector prior to track reconstruction. The cut value is $<= 5$ pixels per cluster. Bottom: Filter on the E_{dep} in the last layer, as calculated by the diffused cluster size. The cut value is 8 keV/mum.

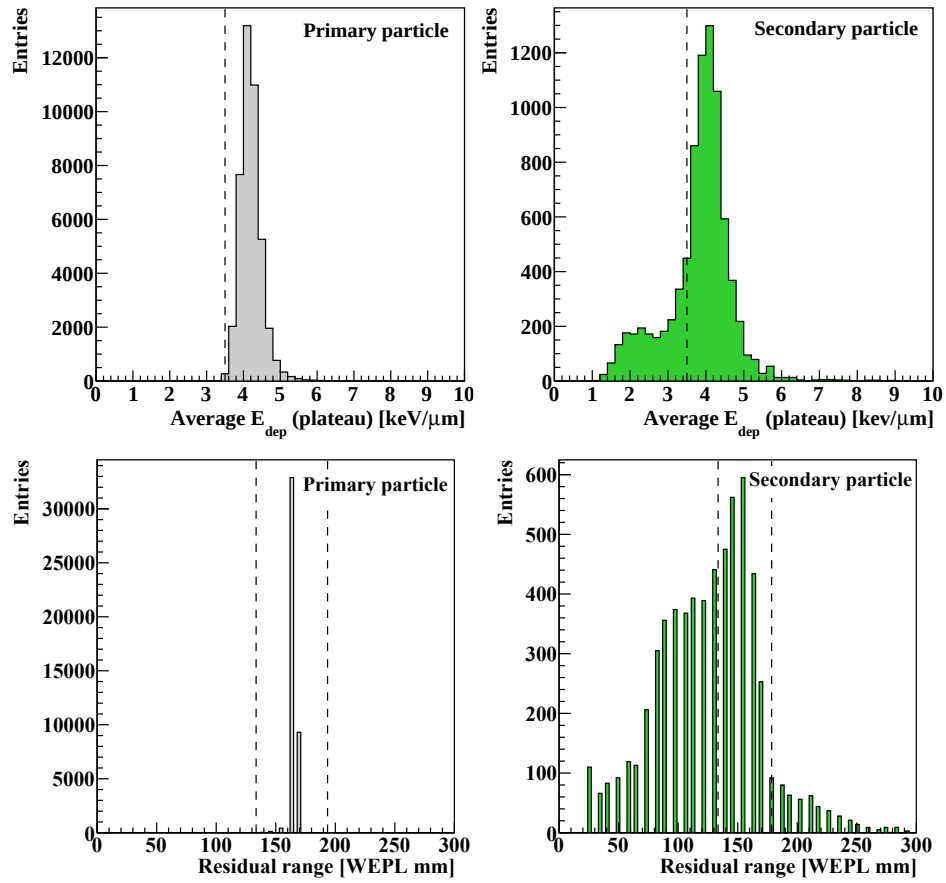

Figure 5.67: Top: Filter on the deposited energy in the plateau region, as calculated by the diffused cluster size. The cut value is 3.5 keV/mum. Bottom: Filter on the range inside a pencil beam. The highest bin μ is chosen together with a 3σ range window.

in Figure 5.66 (bottom). Second, a cut was placed on the deposited energy in the plateau region of a single track, as defined by the mean E_{dep} of the first five traversed layers. A threshold value of 3.5 keV/mum was set as shown in Figure 5.67 (top).

Filtering on the Track's Residual Range

A combined histogram for all the residual ranges yielded the peak range bin μ, and a 3σ cut on the range is performed. The distributions are shown in Figure 5.67 (bottom). This filter is not specific to helium imaging, as it is usually performed during image reconstruction on a pixel-wise basis (Collins-Fekete et al. 2016, Penfold 2010).

Filtering on the Incoming Angle

To remove fragments originating from the object as well as particles that underwent single large angle scattering, a filter on the particle's incoming angle

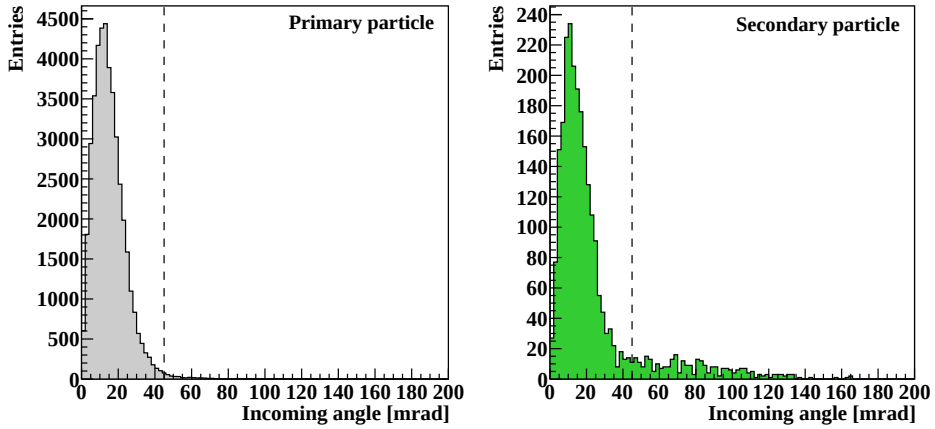

Figure 5.68: Filter on the incoming angle. The filter value is 45 mrad.

was performed. The incoming angle is found from the two tracker layers. The filter also removes primary particles that underwent non-Coulomb scattering events such as elastic nuclear scattering (Krah et al. 2018, Gottschalk 2012). Here a 45 mrad filter was applied, corresponding to the $3\,\sigma$ value of the total angular distribution in Figure 5.68.

Primary Survival Efficiency

A helium primary may be lost to physical processes such as nuclear interactions or large angle scattering, happening inside the imaged object or detector. It may also be lost during the track reconstruction or during the filtering step. To quantify the primary loss from these processes we counted the number of primaries that survived each step using the 16 cm water phantom simulation from Section 5.7.

Intrinsic Efficiency

The transmission through water is given as $\varepsilon_{\mathrm{w}} = N_{\mathrm{w}}/N_0$, where N_0 is the number of particles in the beam and N_{w} number of particles at the phantom exit.

The transmission through the detector is then given as $\varepsilon_{\mathrm{DTC}} = N_{\mathrm{BP}}/N_{\mathrm{w}}$, where N_{BP} is the number of primaries reaching the proximal tail of the range distribution, *i.e.* two layers upstream to the beam's residual WEPL range.

The intrinsic efficiency of the detector due to physical effects can then be found as

$$\varepsilon_{\mathrm{int}} = \varepsilon_{\mathrm{w}} \times \varepsilon_{\mathrm{DTC}} = \frac{N_{\mathrm{BP}}}{N_0}. \tag{5.63}$$

Algorithmic Efficiency

The track reconstruction algorithm analyses N_{BP} hit trajectories, yielding finally N'_{BP} tracks—this number might be higher than N_{BP} due to reconstructed

shorter tracks ending proximal to the Bragg peak area. Thus the tracking efficiency can be given as $\varepsilon_{\text{tracking}} = N'_{\text{BP}}/N_{\text{BP}}$.

The secondary filtering is applied after the tracks have been reconstructed. The primary survival efficiency can then be given as $\varepsilon_{\text{filter}} = N''_{\text{BP}}/N'_{\text{BP}}$, where N''_{BP} is the final number of primaries remaining subsequent to the filtering.

The algorithmic efficiency is then the product of the primary loss due to track reconstruction and due to the secondary filtering.

$$\varepsilon_{\text{alg}} = \varepsilon_{\text{tracking}} \times \varepsilon_{\text{filter}} = \frac{N''_{\text{BP}}}{N_{\text{BP}}} \tag{5.64}$$

Total Efficiency

The total efficiency is the product of the intrinsic (determined by the physics of the setup) and algorithmic efficiency (determined by the effectiveness of the applied algorithms):

$$\varepsilon_{\text{tot}} = \varepsilon_{\text{int}} \times \varepsilon_{\text{tracking}} = \frac{N''_{\text{BP}}}{N_0}. \tag{5.65}$$

Furthermore, the value $\varepsilon_{\text{HeRad}}$ for helium radiography (and $\varepsilon_{\text{pRad}}$ for proton radiography) is the total efficiency of the system (ε_{tot}) multiplied by the additional primary survival efficiency after image reconstruction has been performed.

Single-Sided Helium Trajectory Calculation

To estimate the helium trajectories, we implemented the extended MLP formalism by Krah et al. (2018). The formalism uses the available pencil beam scanning parameters (lateral position of the spot center and beam co-variance matrix) in place of the front tracker information. Within the formalism, the energy loss represented by the integral over the momentum velocity function of the particles was computed numerically using the same polynomial parametrization as used in (Sølie et al. 2020) for protons. This is valid also for helium ions at the same initial energy/range (Collins-Fekete et al. 2017d, Gehrke et al. 2018, Volz et al. 2020a). The MLP accuracy was estimated using the methodology of Sølie et al. (2020) with the realistic tracker geometry and uncertainties of the DTC. The accuracy was compared to a realistic 7 mm FWHM proton beam.

Single-Sided Helium Radiography

To assess the expected image quality for helium ion radiography with the DTC, we investigated an anthropomorphic pediatric head phantom model HN715 (CIRS, Norfolk, Virginia, USA). The phantom was available as a digital geometry from the work of Giacometti et al. (2017a). A detailed material list as implemented in the GATE simulations here can be found in Sølie et al. (2020).

For this work, the same setup geometry for source and phantom positioning relative to the first tracking layers as in Sølie et al. (2020) was used. The primary helium beam with an FWHM of 4 mm consisted of 2150 discrete pencil

beam spots placed in a grid with a 4 mm spacing in both lateral directions, the spacing being equal to the FWHM of the pencil beams. Each pencil beam spot contained 1250 primary helium ions. This corresponds to approx. 25 primaries per mm^2 used for image reconstruction after filtering, based on a recommendation of 100 protons per mm^2 for radiographs and 100 protons per mm^3 for tomographic images (Sadrozinski et al. 2013), and that the reduced straggling of helium reduces the required number of primaries by a factor of four (Gehrke et al. 2018).

The radiation dose given to the head phantom during the acquisition of a HeRad was calculated in GATE, as well as corresponding dose for a proton radiography with approx. 100 protons per mm^2 after filtering. For comparison with x-ray CT, we apply the CT Dose Equivalent Index (CTDEI) framework of Hansen et al. (2014a) where an ion CT weighted quality factor of $Q_W = 2$ is recommended as a safe assumption, and simplify the mean head dose to be the CT Dose Index (accurate to within 1% (Hansen et al. 2014a)). Furthermore, for the calculation of the effective dose of IRCP report 102 (ICRP 2007) for a pediatric head, where a dose conversion factor of $Q_W = 0.0032\,\mathrm{mSv/cm\,mGy}$ is multiplied with the dose length product (CTDEI$\times$scan length).

The helium ion radiograph was reconstructed using the maximum likelihood formalism developed by Collins-Fekete et al. (2016). It was implemented for a similar single-sided setup in Sølie et al. (2020).

Results

Helium Track Reconstruction

An optimization was performed in order to identify the ideal parameters for the track reconstruction. The parameter $S_{\max}$ was reduced from 275 mrad to 175 mrad, while the $\Delta\theta_{i,\max}$ was reduced from 100 mrad to 30 mrad.

After performing the secondary filtering, the fraction of correct tracks (FCR) is slightly lower for helium than for protons. It is also higher for larger traversed phantoms than for smaller (due to the shorter reconstructed path length in the detector). In Figure 5.69 the FCR in a few scenarios are shown, compared to a proton beam with a larger beam spot size (7 mm FHWM).

The time required to reconstruct the helium tracks (excluding the time spent modelling the charge diffusion process) is 1.4 ms per primary on an Intel® Xeon® Gold 6136 CPU @ 3.00 GHz, or approximately 40 seconds for a complete radiograph utilizing a 96 CPU core cluster. It should be stressed that the FCR and speed are subject to continual improvement due to their sensitivity to the applied filtering, beam quality, tracking parameters and constituent algorithms.

Absorber Material Optimization

The depth-dependent survival of the helium beam in three different materials is shown in Figure 5.70. The aluminum absorbers yielded relative improvements of $8.1\% \pm 0.3\%$, $8.9\% \pm 0.3\%$ and $9.2\% \pm 0.3\%$ in track survival compared

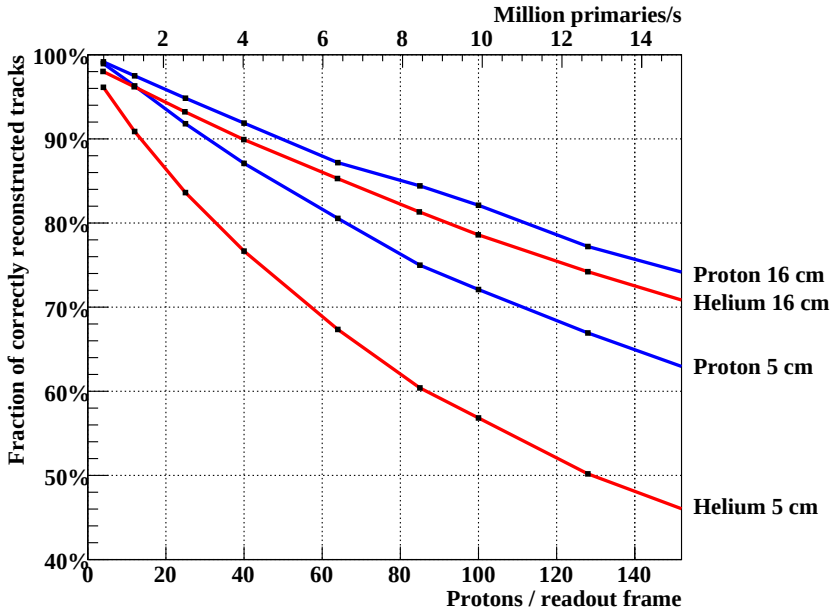

Figure 5.69: The fraction of correctly reconstructed tracks relative to the surviving tracks after filtering, as a function of the number of primary 4 mm FWHM helium ions per reconstruction cycle. The corresponding data for a proton beam with a spot size of 7 mm FWHM in the same detector geometry is shown as well. Tracks originating from a 5 cm and a 16 cm water phantom are used.

to the graphite, carbon foam and PMMA based absorbers, respectively. The survival was evaluated in the last layer before the Bragg peak region (layer number 29 in the figure). This excludes differences in the fluence loss drop due to range straggling, which for helium ions at 230 MeV/u initial energy is $\sim$1.8 mm.

Secondary Filter Performance

In Figure 5.71 an example of the reconstruction of the tracks in a pencil beam is shown before (left hand side) and after (right hand side) application of the above filters.

The fractions of filtered and unfiltered secondaries, and filtered and unfiltered primaries are shown in Table 5.13 for successive application of the filters. Normalized to the number of generated primary particles, 87.6% of the reconstructed tracks were secondary and 50.0% were primary (*i.e.* 1.4 tracks per primary due to helium fragmentation).

The filter on cluster sizes did not directly translate to the filtering strength of the track reconstruction: while the filter removed 63.0% of the clusters originating from secondary particles and only 0.1% of the clusters from the primary beam, the resulting reduction of secondary and primary *tracks* was 47.9% and 2.4%, respectively. This is likely due to fragmentation resulting in multiple secondaries (*i.e.* multiple clusters per fragmenting primary), as well as the production of target fragments without breakup of the primary helium ion.

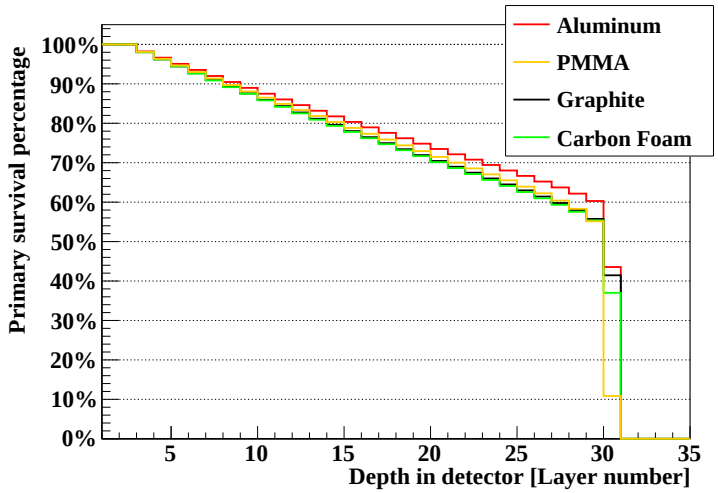

Figure 5.70: Primary helium survival in the DTC for different absorber materials. The absorber thickness was scaled to match the total stopping power of 3.5 mm aluminum. The numbers are normalized to per incoming particle.

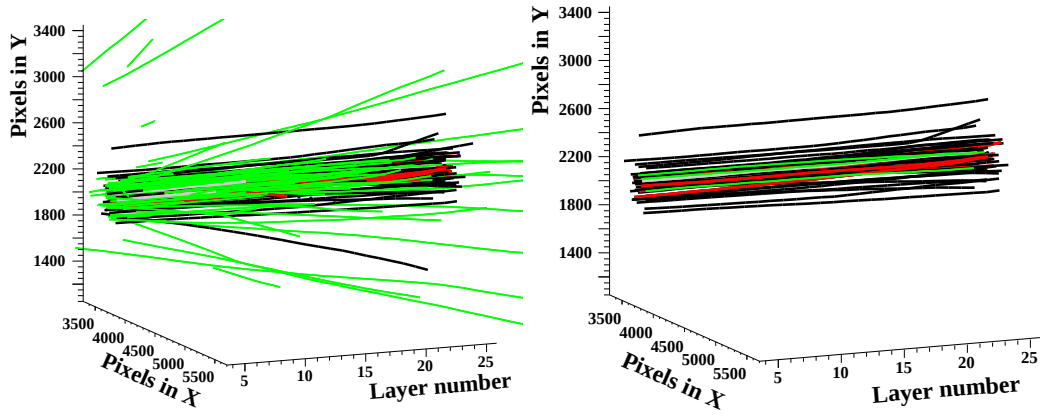

Figure 5.71: A separate readout containing 100 reconstructed primaries slowed down in 10 cm water. The figures includes 124 tracks before filtering (left) and 45 tracks after filtering (right). A black track is a correctly reconstructed primary; a red track is incorrectly reconstructed due to confusion between two tracks; green tracks are secondaries. Grey tracks are incompletely reconstructed (too short).

Filter	UFP (%)	FP (%)	UFS (%)	FS (%)
None	50.0(3)	0	87.6(4)	0
+ Cluster size >5	48.7(3)	1.22(4)	45.7(3)	41.9(2)
+ >4 layers crossed	44.6(3)	5.32(7)	26.2(2)	61.4(3)
+ E_{dep} in last layer	42.9(2)	7.08(9)	8.33(9)	79.3(4)
+ E_{dep} in plateau	42.8(2)	7.16(9)	6.30(8)	81.3(4)
+ Residual range	42.8(2)	7.18(9)	2.49(5)	85.1(4)
+ Incoming angle	42.4(2)	7.57(9)	2.18(5)	85.4(4)

Table 5.13: The efficiencies of the various filters shown after track reconstruction. The percentage values are given relative to the total number of primary particles. UFP: Unfiltered primaries, FP: Filtered primaries, UFS: unfiltered secondaries, FS: Filtered secondaries.

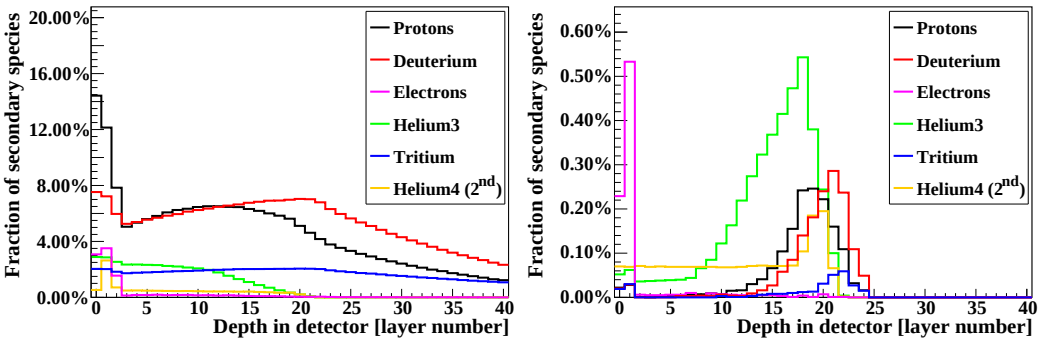

Figure 5.72: Secondary particle species distribution per primary helium ion. Shown before (left) and after (right) applying the filters described in Section 5.7.

When all the filters described in Section 5.7 were applied, 97.5% of the secondaries were identified and removed, whereas 15.2% of the reconstructed primary tracks were lost in the process. Thus 42.4% of all the incoming primary helium ions were available for subsequent image reconstruction.

In Figure 5.72 the fractions of the different secondary particle species are shown as a function of detector depth, before and after filtering. Prior to filtering, protons dominated (with up to 15% percent per generated primary) with a strong bias towards the detector front. The deuterium and tritium components were substantial at 8% and 3%, respectively. After applying the filters, the same particle species were present at around 0.2%–0.6% per generated primary track.

Primary Survival Efficiency

By counting the number of surviving primaries through the various physical and computational steps, we found that $\varepsilon_{\text{w}} = 61.6\% \pm 0.3\%$; $\varepsilon_{\text{DTC}} = 74.5\% \pm 0.4\%$; $\varepsilon_{\text{tracking}} = 108.9\% \pm 0.7\%$; and $\varepsilon_{\text{filter}} = 84.8\% \pm 0.4\%$. Note that $\varepsilon_{\text{tracking}} > 100\%$ is possible since short tracks are reconstructed (but then removed by filtering).

Multiplying them, we find the intrinsic efficiency $\varepsilon_{\text{int}} = 45.9\% \pm 0.3\%$; the algorithmic efficiency $\varepsilon_{\text{alg}} = 92.4\% \pm 0.4\%$; and finally the total efficiency $\varepsilon_{\text{tot}} = 42.4\% \pm 0.2\%$ which is the ratio of usable tracks to the generated primary helium ions: it is the same number as given for unfiltered primaries in Table 5.13.

WEPL Accuracy and Uncertainty

The WEPL accuracy for different imaged water phantom thicknesses in the range 0 to 320 mm WEPL is shown in Figure 5.73 (top). An oscillating bias with a wavelength equal to the spacing between the sensitive layers is seen, with an amplitude of approximately 1 mm. The width of the distribution of WEPL errors for the different thicknesses is 0.54 mm WEPL. For protons, the corresponding width is 0.25 mm WEPL. There is also a small but visible low-frequency component for the helium scenario.

In Figure 5.74 an example between the range distributions of proton and helium is reported. The WEPL uncertainty (measured range straggling) across different object thicknesses for helium is 2.5 to 4.5 mm WEPL, for protons it is 5.0 to 5.8 mm WEPL. In Figure 5.73 (bottom) the range straggling across all phantom thicknesses are shown using the $\pm 2\,\sigma$ width as a metric for layer coverage. The helium beam range straggling covers less than 1.5 layers, while the proton beam covers almost 2 layers.

Helium Trajectory Calculation

The resulting single-sided MLP accuracy (compared to the MC helium paths) is shown in Figure 5.75 when using the extended MLP (Krah et al. 2018). The average deviation from MC at the upstream side of the water phantom (where there is least information) was 0.75 mm for helium ions, as compared to 1.25 mm for protons (Sølie et al. 2020).

Helium Radiography

The generated radiograph is shown in Figure 5.76 (left hand side). The width of the pixel-wise WEPL error distribution of the filtered radiograph was 1.0 mm WEPL. A proton radiograph (not shown) generated using the same setup (but with a 7 mm FWHM pencil beam and 100 protons/mm^2) yielded a comparable WEPL WEPL error envelope of 1.1 mm WEPL. 99% of the pixel-wise errors were between -2.2 mm WEPL and 2.6 mm WEPL: single-pixel regions close to high gradient edges yielded the highest errors. This is due the reduced spatial resolution both from the scattering and the reduced path estimation accuracy.

The oscillating range accuracy bias is visible as rings in the WEPL error map in Figure 5.76 (right hand side) due to the shape of the head phantom, with an amplitude comparable to what was observed in Figure 5.73.

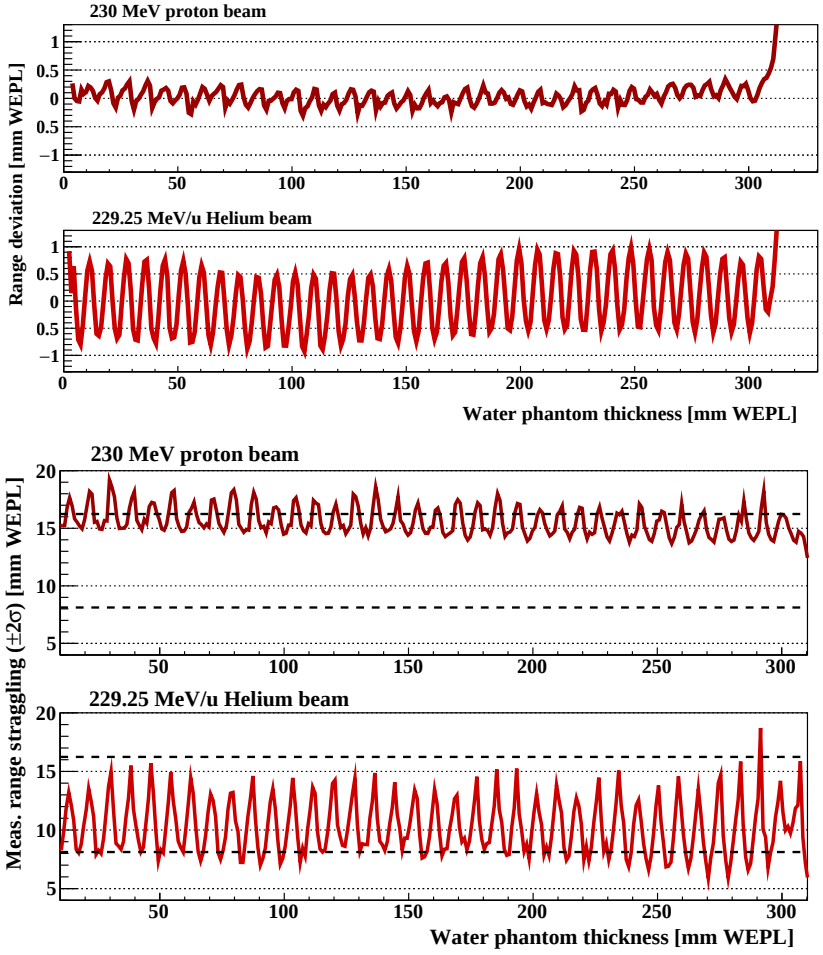

Figure 5.73: Top: WEPL accuracy of protons and helium for increasing phantom thicknesses. Bottom: WEPL uncertainty envelope (measured range straggling of protons and helium for increasing phantom thicknesses, in terms of the width of the $\pm 2\sigma$ distribution as a metric for layer coverage. The two dashed lines represent the thicknesses of one (8.1 mm WEPL) and two (16.2 mm WEPL) layers.

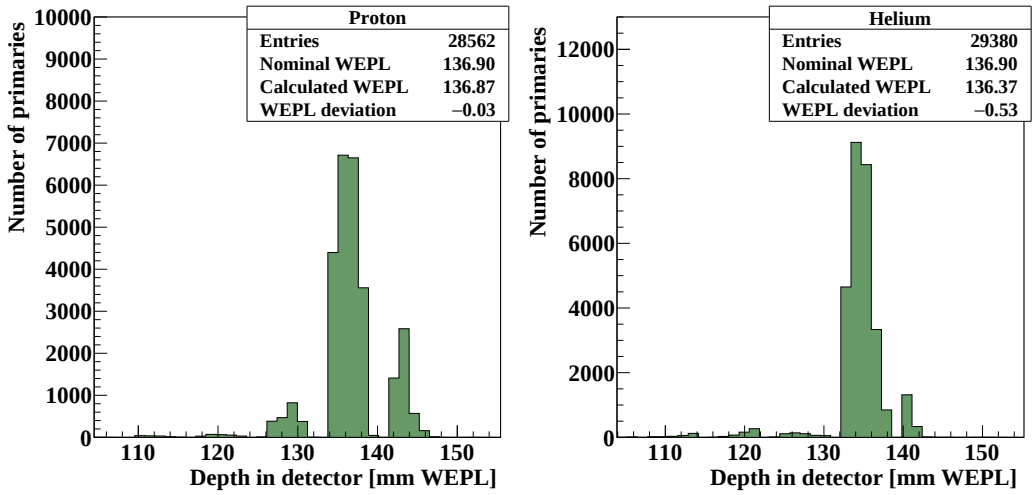

Figure 5.74: Range histogram of the individual filtered tracks. The relative increase in range straggling for protons also increases the range accuracy, due to the increased number of activated sensor layers involved in the range calculation (see also Figure 5.73).

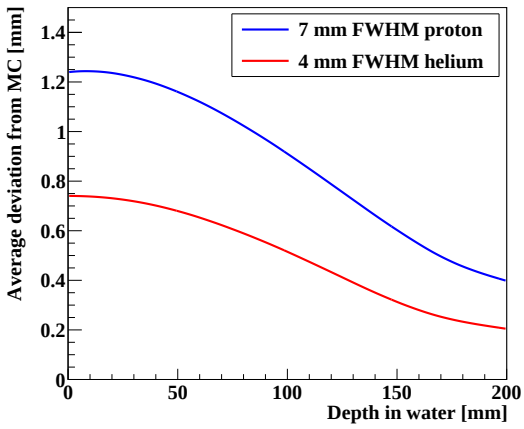

Figure 5.75: The deviation between the primary paths of MC and the estimated MLP using realistic helium and proton beams at energy of 230 MeV/u. The FWHM of the beams correspond to the smallest spot size available at that energy for protons and helium at the Heidelberg Ion-Beam Therapy Center.

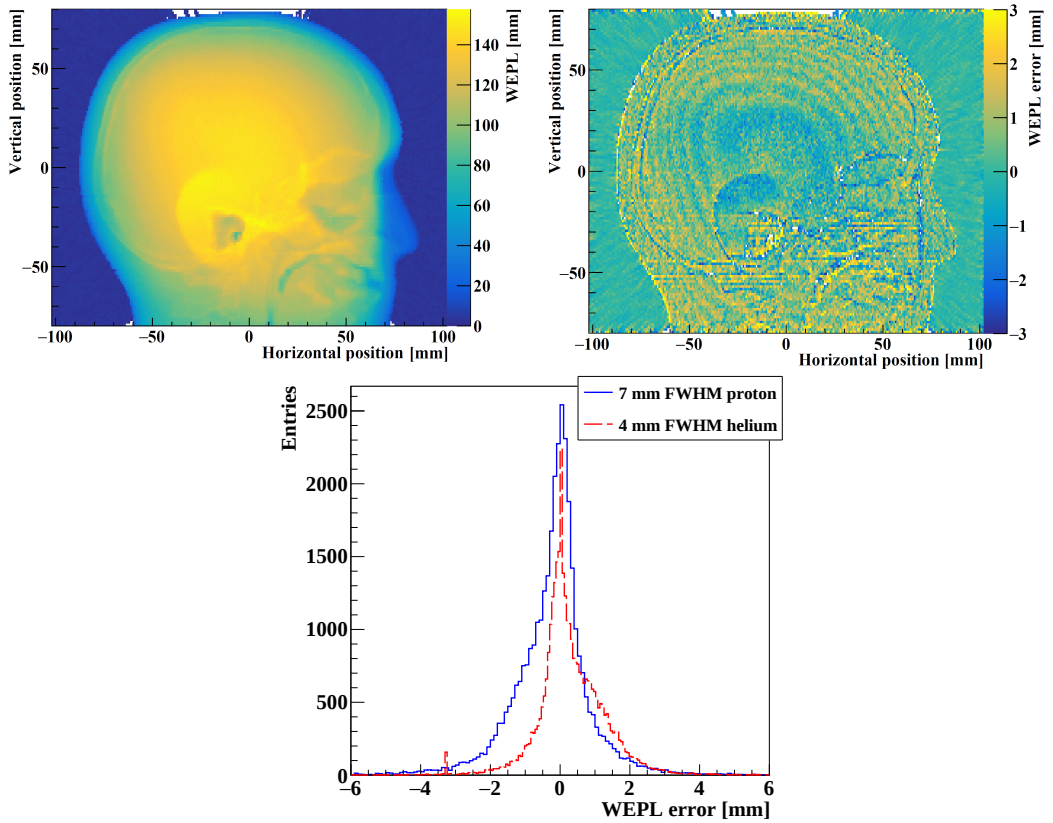

Figure 5.76: Helium single-sided radiograph, generated after applying the filters described in this text. The left figure shows the reconstructed WEPL, while the right figure shows the its error relative to the true WEPL of the head phantom. The bottom figure shows the pixel-wise errors of the filtered helium radiograph in comparison to a proton radiograph with the same setup and a fourfold increase in the number of primaries.

Due to the extra filtering and path curvature estimation steps involved in image reconstruction, the overall primary efficiency for the generated radiograph was somewhat lower at $\varepsilon_{\mathrm{HeRad}} = 31.0\%$. The corresponding number for a proton radiograph is $\varepsilon_{\mathrm{pRad}} = 40.3\%$.

The integral dose given to the head phantom during the acquisition of the radiograph from 2.68×10^6 helium primaries (24.2,mm^{-2} used for image reconstruction) was reported by GATE as 14.8 μGy. Although tomographic helium scans are not discussed in this work, a generalization to 25 primaries/mm^3 would yield 1.46 mGy in the head phantom. The corresponding dose from 8.53×10^6 proton primaries (100 mm^{-2} used for image reconstruction) would be 11.4 μGy for a radiograph and 1.12 mGy for a corresponding tomographic reconstruction.

For a helium CT an effective dose can be estimated at

$$1.46\,\mathrm{mGy} \times 18\,\mathrm{cm} \times 2 \times 0.0032\,\mathrm{mSv\,cm^{-1}\,mGy^{-1}} = 168\,\mu\mathrm{Sv}, \qquad (5.66)$$

far below reported CT doses of 2 to 3 mSv (Hansen et al. 2014a, ICRP 2007).

Discussion

Absorber Material

The planned material for energy absorbing layers of the DTC is aluminum. By considering several carbon-based materials such as graphite, carbon foam and PMMA, it was shown that the primary survival rate was favorable for aluminum by 8%–10%. As such, it is not advisable to substitute the absorber material when applying the DTC for helium imaging, especially considering the increased physical length of the DTC for absorber materials with lower RSP (requiring the same total WEPL).

WEPL Accuracy and Stragglin

The depth-dependent degradation of accuracy for helium can be explained by its reduced range straggling with a factor of $\sigma_{R,\mathrm{He}}/\sigma_{R,\mathrm{p}} = \sqrt{m_\mathrm{p}/m_\mathrm{He}} \simeq 0.5$ (Durante & Paganetti 2016). Thus, fewer detector layers were covered by the range straggling of helium tracks and the range accuracy from the weighing among several layers was reduced. In Figure 5.73 (bottom) it was shown that the broader range straggling of protons spans a larger number of sensor layers. This effect was earlier noted for protons with various absorber thicknesses in Pettersen et al. (2019a) and was here more prominent with a helium beam. These results were reflected in the generated radiographs, where they were shown as ring artefacts in the WEPL error maps. This artefact was not seen in similar proton radiographs (*cf.* figure 9 in Sølie et al. (2020)), consistent with the increased range straggling of protons. Further optimization of the initial energy spread of the helium beam might mitigate the ring artefacts by broadening the range straggling distribution.

There was also a slight low-frequency component in the range deviation for helium. This component is thought to be an artifact from the range calibration of yet undetermined origin. These effects reduced the WEPL error envelope to 0.54 mm WEPL using a water phantom. The comparable envelope when using protons was 0.25 mm WEPL. These WEPL errors are expected to be sufficient for imaging (Poludniowski et al. 2015) before considering further sources of errors (such as from the physical detector, from the experimental setup and beam quality). To improve upon this, thinner absorbers and more sensitive layers would be needed, as investigated for protons in Pettersen et al. (2019a). However, this would in turn negatively affect the cost and complexity of the system. An improved calibration scheme of the detector is currently being evaluated.

For helium ions, the WEPL error envelope was narrower compared to that of protons, shown in the two distributions in Figure 5.76 (bottom; 1.0 mm WEPL for helium ions and 1.1 mm WEPL for protons). However, the WEPL error distribution for the helium radiography showed an extra peak at overestimated WET values corresponding to the systematic ring artifacts present in the reconstruction of Figure 5.76 (right). That the widths of the WEPL error distributions were worse for the head phantom compared to the water phantom

was expected, since the heterogeneity of the phantom complicates the track reconstruction process (track matching errors introduce larger WEPL errors) and the MLP calculation.

Filter Performance

The pre-filter removing small clusters before track reconstruction reduced the number of secondary tracks by approx 48%. This is an important filter that simplifies the track reconstruction, especially given that only a small fraction of the primary tracks was removed (2.4%).

After the track reconstruction, 63.7% of the reconstructed tracks were secondary tracks, or 87.6% per generated primary. Most of them (15% per generated primary) were protons produced in the imaged object. Deuterium, tritium and ^{3}He were also present at 4%–6% levels per primary. This number includes multiplicity events, *i.e.* events where more than one fragment was produced from a primary helium ion.

The remaining secondary tracks after filtering (largely ^{3}He, ^{4}He and hydrogenic isotopes with comparable range) closely resembled a pure primary beam in the reported distributions. As such they are nontrivial to remove, but also are not expected to degrade the WEPL accuracy to a significant degree, especially if they originated from within the range telescope itself. This assumption is strengthened by Figure 5.73 (top) where the final WEPL accuracy was 0.5 to 0.8 mm WEPL in the studied scenarios.

The range filter is expected to be less efficient in removing secondaries when applied to a helium beam passing through heterogeneous geometries. However, range filters are regularly used in particle imaging with good results (Johnson et al. 2016, Volz et al. 2018), and the reconstructed head phantom yielded a good WEPL accuracy.

Various filters were evaluated in addition to the ones mentioned in Section 5.7: combinations of E_{dep} values across the detector layers; χ^2 depth-dose fit goodness (Pettersen et al. 2017); angular change along the track; as well as lateral track positions. However, while some of these filters had a high discriminatory power *per se*, they did not provide further secondary discrimination compared to the filters described in Section 5.7.

Finally, 42.4% of the the primaries in the MC-generated helium beam were reconstructed and survived the applied filters, while keeping 2.5% of the observed secondary tracks. For comparison using similar Monte Carlo studies, Gehrke et al. (2017) using a set of three pixel tracking detectors placed close to the Bragg peak found a ratio of 45% between the incoming primary helium beam (when cropped to the lateral dimensions of the detector) and the image-generating helium tracks. For the $\Delta E - E$ filter used in combination with the prototype pCT detector developed by the US pCT collaboration, Volz et al. (2018) report a reduction of 43% compared to the data set not using the $\Delta E - E$ filter (before applying the $3\,\sigma$ WEPL filter). However, this number does not consider multiplicity fragmentation events originating from within the phantom, as multiple hits on the rear tracker were automatically suppressed and therefore also not considered.

Helium Track Reconstruction

The fraction of correctly reconstructed tracks (FCR) for helium was lower to what was observed with proton track reconstruction in a similar DTC as discussed in Pettersen et al. (2019a). The main effect to reduce the FCR is the higher particle density in the 4 mm FWHM helium beam, compared to the 7 mm FWHM proton beam: these are both the smallest spot sizes realistically attainable. Other complicating factors for reconstructing the helium beam is the increased complexity in tracking due to the higher density of secondary tracks, and an increase in the E_{dep} (higher probability that larger clusters merge). On the other hand, these effects are compensated by the reduced complexity in track reconstruction due to the lower scattering power of helium.

A wrongly reconstructed helium track is expected to degrade the image quality to a smaller degree (when compared to protons), due to the smaller spot size. This is because two pairwise confused tracks in a thin beam are closer together, reducing the added spatial separation.

It was observed in Figure 5.69 that a 5 cm phantom object leads to a decrease in the FCR compared to the 16 cm. This effect can be attributed to the increased residual primary range in the detector and subsequent higher probability of track matching errors.

The current track reconstruction algorithm needs 40 seconds on the applied 96 CPU cluster to reconstruct a radiograph of 2.7 million helium primaries. It is expected that further vectorized implementations of the code (*e.g.* on a graphical processing unit) would perform significantly better in terms of processing time. A future clinical implementation of the imaging setup would need such improvements in order to be viable in terms of reconstruction time.

The ideal beam configuration (spot size, intensity) is a compromise between low uncertainty at the phantom entrance (using the single-sided MLP reconstruction (Sølie et al. 2020)), low uncertainty at the detector entrance (due to pairwise track confusion during reconstruction) and track density (increased beam intensity leads to higher track confusion). The effects of wrongly reconstructed tracks can be further mitigated by lowering the beam intensity, however the images generated at 50 helium primaries per reconstruction cycle (5 million helium ions per second) exhibit a high visual spatial resolution.

Conclusions

In this study, we explored the feasibility of helium detection and track reconstruction in a high granularity DTC. It was shown that the contribution of secondary fragments can efficiently be suppressed with adequate filters. The tracking algorithm was shown to be less efficient for helium ions compared to protons impinging on the detector: the increased focus strength available for helium ions at contemporary facilities works against the track reconstruction due to the increased track density. Different absorber materials to degrade the beam energy inside the calorimeter were investigated with the purpose of maximizing survival of primary particles. The results reported in this study indicate that aluminum absorbers as proposed for proton imaging are also

ideal for helium ions. However, the most interesting result of this study is that—contrary to expectation—the reduced range straggling of helium ions resulted in reduced range accuracy using absorber material of the same water-equivalent thickness as for protons. Still, the range accuracy was found to be sufficient for imaging. Hence, it can be concluded from the results of this study that the current DTC design is feasible not only for proton, but also for helium ion imaging. Further efforts will thus focus on proton as well as helium ion imaging toward finalizing the first DTC prototype system.

Acknowledgements

This work has been funded by the Trond Mohn Foundation (grants BFS2015-PAR03 and BFS2017TMT07) and by the Research Council of Norway (grant 250858). GGB, PG, VKM are partially supported by the Hungarian Research Fund NKFIH under contracts No. K120660, 2019-2.1.11-TÉT-2019-00050 and 2019-2.1.6-NEMZ_KI-2019-00011.

Data availability statement

All data produced and analyzed within this work will be made available upon reasonable request. The code for performing the Monte Carlo simulations, track reconstruction and filtering is openly available at `github.com/HelgeEgil/HeliumImaging`.

CHAPTER 6

Discussion and future perspective

In this thesis, developmental steps towards the implementation of particle imaging for image guidance in particle therapy have been presented. These included theoretical investigations of the achievable image quality in Particle Radiography (PRad), experiments on pre- and intra-treatment particle imaging with novel prototypes, and investigations on how current detector designs could be improved.

Although a lot of effort has been placed in developing particle imaging, this modality has yet to reach clinical implementation. However, with the development of improved particle imaging scanner systems, foremost the US pCT collaboration prototype head scanner (Johnson et al. 2017), improved reconstruction techniques (Rit et al. 2013, Penfold & Censor 2015, Collins-Fekete et al. 2016) and the connected improvements in the experimentally achievable mage quality, particle imaging has seen a rise in interest recently. It is expected that the first pre- or even clinical investigations of particle imaging will commence in the coming years (Parodi & Polf 2018b). The aim of this thesis was therefore to investigate the steps necessary to bring this promising modality into clinical practice. As starting point, the following central questions have been asked:

1. What are the theoretical limitations of image quality for particle imaging, i.e. how accurate can we get?
2. Is helium ion imaging feasible despite the fragment contamination?
3. How relevant is particle imaging given DECT?
4. Can we use particle imaging for online treatment monitoring?
5. What would be an optimized PCT system for the clinics?

In the following, the individual projects presented in this cumulative thesis and their connection with regard to these questions will be discussed. In addition, a critical viewpoint is given on the necessary developments to bring particle imaging closer to clinical reality.

6.1 Limitations and possible solutions

Spatial resolution The reduced spatial resolution from MCS is a key limiting factor for particle imaging. This has recently been explored in Krah et al. (2018) who have developed a comprehensive probabilistic model of the image resolution for different detector, beam and phantom settings. In their work, they investigate the spatial resolution achievable for different particle imaging setups assuming PCT and PRad from plane-of-interest binning (i.e. binning the particles based on their MLP position at the feature depth). However, when binning a projection image onto a single 2D radiography, features at different depths will be projected along the estimated particle paths in the same image plane. This results in the image quality being subject to not only the path estimation accuracy, but also the scattering displacement between imaging depth and depth of the feature. In publication P.IV (Section 5.1), a thorough theoretical framework has been developed to describe the spatial resolution for different contemporary radiography binning methods. Especially, for the maximum-likelihood radiography algorithm proposed by Collins-Fekete et al. (2016), for the first time a full theoretical treatment of the point-spread function was provided. It is demonstrated that even under the assumption of perfect path estimation accuracy, this algorithm is limited by the projection of the particles' WEPL along their scattered paths onto a single image plane. This could also explain observations made in previous experimental studies (Gehrke et al. 2018) observing a drop in spatial resolution towards the object exit for a similar algorithm.

Interestingly, for plane-of-interest binning (Schneider & Pedroni 1994, Rit et al. 2013, Gehrke et al. 2018), the image resolution might benefit from binning the particles slightly closer to the nearest tracking detectors, rather than directly at the object depth as shown in Figure 5.12. This is due to the increase of the MLP accuracy towards the tracking detectors, while the scattering displacement between binning depth and object depth is still small. In terms of Equation 5.10, the MLP σ_{MLP} becomes smaller, while the scattering σ_{scat} remains almost zero. Still, the fact that the spatial resolution achievable is connected with the object depth for the plane-of-interest binning approach opens up an interesting question: is it possible to infer the depth of the object from the spatial resolution of the PRad for plane-of-interest binning? If, yes, this would have important consequences on the use of PRad as pre-treatment verification tool in particle therapy. A single radiography might not only tell differences in the treated anatomy, but also if observed uncertainties are located proximal or distal to the tumor — or in other words, if they affect the treatment or not. One could think of binning a series of radiographs at different binning depths and estimate the feature position from its sharpness in the different planes taking into account the expected slope of the spatial resolution with binning depth as shown in Figure 5.12(a). The accuracy of this method would, of course, depend on the RSP gradient between the feature and the surrounding medium. It has to be noted that the uncertainty at shallow feature depths would be increased for a realistic tracking system, compared to the ideal one: For a realistic tracking system, the improvement of the MLP precision towards the trackers is not

as pronounced as for an ideal system (compare 5.55b). Hence, for shallow features, the spatial resolution will stay almost the same for binning depths closer to the front tracker, due to the small scattering displacement and the small difference in MLP accuracy.

Another implication of this study regards the development of novel improved PRad algorithms. In the best case such algorithms would provide a single radiograph with the best possible spatial resolution for all features without relying on prior knowledge. One possibility would be a deconvolution of the image with the theoretical point-spread function. As the observed image presents a convolution of the object with the point-spread function of the system, a deconvolution method may be applied to retrieve the original image. The central difficulty of this for particle imaging is the shift variance of the point-spread function, arising from the depth dependence of the scattering and the MLP uncertainty. Nevertheless, Khellaf et al. (2020b) have recently demonstrated impressive results using a shift variant deconvolution method in pCT reporting spatial resolution improvements as much as 40%. Given the theoretical point-spread functions provided in publication P.IV, one could think of applying a shift-variant deconvolution also to PRad. However, the projection of different object features (convoluted with different point-spread functions) into the same image pixels would limit the applicability of deconvolution methods for PRad of heterogeneous objects. Based on Figure 5.12, one could, however, think of a focus-stacking technique as used in optical photography: From a series of binning depths in plane-of-interest binning, the final image could be constructed by stacking together the pixel values from the binning depth where the steepest image gradient was observed. When choosing the binning depth from the pixel gradient, methods for noise suppression have to be considered. Nevertheless, such methods could lead to improved spatial resolution in PRad and deserve further attention.

Nuclear interactions In publication P.XII (Section 5.2), helium ion imaging has been investigated at the HIT facility with the pre-clinical prototype pCT scanner developed by the US pCT collaboration (Johnson et al. 2016). The system, shown in Figure 3.5, comprises two tracking detectors (one preceding and one following the patient), and a 5-stage scintillator detector. Secondary fragments, produced in nuclear interactions both inside the patient and the energy detector, have been identified to be a major source of uncertainty and image artifacts for helium ion imaging with the system (see e.g. figure 5.19). This was in accordance with other published literature (Gehrke et al. 2018) and explained the low image quality and RSP accuracy observed in a previous publication (Volz et al. 2017).

However, using a simple threshold filter on the energy deposit in the detector, as used for example in Gehrke et al. (2017), was not sufficient to remove the uncertainties arising from nuclear interactions (see Figure 5.19). This can be attributed to the different detector setup compared to that used in Gehrke et al. (2017): in their work, Gehrke et al. (2017) have used a single silicon pixel sensor as range detector. Setting the helium ions' primary energy such that the proximal side of the Bragg peak is located in the detector, they exploit the

steep rise of the energy loss at that point to infer the particles range. As such, only secondary fragments having an approximately equal or greater range as that of the primaries contaminate the measurement. The lighter fragments that reach the detector have a significantly lower energy deposit compared to the primary helium ions, and can hence be effectively suppressed with a threshold filter. The heavier ^{3}He fragments that are more difficult to identify from the energy deposit, generally have a shorter reach compared to the primaries, and hence, do not play much of a role for this detector setup. On the other hand, the large dynamic range of the prototype detector explored for helium ion imaging in publication P.XII results in the acceptance of also those secondaries that have a shorter range. The inclusion of these particles then results in an increase of the variance of the measured WEPL distribution, and with that in a reduction in the accuracy the 3σ filter usually applied to remove events with unusually large (or short) WEPL diminishing its efficiency. Especially, for the segmented energy detector of the prototype, fragments stopping in an adjacent stage to the primaries greatly reduce the image accuracy. This results in image artifacts at WET values corresponding to the stage interfaces of the multistage detector. In homogeneous, cylindrical objects these appear as ring artifacts (see Figure 5.19) for heterogeneous objects, they appear as ring-like artifacts (as seen in Figure 3A in Volz et al. (2017)).

In order to accurately identify primary helium ions from secondary fragments, the detector segmentation was utilized for a ΔE-E particle identification technique. For a given total kinetic energy, the mean energy loss of a particle in a thin absorber slab is fully determined by its mass and charge. In other words, plotting the energy loss in a thin ΔE absorber versus the total residual energy of the particle results in energy response curves unique to each particle. This is shown in Figure 5.18, where the energy deposit measured in the final scintillator stage reached by the particle in the multistage energy/range detector was used as residual energy E and the energy deposit in the immediately adjacent stage in upstream direction as ΔE. Parametrizing the ΔE-E response for primary particles enabled particle identification during data processing, and hence, an effective removal of the secondary fragment contamination.

With the ΔE-E filter, the feasibility of highly accurate experimental single-event HeCT could be demonstrated for the first time. The large ring artifacts observed in a previously published study on HeCT with the detector (Volz et al. 2017) could be effectively removed. For a phantom featuring 7 different plastic materials, a mean absolute RSP accuracy better than 0.5% was demonstrated both in simulation and experiment. However, the image spatial resolution was limited from the relatively low number of projections acquired. This limitation is best seen in the limited angle artifacts in Figure 5.24 which had also been observed in Piersimoni et al. (2018) for a low number of projections. In the work shown in Section 5.4, an increased number of projections was therefore used to acquire full CT scans.

The difference between simulated and experimental ΔE-E spectra for the detector seen in Figure 5.18 can be explained through the missing modeling of the scintillation light quenching in the simulation. Due to scintillation light quenching, the calibration from ADC to energy derived during the detector

calibration process does not return true energy values. For the detector, the energy calibration is based on the comparison between the peak ADC measured in each of the detector stages for a run without phantom in the beam line, and the expected energy deposit from a Monte Carlo simulation (Giacometti et al. 2017a). A second calibration point is obtained from the ADC noise pedestal of the stage representing 0 MeV energy output. The calibration from ADC to energy therefore assumes a linear relationship, neglecting the light output non-linearity due to scintillation light quenching. In terms of image accuracy, the effect of the quenching is yet to be fully quantified, but it is expected to affect the WEPL accuracy for low energy deposits in a stage. At low energy deposits, i.e. small ranges in the stage, the non-linearity of the scintillation light production is greatest (Birks 1951). Hence, the 1 MeV noise threshold, applied when determining the stopping stage, translates to a larger real energy deposit of the particles, effectively increasing the non-sensitive range between stages. Since the particles would be assumed to have stopped in an earlier stage, where then a systematically to high WEPL would be estimated for them (Bashkirov et al. 2016a), this might be an additional cause of ring artifacts. Using the ΔE-E filter, this issue might, however, be solvable. Instead of finding the stopping stage as the last stage in beam direction for which an energy deposit greater than 1 MeV was measured, it could be defined as the last stage for which an energy deposit compatible with the ΔE-E filter for that stage was measured. The ΔE-E filter would still remove the low energy noise, which also the 1 MeV threshold removes, but would not place any energy threshold for the primaries. This will be detailed in a future work to be brought forward by our group.

As the ΔE-E filter is based on the peak response pattern of the primary particles, it also discerns such particles that stopped due to a fatal nuclear interaction. These particles form the noise in the ΔE-E spectrum around the different main particle spectral lines (Figure 5.18). The ΔE-E filter therefore also proved to be valuable for proton imaging, where particles stopping due to nuclear interactions inside the energy/range detector reduce the image accuracy (publication P.XI; Section 5.3). In proton imaging, usually 3σ filters acting on the angular displacement and WEPL distribution are applied following the work by Schulte et al. (2005). However, these 3σ filters suffer from the increased distribution variance created through events that underwent nuclear interactions inside the energy/range detector or such that scattered outside the detector sensitive area. In publication P.XI, it is demonstrated that the ΔE-E filter could enable to remove such events, and improve the image accuracy in proton imaging. The main effect of the ΔE-E filtering for proton imaging is to remove uncertainties arising at stage interfaces (compare Figure 5.31). For single-stage calorimeters, a tighter 2σ WEPL filter might already be enough to remove the nuclear interaction tails. An experimental comparison of the accuracy of different filtering techniques in proton imaging is needed.

Finally, as the ΔE-E method does not only enable to discern primaries, but also individual secondary fragment species, it opens up the possibility of volumetric reconstruction of the fragment yield from helium ion imaging. This would require to identify if the fragments originated from the object or the

detector, which can be accomplished with a slight modification of the current ΔE-E filter approach: rather than using only the last two stages the particles reached into, the ΔE stage would be defined as the first stage, and E as the summed up energy deposit in the stages after. This might provide information on the fragmentation cross sections within the patient.

Image noise for proton and helium ions The image noise is an important aspect when considering PCT for application in treatment planning for particle therapy. In Appendix A, the WEPL precision achievable with different detector designs for helium ion imaging is investigated. Already Gehrke et al. (2018) have demonstrated that the WEPL variance for helium ions is approximately a factor of 4 reduced compared to that expected for protons for homogeneous phantoms. Although, in their calculation, they did not consider the different loss of primaries for the two ion species, this can easily be added. Assuming that the WEPL resolution of the detector is approximately equal to the range straggling of the particles (see (Bashkirov et al. 2016a) and Appendix A), Equation 2.13 predicts that

$$\sigma_{WEPL,He} = \sqrt{\frac{M_P}{M_He}}\sigma_{WEPL,p}. \tag{6.1}$$

The reduced range straggling by a factor of two results in a factor of two lower single-particle WEPL uncertainty for helium ions compared to that of protons. The noise in an image pixel is calculated as $\sigma_{WEPL}/\sqrt{N}$ (Collins-Fekete et al. 2020), where N is the number of particles contributing to the pixel. This means, compared to protons, using a factor of 4 less helium ions for image reconstruction would result in the same image noise (Gehrke et al. 2018). However, current detector prototypes require the particles to come to a complete stop (or near stop for the detector in Gehrke et al. (2018)) to infer their residual energy/range. For a 200 MeV/u initial energy, approximately 50% of helium ions will thereby be lost in nuclear interactions (compare Figure 2.7), whereas only approximately 25% of protons will be lost. Hence, to get to the factor 4 reduced helium ions *used for image reconstruction*, the number of *primary* helium ions has to be 37.5% that of protons. This results in a factor 1.5 increased physical dose to the patient for helium ion imaging compared to proton imaging at equal image noise. Note, that this is smaller than the factor 2 higher dose requirement stated in the discussion of publication P.XII, where the loss of primary protons had not been considered.

It is important to note, that above calculation only holds for a detector with a perfect acceptance and the same efficiency for both particle species, and assumes a homogeneous object. For example, the small aperture of the detector used by Gehrke et al. (2018) results in an increased loss of primary protons that scatter outside the detector sensitive area compared to helium ions, due to the helium ions reduced MCS (Tim Gehrke (DKFZ), personal communication). In addition, for realistic detectors additional factors like different read-out efficiency for the two ion species, different scintillation light quenching etc. need to be taken into account. Moreover, Rädler et al. (2018) and Collins-Fekete et al.

(2020) have demonstrated that the image noise is inherently tied to MCS. Due to MCS, particles that crossed different parts of the object can end up in the same image pixel resulting in an increase in image noise. This was evaluated recently for a heterogeneous anthropomorphic head phantom in the exhaustive work by Dickmann et al. (2019), who demonstrated that for heterogeneous objects the noise can be greatly increased compared to the noise level for homogeneous phantoms. Hence, a re-evaluation of the comparison between protons and helium ions in heterogeneous media is necessary. Such a comparison is made possible with the data acquired in the project detailed in publication P.I (Section 5.4).

6.2 Particle imaging for daily image guidance

Given the feasibility of high quality helium ion imaging demonstrated in publication P.XII, the next step in this PhD thesis was to investigate possible clinical applications of this promising modality. For this, particle imaging was evaluated in comparison to photon based image guidance methods (SECT and DECT) in order to quantify the benefit of particle imaging for RSP prediction in particle therapy. A novel method for on-line helium ion imaging based on a mixed helium/carbon beam was investigated.

Particle CT for RSP determination The main envisioned application of particle imaging is the acquisition of the patient RSP map for particle therapy treatment planning. However, in recent years, DECT based RSP determination methods have been developed as a more accurate alternative compared to the conventionally used stochiometric calibration from SECT (Yang et al. 2010, Yang et al. 2012, Bourque et al. 2014, Saito & Sagara 2017, Möhler et al. 2016, Taasti et al. 2016, Wohlfahrt et al. 2017b). In recent studies, these methods have been shown to not only be capable of accurate RSP prediction in plastic samples, but also in fresh animal tissues (Bär et al. 2018b, Möhler et al. 2018, Taasti et al. 2017). Hence, when considering the application of particle imaging for RSP determination in clinical practice, it is important to compare the expected benefit not only to SECT, but also to DECT.

In 2019, in collaboration with the US pCT collaboration, our group was awarded project funding by the Particle Therapy Co-Operative Group to further evaluate the potential of helium ion imaging for range uncertainty reduction in particle therapy. The funding enabled another series of beam tests with the US pCT collaboration pre-clinical prototype scanner at the HIT facility. In these beam tests, amongst other, a full experimental comparison between SECT, DECT, pCT and HeCT in animal tissue samples has been performed. In publication P.I (Section 5.4), preliminary results from the ongoing analysis of the experimental data are presented.

For an unbiased comparison between modalities, fresh animal tissue samples were used as the basis of the study. Two phantoms were custom designed

for the tests. The first phantom was a cylindrical PMMA phantom (150 mm diameter and 100 mm height) with 5 cylindrical bores to hold 10 cylindrical sample containers (see Figure 5.40). The phantom size was chosen to get realistic beam hardening (for the x-ray CT) and scattering (for particle imaging) as for a head and neck patient. Each of the samples was filled with finely cut animal tissue (porcine and bovine) samples ranging from lung to cortical bone. Reference RSPs of the samples were acquired through peakfinder (PTW, Freiburg, Germany) range-shift measurements. The samples were placed within the cylindrical phantom, and SECT, DECT, pCT and HeCT scans were acquired.

Preliminary results (Table 5.6) show a similar performance of DECT and HeCT in terms of mean absolute RSP accuracy (0.65% and 0.69%, respectively). As of now, pCT suffers from ring artifacts and a systematic underestimation of the RSP values (Figure 5.43), the cause of which is not yet fully understood. The mean absolute RSP accuracy for pCT was only 1.46%, about three times lower than what is reported in Giacometti et al. (2017a) and publication P.X. Likely this was related to the relatively high particle rate of of 1.6 MHz used (see Figure 5.38) for the pCT experiments at HIT compared to what has been used in previous studies with the detector. While further lowering the particle rate is possible at the HIT facility in an experimental mode, due to limitations in the sensitivity of beam monitoring system, raster-scanning at lower rates was not yet possible. A more in-depth analysis of the pCT data is needed, before conclusions should be drawn from the low RSP accuracy achieved with pCT in this work. Still, despite the uncertainties, pCT outperformed SECT for which the mean absolute error was 2.19%.

The second phantom investigated was a heterogeneous tissue phantom based on a pig head (see Figure 5.42). The phantom was a 3D printed cylindrical container (150 mm diameter, 40 mm height) with a central bore for a cylindrical dosimetry insert. The pig head was cut in shape to fit into the outer cylinder and held in place using a 2% agarose-water mixture. A custom dosimetry insert manufactured by CIRS (Norfolk, Virginia, USA) from brain-equivalent plastic was placed in the dosimetry bore of the phantom. The dosimetry insert held 36 Gafchromic® EBT-XD films with which in-tissue range reference measurements were acquired with a proton beam. This phantom represents the heterogeneity of a patient head, while retaining the control over the setup necessary for driving a reproducible comparison between modalities. A preliminary comparison of the image quality achieved with the different modalities is shown in Figure 5.45. An increased blur of pCT compared to HeCT is visible, resulting from the factor of 2 reduced scattering for helium ions. In both cases, the image resolution visibly is lower compared to that achieved for SECT and DECT. The DECT shows an elevated noise compared to the other modalities, due to the reduced tube current per scan in comparison to the tube current for SECT to keep the total CT dose index equal for both SECT and DECT. It is important to note, that for the iterative algorithm (DROP-TVS; Penfold et al. (2010)) used to reconstruct the presented pCT and HeCT scans the image quality depends on a variety of parameters, foremost the number of iterations used (Hansen et al. 2016, Schultze et al. 2018). So far, the same parameters as used in previous studies with the detector had been

applied, but optimization of the reconstruction parameters for the phantoms presented is currently ongoing. Using a direct reconstruction algorithm, as presented in Rit et al. (2013) would enable a comparison between modalities less subject to the reconstruction parameters. After the image reconstructions are finalized, the range reference measurements acquired with the EBT-XD films will enable a direct comparison of the range prediction accuracy from SECT, DECT, pCT and HeCT.

One general setback for PCT is the time necessary to acquire a full CT scan. In this work, all PCT scans were acquired in a step-and-shoot mode. For the experimental PCT scans acquired with the US pCT collaboration prototype at the HIT facility, each projection was acquired in a single spill, and the spill-pause was used to rotate the phantom. This results in greatly prolonged scan acquisition times compared to what has been achieved with the US pCT collaboration prototype for studies at a cyclotron based facility. The images from 180 projections shown in Section 5.4, for example, needed a minimum of 24 min to be completed, due to the spill duration of $\sim$4 s and spill-pause of 4 s. On the other hand, scan acquisition in as fast as 6 minutes is possible using a continuous data acquisition and phantom rotation mode at a cyclotron (Johnson et al. 2016). Since, half of the scan duration at HIT was attributed to the spill-pause, in order to improve upon the current scan acquisition time, the duration of the spill relative to the spill pause would need to be increased. The HIT facility offers a prolonged spill of up to 12 s at low beam intensities, potentially enabling the acquisition of multiple projections per spill. However, as of now, beam scanning was not yet possible for this setting. The scan acquisition time presents a major obstacle when considering to incorporate daily PCT into the tight schedule at contemporary particle therapy facilities. Hence, future work efforts in particle imaging should include an optimization of the accelerator settings for improved scan duration.

Online treatment monitoring with particle imaging In publication P.VII (Section 5.5), the feasibility of helium imaging as online treatment monitor in carbon ion beam therapy was investigated. Due to the similar mass/charge ratio of fully stripped helium and carbon ions, at the same velocity, the two ions trace approximately the same radius in a circular accelerator. Therefore, the two ion species potentially can be accelerated simultaneously to the same velocity (same energy per nucleon) for which the range of helium ions exceeds that of carbon ions by a factor of 3 (see Figure 2.2). A small percentage of helium ions mixed into a carbon ion beam could therefore enable treatment of the tumor with carbon ions while the helium ions would fully cross the patient, providing on-line treatment feedback (Graeff et al. 2018, Mazzucconi et al. 2018). In order to explore the benefit of this promising modality in clinical scenarios, first experimental tests were conducted at the HIT facility with sequentially irradiated helium and carbon ion beams and anthropomorphic phantom setups.

As beam monitor, the novel scintillator stack range telescope developed by Kelleter et al. (2020) (publication P.V) was chosen, i.e. an integration mode detector. An integration mode detector comes at the advantage that it can

cope with the high beam intensities expected in a mixed helium/carbon beam: While the rate of the mixed-in helium ions (800 kHz at the highest clinical carbon intensity of 80 MHz available at HIT for a 1/10 helium/carbon ratio) could be handled already with contemporary single-event prototypes (compare publication P.XII and publication P.I), the high rate of fragments produced during therapy poses a great obstacle for a single-event measuring system. On the other hand, already with the integration mode scintillator stack used in the study, relative range changes as small as 1 mm affecting less than a quarter of the pencil beam particles could be detected (Figure 5.49) — despite the signal contamination with fragments produced during carbon ion therapy. The sensitivity of the method is the key advantage over other range monitoring techniques like prompt γ or in-beam PET imaging. The achievable range resolution with the helium/carbon ion mixed beam only depends on the sensitivity of the system used to monitor the helium ions. In principle, already only few helium ions mixed into the primary beam would provide significant information. One general drawback, however, is that the range changes observed for the helium ions are also subject to uncertainties *distal* to the tumor volume. In order to achieve best results, this method may therefore be combined with other existing range monitoring techniques, like prompt γ.

For testing the method in a clinically relevant scenario, different motion patterns in prostate cancer treatments were studied with two anthropomorphic pelvis phantoms. Prostate cancer cases are a good example for the potential benefit of an online treatment monitor: The typical particle treatment of prostate cancer consists of two parallel-opposing fields. While this places the Bragg peak and the connected range uncertainties inside the target volume, it also results in an increased dose to healthy tissue as would be achievable with anterior, or anterior-oblique treatment direction aiming directly at the rectum (Christodouleas et al. 2013). Anterior-oblique or anterior treatment directions are avoided due to concerns regarding unwanted dose to the rectum, arising, for example, from random bowel gas movements. These motion patterns are difficult to predict or mitigate without treatment feedback (Ammazzalorso et al. 2014). Especially, bowel gas movements result in a systematic displacement of the prostate, i.e. a systematic displacement of the dose compared to the treatment plan. This is a major issue when considering dose escalation in hypofractionated prostate therapy, where such a shift could mean a significant under-dosage of the prostate and over-dosage of the healthy tissue. With the mixed helium/carbon beam, the large range changes associated with bowel gas movements were clearly observable (Figure 5.51).

As of now, the feasibility of simultaneous acceleration of helium and carbon ions has yet to be demonstrated. At the HIT facility, the experimental investigation of the mixed helium/carbon ion beam is unfortunately not possible due to the design limitation of the LINAC pre-accelerator. Without this limitation (discussed in more detail in publication P.II, Section 5.5), there is a strong reasoning that a mixed helium carbon beam can be accelerated. The momentum acceptance of the HIT synchrotron is specified at roughly 0.1% at injection (Eickhoff et al. 2003) and a similar momentum acceptance can also be assumed at the extraction (C. Schömers (HIT); personal communication). Given that in

terms of magnetic rigidity, a momentum difference has the same effect as a difference in mass to charge ratio, it can be argued that the 0.065% difference between helium and carbon ions mass to charge ratio would be acceptable for the simultaneous acceleration. The difference between helium and carbon ions would, however, be systematic and result change in the mean ion trajectory in the synchrotron. For the HIT synchrotron which has a circumference of 65 m (Kleffner et al. 2009), the difference in the mean ion trajectory between helium ions and carbon ions would be less than 5 mm. In terms of the ion sources, it would be feasible to produce both helium ions and carbon ions from methane source gas, with helium as support gas. The mixture could potentially even increase the performance of the source in producing high charge state carbon ions (Drentje et al. 2008).

The above concerns about the feasibility of acceleration of a mixed beam only apply to synchrotrons. For a carbon ion accelerating cyclotron, on the other hand, the slight difference in mass/charge ratio of the helium and carbon ions would only result in a slight energy difference at extraction. As the key for a cyclotron is that the extraction occurs at a specific radius (i.e. a specific magnetic rigidity), this energy difference would correct for the A/Q difference, benefiting beam transport and scanning after the main accelerator. Since such a cyclotron is currently under development (Cyclone®400; IBA, Louvain-La-Neuve, Belgium), first tests on the helium/carbon mixing method with a real mixed beam might become feasible in the near future. The quasi-continuous cyclotron beam would also be advantageous, as rather than stopping the beam completely if a change is detected, only the carbon contribution would need to be stopped, if such a switch is feasible from the source perspective. The helium ion beam would continue to provide image guidance, which is important for the tracking of periodically moving targets.

The results presented in publication P.VII are in general descriptive of the potential of particle imaging for online beam monitoring which might also be accomplished with sequentially irradiated beams. Rather than switching the ions, which takes at least one full acceleration circle of several seconds at a synchrotron, one could use the same beam particles both for imaging and treatment by switching the beam energy. At the HIT facility, fast energy switching is currently under investigation and has been demonstrated already for small energy steps (Schömers et al. 2017). The time latency for switching between imaging and treatment energies, however, would need to be investigated and is likely in the order of 1 s, due to the time needed for adjusting the HEBT magnets to the energy difference. Still, this would already be very useful for treatment monitoring of slowly moving targets such as the prostate. Here, few imaging spills interleaved with the treatment could prevent large excess doses given to organs at risk, for example due to rectal gassing. For periodically moving targets such as lung tumors, faster imaging/treatment switching times are required (<1 s). By using fast passive degraders for energy variation, fast switching between the highest energy available and the treatment energy would already be feasible. In order to avoid latency from the HEBT magnets, the degrader might, however, need to be placed after the nozzle, and the beam quality of such a setup would need to be investigated. On the

other hand, LINAC based facilities (as e.g. developed by Advanced Oncotherapy plc) would not need passive degraders, and might achieve the necessary energy variation between treatment and imaging energy on a pulse by pulse basis. Such a technique might enable particle fluoroscopy for tumor tracking as initially proposed by Han et al. (2011). This would open the door for online tumor tracking from ultra-fast radiography imaging.

The main advantage of particle imaging for online treatment monitoring comes in the fact that it would enable to reconstruct 2D images of the treated anatomy from beams eye view. This would provide valuable feedback for the treating physician, for instance by not only indicating a range deviation but also helping to identify which anatomical structure caused the change. In case of the prostate, gas inflation of the rectum would be visible as the rectum pushing into the beam field-of-view in a difference map with a radiograph obtained . This is especially advantageous when considering the use of online monitoring to adapt the following fractions, where dose reconstruction is needed. In addition, a fast enough imaging system might enable to depict motion trends, useful either for gating the dose delivery or even tracking the tumor. Recently, Deffet et al. (2020) have proposed a method for optimized integration mode radiography which yields a high image accuracy. Adopting such techniques to on-line treatment monitoring could provide high resolution images of the patient. For a mixed beam, however, also the carbon fragment background would need to be considered in the image reconstruction algorithm. Hence, implementation of an optimized image reconstruction technique for integration mode imaging in a mixed helium/carbon beam is not a trivial task. The potentially ideal system for the helium/carbon mixing would be a hybrid between integration mode and single-event system, as for example, the high granularity digital tracking calorimeter developed by Pettersen et al. (2017) (further investigated in publication P.II, publication P.III, publication P.VIII and publication P.IX). Measuring a large number of particles simultaneously during treatment could enable fast decision making from Bragg-peak shifts, while resolving single events in post-treatment data processing would make use of the increased sensitivity and spatial resolution of single-event imaging.

6.3 Investigating different detector designs

Based on the physical limitations and the clinical needs for particle imaging, in this thesis, different detector setups for single-event particle imaging were investigated. These include investigations of novel tracking detector setups and assessment of a recent digital tracking calorimeter energy detector system for HeRad with regard to secondary fragment filtering, noise and systematic effects. In addition, the theoretical WEPL resolution of different detector design concepts is provided in Appendix A.

Tracking detectors In a clinical beam line, the limited space between nozzle and patient limits the inclusion of a front tracker for a single-event particle imaging system. In addition, for systems measuring a large multiplicity of

events simultaneously and only resolving single-events in data processing (e.g. publications P.II, P.III, P.VIII and P.IX), the particle scattering inside the patient works against matching particle histories between the front and rear tracker. Finally, for single-event particle imaging in a mixed helium/carbon therapy beam removing the front tracker would be desirable to limit the production of secondary particles in front of the patient.

As such, in publication P.VI (Section 5.6) the image quality of single-event particle imaging without a front trackers was investigated from Monte Carlo simulations. As substitution for the missing front tracker information, the pencil beam mean position can be used as input to a regular MLP estimate, or particle paths can be estimated based on the extended MLP formalism by Krah et al. (2018). In case of using just the pencil beam mean position, the acquired pRad images exhibited strong sampling artifacts resulting from the systematic misrepresentation of the particle path (Figure 5.56a). With the extended MLP, where also the pencil beam uncertainty matrix is included, such artifacts were largely suppressed, but still present for a combination of thin pencil beams and large scattering uncertainty in the phantom (Figure 5.58a). In such cases, due to the uncertainty of the scattering, the rear tracker measurement adds little to the inference of the entrance position of the protons, resulting in a systematic shift of the estimated most likely entrance position towards the pencil beam center. The larger the pencil beam spot size compared to the particle scattering in the patient/object, the more the rear tracker measurement contributes to the inference of the particle entrance position.

In general, the performance of the system without front tracker was reduced compared to the ideal system relying on both front and rear trackers, as expected. For radiography an average decrease in spatial resolution of 40% was observed when assuming ideal tracking detector properties. However, the difference between the two setups was smaller for a realistic setup, where 30% lower spatial resolution for the system without front trackers was observed. For the system with both front and rear trackers, the additional material budget and limited resolution of the front trackers reduces the accuracy compared to the ideal tracker scenario. For the system without front tracker, the performance is only affected by the less accurate rear tracker position and direction measurement. Due to the increased scattering at the rear tracker, this information is anyways already associated with a greater uncertainty compared to the front tracker measurement. Adding realistic tracker properties does not reduce the overall system performance by much. For a system without front trackers, helium ions as image generating particles would be especially advantageous: not only is the scattering inside the object reduced, which enables a better inference of the entrance position of each particle, i.e. a higher MLP precision, but in addition, greater focus strength of the pencil beam can be achieved due to the smaller scattering in the beam monitoring system.

The recent advances made by Khellaf et al. (2020b) using a deconvolution method for improving spatial resolution could also benefit particle imaging without front tracker. The path estimation precision, and with that the shift variant point-spread function of the system can be computed also in the case

without front tracker. Hence, it would be very interesting to adopt the methods by Khellaf et al. (2020b) for the system explored in publication P.VI, as well. The reduced cost and complexity of a system without front tracker would benefit the implementation of particle imaging in the clinical practice. More investigations are needed in regards of the accuracy of treatment planning and pre-treatment optimization with a system without front tracker. Only then, definitive conclusions on the feasibility of a single-event particle imaging system without front trackers can be made.

Digital tracking calorimeter As discussed above, a key challenge in PCT is the scan duration. In order to shorten this time, a particle acquisition rate in the order of 10 MHz would be needed (Sadrozinski et al. 2013). However, for a synchrotron, the bunch structure of the beam poses a great challenge for a single-event particle imaging system, when considering to increase the average particle rate. With individual beam bunches spaced in the order of 100-200 ns apart (Krimmer et al. 2018, Magalhaes Martins et al. 2019), above an average particle rate of 5-10 MHz, more than one particle is delivered per punch on average. The bunches have a typical time width of 20 ns to 50 ns (Krimmer et al. 2018), and within the bunches the particle arrival time is Poisson-distributed. This means, at a synchtrotron facility, higher beam intensities than those with $\leq$1 particle per bunch require a single-event PCT system to be able resolve the beam nano-structure, i.e. an effective particle rate in the nanosecond regime. Otherwise, the average event would be a pile-up event, resulting in unnecessary excess dose given to the patient.

While feasible from the tracker perspective (e.g. Magalhaes Martins et al. (2019) resolved single-events in the bunch nano-structure with a scintillating fibre hodoscope at the HIT facility), measuring the energy/range of each individual particle at this rate is challenging. One approach to this problem, proposed e.g. in Pettersen et al. (2017), is to measure a large number of particles simultaneously per read out cycle in a range telescope comprising multiple layers of silicon pixel sensors. In data processing, the fine spatial resolution of the sensors then enables to trace individual particle tracks (Pettersen et al. 2019b), resolving the single-event information. In Pettersen et al. (2019a) (publication P.IX), the optimization of this detector system is investigated. In order to save overall detector costs, the final system will use aluminum degraders of 3.5 mm thickness interleaved between the sensitive silicon pixel sensor layers. In order to still accurately predict the particles' residual range inside this so-called digital tracking calorimeter, a Bragg peak fit on the measured energy deposit in each sensitive layer is performed. The final system will rely on the ALPIDE (Mager 2016) CMOS monolithic-active-pixel-sensors (MAPS) to construct the position sensitive layers. First tests with these sensors at the HIT facility have been performed in 2018, assessing their performance with protons, helium ions and carbon ions at different energies and particle rates. One aim of these tests was to investigate the charge cluster size as function of the particle energy deposit, i.e. the number of pixels firing around a primary particle hit due to the dispersion of the produced ionization electrons. As the ALPIDE sensor does not measure energy directly, the energy deposit of the particles is inferred

from the charge cluster size. Hence, the determination of the energy to charge cluster relationship was crucial for realistic representation of the detector in simulation, especially also for the secondary particle filtering investigated in publication P.III. Parts of the results of the beam tests with the ALPIDE chips at HIT have been published in publication P.VIII and publication P.II, as well as conference contribution C.IX.

The design optimization of the digital tracking calorimeter had considered only protons, as proton imaging is the intended use case for the system at the University of Bergen. In order to test the feasibility of using the system in a mixed helium/carbon beam, as a first step, in publication P.III a detailed analysis of the performance of the system with helium ion beams is presented. Especially, the capability of the system to remove secondary fragments has been systematically studied. As the construction of the full system is currently ongoing, the presented study was based on a detailed Monte Carlo simulation. The proposed methods for filtering the secondary fragments were a threshold on the charge cluster size, the goodness of the Bragg peak fit, and the structure of the particle track inside the range telescope. Here, it was shown that the system enables accurate filtering of secondary particles, where a large portion of secondary tracks was removed due to their charge cluster size in the last sensitive layer. However, when studying HeRad of a anthropomorphic head phantom, systematic ring artifacts were observed. These ring artifacts arise from the aluminum degrader used in the system, which were optimized for the use with protons rather than helium ions. Due to the degrader being non-sensitive detector material, discrete discontinuities in the range distribution of the particles are observed despite the performed Bragg-peak fit (Figure 5.74). While also present for protons, the smaller width of the straggling distribution for helium ions increases the relative importance of these discontinuities when calculating the mean WET in a pixel. An improved calibration method to remove these systematic effects is currently being investigated.

As of now, the rate capabilities of the system for helium ions are limited, if the smallest clinically available beam spot size is used, with the ratio of tracks that are correctly reconstructed decreasing below 90% at less than 2 MHz average particle rate for a helium ion beam stopping in the detector after traversing 5 cm of water (Figure 5.69). While the ratio of correctly reconstructed tracks increases for thicker phantoms (due to their lower residual range), it is not yet close to the goal of a 10 MHz particle rate. Further efforts should therefore focus on improving the tracking accuracy, for example by applying machine learning algorithms as used for single particle tracking in high-multiplicity particle physics experiments (Farrell et al. 2018). Still, despite the loss of tracking efficiency, the current system would already be interesting for the use in a mixed helium/carbon beam. The integrated information of the system could be used for fast online range checks on a spot-by-spot basis. Resolving the single-event information post treatment would then only add additional information, where the reduced tracking efficiency is not as relevant. Preliminary tests of using the system in a mixed helium/carbon ion beam in simulation have been conducted. Assuming the highest clinical carbon rate at HIT, promising results were obtained for a 10% contamination of helium ions. A

large number of secondary carbon fragments could be efficiently removed due to their broader lateral distribution compared to that of the primary helium ion beam. The carbon fragment contamination in the beam core could be reduced using the same filters as anyways applied for helium ion imaging with the system. Further investigation of this system for the helium/carbon mixing therefore is promising.

6.4 Bringing particle imaging into clinical practice

Given the accuracy and speed of a DECT scan, the question arises if a PCT scan is needed at all. Indeed, the main argument for using a PCT scan over a DECT scan is the imaging dose: Following the ALARA (as low as reasonably achievable) principle, a lower dose to the patient from the image guidance should always be preferred. Particle imaging already enables to achieve CT doses of less than 5 mGy which is better than achievable with x-ray CT even when considering recent advances in dose saving with improved image reconstruction algorithms (Wohlfahrt & Richter 2020). Meyer et al. (2019) have recently demonstrated that not only the physical dose per scan would be reduced for particle imaging, but that this might also hold when considering the biological effective dose. Especially for daily RSP reassessment, the low dose of PCT would be of advantage compared to DECT methods. In addition, by design, PCT is acquired at iso-center and from beams-eye view, limiting registration uncertainties or the need for an additional CT scanner in the treatment room.

On the other hand, the key limiting factor of pCT is the scan acquisition time, for which the benchmark is currently set at $\sim$6 min in a continuous data acquisition mode at a cyclotron (Johnson et al. 2016). Reduction of the scan duration is of utmost importance when considering to incorporate PCT into the daily routine at a particle therapy center. Aside from patient comfort, the major concern is the overall cost efficiency of the center, where faster treatment, and with that higher patient throughput, is highly desired (Bortfeld et al. 2020). Ultimately, it would be desirable for a PCT to not take longer than the image guidance with other CT modalities. For example, a gantry mounted cone-beam x-ray CT would need one gantry rotation to be completed, or $\sim$1 min (at HIT). Achieving a target of 1 min for a full PCT might be possible, if particle acquisition at an event rate of $\sim$10 MHz is feasible (Sadrozinski et al. 2013) which is not unreasonable considering recent prototype developments (Welsh et al. 2017, Esposito et al. 2018, Pettersen et al. 2019a). Interestingly, the fact that fewer helium ions are needed to produce an image of equal noise quality (Gehrke et al. 2018) also translates to a reduced scan duration needed. Considering the loss of primaries as calculated above, the beam-on time for helium ions may be reduced to only 37% of that needed for protons while retaining the same image noise. Hence, greatly reduced scan duration compared to what is currently reported in the literature might be feasible in the near future. Still, it has to be considered that the time uptake of a PCT is beam-on time, and not only setup time, as it is for a cone-beam x-ray CT. For a multi-room facility with one accelerator, it has to be evaluated if 1 to 2 min of additional beam

time requirement per patient would be acceptable when considering PCT for daily image guidance.

If scan duration can be reduced, PCT has a great potential as tool for daily image guidance. Future efforts should therefore conjointly optimize accelerator settings and particle imaging system development to get the maximum performance. As of now, PCT might be useful for certain cases, for instance patients with metal implants, where the photon based CT modalities suffer from strong metal artifacts. A single PCT could be acquired at the beginning of the treatment duration, and used directly for treatment planning or to correct artifacts in the SECT/DECT, for example through a frequency split technique. PCT would also be interesting as a quality assurance tool for RSP acquisition methods in heterogeneous geometries.

Nevertheless, the first step of bringing particle imaging into clinical practice will likely not be in the form of PCT, but rather PRad. Already with contemporary equipment PRads can be acquired in less than half a minute (Volz et al. (2017) and this work). With the methods from Palaniappan et al. (2019) and Collins-Fekete et al. (2017a), the projection data could be used for patient alignment and optimization of the HU to RSP lookup table. In addition, the HeRads could be used as visual feedback for the treating physician on potential uncertainties in the patient setup. Only if these uncertainties are deemed too grave, a CT scan (either with photons or particles) would need to be acquired. The adaptation of PRad in clinical practice would also have the benefit of familiarizing physicians and medical physicists with the use of particle imaging, in return providing feedback from the clinical point of view for the development of improved proton imaging systems.

Compared to a PCT system, for PRad, rate requirements and dose limits are much relaxed. Hence, inexpensive scintillator detectors may be used for the energy/range detection. Systematic artifacts arising at stage interfaces would also not be as problematic, as the corresponding WET regions for a given initial energy would be known (publication P.X). These artifacts may be mitigated for example by choosing the beam energy according to the expected WET of the patient region of interest. In addition, when considering HU to RSP optimization, particles with a WET close to the critical regions may simply be omitted.

While for helium ions, the need to accurately separate fragments from primaries so far requires energy loss information within a segmented detector, for proton imaging, the potentially ideal energy detection system could be a binary range counter. For example composed of thin scintillator slabs read out by SiPMs, as already investigated in (Sadrozinski et al. 2013). The straightforward connection between the range measured in the stack and the WEPL would require only a very relaxed readout requirement compared to multistage calorimeter approaches. In addition, based on the findings in publication P.XI, a 2σ WEPL filter or a filter based on the FWHM of the WEPL distribution may already be sufficient in removing the nuclear interaction contamination that occurred within the detector. The relaxed readout requirements for a binary range counter would make it better suited for everyday clinical routine,

where the simplicity and robustness of the system are important factors. In order to open up the use of a range counter for single-event helium ion imaging, more sophisticated filtering techniques are needed. These could, for example, utilize prior information on the object to identify a region of validity for the WEPL measurement of each particle. Such a filter is currently being developed in our group (see Collins-Fekete & Romano (2018)) and has achieved promising results when tested on experimental data.

Finally, for reduction of overall system cost and for simplifying the installation of the particle imaging device in a clinical environment, optimized single-event particle imaging systems should use the nozzle information either to complement or substitute the front tracker. The reduction of the amount of material in the beam line would also be beneficial for reducing the beam energy spread before entering the patient. This was found in Dickmann et al. (2019) to add substantially to the overall image noise. Reduction of the energy spread could therefore lead to even better dose saving at the same noise level in the image. The potentially ideal case would be if the tracking system in the nozzle would be capable not only of pencil beam position measurements at high particle rates, but also single-event measurements at sufficiently low rates. A candidate technology for such a system might be scintillating fibre hodoscopes (Magalhaes Martins et al. 2019). The fine spatial resolution of the fibres paired with the good time resolution would be suitable for single-event imaging. At the same time, this technology is currently under development as a future beam monitoring system (Leverington et al. 2018). Alternatively, one could consider to remove all beam monitoring systems from the beam line during imaging runs, and substituting their information with the measurements of the particle imaging system. The front tracker information would provide feedback on the spot position and beam current. In either case, the particle imaging system should be seen as an extension of the nozzle, rather than a fully independent system.

CHAPTER 7

Summary

Particle imaging is a promising modality for both pre- and intra-treatment image guidance. Current detector prototypes offer images of high quality and RSP accuracy, which has been demonstrated in this thesis to be on par with that of contemporary DECT — despite the clinical maturity of the latter. At the same time, particle imaging offers reduced imaging dose, which should be preferred considering the ALARA principle. With the development of next generation particle imaging systems, faster image acquisition can be expected, which is a key necessity for adopting this imaging modality into clinical practice at charged particle therapy centers.

In this thesis, the feasibility of high quality helium ion imaging has been demonstrated, which offers the potential of increased image spatial resolution and reduced scan duration at equal image noise compared to proton imaging. In addition, the clinical potential of a highly novel on-line helium ion imaging technique based on a mixed helium/carbon beam has been evaluated. This method has shown to be highly sensitive to relative range changes, and might enable reconstruction of 2D images of the treated anatomy, offering a distinct advantage over other current treatment monitoring techniques. The experiences with the physical limitations and the potential clinical use cases of particle imaging have been channeled in investigations of novel detector designs. A single-event particle imaging design without a front tracker has been investigated which would be beneficial for clinical application in terms of cost and setup complexity. While reduction of the image quality was observed compared to a setup with front tracker, the results were promising and the feasibility of treatment planning based on such a design is currently being investigated. The silicon pixel detector stack under development by the University of Bergen has been identified to yield a great potential for both proton, but also helium ion imaging at a synchrotron facility. In conclusion, this thesis has investigated developmental steps towards the implementation of particle imaging for image guidance in particle therapy. The acquired results especially point out the potential of helium ions for both pre- and intra-treatment imaging. This thesis therefore paves the way for further development of helium ion imaging for improving range accuracy in particle therapy.

APPENDIX A

Energy detector designs for helium ion imaging

Introduction

The energy/range detector of any particle imaging system is the most crucial device, as it directly produces the contrast in the image. The accuracy and precision of the energy/range detection directly determines the achievable accuracy and precision of the RSP reconstruction inside the patient. So far, with one exception (Gehrke et al. 2018), attempts on optimizing the energy detector have focused on proton imaging. Here, we re-evaluate a recent study on the energy detector for proton imaging (Bashkirov et al. 2016a) in the context of helium ion imaging. Three different energy/range detector designs are evaluated for their use in helium ion imaging: energy detectors in form of a single (SSD) or multiple (MSD) plastic scintillator stages, range counters (RC) composed of thin scintillator slabs, as well as time-of-flight energy detectors (denoted TOF). As a benchmark for comparison, we will use the US pCT collaboration prototype detector system (Bashkirov et al. 2016b, Johnson et al. 2017) with which high quality helium imaging has been demonstrated already (publication P.XII and Publication P.I).

Accurate helium ion imaging requires to remove the fragmentation contamination from the primary responses. As of now, the only method that can accurately achieve that task is the ΔE-E filter proposed in publication P.XII. To enable ΔE-E filtering, for the SSD and RC designs, an additional ΔE stage needs to be added upstream of the main detector. Here, we propose the water equivalent thickness of this additional stage to be equal to the range of 80 MeV/u helium ions, which represents the minimum residual energy required for the helium ion energy within the patient to remain in the region of almost energy-independent RSP (Arbor et al. 2015).

The major advantage of the TOF design is that it does not require the particles to come to a complete stop, resulting in reduced loss of primaries and reduced straggling noise. To enable ΔE-E filtering, for the TOF design, the ΔE

stage needs to be placed after the TOF planes. This would allow the use of the TOF planes also as tracking detectors. On the other hand, the additional thickness of the ΔE stage would be slightly beneficial in terms of the TOF noise by slowing down the particles. In terms of the ΔE-E filter, there is no significant difference between a ΔE-TOF and TOF-ΔE configuration.

In the following, we will assume that the for the RC, SSD and MSD designs, the beam has traversed 52.15 mm of WET. For the TOF designs, we will assume only a residual energy of 80 MeV/u, and a ΔE stage after the TOF (TOF-ΔE). This design is more compact, and requires less cost intensive position sensitive detector planes, compared to a ΔE-TOF.

Stochastic uncertainty

In the following, we will compare the imaging noise for helium imaging with the different energy/range detector designs based on the formulas provided in Bashkirov et al. (2016b). We will only focus on the energy/range detector contribution to the noise and the reader is referred to the extensive study by Dickmann et al. (2019) for a detailed analysis of different noise components in pCT images with the multistage detector described in Johnson et al. (2016).

Here, WEPL refers to the water equivalent path length a particle travelled through the object. W_0 is the cumulative water equivalent thickness (WET) of any material leading up to the energy/range detector in addition to the object, e.g. the beam monitoring system, the air between nozzle and iso-center and the tracker planes. For this work we assume W_0 to be 7.05 mm, where 3.05 mm are contributed by the thickness of the beam monitoring system and air at the HIT facility, and 4 mm are based on the thickness of the tracking detectors as assumed in Bashkirov et al. (2016a). The residual range of a particle after the object is then calculated from its initial range in water (RW) as

$$R_{res} = RW - WEPL - W_0. \tag{A.1}$$

Binary range counters For binary range counters composed of n slabs with water equivalent thickness S_i ($i \in \{1, \ldots, n\}$), the uncertainty of the residual range is given as the range straggling up to the final slab S_f the particle reached into and the slab resolution.

$$\sigma_{\text{WEPL}} = \sqrt{(\sigma_{rs} \times \left(\text{WEPL} + W_0 + \sum_{i=0}^{f-1} S_i\right)^2 + (\sqrt{12} \times S_f)^2}. \tag{A.2}$$

Here, σ_{rs} denotes the range straggling which for protons is approximately 1.1% of the protons range in water (Bashkirov et al. 2016a). For helium ions, the range straggling is half that of protons (Durante & Paganetti 2016), i.e. 0.55% of the helium ions range. It is important to highlight that the slab thickness also considers the dead material between stages (e.g. reflective foils to separate the scintillation light output), as well as the minimum range required in a slab for the signal to reach above any noise threshold applied to the read out.

Scintillation detectors For calorimeter detectors composed of n individual scintillator stages with stage thicknesses S_i ($i \in \{1, \ldots, n\}$), Bashkirov *et al.* find

$$\sigma_{\mathrm{WEPL}} = \sqrt{\left(\sigma_{rs} \times \left(\mathrm{WEPL} + W_0 + \sum_{i=1}^{f-1} S_i\right)\right)^2 + \left(pR_{res}\frac{\sigma_E}{E}\right)^2}. \tag{A.3}$$

where R_{res} marks the residual range of the particles in the final stage they reach into, and E is the measured energy deposit in that stage, with σ_E the read-out uncertainty. The parameter p is the exponent of the Bragg-Kleemann energy-range power law (Bortfeld 1997), and is found to be 1.738 by fitting NIST energy-range tables for helium ions (Berger et al. 2005).

Time-of-flight detector Since a TOF detector provides the total residual energy of the particles, it functions equivalently to a single-stage detector. The corresponding WET resolution can be found with $n = 1$ from equation A.3. The energy resolution is determined by the time resolution of the detector panels. The energy resolution of the detector can then be calculated using the description of the relativistic kinetic energy.

$$\frac{\sigma_E}{E} = \frac{1}{E}\frac{\partial((\gamma-1)mc^2)}{\partial t}\sigma_t = \frac{mv^2\gamma^3}{t}\frac{\sigma_t}{E}, \tag{A.4}$$

where $\gamma = 1/\sqrt{1 - v^2/c^2}$ is the Lorentz factor, $v = s/t$ is the particles velocity determined by time of flight t and distance traveled between the detector planes s, $m = 3727.38\,\mathrm{MeV/c^2}$ is the helium ions mass and c is the speed of light. The uncertainty σ_t is computed by quadratically adding the time resolution of each detector plane. Equation A.4 is then inserted in Equation A.3 setting $f = 1$.

Loss of primaries

An important aspect of the different detector designs is the loss of primaries through nuclear interactions. In Figure A.1, we show the loss of primaries as simulated with the Geant4 Monte Carlo particle transport toolkit (Agostinelli et al. 2003, Allison et al. 2006, Allison et al. 2016) version 10.05. The G4EM-StandardPhyiscs_option4 physics class has been used to model electromagnetic interactions. G4BinaryIonCascadePhyisic and G4HadronElasticPhysics-HP have been activated to model inelastic and elastic nuclear interactions, respectively. An ideal helium ion beam 200 MeV/u (mono-energetic, no angular spread) has been irradiated on a water target. At depth intervals of 0.5 mm in the water target, the number of primary particles relative to the initial number of helium ions has been stored in a histogram (shown as blue curve in Figure 2.7). In order to parametrize the loss of primaries, a third order polynomial fit has been performed in an interval from 0 to 250 mm depth (orange curve). The

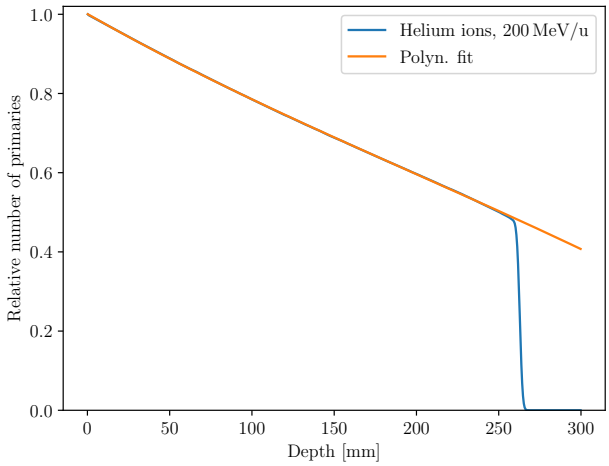

Figure A.1: Number of primary helium ions relative to the initial number of primaries as a function of depth in a homogeneous water target (blue) as obtained from a Geant4 simulation. The beam initial energy was 200 MeV/u and generated directly at the water absorber entrance. No energy or angular spread was assumed. The loss of primaries was fitted with a thrid order polynomial (orange).

polynomial parameters were

$$f(WEPL) = 1 - 0.0024WEPL + 2.7 \times 10^{-6}WEPL^2 - 4.4 \times 10^{-9}WEPL^3. \quad \text{(A.5)}$$

This was then used to calculate the relative loss of primaries for a given WEPL. Except for the TOF detector, all detector designs require the particles to come to a complete stop within the detector, meaning a loss of ∼50% of particles. The pixel noise is given as the WEPL standard deviation divided by the square root of the particles used in the pixel ($\sigma_{WEPL}/\sqrt{N}$) (Collins-Fekete et al. 2020). For a TOF design, the lower loss of primaries results in an advantage over the other detector designs in terms of the primary particles needed to arrive at a certain number of particles useful for imaging (assuming the particle detection efficiency to be the same between the setups). Denoting the number of initial primary particles N_{prim}, and the number of particles used for image reconstruction as N_{TOF} for TOF and $N_{RS,SSD,MSD}$ for the other detectors, this can be quantified as

$$N_{TOF} = N_{prim} \times f(WEPL) \quad \text{(A.6)}$$

$$N_{RC,SSD,MSD} \approx 0.5 N_{prim} \quad \text{(A.7)}$$

$$\Rightarrow N_{TOF} = 2f(WEPL) N_{RC,SSD,MSD} \quad \text{(A.8)}$$

In terms of the pixel noise ($\sigma_{WEPL}/\sqrt{N}$), the reduced loss of primaries for the TOF detector means a decrease in noise by a factor of $1/\sqrt{2f(WEPL)}$ per irradiated primary particle compared to the other detector designs.

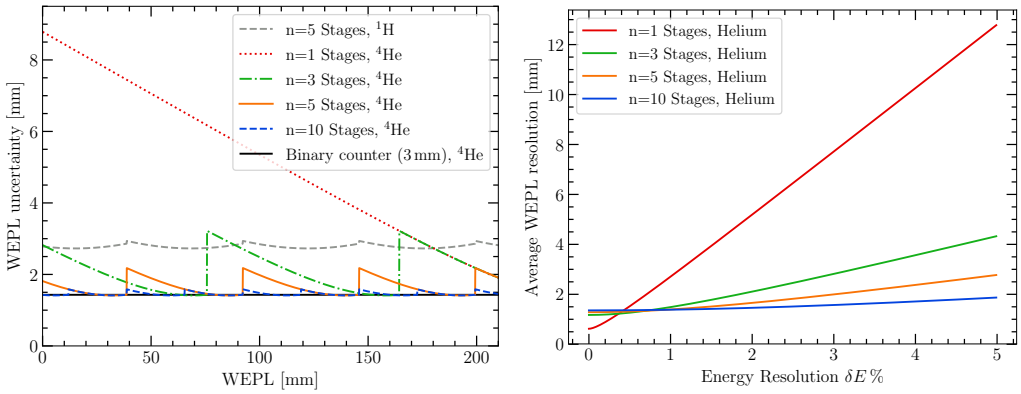

(a) **(b)**

Figure A.2: WEPL resolution of different detector configurations for helium ions at 200 MeV/u initial energy. (a) The WEPL resolution as function of the traversed WEPL for an energy resolution of $\sigma_E/E = 0.02$. In addition, the WEPL resolution of a binary range counter with 3 mm slab thickness is shown. For comparison, the WEPL resolution of a 5-stage detector for protons at 200 MeV is depicted. (b) Average WEPL resolution of the different multistage scintillator designs for 200 MeV/u helium ions as function of the detector energy resolution.

Results

In Figure A.2, the WEPL resolution of different multi-stage energy detector setups for helium ions is shown. Figure A.2(a) shows the WEPL resolution as function of the WEPL traversed by the particles for a fixed energy resolution of 2 %, and Figure A.2(b) shows the average resolution achievable with the different designs as function of the stage energy resolution. For comparison, the resolution of a 5-stage energy detector for protons is shown. The beam energy was assumed constant and set to 200 MeV/u (260.1 mm range in water).

It can be seen, that due to the helium's reduced range straggling compared to that of protons, the average WEPL resolution is improved at the same detector parameters. For helium ions, a 10 stage detector design provides an energy resolution close to the helium ions range straggling with only little dependence on the energy resolution of the stages. However, the average gain over the 5-stage design currently employed in the pCT collaboration prototype (Bashkirov et al. 2016b, Johnson et al. 2017) is little.

Figure A.3 shows the WEPL resolution of different TOF detector setups. In Figure A.3(a), the WEPL resolution is shown as a function of traversed WEPL for a fixed distance of 300 mm in between the two TOF planes for time resolutions per plane of 10 ps and 20 ps. The solid lines indicate the intrinsic single particle WEPL uncertainty. The dashed lines take into account the lower loss of primaries for the TOF design compared to detector designs that require the particle to come to a complete stop, for a better comparison between the different detector designs. It can be seen, that the resolution quickly deteriorates with decreasing time resolution. The benefit of the lower loss of primaries for

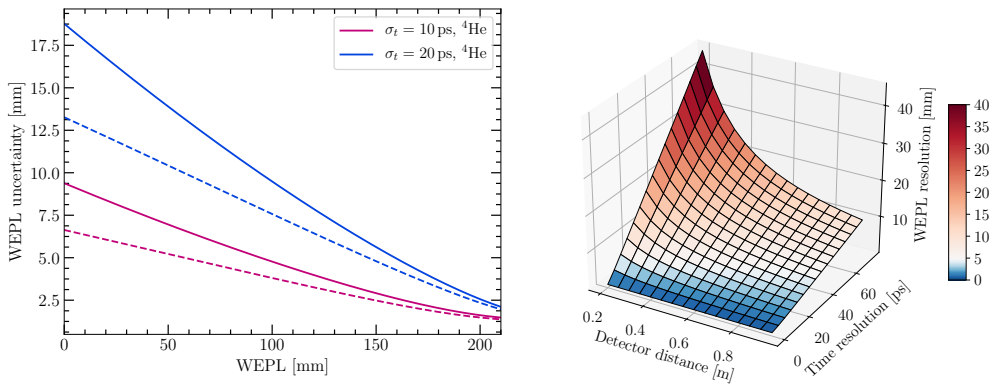

(a) **(b)**

Figure A.3: WEPL resolution of a TOF detector for helium ion imaging at 200 MeV/u initial energy. (a) The WEPL resolution as function of the traversed WEPL for a distance of $s = 300$ mm between the TOF detector planes. Solid lines indicate the intrinsic per-particle WEPL resolution. Dashed lines also take into account the lower loss of particles for the TOF design compared to the other detector designs. (b) Average WEPL resolution of the detector over the whole WEPL range as function of the time resolution and distance between the detector planes. The bins correspond to steps of 5 cm in detector distance and 5 ps in time resolution. Cases with average WEPL resolution better than 5 mm are shaded in blue, those above in red.

thinner objects is drastically overshadowed by the low intrinsic WEPL resolution of the TOF at thin phantoms, i.e. high residual kinetic energies. For a time resolution of 10 ps per TOF plane, however, a pixel noise better than that of a single stage energy calorimeter may be achievable for the same number of primaries, i.e at the same dose to the object.

Figure A.3(b) shows the average WEPL resolution of a TOF setup as function of the distance between the detector planes and the time resolution of each plane. The intrinsic WEPL resolution is shown, i.e. the lower loss of primaries is not taken into account in that figure. Configurations with average WEPL resolution better than 5 mm are shaded in blue, those with lower WEPL resolution in red. From the plot, it can be deduced, that either a very high time resolution or large distance between detector planes is necessary to provide a WEPL resolution comparable with that of a multistage design. For a TOF detector comparable in size to the rear detector components of the pCT collaboration prototype, i.e. ∼300 mm (including the size of the rear tracker setup, which for a TOF detector can be removed), the time resolution of each of the detector planes would need to be 3.5 ps to achieve an average WEPL resolution equal to the helium ions range straggling over the full range.

Finally, Figure A.4 shows the achievable WEPL resolution with the different detector designs while allowing for a modulated initial beam energy. The highest beam energy was set to 200 MeV/u, which is sufficient for imaging of head sized objects. We required the minimum residual energy of the beam to be 80 MeV/u following the work by Arbor et al. (2015) which we also used to

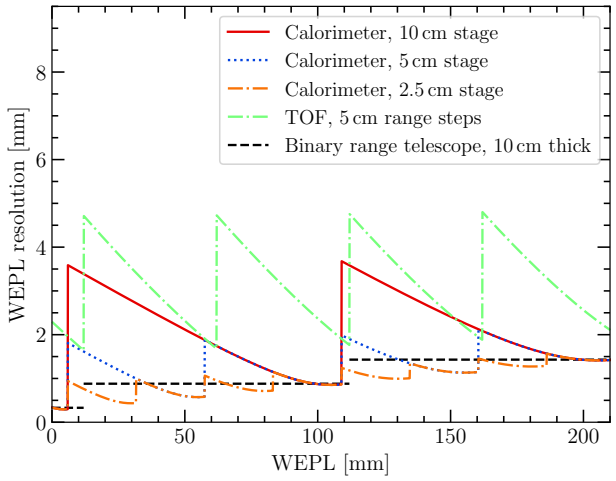

Figure A.4: WEPL resolution as function of the traversed WEPL for different detector designs and modulated initial energy. The change in energy occurs at the point were the residual range of the particles after the phantom is at the limit of the detector's dynamic range. The resolution for the calorimeter detectors was set to 2 %. For the TOF detector, the distance between the two TOF planes was 300 mm, the time resolution of each plane was 20 ps. For the binary range counter, the slab thickness was 3 mm.

define the thickness of the ΔE stage placed in front of the SSD and RC designs. For the multistage designs, the energy resolution was set to 2 %. For the TOF detector a distance of 300 mm between the detector planes was set, and the time resolution of each of the planes was set to 20 ps. The intrinsic WEPL resolution is shown, i.e. the lower loss of primaries is not taken into account in that figure. For the binary range counter, the thickness of each slab was set to 3 mm. Here, we assumed the individual energy steps to correspond to a separation in range equal to the detector dynamic range. This means, no threshold was set on the minimum range in the detector, and the maximum range was given by the WET of the detector. Note, however, that the energy modulation does not necessarily need to follow the physical limitation of the detector size. It might even be preferential to require the minimum and maximum range in the detector such that the full straggling distribution of the particles is recorded inside the detector. This would avoid a truncation of the straggling distribution and might be advantageous in order to avoid uncertainties arising from stage interfaces (publication P.XII, publication P.XI, publication P.X). A minimum range in the detector of 3 standard deviations of the range straggling (anything more is cut anyways by the 3σ WET filter) might avoid a shift in the distribution mean from truncation. In turn, requiring a minimum range of 4.3 mm (for helium ions) would not largely affect the noise shown in Figure A.4.

As expected, the WEPL resolution benefits from the lower range straggling for the reduced initial energy. Especially, the TOF detector benefits from the smaller particle velocities at the object exit, resulting in an average WEPL resolution of 3.13 mm with 5 energy steps. For the RC, any energy modulation

will provide better results, as the noise is largely dominated by the range straggling. For a telescope with 10 cm dynamic WEPL range (3 energy steps needed to cover 210 mm WEPL), the average resolution was 1.11 mm.

Discussion

Choice of detector setup

Here the noise property of different detector setups to measure the residual energy/range of the helium ions after traversing the patient has been investigated. We started from the segmented scintillator energy/range detector design proposed by Bashkirov et al. (2016a). It was shown, that the lower range straggling of helium ions would favor an increased number of stages compared to that used for proton imaging, when looking at the energy dependence of the WEPL resolution (Figure A.2(b)). However, at an assumed 2% energy resolution, the benefit of even a 10 stage design over the currently used 5 stage design is meager, and would not justify the increased setup complexity and cost. For both designs, the average WEPL resolution in that case is already close to the helium ions range straggling. In addition, in terms of the ΔE-E filter, there is no significant difference between the two setups (B.Sc. thesis of Tom Vichtl, DKFZ/Heidelberg University, Supervisor: L. Volz and J. Seco). One major drawback of segmented energy detectors are ring artifacts in the reconstructed images corresponding to the stage interfaces (as seen in publication P.XII, P.XI, P.X and Section 5.4). Various causes for ring artifacts have been identified, and it has yet to be demonstrated that images without ring artifacts can be achieved experimentally with a segmented detector design.

As a direct method to infer the range, a binary RC has been assessed. The binary RC has the advantage of a very relaxed readout requirement compared to calorimeter approaches, as it does not need to measure a correct energy value in the slab. Especially, the direct measurement of range would avoid the conversion from energy to WEPL, which is sensitive to the calibration setup and parameters set in the calibration procedure. In addition, a RC would avoid systematic artifacts corresponding to the segmentation of a multistage calorimeter. At the same time, a RC with sufficiently small slab size would yield a very high WEPL resolution, which for 3 mm slabs (1.67 mm WEPL resolution) is close to the helium ions' range straggling (1.43 mm). As readout of the slabs, for example SiPMs can be used, which have shown promising results in the past (Sadrozinski et al. 2013). However, it has yet to be determined how accurate secondary fragments can be removed with a ΔE-RC setup. If no lack in accuracy is observed, we put forward the RC design as a robust solution. For proton imaging, publication P.XI already indicates that a ΔE-E filter may not be needed, if a better filter acting on the WEPL variance per pixel (i.e. a tighter 2 sigma filter or a filter based on the distribution FWHM) were used. Hence for pCT, the range counter would be the ideal design in terms of robustness, cost and WEPL noise. Finally, as demonstrated in publication P.V, a scintillator range telescope design is very useful as a quality assurance tool. For example,

a second generation of the scintillator developed in that work could be envisioned featuring a CMOS readout on one side for integration range measurements for particle therapy quality assurance, and a SiPM readout on another for high sensitivity single-event measurements. Such a compact, affordable and multipurpose design could be very useful in everyday clinical practice.

A setback of the detector designs that require the particles to stop in order to infer their residual energy/range is the increased loss of primaries and the increased straggling noise (equal to the total range straggling rather than just that of the object). Especially, for scintillator detectors that are similar in chemical composition to tissue (Beddar & Beaulieu 2016), the loss of primaries and straggling noise is independent of the object WET. This is in contrast to what has been assumed in recent theoretical studies (Rädler et al. 2018, Collins-Fekete et al. 2020). This also means that with such detector designs the only factor object related factor producing noise variations in the reconstruction is the MCS.

We investigated a TOF detector design as a potential alternative to the designs that require the particle to come to a complete stop. While a TOF design in terms of straggling and primary loss would behave like the theoretical prediction in Rädler et al. (2018) and Collins-Fekete et al. (2020), the low contrast offered by the time-of-flight for high residual kinetic energies requires a very high time resolution per TOF plane (<10 ps) for the detector to offer a WEPL resolution comparable with that of the other designs at a reasonable detector size. Such a time resolution does not seem unreasonable considering the recent advances made in ultra-fast silicon pixel detectors (compare Worstell et al. (2019)). Especially, depending on the detector dead time, high particle rates would not be an issue with such a system. If pico-second time resolution tracking detectors become affordable, a TOF design would have enormous potential for particle imaging.

Dynamic WEPL range

The WEPL range the detector has to cover depends on the particular application: for HeCT the full WET of the object needs to be completely covered in order to avoid artifacts in the CT reconstruction. On the other hand, if only single helium ion projections are to be used for pre-treatment alignment as well as optimization of the RSP in combination with a planning x-ray CT (Schneider et al. 2005, Collins-Fekete et al. 2017a, Krah et al. 2019), a lower dynamic WEPL range could be already useful. In that case, already a small field of view of the patient could provide sufficient information for accurate optimization of the HU to RSP lookup table (Krah et al. 2019), which for a head can result in a much relaxed requirement on the detector WEPL range.

With the goal to save on detector cost and size, it has been proposed by some groups to use a detector with limited dynamic WEPL range (Welsh et al. 2017, Gehrke et al. 2018). In order for the particles' residual range after the phantom to remain within the detector limits, the initial energy is modeled appropriately to the water equivalent thickness of the object. Taking into account fast energy variation available at cyclotrons, the use of different energies per

projections might not prolong the scan duration by much. In order to avoid unnecessary additional dose to healthy tissue, however, a prior information on the object would be required.

For the scintillator and range telescope approaches, a modulated energy would reduce the noise from range straggling and result in decreased loss of primaries. In addition, energy modulation would enable to largely reduce the overall detector size, which is beneficial for clinical implementation. Moreover, if the energy steps are not chosen from the detector WET, but in a way, that particles stopping close to the detector boarders is avoided, systematic artifacts corresponding to stage interfaces might be mitigated. However, a more in depth study on that aspect of energy modulation is needed. The WEPL resolution of TOF designs would especially benefit from energy modulation. The slope of the velocity as function of energy provides more contrast at lower energies (Worstell et al. 2019), drastically improving the overall WEPL resolution of the system (Figure A.4).

APPENDIX B

Additional data for the helium/carbon mixing method

In this appendix, additional unpublished data for the helium/carbon method presented in publication P.VII (Section 5.5) are provided that were acquired in the beam tests at the HIT facility with the University College London scintillator prototype. As for the publication, the experimental data have been processed by Laurent Kelleter (University College London, UK), while additional simulations were carried out by the author of this thesis. In detail, additional experiments and simulations for different sized air-filled gaps in the PMMA degrader setup (Section 5.5 and Figure 5.46) are shown. Results for a thinner pencil beam focus ($\sim$5 mm FWHM) instead of the one used for the published results ($\sim$8 mm FWHM) are shown, to demonstrate the increase in sensitivity of the method for a finer beam spot focus. Data for a 1 mm thick air-filled gap in the PMMA setup at different slit widths are presented to highlight the potential of the helium carbon method for detecting small relative range changes. Finally, a 10 mm thick air gap is investigated to provide a more quantitative context for the results presented for the ADAM anthropomorphic pelvis phantoms for which comparatively large range changes had been observed. Except for the beam focus and air gap size, the setup was the same as described in Section 5.5: the beam initial energy was 220.5 MeV/u for helium ions, and 219.8 MeV/u for carbon ions. The beam intensity was 8×10^7 particles/s for the experiments, and the measured helium data was scaled to match a 1/10 ratio between primary helium and carbon ions. For the simulations, 10^6 primary carbon ions and 10^5 primary helium ions were generated. Beam mixing was then achieved by summing up the helium and carbon data.

Investigation of different pencil beam focus size

In the published manuscript we had presented results only for a $\sim$8 mm FWHM focus of the carbon and helium ion pencil beam, as this corresponds to a typical focus setting for carbon beam therapy. However, the sensitivity of the

helium/carbon mixing method is increased for smaller focus sizes, as more of the beam particles traverses the air-filled gap in the PMMA setup. To quantify this, we took data with a carbon ion beam at a spot FWHM of 4.7 mm, corresponding to a helium ion beam at a FWHM of 4.9 mm. The results are shown in Figure B.1. For the 4.7 mm FWHM beam, ∼38% of the beam particles crossed the air-filled gap for a slit width of 2 mm. This is reflected in the increased relative change observed in Figure B.1, compared to what was reported in Figure 5.49. For the 5 mm wise gap, 79% of the helium beam crossed the slit. In Figure B.1(c) we also included a slit thickness of 10 mm. The shift of the helium range is clearly visible in that case. From the relative weight of the individual Bragg peaks contributing to the observed depth-light profile, it would be possible to estimate the number of particles that traversed the uncertainty. This would be especially useful for dose reconstruction, as it would provide an estimate of the portion of the pencil beam dose that was misplaced.

Different slit widths for a 1 mm air-filled gap

In the published manuscript, we had shown the helium/carbon mixed signal for the 1 mm thick air gap only for the thinnest slit width set in the measurements (2 mm), in order to showcase the sensitivity of the method. The acquired data for wider slit widths (5 mm and 10 mm) are provided in Figure B.2. Due to limited beam time, the 1 mm thick air-filled gap settings were not measured for the ∼5 mm FWHM beam setting, but this is provided from simulation. For the ∼8 mm FWHM beam, 85% of the beam particles crossed the air-filled gap in case of a 10 mm slit width. For the ∼5 mm FWHM beam, the 10 mm wide air-filled gap is traversed by 99% of the beam particles. This highlights the potential of the helium/carbon mixing method: not only are range shifts affecting the whole pencil beam observable, but also range shifts that affected only a fraction of the pencil beam particles.

Investigation of a 10 mm slit thickness

Finally, Figure B.3 shows the results for a 10 mm thick air-filled gap in the PMMA absorber. The width of the slit was set to 2 mm, 5 mm ant 10 mm. Both, the ∼5 mm and ∼8 mm beam focus settings are shown. The 10 mm thick slit results in large observed differences in the mixed helium/carbon signal. These changes are comparable to what was seen for the investigation of rectal gassing with the ADAM pelvis phantom for the treatment spot close to the rectal wall. Hence, these results serve to provide a quantitative context for the qualitative results shown in Figure 5.51.

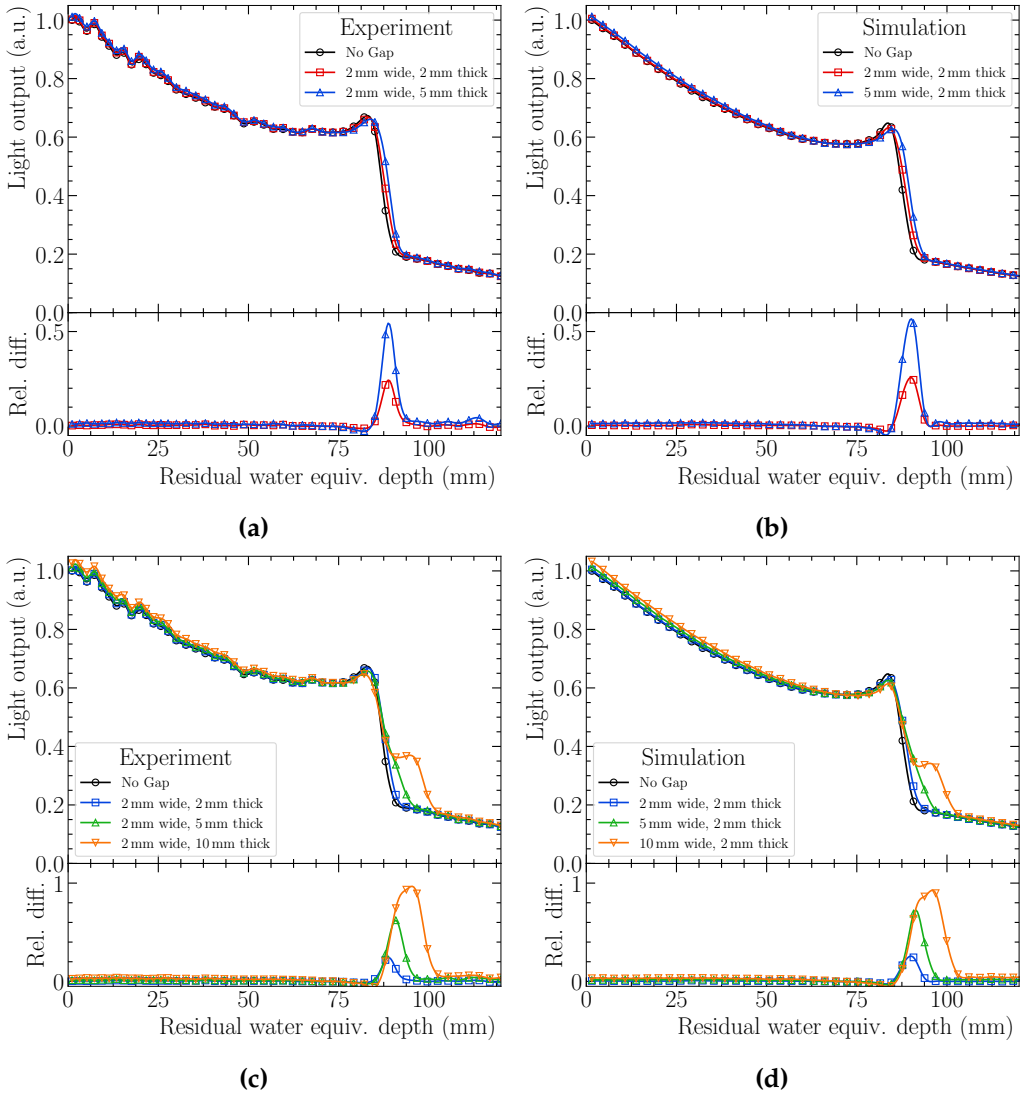

Figure B.1: Result of introducing an air-filled slit of width 2 mm and thicknesses of 2 mm and 5 mm (top), as well as a fixed width of 2 mm and thickness of 2 mm to 5 mm (bottom) in the beam path: measurement (left) and simulation(right). The beam focus was 4.9 mm FWHM for the helium ion, and 4.7 mm FWHM for the carbon ion beam.

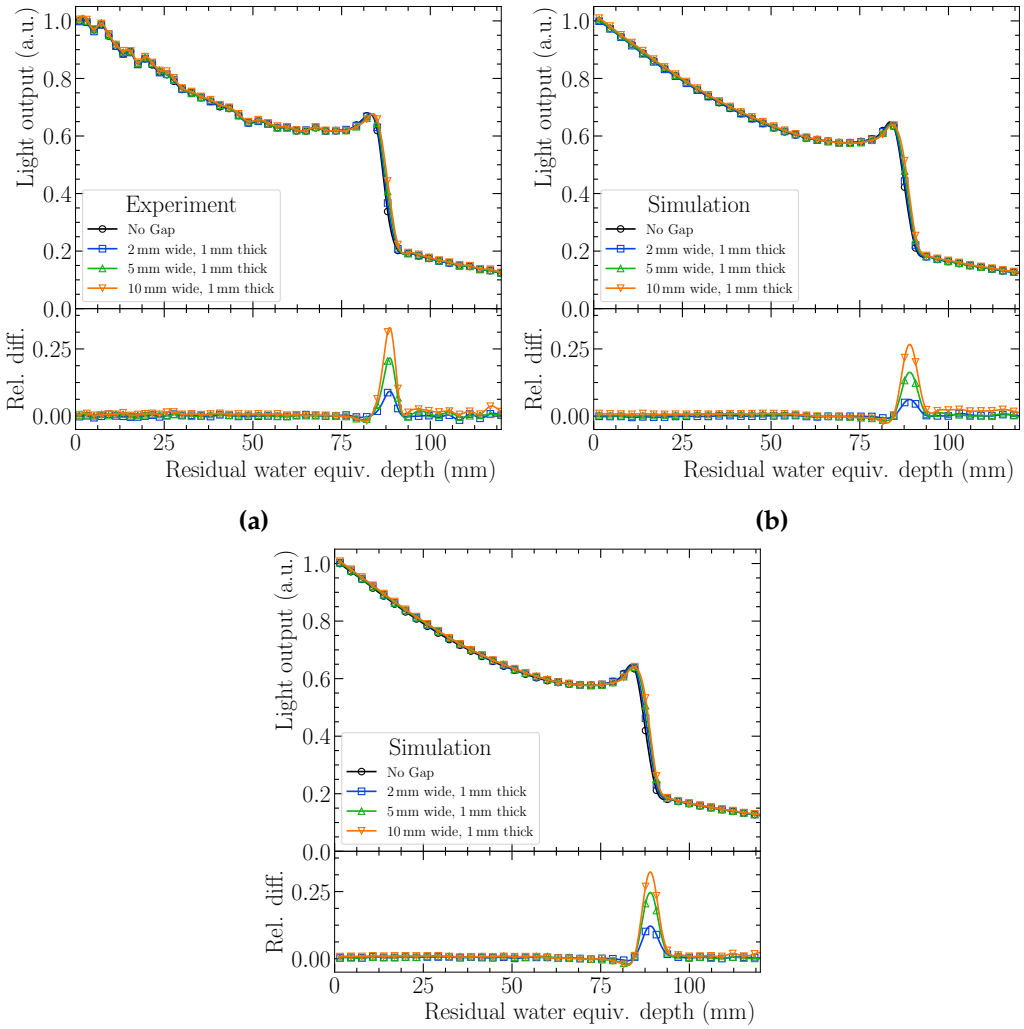

Figure B.2: Result of introducing an air-filled slit of 1 mm thickness and width of 2 mm, 5 mm and 10 mm in the beam path: measurement (left) and simulation(right). Top: The beam focus was 8.1 mm FWHM for the helium ion, and 8.5 mm FWHM for the carbon ion beam. Bottom: The beam focus was 4.9 mm FWHM for the helium ion, and 4.7 mm FWHM for the carbon ion beam.

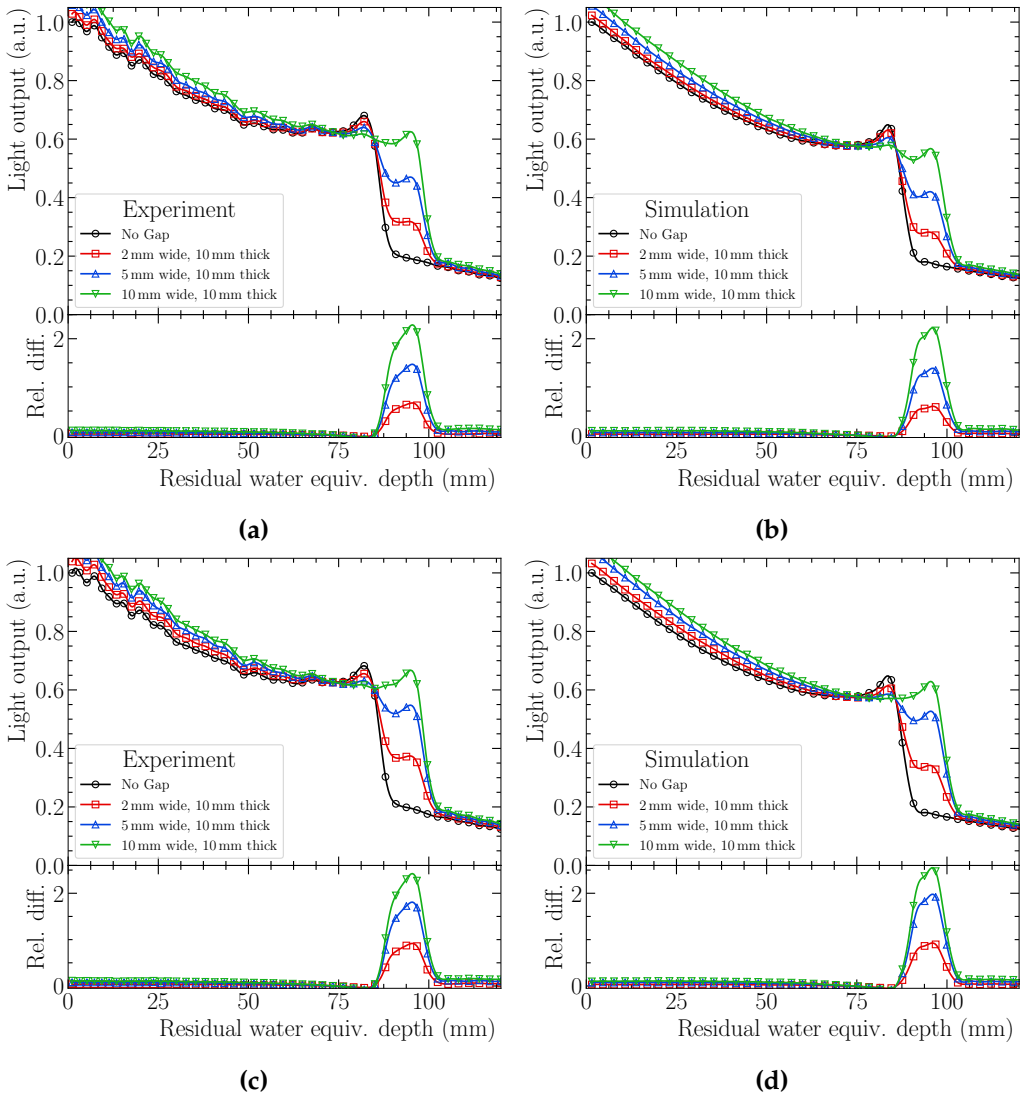

Figure B.3: Result of introducing an air-filled slit of width 2 mm to 10 mm and thickness of 10 mm into the PMMA setup: measurement (left) and simulation(right). Top: The beam focus was 8.1 mm FWHM for the helium ion, and 8.5 mm FWHM for the carbon ion beam. Bottom: The beam focus was 4.9 mm FWHM for the helium ion, and 4.7 mm FWHM for the carbon ion beam.

List of publications

Peer-reviewed journal articles

P.I **L. Volz**, E. Bär, C.-A. Collins-Fekete et al. (2020) "Experimental comparison of proton CT and helium ion CT with single- and dual-energy x-ray CT in heterogeneous biological tissue samples" *In Preparation*, **Presented in this thesis**

P.II J. Alme, G. G. Barnaföldi, R. Barthel et al. (2020) "A High-Granularity Digital Tracking Calorimeter Optimized for Proton CT", Accepted for publication in *Frontiers in Physics*

P.III H. E. S., Pettersen, **L. Volz**, J. R. Sølie et al. (2020) "Helium Radiography with a Digital Tracking Calorimeter—a Monte Carlo Study for Secondary Track Rejection", Submitted to *Physics in Medicine and Biology*, **Presented in this thesis**

P.IV **L. Volz**, C.-A. Collins-Fekete, J. R. Sølie and Seco, J. (2019) Theoretical considerations on the spatial resolution limit of single-event particle radiography, *Biomedical Physics and Engineering express*, (6)055002, **Presented in this thesis**

P.V L. Kelleter, R. Radogna, **L. Volz** et al. (2020) "A scintillator-based range telescope for particle therapy", *Physics in Medicine and Biology*, (65)165001

P.VI J. R. Sølie, **L. Volz**, H. E. S. Pettersen et al. (2020) "Image quality of list-mode proton imaging without front tracker", *Physics in Medicine and Biology*, 65 135012, **Presented in this thesis**

P.VII **L. Volz**, L. Kelleter, S. Brons et al. (2020) "Experimental exploration of a mixed helium/carbon beam for online monitoring in carbon ion beam therapy", *Physics in Medicine and Biology*, (65)055002, **Presented in this thesis**

P.VIII G. Tambave, J. Alme, G. Barnaföldi et al. (2019) "Characterization of monolithic CMOS pixel sensor chip with ion beams for application in particle computed tomography", *Nuclear instruments and measurements: Section A*, (918)162626

P.IX H. E. S. Pettersen, J. Alme, G. Barnaföldi et al. (2019) “Design Optimization of a Pixel-Based Range Telescope for Proton Computed Tomography”, *Physica Medica*, (63)pp83-97

P.X G. Dedes, J. Dickmann, K. Niepel et al. (2019) “Experimental comparison of proton CT and dual energy X-ray CT for relative stopping power estimation in proton therapy”, *Physics in Medicine and Biology*, (64)165002

P.XI **L. Volz**, P. Piersimoni, R. P. Johnson et al. (2019) Improving single-event proton CT by removing nuclear interactions with the energy/range detector, *Physics in Medicine and Biology*, (64)15NT01, **Presented in this thesis**

P.XII **L. Volz**, P. Piersimoni, S. Brons et al. (2018) “The Impact of secondary fragments on the image quality of helium ion imaging”, *Physics in Medicine and Biology*, (63)195016, **Presented in this thesis**

Contributions at conferences

C.I **L. Volz**, E. Bär, C.-A. Collins-Fekete et al. (2020) "Status update on the PTCOG funded project: Proof-of-concept for range accuracy improvement with helium ion imaging" **Poster:** PTCOG59, 59th annual meeting of the Particle Therapy Co-Operative Group (PTCOG) (virutal)

C.II **L. Volz**, C.-A. Collins-Fekete, J. R. Sølie et al. (2020) "Theoretical investigation of the spatial resolution in particle radiography" **Poster:** PTCOG59, 59th annual meeting of the Particle Therapy Co-Operative Group (PTCOG) (virutal)

C.III E. Bär, **L. Volz**, C.-A. Collins-Fekete et al. (2020) “Comparing photon and particle imaging modalities for stopping power prediction in particle therapy” **Talk:** Joint AAPM/COMP meeting (virtual)

C.IV **L. Volz**, J. R. S. Sølie, H. E. S. Pettersen et al. (2019) “Single-event particle imaging without front tracker” **Poster highlight:** 50th Annual Meeting of the German Medical Physics Society, Stuttgart, Germany

C.V **L. Volz**, L. Kelleter, S. Brons et al. (2019) “Investigation of motion monitoring with a mixed He/C beam” **Poster:** 50th Annual Meeting of the German Medical Physics Society, Stuttgart, Germany

C.VI **L. Volz**, P. Piersimoni, V. A. Bashkirov et al. (2019) “Improving single-event particle imaging by ΔE-E filtering” **Poster:** PTCOG58, 58th annual meeting of the Particle Therapy Co-Operative Group (PTCOG), Manchester, United Kingdom

C.VII **L. Volz**, L. Kelleter, S. Brons et al. (2019) “Using a mixed helium/carbon treatment beam for monitoring intrafractional motion” **Talk:** PTCOG58, 58th annual meeting of the Particle Therapy Co-Operative Group (PTCOG), Manchester, United Kingdom

C.VIII L. Kelleter, R. Radogna, **L. Volz** et al. (2019) "A novel scintillator range telescope for particle therapy" **Poster:** PTCOG58, 58th annual meeting of the Particle Therapy Co-Operative Group (PTCOG), Manchester, United Kingdom

C.IX J. R. Sølie, **L. Volz**, H. E. S. Pettersen et al. (2019) "Optimizing image quality of single-sided list mode particle imaging" **Poster:** PTCOG58, 58th annual meeting of the Particle Therapy Co-Operative Group (PTCOG), Manchester, United Kingdom

C.X H. E. S. Pettersen, **L. Volz**, J. R. S. Sølie et al. (2019) "Estimating a proton's position in a pencil beam for proton imaging" **Poster:** PTCOG58, 58th annual meeting of the Particle Therapy Co-Operative Group (PTCOG), Manchester, United Kingdom

C.XI P. Piersimoni, J. Alme, G. Barnaföldi et al. (2019) "Using the ALPIDE chip as a beam monitoring system with a micrometric spatialresolution" **Poster:** PTCOG58, 58th annual meeting of the Particle Therapy Co-Operative Group (PTCOG), Manchester, United Kingdom

C.XII **L. Volz**, P. Piersimoni, V. A. Bashkirov et al. (2018) "Filtering of fragmentation events in helium ion imaging" **Talk:** 49th Annual Meeting of the German Medical Physics Society, Nürnberg, Germany

C.XIII C. Graeff, N. Saito, C. Shuy et al. (2018) "Investigation of Helium as a Range Probe in Carbon Ion Therapy" **Talk:** PTCOG57, 57th Annual Meeting of the Particle Therapy Co-Operative Group (PTCOG), Cincinnati, Ohio, USA

Honors and Awards

H.I March 2020: Selected for a travel grant awarded by PTCOG to attend the PTCOG 59 meeting in Taipei, Taiwan (Conference postponed due to COVID-19 pandemic)

H.II Feb 2020: Publication P.VII featured in IOP publishing ltd.'s magazine "physics world" (www.physicsworld.com)

H.III Sep 2019: Travel stipend awarded by the German Medical Physics Society (DGMP) to attend the 50th annual meeting in Stuttgart, Germany

H.IV June 2019: Particle Therapy Co-Operative Group (PTCOG) funded project "Proof-of-principle evaluation of helium ion imaging to reduce range uncertainty in particle therapy", Co-Investigator, Principle Investigators: Prof. Joao Seco and Prof. Reinhard W. Schulte

Acknowledgements

Taking on the endeavor of pursuing the degree of Dr. rer. nat has been a great adventure. Not only did I learn more about physics through my research, but the last three years have taught me many valuable things about myself and helped me grow personally. From the stress before deadlines, the frustration when things do not go as smooth as one would like, to the excitement when they finally do, leading to new and interesting discoveries, and the great feeling of achievement when results are published in a research journal — I am grateful that I could experience all this. Of course, I was not alone in this journey, and none of the results presented in this thesis would have been possible if it were not for my collaborators, colleagues and friends. As such, I have to express many thanks to several people.

First of all, I would like to thank Prof. Dr. Joao Seco. Not only did he take me into his research group and guide me throughout my thesis as my main supervisor, part of my thesis advisory committee and first examiner in the defense, but his enthusiasm and plentiful ideas for the project constantly pushed me forward. I am certain that his energetic supervision is a main reason for the thesis success. He also provided me the opportunity to work in an international environment with collaboration partners from the US, Norway and the UK which I am very grateful for.

One of these collaboration partners is Dr. Charles-Antoine Collins-Fekete who was a key factor for the thesis success and through his mentorship, especially during my time at the MGH in Boston, helped shaping me as a researcher. His brilliant ideas, the countless hours of discussions we shared (not seldom over a pint of beer or two), and the different investigations we conducted have boosted my understanding of particle imaging and physics in general. He is an amazing person to work with, and a truly wonderful friend.

Next, I would like to thank Dr. Pierluigi Piersimoni, who contributed a great deal to this PhD thesis. Not only did we work closely together during the first year of my thesis, sharing ideas and discussion of the results, setting the basis for this thesis research, but also continued our collaboration when he joined the University of Bergen pCT group.

Further, I express many thanks to Jarle Rambo Sølie and Dr. Helge Egil Seime Pettersen. The idea to leave out the front trackers of a single-event particle imaging system and the following research campaigns have been fascinating, and I am grateful that I have been part of this fruitful research team. This I would like to extend to the whole of the University of Bergen pCT group: I feel very grateful to be part of this fruitful collaboration, and that I have been

able to contribute to the benchmarking of the ALPIDE chips in Oslo, and the Heidelberg Ion-Beam Therapy facility.
I would like to express my gratitude to the US pCT collaboration, especially for enabling me to do experiments with their pre-clinical prototype pCT detector system at the Heidelberg Ion-Beam Therapy Facility. Above all, I would like to express my gratitude to Prof. Dr. Reinhard Schulte, Prof. Dr. Robert P. Johnson, and Assoc. Prof. Dr. Vladimir Bashkirov. Their vast expertise in particle imaging and detector construction has been inspiring. I am tremendously thankful for their support throughout this research project, and to be part of this multi-center collaboration.
I would also like to thank Dr. Esther Bär. Without her immense expertise in stopping power estimation from dual-energy CT, the comparison between particle and photon imaging would not have been possible.
Further, I thank Assoc. Prof. Simon Jolly, Dr. Raffaella Radogna and, especially, Laurent Kelleter for their contributions to the experimental investigation of the helium/carbon mixing method. Not only did they provide the prototype detector to experimentally test this novel method, their contribution has been vital to the overall success of this project and I learned a great deal about detector physics in the discussions we shared. In that context, I would also like to thank Dr. Christian Graeff, who provided the idea for the helium/carbon mixing method and helped guiding me through my research project as part of my thesis advisory committee.
I acknowledge the Heidelberg Ion-Beam Therapy facility, and especially Dr. Stephan Brons, for making the experimental campaigns presented in this thesis possible. Stephan Brons' inexhaustible help in beam time preparation has been invaluable.
Many thanks also go to everyone in the departments of *Biomedical Physics in Radiation Oncology*, and *Medical Physics in Radiation Oncology* at the German Cancer Research Center (DKFZ) for providing such a nice working environment, all the discussions shared over a cup of coffee and the good memories from group nights-out at conferences. I especially thank Jeannette Jansen for her help in proof-reading this thesis.
Not least, I would like to express my thanks to Prof. Oliver Jäkel for reading and evaluating this thesis and being the second examiner in the final defense.

And finally, I would like to thank my family, my wife and my son. I cannot express how grateful I am for their support throughout my PhD studies and their patience in the more stressful phases of this project.

Bibliography

Agostinelli, S., Allison, J., Amako, K., Apostolakis, J., Araujo, H. et al. (2003). Geant4—a simulation toolkit, *Nuclear Instruments and Methods in Physics Research Section A: Accelerators, Spectrometers, Detectors and Associated Equipment* **506**(3): 250–303.
DOI: *10.1016/S0168-9002(03)01368-8*

Allison, J., Amako, K., Apostolakis, J., Araujo, H., Dubois, P. A. et al. (2006). Geant4 developments and applications, *IEEE Transactions on Nuclear Science* **53**(1): 270–278.
DOI: *10.1109/TNS.2006.869826*

Allison, J., Amako, K., Apostolakis, J., Arce, P., Asai, M. et al. (2016). Recent developments in geant4, *Nuclear Instruments and Methods in Physics Research Section A: Accelerators, Spectrometers, Detectors and Associated Equipment* **835**: 186 – 225.
DOI: *https://doi.org/10.1016/j.nima.2016.06.125*

Alme, J., Barnaföldi, G. G., Barthel, R., Borshchov, V., Bodeva, T., van den Brink, A. et al. (2020). A High-Granularity Digital Tracking Calorimeter Optimized for Proton CT, *Frontiers in Physics–Medical Physics and Imaging* . Accepted for publication.

Almeida, I. P., Schyns, L. E. J. R., Vaniqui, A., van der Heyden, B., Dedes, G., Resch, A. F., Kamp, F., Zindler, J. D., Parodi, K., Landry, G. & et al. (2018). Monte carlo proton dose calculations using a radiotherapy specific dual-energy ct scanner for tissue segmentation and range assessment, *Physics in Medicine & Biology* **63**(11): 115008. 00000.
DOI: *10.1088/1361-6560/aabb60*

Amato, C., Gehrke, T. & Martisikova, M. (2018). Spatial resolution improvements in helium-beam radiography.
URL: *https://protonimaging.sciencesconf.org/214291*

Amato, C., Martisikova, M. & Gehrke, T. (2020). A technique for spatial resolution improvement in helium-beam radiography, *Medical Physics* **47**(5): 2212–2221.
DOI: *10.1002/mp.14051*

Ammazzalorso, F., Graef, S., Weber, U., Wittig, A., Engenhart-Cabillic, R. & Jelen, U. (2014). Dosimetric consequences of intrafraction prostate motion in scanned ion beam radiotherapy, *Radiotherapy and Oncology* **112**(1): 100 – 105.
DOI: *https://doi.org/10.1016/j.radonc.2014.03.022*

Arbor, N., Dauvergne, D., Dedes, G., Létang, J. M., Parodi, K., Quiñones, C. T., Testa, E. & Rit, S. (2015). Monte Carlo comparison of x-ray and proton CT for range calculations of proton therapy beams, *Physics in Medicine and Biology* **60**(19): 7585–7599.
DOI: *10.1088/0031-9155/60/19/7585*

Arico, G. (2016). *Ion Spectroscopy for improvement of the Physical Beam Model for Therapy Planning in Ion Beam Therapy*, PhD thesis, The Faculty of Physics and Astronomy, Heidelberg University.
DOI: *www.doi.org/10.11588/heidok.00022292*

Artikov, A., Budagov, J., Chirikov-Zorin, I., Chokheli, D., Lyablin, M., Bellettini, G., Menzione, A., Tokar, S., Giokaris, N. & Manousakis-Katsikakis, A. (2005). Properties of the ukraine polystyrene-based plastic scintillator ups 923a, *Nuclear Instruments and Methods in Physics Research Section A: Accelerators, Spectrometers, Detectors and Associated Equipment* **555**(1): 125 – 131.
DOI: *https://doi.org/10.1016/j.nima.2005.09.021*

Badhwar, G., Deney, C., Dennis, B. & Kaplon, M. (1967). The non-linear response of the plastic scintillator ne102, *Nuclear Instruments and Methods* **57**: 116 – 120.
DOI: *https://doi.org/10.1016/0029-554X(67)90507-1*

Bär, E., Andreo, P., Lalonde, A., Royle, G. & Bouchard, H. (2018a). Optimized i-values for use with the bragg additivity rule and their impact on proton stopping power and range uncertainty, *Physics in Medicine & Biology* **63**(16): 165007.
DOI: *10.1088/1361-6560/aad312*

Bär, E., Lalonde, A., Royle, G., Lu, H.-M. & Bouchard, H. (2017). The potential of dual-energy ct to reduce proton beam range uncertainties, *Medical Physics* **44**(6): 2332–2344.
DOI: *10.1002/mp.12215*

Bär, E., Lalonde, A., Zhang, R., Jee, K., Yang, K., Sharp, G., Liu, B., Royle, G., Bouchard, H. & Lu, H. (2018b). Experimental validation of two dual-energy ct methods for proton therapy using heterogeneous tissue samples, *Medical Physics* **45**(1): 48–59.
DOI: *10.1002/mp.12666*

Bashkirov, V. A., Johnson, R. P., Sadrozinski, H. F.-W. & Schulte, R. W. (2016a). Development of proton computed tomography detectors for applications in hadron therapy, *Nuclear Instruments & Methods in Physics Research.*

Section A, Accelerators, Spectrometers, Detectors and Associated Equipment **809**: 120–129.
DOI: *10.1016/j.nima.2015.07.066*

Bashkirov, V. A., Schulte, R. W., Hurley, R. F., Johnson, R. P., Sadrozinski, H. F.-W., Zatserklyaniy, A., Plautz, T. & Giacometti, V. (2016b). Novel scintillation detector design and performance for proton radiography and computed tomography, *Medical Physics* **43**(2): 664–674.
DOI: *10.1118/1.4939255*

Bashkirov, V., Schulte, R., Coutrakon, G., Erdelyi, B., Wong, K., Sadrozinski, H., Penfold, S., Rosenfeld, A., McAllister, S. & Schubert, K. (2009). Development of proton computed tomography for applications in proton therapy, *Application of accelerators in research and industry: Twentieth International Conference, AIP Conference Proceedings*, Vol. 1099, pp. 460–463.

Bashkirov, V., Schulte, R., Penfold, S. & Rosenfeld, A. (2007). Proton computed tomography: Update on current status, *IEEE Nuclear Science Symposium Conference Record, 2007. NSS '07*, Vol. 6, pp. 4685–4688.
DOI: *10.1109/NSSMIC.2007.4437152*

Bazalova, M., Carrier, J.-F., Beaulieu, L. & Verhaegen, F. (2008). Dual-energy CT-based material extraction for tissue segmentation in Monte Carlo dose calculations, *Physics in Medicine and Biology* **53**(9): 2439.
DOI: *10.1088/0031-9155/53/9/015*

Beddar, S. & Beaulieu, L. (2016). *Scintillation Dosimetry*, Imaging in Medical Diagnosis and Therapy, CRC Press.
URL: *https://books.google.de/books?id=UAjYCwAAQBAJ*

Benton, E. V., Henke, R. P. & Tobias, C. A. (1973). Heavy-particle radiography, *Science* **182**(4111): 474–476.
DOI: *10.1126/science.182.4111.474*

Berger, M. J., Coursey, J. S., Zucker, M. A. & Chang, J. (2005). *ESTAR, PSTAR and ASTAR: Computer Programs for Calculating Stopping–Power and Range Tables for Electrons, Protons and Helium Ions*, National Institue of Standards and Technology.
URL: *http://physics.nist.gov/Star*

Bert, C., Grözinger, S. O. & Rietzel, E. (2008). Quantification of interplay effects of scanned particle beams and moving targets, *Physics in Medicine and Biology* **53**(9): 2253–2265.
DOI: *10.1088/0031-9155/53/9/003*

Bethe, H. (1930). Zur theorie des durchgangs schneller korpuskularstrahlen durch materie, *Annalen der Physik* **397**(3): 325–400.
DOI: *10.1002/andp.19303970303*

Bethe, H. A. & Ashkin, J. (1953). *Passage of radiation through matter*, John Wiley & Sons ; Chapman & Hall, New York; London, chapter 2, pp. 104–357.

Biegun, A., Takatsu, J., van Goethem, M.-J., van der Graaf, E., van Beuzekom, M., Visser, J. & Brandenburg, S. (2016). Proton radiography to improve proton radiotherapy: Simulation study at different proton beam energies, *Acta Physica Polonica B* **47**(2): 329.
DOI: *10.5506/aphyspolb.47.329*

Birks, J. B. (1951). Scintillations from organic crystals: Specific fluorescence and relative response to different radiations, *Proc. Phys. Soc.* **A64**: 874–877.
DOI: *10.1088/0370-1298/64/10/303*

Birks, J. B. (1952). Theory of the response of organic scintillation crystals to short-range particles, *Phys. Rev.* **86**: 569–569.
DOI: *10.1103/PhysRev.86.569*

Bisogni, M. G., Attili, A., Battistoni, G., Belcari, N., Camarlinghi, N. et al. (2017). Inside in-beam positron emission tomography system for particle range monitoring in hadrontherapy, *Journal of medical imaging (Bellingham, Wash.)* **4**(1): 011005–011005.
DOI: *10.1117/1.JMI.4.1.011005*

Bolst, D., Cirrone, G., Cuttone, G., Folger, G., Incerti, S. et al. (2017). Abstract id: 22 validation of geant4 fragmentation for heavy ion therapy, *Physics Medica* **Volume 42**(1): 4.
DOI: *10.1016/j.ejmp.2017.09.010*

Bopp, C., Colin, J., Cussol, D., Finck, C., Labalme, M., Rousseau, M. & Brasse, D. (2013). Proton computed tomography from multiple physics processes, *Physics in Medicine and Biology* **58**(20): 7261.
DOI: *10.1088/0031-9155/58/20/7261*

Bopp, C., Rescigno, R., Rousseau, M. & Brasse, D. (2014). The impact of tracking system properties on the most likely path estimation in proton CT, *Physics in Medicine and Biology* **59**(23): N197–N210.
DOI: *10.1088/0031-9155/59/23/N197*

Bortfeld, T. (1997). An analytical approximation of the Bragg curve for therapeutic proton beams, *Medical Physics* **24**(12): 2024–2033.
DOI: *10.1118/1.598116*

Bortfeld, T. R., Viana, M. F. d. & Yan, S. (2020). The societal impact of ion beam therapy, *Zeitschrift fur medizinische Physik* pp. S0939–3889(20)30066–0.
DOI: *10.1016/j.zemedi.2020.06.007*

Bourque, A. E., Carrier, J.-F. & Bouchard, H. (2014). A stoichiometric calibration method for dual energy computed tomography, *Physics in Medicine and Biology* **59**(8): 2059.
DOI: *10.1088/0031-9155/59/8/2059*

Bradt, H. L. & Peters, B. (1950). The heavy nuclei of the primary cosmic radiation, *Phys. Rev.* **77**: 54–70.
DOI: *10.1103/PhysRev.77.54*

Bromiley, P. A. (2003). Products and convolutions of gaussian distributions, *TINA report* **2003-003**. Internal report.
URL: *www.tina-vision.org*

Bryant, P. J., Badano, L., Benedikt, M., Crescenti, M., Holy, P. et al. (2000). Proton-Ion Medical Machine Study (PIMMS), 2, *Technical Report CERN-PS-2000-007-DR*, CERN.
URL: *https://cds.cern.ch/record/449577*

Böhlen, T. T., Cerutti, F., Dosanjh, M., Ferrari, A., Gudowska, I., Mairani, A. & Quesada, J. M. (2010). Benchmarking nuclear models of FLUKA and GEANT4 for carbon ion therapy, *Physics in Medicine and Biology* **55**(19): 5833–5847.
DOI: *10.1088/0031-9155/55/19/014*

Carboni, S., Barlini, S., Bardelli, L., Le Neindre, N., Bini, M. et al. (2012). Particle identification using the (DELTA)E-E technique and pulse shape discrimination with the silicon detectors of the FAZIA project, *Nuclear Instruments and Methods in Physics Research Section A: Accelerators, Spectrometers, Detectors and Associated Equipment* **664**: 251–263.
DOI: *10.1016/j.nima.2011.10.061*

Chou, C. N. (1952). The nature of the saturation effect of fluorescent scintillators, *Phys. Rev.* **87**: 904–905.
DOI: *10.1103/PhysRev.87.904*

Christodouleas, J. P., Tang, S., Susil, R. C., McNutt, T. R., Song, D. Y., Bekelman, J., Deville, C., Vapiwala, N., Deweese, T. L., Lu, H.-M. & Both, S. (2013). The effect of anterior proton beams in the setting of a prostate-rectum spacer, *Medical dosimetry : official journal of the American Association of Medical Dosimetrists* **38**(3): 315–319.
DOI: *10.1016/j.meddos.2013.03.002*

Cirrone, G., Bucciolini, M., Bruzzi, M., Candiano, G., Civinini, C. et al. (2011). Monte carlo evaluation of the filtered back projection method for image reconstruction in proton computed tomography, *Nuclear Instruments and Methods in Physics Research Section A: Accelerators, Spectrometers, Detectors and Associated Equipment* **658**(1): 78 – 83. RESMDD 2010.
DOI: *10.1016/j.nima.2011.05.061*

Collins-Fekete, C.-A., Brousmiche, S., Hansen, D. C., Beaulieu, L. & Seco, J. (2017a). Pre-treatment patient-specific stopping power by combining list-mode proton radiography and x-ray ct, *Physics in Medicine and Biology* **62**(17): 6836.
DOI: *10.1088/1361-6560/aa7c42*

Collins-Fekete, C.-A., Brousmiche, S., Portillo, S. K. N., Beaulieu, L. & Seco, J. (2016). A maximum likelihood method for high resolution proton radiography/proton CT, *Physics in Medicine and Biology* **61**(23): 8232.
DOI: *10.1088/0031-9155/61/23/8232*

Collins-Fekete, C.-A., Bär, E., Volz, L., Bouchard, H., Beaulieu, L. & Seco, J. (2017b). Extension of the fermi–eyges most-likely path in heterogeneous medium with prior knowledge information, *Physics in Medicine & Biology* **62**(24): 9207–9219.
DOI: *10.1088/1361-6560/aa955d*

Collins-Fekete, C.-A., Dikaios, N., Royle, G. J. & Evans, P. M. (2020). Statistical limitations in proton imaging, *Physics in Medicine & Biology* .
DOI: *10.1088/1361-6560/ab7972*

Collins-Fekete, C.-A., Doolan, P., Dias, M. F., Beaulieu, L. & Seco, J. (2015). Developing a phenomenological model of the proton trajectory within a heterogeneous medium required for proton imaging, *Physics in Medicine and Biology* **60**(13): 5071–5082.
DOI: *10.1088/0031-9155/60/13/5071*

Collins-Fekete, C.-A. & Romano, F. (2018). A most likely generating process filter in particle imaging.
URL: *https://protonimaging.sciencesconf.org/213983*

Collins-Fekete, C.-A., Volz, L., Piersimoni, P., Ordonez, C., Bashkirov, V., Coutrakon, G., Johnson, R., Beaulieu, L., Schulte, R. & Seco, J. (2017c). We-g-605-5: Theoretical prediction and experimental verification of the spatial resolution and stopping power accuracy of ion radiography/tomography, *American Association of Physics in Medicine* .
URL: *https://www.aapm.org/meetings/2017AM/PRAbs.asp?mid=127&aid=37717*

Collins-Fekete, C.-A., Volz, L., Portillo, S. K. N., Beaulieu, L. & Seco, J. (2017d). A theoretical framework to predict the most likely ion path in particle imaging, *Physics in Medicine and Biology* **62**(5): 1777.
DOI: *10.1088/1361-6560/aa58ce*

Cormack, A. M. (1963). Representation of a Function by Its Line Integrals, with Some Radiological Applications, *Journal of Applied Physics* **34**(9): 2722–2727.
DOI: *10.1063/1.1729798*

Cucinotta, F. A., Townsend, L. W. & Wilson, J. W. (1993). Description of alpha-nucleus interaction cross sections for cosmic ray shielding studies, *NASA technical paper* **3285**.

Dal Bello, R. (2020). Nuclear prompt gamma spectroscopy for range verification in ion-beam therapy. Dissertation at the combined faculty of Natural Sciences and Mathematics, Heidelberg University.
DOI: *10.11588/heidok.00027869*

Dal Bello, R., Magalhaes Martins, P., Brons, S., Hermann, G., Kihm, T., Seimetz, M. & Seco, J. (2020). Prompt gamma spectroscopy for absolute range verification of 12c ions at synchrotron-based facilities, *Physics in Medicine & Biology* **65**(9): 095010.
DOI: *10.1088/1361-6560/ab7973*

Darne, C. D., Alsanea, F., Robertson, D. G., Guan, F., Pan, T., Grosshans, D. & Beddar, S. (2019). A proton imaging system using a volumetric liquid scintillator: a preliminary study, *Biomedical Physics & Engineering Express* **5**(4): 045032.
DOI: *10.1088/2057-1976/ab2e4a*

Dedes, G., Dickmann, J., Niepel, K., Wesp, P., Johnson, R. P. et al. (2019). Experimental comparison of proton CT and dual energy x-ray CT for relative stopping power estimation in proton therapy, *Physics in Medicine & Biology* **64**(16): 165002.
DOI: *10.1088/1361-6560/ab2b72*

Deffet, S., Farace, P. & Macq, B. (2020). Sparse deconvolution of proton radiography data to estimate water equivalent thickness maps, *Medical Physics* **47**(2): 509–517.
DOI: *10.1002/mp.13917*

Depauw, N. & Seco, J. (2011). Sensitivity study of proton radiography and comparison with kV and MV x-ray imaging using GEANT4 Monte Carlo simulations, *Physics in Medicine and Biology* **56**(8): 2407–2421.
DOI: *10.1088/0031-9155/56/8/006*

Dias, M. F., Collins-Fekete, C.-A., Volz, L., Riboldi, M. & Seco, J. (2019). Optimal particle type and projection number in multi-modality relative stopping power acquisition. arXiv preprint: 1910.02242.

Dickmann, J., Wesp, P., Rädler, M., Rit, S., Pankuch, M., Johnson, R. P., Bashkirov, V., Schulte, R. W., Parodi, K., Landry, G. & Dedes, G. (2019). Prediction of image noise contributions in proton computed tomography and comparison to measurements, *Physics in Medicine & Biology* **64**(14): 145016.
DOI: *10.1088/1361-6560/ab2474*

Dolde, K., Naumann, P., Dávid, C., Gnirs, R., Kachelrieß, M., Lomax, A. J., Saito, N., Weber, D. C., Pfaffenberger, A. & Zhang, Y. (2018). 4d dose calculation for pencil beam scanning proton therapy of pancreatic cancer using repeated 4dmri datasets, *Physics in Medicine & Biology* **63**(16): 165005.
DOI: *10.1088/1361-6560/aad43f*

Doolan, P. J., Bentefour, E. H., Testa, M., Cascio, E., Sharp, G., Royle, G. & Lu, H.-M. (2019). Higher order analysis of time-resolved proton radiographs, *Biomedical Physics & Engineering Express* **5**(5): 057002.
DOI: *10.1088/2057-1976/ab36ea*

Doolan, P. J., Collins-Fekete, C.-A., Dias, M. F., Ruggieri, T. A., D'Souza, D. & Seco, J. (2016). Inter-comparison of relative stopping power estimation models for proton therapy, *Physics in Medicine & Biology* **61**(22): 8085.
URL: *http://stacks.iop.org/0031-9155/61/i=22/a=8085*

Doolan, P. J., Royle, G., Gibson, A., Lu, H.-M., Prieels, D. & Bentefour, E. H. (2015a). Dose ratio proton radiography using the proximal side of the Bragg peak, *Medical Physics* **42**(4): 1871–1883.
DOI: *10.1118/1.4915492*

Doolan, P. J., Testa, M., Sharp, G., Bentefour, E. H., Royle, G. & Lu, H.-M. (2015b). Patient-specific stopping power calibration for proton therapy planning based on single-detector proton radiography, *Physics in Medicine and Biology* **60**(5): 1901.
DOI: *10.1088/0031-9155/60/5/1901*

Drentje, A. G., Kitagawa, A. & Muramatsu, M. (2008). Experiments with fundamental aspects performed in a small ecr ion source for a new carbon therapy facility, *IEEE Transactions on Plasma Science* **36**(4): 1502–1511.

Dudouet, J., Cussol, D., Durand, D. & Labalme, M. (2014). Benchmarking geant4 nuclear models for hadron therapy with 95 mev/nucleon carbon ions, *Phys. Rev. C* **89**: 054616.
DOI: *10.1103/PhysRevC.89.054616*

Durante, M. & Paganetti, H. (2016). Nuclear physics in particle therapy: a review, *Reports on Progress in Physics* **79**(9): 096702.
DOI: *10.1088/0034-4885/79/9/096702*

Eickhoff, H., Bar, R., Dolinskii, A., Haberer, T., Schlitt, B., Spiller, P. & Weinrich, U. (2003). Hicat - the german hospital-based light ion cancer therapy project, *Proceedings of the 2003 Particle Accelerator Conference*, Vol. 1, pp. 694–698 Vol.1.

Erdelyi, B. (2009). A comprehensive study of the most likely path formalism for proton-computed tomography, *Physics in Medicine and Biology* **54**(20): 6095–6122.
DOI: *10.1088/0031-9155/54/20/005*

Esposito, M., Waltham, C., Taylor, J. T., Manger, S., Phoenix, B. et al. (2018). Pravda: The first solid-state system for proton computed tomography, *Physica Medica* **55**: 149 – 154.
DOI: *https://doi.org/10.1016/j.ejmp.2018.10.020*

Eyges, L. (1948). Multiple Scattering with Energy Loss, *Physical Review* **74**(10): 1534–1535.
DOI: *10.1103/PhysRev.74.1534*

Farr, J. B., Flanz, J. B., Gerbershagen, A. & Moyers, M. F. (2018). New horizons in particle therapy systems, *Medical Physics* **45**(11): e953–e983.
DOI: *10.1002/mp.13193*

Farrell, S., Calafiura, P., Mudigonda, M., Prabhat, Anderson, D. et al. (2018). Novel deep learning methods for track reconstruction.
URL: *https://arxiv.org/abs/1810.06111*

Félix-Bautista, R., Gehrke, T., Ghesquière-Diérickx, L., Reimold, M., Amato, C., Turecek, D., Jakubek, J., Ellerbrock, M. & Martišíková, M. (2019). Experimental verification of a non-invasive method to monitor the lateral pencil beam position in an anthropomorphic phantom for carbon-ion radiotherapy, *Physics in Medicine & Biology* **64**(17): 175019.
DOI: *10.1088/1361-6560/ab2ca3*

Ferrero, V., Fiorina, E., Morrocchi, M., Pennazio, F., Baroni, G. et al. (2018). Online proton therapy monitoring: clinical test of a silicon-photodetector-based in-beam pet, *Scientific Reports* **8**(1): 4100.
DOI: *10.1038/s41598-018-22325-6*

Gehrke, T., Amato, C., Berke, S. & Martišíková, M. (2018). Theoretical and experimental comparison of proton and helium-beam radiography using silicon pixel detectors, *Physics in Medicine & Biology* **63**(3): 035037.
URL: *http://stacks.iop.org/0031-9155/63/i=3/a=035037*

Gehrke, T., Gallas, R., Jäkel, O. & Martišíková, M. (2017). Proof of principle of helium-beam radiography using silicon pixel detectors for energy deposition measurement, identification, and tracking of single ions, *Medical Physics* pp. n/a–n/a.
DOI: *10.1002/mp.12723*

Giacometti, V., Bashkirov, V. A., Piersimoni, P., Guatelli, S., Plautz, T. E. et al. (2017a). Software platform for simulation of a prototype proton ct scanner, *Medical Physics* **44**(3): 1002–1016.
DOI: *10.1002/mp.12107*

Giacometti, V., Guatelli, S., Bazalova-Carter, M., Rosenfeld, A. B. & Schulte, R. W. (2017b). Development of a high resolution voxelised head phantom for medical physics applications, *Phys Med* **33**: 182–188.
DOI: *10.1016/j.ejmp.2017.01.007*

Gianoli, C., Göppel, M., Meyer, S., Palaniappan, P., Rädler, M., Kamp, F., Belka, C., Riboldi, M. & Parodi, K. (2020). Patient-specific ct calibration based on ion radiography for different detector configurations in 1h, 4he and 12c ion pencil beam scanning, *Physics in Medicine & Biology* .
URL: *http://iopscience.iop.org/10.1088/1361-6560/aba319*

Goldhaber, A. (1974). Statistical models of fragmentation processes, *Physics Letters B* **53**(4): 306 – 308.
DOI: *https://doi.org/10.1016/0370-2693(74)90388-8*

Gottschalk, B. (2010). On the scattering power of radiotherapy protons, *Medical Physics* **37**(1): 352. arXiv: 0908.1413.
DOI: *10.1118/1.3264177*

Gottschalk, B. (2012). Techniques of Proton Radiotherapy: Transport Theory, *arXiv:1204.4470 [physics]* . arXiv: 1204.4470.

Gottschalk, B., Cascio, E. W., Daartz, J. & Wagner, M. S. (2014). On the nuclear halo of a proton pencil beam stopping in water, *arXiv:1412.0045 [physics]* . arXiv: 1412.0045.

Gottschalk, B., Koehler, A. M., Schneider, R. J., Sisterson, J. M. & Wagner, M. S. (1993). Multiple Coulomb scattering of 160 MeV protons, *Nuclear Instruments and Methods in Physics Research Section B: Beam Interactions with Materials and Atoms* **74**(4): 467–490.
DOI: *10.1016/0168-583X(93)95944-Z*

Graeff, C., Weber, U., Schuy, C., Saito, N., Volz, L., Piersimoni, P., Seco, J. & Kraemer, M. (2018). [oa027] helium as a range probe in carbon ion therapy, *Physica Medica: European Journal of Medical Physics* **52**: 11.
DOI: *10.1016/j.ejmp.2018.06.099*

Grevillot, L., Frisson, T., Zahra, N., Bertrand, D., Stichelbaut, F., Freud, N. & Sarrut, D. (2010). Optimization of GEANT4 settings for Proton Pencil Beam Scanning simulations using GATE, *Nuclear Instruments and Methods in Physics Research Section B: Beam Interactions with Materials and Atoms* **268**(20): 3295–3305.
DOI: *10.1016/j.nimb.2010.07.011*

Haberer, T., Debus, J., Eickhoff, H., Jäkel, O., Schulz-Ertner, D. & Weber, U. (2004). The heidelberg ion therapy center, *Radiotherapy and Oncology* **73**: S186–S190.
DOI: *10.1016/S0167-8140(04)80046-X*

Hammi, A., Koenig, S., Weber, D. C., Poppe, B. & Lomax, A. J. (2018). Patient positioning verification for proton therapy using proton radiography, *Physics in Medicine & Biology* **63**(24): 245009.
DOI: *10.1088/1361-6560/aadf79*

Hammi, A., Lomax, T. & Weber, D. (2017). Su-f-601-1: A new technique for increasing spatial resolution of proton radiography, Presented at the American Association of Physics in Medicine annual meeting, Denver, USA.
URL: *https://www.aapm.org/meetings/2017AM/PRAbs.asp?mid=127&aid=37891*

Han, B., Xu, X. G. & Chen, G. T. Y. (2011). Proton radiography and fluoroscopy of lung tumors: A Monte Carlo study using patient-specific 4dct phantoms, *Medical Physics* **38**(4): 1903–1911.
DOI: *10.1118/1.3555039*

Handrack, J., Parodi, K., Bauer, J., Chen, W., Liebl, J., Tessonnier, T. & Debus, J. (2017). Sensitivity of post treatment positron emission tomography/computed tomography to detect inter-fractional range variations in scanned ion beam therapy, *Acta Oncologica* **56**(11): 1451–1458.
DOI: *10.1080/0284186x.2017.1348628*

Hansen, D. C., Bassler, N., Sørensen, T. S. & Seco, J. (2014a). The image quality of ion computed tomography at clinical imaging dose levels, *Medical Physics* **41**(11): 111908.
DOI: *10.1118/1.4897614*

Hansen, D. C., Petersen, J. B. B., Bassler, N. & Sørensen, T. S. (2014b). Improved proton computed tomography by dual modality image reconstruction, *Medical Physics* **41**(3): 031904.
DOI: *10.1118/1.4864239*

Hansen, D. C., Seco, J., Sørensen, T. S., Petersen, J. B. B., Wildberger, J. E., Verhaegen, F. & Landry, G. (2015). A simulation study on proton computed tomography (CT) stopping power accuracy using dual energy CT scans as benchmark, *Acta Oncologica* **54**(9): 1638–1642.
DOI: *10.3109/0284186X.2015.1061212*

Hansen, D. C., Sørensen, T. S. & Rit, S. (2016). Fast reconstruction of low dose proton CT by sinogram interpolation, *Physics in Medicine and Biology* **61**(15): 5868–5882.
DOI: *10.1088/0031-9155/61/15/5868*

Highland, V. L. (1975). Some practical remarks on multiple scattering, *Nuclear Instruments and Methods* **129**(2): 497–499.
DOI: *10.1016/0029-554X(75)90743-0*

Hoffmann, A., Oborn, B., Moteabbed, M., Yan, S., Bortfeld, T. et al. (2020). Mr-guided proton therapy: a review and a preview, *Radiation Oncology* **15**(1): 129.
DOI: *10.1186/s13014-020-01571-x*

Homolka, N., Pfaffenberger, A., Beuthien-Baumann, B., Mann, P., Schneider, V. et al. (2019). Pv-0479: Development of an anthropomorphic multimodality pelvis phantom for pet/mri-and ct-based radiation treatment planning of prostate cancer, *Radiotherapy & Oncology* **133**(1).
DOI: *10.3252/pso.eu.ESTRO38.2019*

Horst, F., Aricò, G., Brinkmann, K.-T., Brons, S., Ferrari, A. et al. (2019). Measurement of ^{4}He charge- and mass-changing cross sections on h, c, o, and si targets in the energy range 70–220 mev/u for radiation transport calculations in ion-beam therapy, *Phys. Rev. C* **99**: 014603.
DOI: *10.1103/PhysRevC.99.014603*

Horst, F., Schuy, C., Weber, U., Brinkmann, K.-T. & Zink, K. (2017). Measurement of charge- and mass-changing cross sections for ^{4}He $+^{12}$C collisions in the energy range 80–220 mev/u for applications in ion beam therapy, *Phys. Rev. C* **96**: 024624.
DOI: *10.1103/PhysRevC.96.024624*

Hueso-González, F., Rabe, M., Ruggieri, T. A., Bortfeld, T. & Verburg, J. M. (2018). A full-scale clinical prototype for proton range verification

using prompt gamma-ray spectroscopy, *Physics in Medicine & Biology* **63**(18): 185019.
DOI: *10.1088/1361-6560/aad513*

Hünemohr, N., Krauss, B., Dinkel, J., Gillmann, C., Ackermann, B., Jäkel, O. & Greilich, S. (2013). Ion range estimation by using dual energy computed tomography, *Zeitschrift für Medizinische Physik* **23**(4): 300–313.
DOI: *10.1016/j.zemedi.2013.03.001*

Hünemohr, N., Krauss, B., Tremmel, C., Ackermann, B., Jäkel, O. & Greilich, S. (2014a). Experimental verification of ion stopping power prediction from dual energy CT data in tissue surrogates, *Physics in Medicine and Biology* **59**(1): 83.
DOI: *10.1088/0031-9155/59/1/83*

Hünemohr, N., Paganetti, H., Greilich, S., Jäkel, O. & Seco, J. (2014b). Tissue decomposition from dual energy CT data for MC based dose calculation in particle therapy, *Medical Physics* **41**(6): 061714.
DOI: *10.1118/1.4875976*

ICRP (2002). Basic anatomical and physiological data for use in radiological protection reference values, *Ann. ICRP* **32**. ICRP Publication 89.

ICRP (2007). Managing Patient Dose in Multi-Detector Computed Tomography (MDCT). ICRP Publication 102, *Annals of ICRP* **37**(1).

ICRU (2009). Errata and Addenda for ICRU Report 73, Stopping of ions heavier than helium, *Journal of the ICRU* **5**(1).

Jan, S., Benoit, D., Becheva, E., Carlier, T., Cassol, F., Descourt, P., Frisson, T., Grevillot, L., Guigues, L., Maigne, L. et al. (2011). GATE V6: a major enhancement of the GATE simulation platform enabling modelling of CT and radiotherapy, *Physics in Medicine & Biology* **56**(4): 881–901.
DOI: *10.1088/0031-9155/56/4/001*

Jan, S., Santin, G., Strul, D., Staelens, S., Assie, K., Autret, D., Avner, S., Barbier, R., Bardies, M., Bloomfield, P. M. et al. (2004). GATE: a simulation toolkit for PET and SPECT, *Physics in medicine & biology* **49**(19): 4543.
DOI: *10.1088/0031-9155/49/19/007*

Janni, J. F. (1982). Energy loss, range, path length, time-of-flight, straggling, multiple scattering, and nuclear interaction probability: In two parts. Part 1. For 63 compounds Part 2. For elements $1 < Z < 92$, *Atomic Data and Nuclear Data Tables* **27**(2–3): 147–339.
DOI: *10.1016/0092-640X(82)90004-3*

Jermann, M. (2019). Particle therapy statistics in 2018. Data Collected by the Particle Therapy Co-Operative Group.
URL: *https://www.ptcog.ch/index.php/patient-statistics*

Johnson, R. P. (2017). Review of medical radiography and tomography with proton beams, *Reports on Progress in Physics* **81**(1): 016701.
DOI: *10.1088/1361-6633/aa8b1d*

Johnson, R. P., Bashkirov, V., Coutrakon, G., Giacometti, V., Karbasi, P., Karonis, N., Ordoñez, C., Pankuch, M., Sadrozinski, H.-W., Schubert, K. & Schulte, R. (2017). Results from a prototype proton-ct head scanner, *Physics Procedia* **90**: 209 – 214. Conference on the Application of Accelerators in Research and Industry, CAARI 2016, 30 October – 4 November 2016, Ft. Worth, TX, USA.
DOI: *https://doi.org/10.1016/j.phpro.2017.09.060*

Johnson, R. P., Bashkirov, V., DeWitt, L., Giacometti, V., Hurley, R. F. et al. (2016). A fast experimental scanner for proton ct: Technical performance and first experience with phantom scans, *IEEE transactions on nuclear science* **63**: 52–60.
DOI: *10.1109/TNS.2015.2491918*

Kanai, T., Furusawa, Y., Fukutsu, K., Itsukaichi, H., Eguchi-Kasai, K. & Ohara, H. (1997). Irradiation of mixed beam and design of spread-out bragg peak for heavy-ion radiotherapy, *Radiation Research* **147**(1): 78–85.
DOI: *10.2307/3579446*

Kelleter, L. (2020). *A Scintillator-Based Range Telescope for Particle Beam Radiotherapy*, PhD thesis, University College London, Department of Physics and Astronomy.

Kelleter, L. & Jolly, S. (2020). A mathematical expression for depth-light curves of therapeutic proton beams in a quenching scintillator, *Medical Physics* **47**(5): 2300–2308.
DOI: *10.1002/mp.14099*

Kelleter, L., Radogna, R., Volz, L., Attree, D., Basharina-Freshville, A., Seco, J., Saakyan, R. & Jolly, S. (2020). A scintillator-based range telescope for particle therapy, *Physics in Medicine & Biology* .
URL: *http://iopscience.iop.org/10.1088/1361-6560/ab9415*

Khellaf, F., Krah, N., Létang, J. M., Collins-Fekete, C.-A. & Rit, S. (2020a). A comparison of direct reconstruction algorithms in proton computed tomography, *Physics in Medicine & Biology* **65**(10): 105010.
DOI: *10.1088/1361-6560/ab7d53*

Khellaf, F., Krah, N., Letang, J.-M. & Rit, S. (2020b). A deconvolution method to improve spatial resolution inproton ct. Presented at the 6th Loma Linda Workshop on particle imaging and treatment planning.
URL: *http://ionimaging.org/assets/talks/ws2020llu-ferielkhellaf.pdf*

Kleffner, C., Ondreka, D. & Weinrich, U. (2009). The heidelberg ion therapy (hit) accelerator coming into operation, *AIP Conference Proceedings* **1099**(1): 426–428.
DOI: *10.1063/1.3120065*

Knoll, G. (2010). *Radiation Detection and Measurement*, Wiley.
URL: *https://books.google.de/books?id=4vTJ7UDel5IC*

Knopf, A.-C. & Lomax, A. (2013). In vivo proton range verification: a review, *Physics in Medicine and Biology* **58**(15): R131.
DOI: *10.1088/0031-9155/58/15/R131*

Koehler, A. M. (1968). Proton radiography, *Science* **160**(3825): 303–304.
DOI: *10.1126/science.160.3825.303*

Kopp, B., Meyer, S., Gianoli, C., Magallanes, L., Voss, B., Brons, S. & Parodi, K. (2020). Experimental comparison of clinically used ion beams for imaging applications using a range telescope, *Physics in Medicine & Biology* **65**(15): 155004.
DOI: *10.1088/1361-6560/ab87f6*

Krah, N., Khellaf, F., Létang, J. M., Rit, S. & Rinaldi, I. (2018). A comprehensive theoretical comparison of proton imaging set-ups in terms of spatial resolution, *Physics in Medicine & Biology* **63**(13): 135013.
DOI: *10.1088/1361-6560/aaca1f*

Krah, N., Patera, V., Rit, S., Schiavi, A. & Rinaldi, I. (2019). Regularised patient-specific stopping power calibration for proton therapy planning based on proton radiographic images, *Physics in Medicine & Biology* **64**(6): 065008.
DOI: *10.1088/1361-6560/ab03db*

Krah, N., Testa, M., Brons, S., Jäkel, O., Parodi, K., Voss, B. & Rinaldi, I. (2015). An advanced image processing method to improve the spatial resolution of ion radiographies, *Physics in Medicine and Biology* **60**(21): 8525.
DOI: *10.1088/0031-9155/60/21/8525*

Krämer, M., Scifoni, E., Schuy, C., Rovituso, M., Tinganelli, W. et al. (2016). Helium ions for radiotherapy? physical and biological verifications of a novel treatment modality, *Medical Physics* **43**(4): 1995–2004.
DOI: *10.1118/1.4944593*

Krimmer, J., Dauvergne, D., Létang, J. & Testa, E. (2018). Prompt-gamma monitoring in hadrontherapy: A review, *Nuclear Instruments and Methods in Physics Research Section A: Accelerators, Spectrometers, Detectors and Associated Equipment* **878**: 58 – 73. Radiation Imaging Techniques and Applications.
DOI: *10.1016/j.nima.2017.07.063*

Lalonde, A. & Bouchard, H. (2016). A general method to derive tissue parameters for Monte Carlo dose calculation with multi-energy CT, *Physics in Medicine and Biology* **61**(22): 8044.
DOI: *10.1088/0031-9155/61/22/8044*

Lalonde, A., Simard, M., Remy, C., Bär, E. & Bouchard, H. (2018). The impact of dual- and multi-energy CT on proton pencil beam range uncertainties:

a monte carlo study, *Physics in Medicine & Biology* **63**(19): 195012.
DOI: *10.1088/1361-6560/aadf2a*

Landau, L. (1965). 56 - on the energy loss of particles by ionization, *in* D. T. HAAR] (ed.), *Collected Papers of L.D. Landau*, Pergamon, pp. 417 – 424.
DOI: *10.1016/B978-0-08-010586-4.50061-4*

Landry, G., Parodi, K., Wildberger, J. E. & Verhaegen, F. (2013). Deriving concentrations of oxygen and carbon in human tissues using single- and dual-energy CT for ion therapy applications, *Physics in Medicine and Biology* **58**(15): 5029.
DOI: *10.1088/0031-9155/58/15/5029*

Langen, K. M., Willoughby, T. R., Meeks, S. L., Santhanam, A., Cunningham, A., Levine, L. & Kupelian, P. A. (2008). Observations on real-time prostate gland motion using electromagnetic tracking, *International Journal of Radiation Oncology*Biology*Physics* **71**(4): 1084 – 1090.
DOI: *10.1016/j.ijrobp.2007.11.054*

Leverington, B., Dziewiecki, M., Renner, L. & Runze, R. (2018). A prototype scintillating fibre beam profile monitor for Ion Therapy beams, *Journal of Instrumentation* **13**(05): P05030–P05030.
DOI: *10.1088/1748-0221/13/05/P05030*

Li, T., Liang, Z., Singanallur, J. V., Satogata, T. J., Williams, D. C. & Schulte, R. W. (2006). Reconstruction for proton computed tomography by tracing proton trajectories: A Monte Carlo study, *Medical Physics* **33**(3): 699.
DOI: *10.1118/1.2171507*

Lomax, A. J. (2020). Myths and realities of range uncertainty, *The British Journal of Radiology* **93**(1107): 20190582. PMID: 31778317.
DOI: *10.1259/bjr.20190582*

Loveland, W., Aleklett, K. & Seaborg, G. (1986). Target fragmentation in intermediate energy heavy ion collisions, *Nuclear Physics A* **447**: 101–114.
DOI: *10.1016/0375-9474(86)90600-7*

Lynch, G. R. & Dahl, O. I. (1991). Approximations to multiple coulomb scattering, *Nuclear Instruments and Methods in Physics Research Section B: Beam Interactions with Materials and Atoms* **58**(1): 6–10.
DOI: *10.1016/0168-583X(91)95671-Y*

Magalhaes Martins, P., Dal Bello, R., Hermann, G., Kihm, T., Seimetz, M. & Seco, J. (2019). Hadron beam time tracker for time-of-flight measurements of prompt-gamma, *Technical report*, GSI-2019-00596.
DOI: *10.15120/GSI-2019-00596*

Mager, M. (2016). Alpide, the monolithic active pixel sensor for the alice its upgrade, *Nuclear Instruments and Methods in Physics Research Section A: Accelerators, Spectrometers, Detectors and Associated Equipment* **824**: 434 – 438. Frontier Detectors for Frontier Physics: Proceedings of the 13th Pisa

Meeting on Advanced Detectors.
DOI: *https://doi.org/10.1016/j.nima.2015.09.057*

Mairani, A., Dokic, I., Magro, G., Tessonnier, T., Kamp, F. et al. (2016). Biologically optimized helium ion plans: calculation approach and its in vitro validation, *Physics in Medicine & Biology* **61**(11): 4283.
URL: *http://stacks.iop.org/0031-9155/61/i=11/a=4283*

Mazzucconi, D., Agosteo, S., Ferrarini, M., Fontana, L., Lante, V., Pullia, M. & Savazzi, S. (2018). Mixed particle beam for simultaneous treatment and online range verification in carbon ion therapy: Proof-of-concept study, *Medical Physics* **45**(11): 5234–5243.
DOI: *10.1002/mp.13219*

Meyer, S., Gianoli, C., Magallanes, L., Kopp, B., Tessonnier, T., Landry, G., Dedes, G., Voss, B. & Parodi, K. (2017). Comparative monte carlo study on the performance of integration- and list-mode detector configurations for carbon ion computed tomography, *Physics in Medicine & Biology* **62**(3): 1096–1112.
DOI: *10.1088/1361-6560/aa5602*

Meyer, S., Kamp, F., Tessonnier, T., Mairani, A., Belka, C., Carlson, D. J., Gianoli, C. & Parodi, K. (2019). Dosimetric accuracy and radiobiological implications of ion computed tomography for proton therapy treatment planning, *Physics in Medicine & Biology* **64**(12): 125008.
DOI: *10.1088/1361-6560/ab0fdf*

Min, C. H., Lee, H. R., Kim, C. H. & Lee, S. B. (2012). Development of array-type prompt gamma measurement system for in vivo range verification in proton therapy, *Medical Physics* **39**: 2100.
URL: *http://link.aip.org/link/?MPHYA6/39/2100/1*

Möhler, C., Russ, T., Wohlfahrt, P., Elter, A., Runz, A., Richter, C. & Greilich, S. (2018). Experimental verification of stopping-power prediction from single- and dual-energy computed tomography in biological tissues, *Physics in Medicine & Biology* **63**(2): 025001.
URL: *http://stacks.iop.org/0031-9155/63/i=2/a=025001*

Möhler, C., Wohlfahrt, P., Richter, C. & Greilich, S. (2016). Range prediction for tissue mixtures based on dual-energy CT, *Physics in medicine and biology* **61**(11): N268–N275.
DOI: *10.1088/0031-9155/61/11/N268*

Molière, G. (1948). Theorie der Streuung schneller geladener Teilchen II. Mehrfach- und Vielfachstreuung, *Zeitschrift Naturforschung Teil A* **3**: 78.
DOI: *10.1515/zna-1948-0203*

Morrissey, D. J. (1989). Systematics of momentum distributions from reactions with relativistic ions, *Phys. Rev. C* **39**: 460–470.
DOI: *10.1103/PhysRevC.39.460*

Morrissey, D. J. (1993). Comment on "fragmentation of gold projectiles with energies of 200-980 mev/nucleon. i. experimental method, charge yields, and transverse momenta", *Phys. Rev. C* **47**: 413–414.
DOI: *10.1103/PhysRevC.47.413*

Muramatsu, M. & Kitagawa, A. (2012). A review of ion sources for medical accelerators (invited), *Review of Scientific Instruments* **83**(2): 02B909.
DOI: *10.1063/1.3671744*

Mustapha, B., Aydogan, B., Nolen, J., Nassiri, A., Noonan, J., Pankuch, M., Welsh, J., Schulte, R. & Robb, J. (2019). Prospects for an advanced heavy ion therapy center in the chicago area, *AIP Conference Proceedings* **2160**(1): 050009.
DOI: *10.1063/1.5127701*

Niebuhr, N. I., Johnen, W., Echner, G., Runz, A., Bach, M., Stoll, M., Giske, K., Greilich, S. & Pfaffenberger, A. (2019). The ADAM-pelvis phantom—an anthropomorphic, deformable and multimodal phantom for MRgRT, *Physics in Medicine & Biology* **64**(4): 04NT05.
DOI: *10.1088/1361-6560/aafd5f*

Niebuhr, N. I., Johnen, W., Güldaglar, T., Runz, A., Echner, G., Mann, P., Möhler, C., Pfaffenberger, A., Jäkel, O. & Greilich, S. (2016). Technical note: Radiological properties of tissue surrogates used in a multimodality deformable pelvic phantom for mr-guided radiotherapy, *Medical Physics* **43**(2): 908–916.
DOI: *10.1118/1.4939874*

Nystrom, H., Jensen, M. F. & Nystrom, P. W. (2020). Treatment planning for proton therapy: what is needed in the next 10 years?, *The British Journal of Radiology* **93**(1107): 20190304. PMID: 31356107.
DOI: *10.1259/bjr.20190304*

Oancea, C., Shipulin, K., Mytsin, G., Gao, M., Pankuch, M., Coutrakon, G., Ordonez, C., Johnson, R., Bashkirov, V. & Schulte, R. (2018). Po-0888: Comparison of x-ray ct and proton based ct planning in the presence of titanium dental implants, *Radiotherapy and Oncology* **127**: S470 – S471. ESTRO 37, April 20-24, 2018, Barcelona, Spain.
DOI: *10.1016/S0167-8140(18)31198-8*

Ordoñez, C. E., Karonis, N. T., Duffin, K. L., Winans, J. R., DeJongh, E. A., DeJongh, D. F., Coutrakon, G., Myers, N. F., Pankuch, M. & Welsh, J. S. (2019). Fast in situ image reconstruction for proton radiography, *Journal of Radiation Oncology* **8**(2): 185–198.
DOI: *10.1007/s13566-019-00387-x*

Ordoñez, C. E., Karonis, N., Duffin, K., Coutrakon, G., Schulte, R., Johnson, R. & Pankuch, M. (2017). A real-time image reconstruction system for particle treatment planning using proton computed tomography (pct), *Physics Procedia* **90**: 193 – 199. Conference on the Application of Accelerators in

Research and Industry, CAARI 2016, 30 October – 4 November 2016, Ft. Worth, TX, USA.
DOI: *10.1016/j.phpro.2017.09.058*

Owen, H., Lomax, A. & Jolly, S. (2016). Current and future accelerator technologies for charged particle therapy, *Nuclear Instruments and Methods in Physics Research Section A: Accelerators, Spectrometers, Detectors and Associated Equipment* **809**: 96 – 104. Advances in detectors and applications for medicine.
DOI: *10.1016/j.nima.2015.08.038*

Paganetti, H. (2012). Range uncertainties in proton therapy and the role of Monte Carlo simulations, *Physics in Medicine and Biology* **57**(11): R99.
DOI: *10.1088/0031-9155/57/11/R99*

Palaniappan, P., Meyer, S., Kamp, F., Belka, C., Riboldi, M., Parodi, K. & Gianoli, C. (2019). A 2d-3d deformable image registration framework for proton radiographies in adaptive radiation therapy, *2019 IEEE Nuclear Science Symposium and Medical Imaging Conference (NSS/MIC)*, pp. 1–3.

Parodi, K. (2014). Heavy ion radiography and tomography, *Physica Medica* **30**(5): 539 – 543. Particle Radiosurgery Conference.
DOI: *10.1016/j.ejmp.2014.02.004*

Parodi, K. & Polf, J. C. (2018a). In vivo range verification in particle therapy, *Medical Physics* **45**(11): e1036–e1050.
DOI: *10.1002/mp.12960*

Parodi, K. & Polf, J. C. (2018b). In vivo range verification in particle therapy, *Medical Physics* **45**(11): e1036–e1050.
DOI: *10.1002/mp.12960*

Payne, M. G. (1969). Energy straggling of heavy charged particles in thick absorbers, *Phys. Rev.* **185**: 611–623.
DOI: *10.1103/PhysRev.185.611*

Penfold, S. & Censor, Y. (2015). Techniques in Iterative Proton CT Image Reconstruction, *Sensing and Imaging* **16**: 21.
DOI: *10.1007/s11220-015-0122-3*

Penfold, S. N. (2010). *Image reconstruction and Monte Carlo simulations in the development of proton computed tomography for applications in proton radiation therapy*, Doctor of philosophy thesis, Centre for Medical Radiation Physics, University of Wollongong.
URL: *https://ro.uow.edu.au/theses/3305*

Penfold, S. N., Schulte, R. W., Censor, Y. & Rosenfeld, A. B. (2010). Total variation superiorization schemes in proton computed tomography image reconstruction, *Medical Physics* **37**(11): 5887–5895.
DOI: *10.1118/1.3504603*

Perl, J., Shin, J., Schumann, J., Faddegon, B. & Paganetti, H. (2012). TOPAS: an innovative proton Monte Carlo platform for research and clinical applications, *Medical Physics* **39**(11): 6818–6837.
DOI: *10.1118/1.4758060*

Pettersen, H., Alme, J., Biegun, A., van den Brink, A., Chaar, M. et al. (2017). Proton tracking in a high-granularity digital tracking calorimeter for proton ct purposes, *Nuclear Instruments and Methods in Physics Research Section A: Accelerators, Spectrometers, Detectors and Associated Equipment* **860**: 51–61.
DOI: *10.1016/j.nima.2017.02.007*

Pettersen, H. E. S., Alme, J., Barnaföldi, G. G., Barthel, R., van den Brink, A., Chaar, M., Eikeland, V., García-Santos, A., Genov, G., Grimstad, S. et al. (2019a). Design optimization of a pixel-based range telescope for proton computed tomography, *Physica Medica* **63**: 87–97.
DOI: *10.1016/j.ejmp.2019.05.026*

Pettersen, H. E. S., Meric, I., Odland, O. H., Shafiee, H., Sølie, J. R. & Röhrich, D. (2019b). Proton tracking algorithm in a pixel-based range telescope for proton computed tomography, *EPJ Web of Conferences* . In press. arXiv preprint: 2006.09751.

Pettersen, H., Volz, L., Sølie, J., Röhrich, D. & Seco, J. (2019c). Estimating a proton's position in a pencil beam for proton imaging. Poster session presented at PTCOG59, the Annual Conference of PTCOG.

Piersimoni, P., Faddegon, B. A., Méndez, J. R., Schulte, R. W., Volz, L. & Seco, J. (2018). Helium ct: Monte carlo simulation results for an ideal source and detector with comparison to proton ct, *Medical Physics* **0**(0).
DOI: *10.1002/mp.12942*

Piersimoni, P., Ramos-Méndez, J., Geoghegan, T., Bashkirov, V. A., Schulte, R. W. & Faddegon, B. A. (2017). The effect of beam purity and scanner complexity on proton ct accuracy, *Medical Physics* **44**(1): 284–298.
DOI: *10.1002/mp.12013*

Plautz, T. E., Bashkirov, V., Giacometti, V., Hurley, R. F., Johnson, R. P., Piersimoni, P., Sadrozinski, H. F.-W., Schulte, R. W. & Zatserklyaniy, A. (2016). An evaluation of spatial resolution of a prototype proton ct scanner, *Medical Physics* **43**(12): 6291–6300.
DOI: *10.1118/1.4966028*

Poludniowski, G., Allinson, N. M. & Evans, P. M. (2014). Proton computed tomography reconstruction using a backprojection-then-filtering approach, *Physics in Medicine and Biology* **59**(24): 7905–7918.
DOI: *10.1088/0031-9155/59/24/7905*

Poludniowski, G., Allinson, N. M. & Evans, P. M. (2015). Proton radiography and tomography with application to proton therapy, *The British Journal of*

Radiology **88**(1053): 20150134.
DOI: *10.1259/bjr.20150134*

Price, T. (2016). Pravda: High energy physics towards proton computed tomography, *Nuclear Instruments and Methods in Physics Research Section A: Accelerators, Spectrometers, Detectors and Associated Equipment* **824**: 226–227.
DOI: *10.1016/j.nima.2015.12.013*

Rädler, M., Landry, G., Rit, S., Schulte, R. W., Parodi, K. & Dedes, G. (2018). Two-dimensional noise reconstruction in proton computed tomography using distance-driven filtered back-projection of simulated projections, *Physics in Medicine & Biology* **63**(21): 215009.
DOI: *10.1088/1361-6560/aae5c9*

Rinella, G. A. (2016). The ALPIDE pixel sensor chip for the upgrade of the ALICE Inner Tracking System, *Nuclear Instruments and Methods in Physics Research Section A: Accelerators, Spectrometers, Detectors and Associated Equipment* **845**: 583–587.
DOI: *10.1016/j.nima.2016.05.016*

Rit, S., Dedes, G., Freud, N., Sarrut, D. & Létang, J. M. (2013). Filtered backprojection proton CT reconstruction along most likely paths, *Medical Physics* **40**(3): 031103.
DOI: *10.1118/1.4789589*

Rossi, B. & Greisen, K. (1941). Cosmic-Ray Theory, *Reviews of Modern Physics* **13**(4): 240–309.
DOI: *10.1103/RevModPhys.13.240*

Rovituso, M., Schuy, C., Weber, U., Brons, S., Cortés-Giraldo, M. A. et al. (2017). Fragmentation of 120 and 200 mev u^{-1} ^{4}he ions in water and pmma targets, *Physics in Medicine & Biology* **62**(4): 1310.
URL: *http://stacks.iop.org/0031-9155/62/i=4/a=1310*

Sadrozinski, H. F.-W., Geoghegan, T., Harvey, E., Johnson, R. P., Plautz, T. E. et al. (2016). Operation of the preclinical head scanner for proton ct, *Nucl Instrum Methods Phys Res A* **831**: 394–399. 27818559[pmid].
DOI: *10.1016/j.nima.2016.02.001*

Sadrozinski, H. F.-W., Johnson, R. P., Macafee, S., Plumb, A., Steinberg, D., Zatserklyaniy, A., Bashkirov, V., Hurley, F. & Schulte, R. (2013). Development of a head scanner for proton ct, *Nuclear Instruments & Methods in Physics Research. Section A, Accelerators, Spectrometers, Detectors and Associated Equipment* **699**: 205–210.
DOI: *10.1016/j.nima.2012.04.029*

Saito, M. & Sagara, S. (2017). A simple formulation for deriving effective atomic numbers via electron density calibration from dual-energy CT data in the human body, *Medical Physics* **44**(6): 2293 –2303.
DOI: *10.1002/mp.12176*

Sarosiek, C., Ricci, J., Coutrakon, G. & Pankuch, M. (2019). Distribution of patients that can be imaged with 235 mev protons for radiography and computed tomography. Presented at the PTCOG 58 annual meeting of the Particle Therapy Cooperative Group.
DOI: *https://doi.org/10.26226/morressier.5cb72192ae0a090015830aac*

Sarrut, D., Bardiès, M., Boussion, N., Freud, N., Jan, S., Létang, J.-M., Loudos, G., Maigne, L., Marcatili, S., Mauxion, T. et al. (2014). A review of the use and potential of the GATE monte carlo simulation code for radiation therapy and dosimetry applications, *Medical Physics* **41**(6): 064301.
DOI: *10.1118/1.4871617*

Schaffner, B. & Pedroni, E. (1998). The precision of proton range calculations in proton radiotherapy treatment planning: experimental verification of the relation between CT-HU and proton stopping power, *Physics in Medicine and Biology* **43**(6): 1579–1592.
DOI: *10.1088/0031-9155/43/6/016*

Schellhammer, S. M., Hoffmann, A. L., Gantz, S., Smeets, J., van der Kraaij, E., Quets, S., Pieck, S., Karsch, L. & Pawelke, J. (2018). Integrating a low-field open MR scanner with a static proton research beam line: proof of concept, *Physics in Medicine & Biology* **63**(23): 23LT01.
DOI: *10.1088/1361-6560/aaece8*

Schneider, U. & Pedroni, E. (1994). Multiple Coulomb scattering and spatial resolution in proton radiography, *Medical Physics* **21**(11): 1657–1663.
DOI: *10.1118/1.597212*

Schneider, U., Pedroni, E., Hartmann, M., Besserer, J. & Lomax, T. (2012). Spatial resolution of proton tomography: Methods, initial phase space and object thickness, *Zeitschrift für Medizinische Physik* **22**(2): 100–108.
DOI: *10.1016/j.zemedi.2011.06.001*

Schneider, U., Pedroni, E. & Lomax, A. (1996). The calibration of CT Hounsfield units for radiotherapy treatment planning, *Physics in medicine and biology* **41**(1): 111.
DOI: *10.1088/0031-9155/41/1/009*

Schneider, U., Pemler, P., Besserer, J., Pedroni, E., Lomax, A. & Kaser-Hotz, B. (2005). Patient specific optimization of the relation between CT-Hounsfield units and proton stopping power with proton radiography, *Medical Physics* **32**(1): 195.
DOI: *10.1118/1.1833041*

Schoemers, C., Feldmeier, E., Naumann, J., Panse, R., Peters, A. & Haberer, T. (Sep 2015). The intensity feedback system at heidelberg ion-beam therapy centre, *Nuclear Instruments and Methods in Physics Research Section A, Accelerators, Spectrometers, Detectors and Associated Equipment* pp. 92–99.

Schömers, C., Feldmeier, E., Galonska, M., Horn, J., Peters, A. & Haberer, T. (2017). Thpva083: First tests of a re-accelerated beam at heidelberg ion-beam therapy center (hit), *in* V. R. W. Schaa, G. Arduini, M. Lindroos & J. Pranke (eds), *Proceedings of IPAC2017*, JACoW.

Schulte, R., Bashkirov, V., Tianfang Li, Zhengrong Liang, Mueller, K. et al. (2004). Conceptual design of a proton computed tomography system for applications in proton radiation therapy, *IEEE Transactions on Nuclear Science* **51**(3): 866–872.
DOI: *10.1109/TNS.2004.829392*

Schulte, R. W., Bashkirov, V., Klock, M. C. L., Li, T., Wroe, A. J., Evseev, I., Williams, D. C. & Satogata, T. (2005). Density resolution of proton computed tomography, *Medical Physics* **32**(4): 1035–1046.
DOI: *10.1118/1.1884906*

Schulte, R. W., Penfold, S. N., Tafas, J. T. & Schubert, K. E. (2008). A maximum likelihood proton path formalism for application in proton computed tomography, *Medical Physics* **35**(11): 4849–4856.
DOI: *10.1118/1.2986139*

Schultze, B., Censor, Y., Karbasi, P., Schubert, K. E. & Schulte, R. W. (2018). An Improved Method of Total Variation Superiorization Applied to Reconstruction in Proton Computed Tomography, *ArXiv e-prints* . arXiv:1803.01112.

Schultze, B., Witt, M., Censor, Y., Schubert, K. & Schulte, R. (2015). Performance of hull-detection algorithms for proton computed tomography reconstruction, *in* S. Reich & A. Zaslavski (eds), *Infinite Products of Operators and Their Applications*, Vol. 636 of *Contemporary Mathematics*, American Mathematical Society.

Schultze, B., Witt, M., Censor, Y., Schulte, R. & Schubert, K. E. (2014). Performance of Hull-Detection Algorithms For Proton Computed Tomography Reconstruction, *arXiv:1402.1720 [physics]* .

Seco, J., Clasie, B. & Partridge, M. (2014). Review on the characteristics of radiation detectors for dosimetry and imaging, *Physics in Medicine and Biology* **59**(20): R303.
DOI: *10.1088/0031-9155/59/20/R303*

Seco, J. & Depauw, N. (2011). Proof of principle study of the use of a CMOS active pixel sensor for proton radiography, *Medical Physics* **38**(2): 622–623.
DOI: *10.1118/1.3496327*

Seco, J., Oumano, M., Depauw, N., Dias, M. F., Teixeira, R. P. & Spadea, M. F. (2013). Characterizing the modulation transfer function (MTF) of proton/carbon radiography using Monte Carlo simulations, *Medical Physics* **40**(9): 091717.
DOI: *10.1118/1.4819816*

Seco, J., Robertson, D., Trofimov, A. & Paganetti, H. (2009). Breathing interplay effects during proton beam scanning: simulation and statistical analysis, *Physics in Medicine and Biology* **54**(14): N283–N294.
DOI: *10.1088/0031-9155/54/14/N01*

Shannon, C. E. (1948). A mathematical theory of communication, *Bell System Technical Journal* **27**(3): 379–423.
DOI: *10.1002/j.1538-7305.1948.tb01338.x*

Shen, W.-q., Wang, B., Feng, J., Zhan, W.-l., Zhu, Y.-t. & Feng, E.-p. (1989). Total reaction cross section for heavy-ion collisions and its relation to the neutron excess degree of freedom, *Nuclear Physics A* **491**(1): 130–146.
DOI: *10.1016/0375-9474(89)90209-1*

Sihver, L., Tsao, C. H., Silberberg, R., Kanai, T. & Barghouty, A. F. (1993). Total reaction and partial cross section calculations in proton-nucleus ($z_t \leq 26$) and nucleus-nucleus reactions (z_p and $z_t \leq 26$), *Phys. Rev. C* **47**: 1225–1236.
DOI: *10.1103/PhysRevC.47.1225*

Sølie, J. R., Volz, L., Pettersen, H. E. S., Piersimoni, P., Odland, O. H. et al. (2020). Image quality of list-mode proton imaging without front trackers, *Physics in Medicine & Biology* **65**(13): 135012.
DOI: *10.1088/1361-6560/ab8ddb*

Strandlie, A. & Frühwirth, R. (2010). Track and vertex reconstruction: From classical to adaptive methods, *Reviews of Modern Physics* **82**(2): 1419–1458.
DOI: *10.1103/RevModPhys.82.1419*

Taasti, V. T., Michalak, G. J., Hansen, D. C., Deisher, A. J., Kruse, J. J., Krauss, B., Muren, L. P., Petersen, J. B. B. & McCollough, C. H. (2017). Validation of proton stopping power ratio estimation based on dual energy ct using fresh tissue samples, *Physics in Medicine & Biology* **63**(1): 015012.
URL: *http://stacks.iop.org/0031-9155/63/i=1/a=015012*

Taasti, V. T., Petersen, J. B. B., Muren, L. P., Thygesen, J. & Hansen, D. C. (2016). A robust empirical parametrization of proton stopping power using dual energy CT, *Medical Physics* **43**(10): 5547–5560.
DOI: *10.1118/1.4962934*

Talamonti, C., Bruzzi, M., Bucciolini, M., Carpinelli, M., Cirrone, G. A. P. et al. (2012). Prima proton imaging for clinical application, *2012 IEEE Nuclear Science Symposium and Medical Imaging Conference Record (NSS/MIC)*, pp. 2218–2221.
DOI: *10.1109/NSSMIC.2012.6551505*

Tambave, G., Alme, J., Barnaföldi, G., Barthel, R., van den Brink, A., Brons, S., Chaar, M., Eikeland, V., Genov, G., Grøttvik, O. et al. (2019). Characterization of monolithic CMOS pixel sensor chip with ion beams for application in particle computed tomography, *Nuclear Instruments and Methods in*

Physics Research Section A: Accelerators, Spectrometers, Detectors and Associated Equipment **958**: 162626.
DOI: *10.1016/j.nima.2019.162626*

Tanabashi, M., Hagiwara, K., Hikasa, K., Nakamura, K., Sumino, Y. et al. (2018). Review of particle physics, *Phys. Rev. D* **98**: 030001.
DOI: *10.1103/PhysRevD.98.030001*

Tassan-Got, L. (2002). A new functional for charge and mass identification in δe-e telescopes, *Nuclear Instruments and Methods in Physics Research Section B: Beam Interactions with Materials and Atoms* **194**(4): 503 – 512.
DOI: *10.1016/S0168-583X(02)00957-6*

Taylor, J. T., Poludniowski, G., Price, T., Waltham, C., Allport, P. P. et al. (2016). An experimental demonstration of a new type of proton computed tomography using a novel silicon tracking detector, *Medical Physics* **43**(11): 6129.
DOI: *10.1118/1.4965809*

Testa, M., Schümann, J., Lu, H.-M., Shin, J., Faddegon, B., Perl, J. & Paganetti, H. (2013a). Experimental validation of the topas monte carlo system for passive scattering proton therapy, *Med Phys* **40**(12): 121719.
DOI: *10.1118/1.4828781*

Testa, M., Verburg, J. M., Rose, M., Min, C. H., Tang, S., Bentefour, E. H., Paganetti, H. & Lu, H.-M. (2013b). Proton radiography and proton computed tomography based on time-resolved dose measurements, *Physics in Medicine and Biology* **58**(22): 8215.
DOI: *10.1088/0031-9155/58/22/8215*

Torikoshi, M., Tsunoo, T., Sasaki, M., Endo, M., Noda, Y., Ohno, Y., Kohno, T., Hyodo, K., Uesugi, K. & Yagi, N. (2003). Electron density measurement with dual-energy x-ray CT using synchrotron radiation, *Physics in Medicine and Biology* **48**(5): 673.
DOI: *10.1088/0031-9155/48/5/308*

Tripathi, R., Cucinotta, F. A. & Wilson, J. W. (1996). Accurate universal parameterization of absorption cross sections, *Nuclear Instruments and Methods in Physics Research Section B: Beam Interactions with Materials and Atoms* **117**(4): 347 – 349.
DOI: *10.1016/0168-583X(96)00331-X*

Tschalär, C. & Maccabee, H. D. (1970). Energy-straggling measurements of heavy charged particles in thick absorbers, *Phys. Rev. B* **1**: 2863–2869.
DOI: *10.1103/PhysRevB.1.2863*

Tschalär, C. (1968). Straggling distributions of large energy losses, *Nuclear Instruments and Methods* **61**(2): 141 – 156.
DOI: *10.1016/0029-554X(68)90535-1*

Uzunyan, S. A., Blazey, G., Boi, S., Coutrakon, G., Dyshkant, A. et al. (2015). Development of a proton ct head scanner, *2015 IEEE Nuclear Science Symposium and Medical Imaging Conference (NSS/MIC)*, pp. 1–2.
DOI: *10.1109/NSSMIC.2015.7582123*

Vavilov, P. (1957). Ionization losses of high-energy heavy particles, *Sov. Phys. JETP* **5**: 749–751.

Verburg, J. M., Shih, H. A. & Seco, J. (2012). Simulation of prompt gamma-ray emission during proton radiotherapy, *Physics in Medicine and Biology* **57**(17): 5459–5472.
DOI: *10.1088/0031-9155/57/17/5459*

Verburg, J. M., Testa, M. & Seco, J. (2015). Range verification of passively scattered proton beams using prompt gamma-ray detection, *Physics in Medicine and Biology* **60**(3): 1019.
DOI: *10.1088/0031-9155/60/3/1019*

Volz, L., Collins-Fekete, C.-A., Piersimonii, P., Johnson, R. P., Bashkirov, V., Schulte, R. & Seco, J. (2017). Stopping power accuracy and spatial resolution of helium ion imaging using a prototype particle ct detector system, *Current Directions in Biomedical Engineering* **3**(2): 401–404.
DOI: *10.1515/cdbme-2017-0084*

Volz, L., Collins-Fekete, C.-A., Sølie, J. R. & Seco, J. (2020a). Theoretical considerations on the spatial resolution limit of single-event particle radiography, *Biomedical Physics & Engineering Express* **6**(5): 055002.
DOI: *10.1088/2057-1976/ab9c3f*

Volz, L., Kelleter, L., Brons, S., Burigo, L., Graeff, C., Niebuhr, N. I., Radogna, R., Scheloske, S., Schömers, C., Jolly, S. & et al. (2020b). Experimental exploration of a mixed helium/carbon beam for online treatment monitoring in carbon ion beam therapy, *Physics in Medicine & Biology* **65**(5): 055002.
DOI: *10.1088/1361-6560/ab6e52*

Volz, L., Piersimoni, P., Bashkirov, V. A., Brons, S., Collins-Fekete, C.-A., Johnson, R. P., Schulte, R. W. & Seco, J. (2018). The impact of secondary fragments on the image quality of helium ion imaging, *Physics in Medicine & Biology* **63**(19): 195016.
DOI: *10.1088/1361-6560/aadf25*

Volz, L., Piersimoni, P., Johnson, R. P., Bashkirov, V. A., Schulte, R. W. & Seco, J. (2019). Improving single-event proton CT by removing nuclear interaction events within the energy/range detector, *Physics in Medicine & Biology* **64**(15): 15NT01.
DOI: *10.1088/1361-6560/ab2671*

Wang, D., Mackie, T. R. & Tomé, W. A. (2012). On proton CT reconstruction using MVCT-converted virtual proton projectionsa), *Medical Physics* **39**(6): 2997–3008.
DOI: *10.1118/1.4711752*

Welsh, J. S., DeJongh, F., Rykalin, V., Karonis, N., DeJongh, E., Coutrakon, G., Ordonez, C., Winans, J. & Pankuch, M. (2017). Image reconstruction with a fast, monolithic proton radiography system, *International Journal of Radiation Oncology * Biology * Physics* **99**(2): E737–E738.
DOI: *10.1016/j.ijrobp.2017.06.2376*

White, D. R., Woodard, H. Q. & Hammond, S. M. (1987). Average soft-tissue and bone models for use in radiation dosimetry, *The British Journal of Radiology* **60**(717): 907–913.
DOI: *10.1259/0007-1285-60-717-907*

Wieser, H.-P., Cisternas, E., Wahl, N., Ulrich, S., Stadler, A. et al. (2017). Development of the open-source dose calculation and optimization toolkit matrad, *Medical Physics* **44**(6): 2556–2568.
DOI: *10.1002/mp.12251*

Williams, D. C. (2004). The most likely path of an energetic charged particle through a uniform medium, *Physics in Medicine and Biology* **49**(13): 2899.
DOI: *10.1088/0031-9155/49/13/010*

Wilson, J. W. (1983). Heavy ion transport in the straight ahead approximation, *NASA Technical Paper* **2178**.
URL: *https://ntrs.nasa.gov/search.jsp?R=19830020898*

Wilson, R. R. (1946). Radiological use of fast protons, *Radiology* **47**(5): 487–491.
DOI: *10.1148/47.5.487*

Winkelmann, T., Cee, R., Haberer, T., Naas, B., Peters, A., Scheloske, S., Spädtke, P. & Tinschert, K. (2008). Electron cyclotron resonance ion source experience at the heidelberg ion beam therapy center, *Review of Scientific Instruments* **79**(2): 02A331.
DOI: *10.1063/1.2823952*

Winkelmann, T. W., Cee, R., Haberer, T., Naas, B., Peters, A., Schreiner, J. & Ritter, E. (2014). Status report at the heidelberg ion-beam therapy (hit) ion sources and the testbench. Proceedings of the ECRIS-2014 conference in Nizhny Novgorod, Russia.
URL: *https://accelconf.web.cern.ch/ECRIS2014/papers/mopph004.pdf*

Wohlfahrt, P., Möhler, C., Stützer, K., Greilich, S. & Richter, C. (2017a). Dual-energy ct based proton range prediction in head and pelvic tumor patients, *Radiotherapy and Oncology* **125**(3): 526 – 533.
DOI: *10.1016/j.radonc.2017.09.042*

Wohlfahrt, P., Möhler, C., Hietschold, V., Menkel, S., Greilich, S., Krause, M., Baumann, M., Enghardt, W. & Richter, C. (2017b). Clinical implementation of dual-energy ct for proton treatment planning on pseudo-monoenergetic ct scans, *International Journal of Radiation Oncology*Biology*Physics* **97**(2): 427 – 434.
DOI: *10.1016/j.ijrobp.2016.10.022*

Wohlfahrt, P. & Richter, C. (2020). Status and innovations in pre-treatment ct imaging for proton therapy, *The British Journal of Radiology* **93**(1107): 20190590. PMID: 31642709.
DOI: *10.1259/bjr.20190590*

Woodard, H. Q. & White, D. R. (1986). The composition of body tissues, *The British Journal of Radiology* **59**(708): 1209–1218.
DOI: *10.1259/0007-1285-59-708-1209*

Worstell, W. A., Adams, B. W., Aviles, M., Bond, J., Cascio, E. et al. (2019). First results developing time-of-flight proton radiography for proton therapy applications, *in* T. G. Schmidt, G.-H. Chen & H. Bosmans (eds), *Medical Imaging 2019: Physics of Medical Imaging*, Vol. 10948, International Society for Optics and Photonics, SPIE, pp. 101 – 109.
DOI: *10.1117/12.2511804*

Yang, M., Virshup, G., Clayton, J., Zhu, X. R., Mohan, R. & Dong, L. (2010). Theoretical variance analysis of single- and dual-energy computed tomography methods for calculating proton stopping power ratios of biological tissues, *Physics in Medicine and Biology* **55**(5): 1343.
DOI: *10.1088/0031-9155/55/5/006*

Yang, M., Zhu, X. R., Park, P. C., Titt, U., Mohan, R., Virshup, G., Clayton, J. E. & Dong, L. (2012). Comprehensive analysis of proton range uncertainties related to patient stopping-power-ratio estimation using the stoichiometric calibration, *Physics in Medicine and Biology* **57**(13): 4095–4115.
DOI: *10.1088/0031-9155/57/13/4095*

Zeitlin, C. & La Tessa, C. (2016). The role of nuclear fragmentation in particle therapy and space radiation protection, *Frontiers in Oncology* **6**: 65.
DOI: *10.3389/fonc.2016.00065*

Zhu, J. & Penfold, S. N. (2016). Review of 3d image data calibration for heterogeneity correction in proton therapy treatment planning, *Australasian Physical & Engineering Sciences in Medicine* **39**(2): 379–390.
DOI: *10.1007/s13246-016-0447-9*

Zygmanski, P., Gall, K. P., Rabin, M. S. Z. & Rosenthal, S. J. (2000). The measurement of proton stopping power using proton-cone-beam computed tomography, *Physics in Medicine and Biology* **45**(2): 511.
DOI: *10.1088/0031-9155/45/2/317*